Simulating molecular cloud regulated star formation in Galaxies

Booth, Craig Martin

Simulating Molecular Cloud Regulated Star Formation in Galaxies

by Craig Martin Booth

A thesis submitted to the University of Durham
in accordance with the regulations for
admittance to the Degree of Doctor of Philosophy.

Department of Physics
University of Durham
January 2007

Simulating Molecular Cloud Regulated Star Formation in Galaxies

Craig Martin Booth

Abstract

This thesis is primarily concerned with understanding the process of galaxy formation via the simulation of the interstellar medium, star formation and supernova feedback. In order to probe galaxy formation it is necessary that we first obtain a basic knowledge of the cosmological framework in which we are working. Therefore in chapter 1 we provide a brief overview of the salient features of the current cosmological paradigm in addition to discussing in some detail the physics of the interstellar medium

In chapter 2 we focus on the numerical methods necessary to perform accurate cosmological simulations. We begin by providing an overview of the different simulation techniques currently in use in the field before performing comparisons of two simulation codes that work via two completely different methods. We then introduce a code for generating high-resolution initial conditions for the simulation of individual objects and investigate the numerical effects of mass resolution in cosmological simulation.

In chapter 3 we describe a statistical model of the interstellar medium, in which the conversion of cooling gas to stars in the multiphase interstellar medium is governed by the rate at which molecular clouds are formed and destroyed. In the model, clouds form from thermally unstable ambient gas and get destroyed by star formation, feedback and thermal conduction.

In chapter 4 this statistical model is applied to the simulation of isolated disk galaxies. We show that it naturally produces a multiphase medium with cold clouds, a warm disk and hot supernova bubbles. We illustrate this by evolving an isolated Milky Way-like galaxy. Many observed properties of disk galaxies are reproduced well, including the molecular cloud mass spectrum, the molecular fraction as a function of radius, the Schmidt law, the stellar density profile and the appearance of a galactic fountain.

Finally in chapter 5 we perform an investigation into more dynamic situations, namely the evolution of gravitationally interacting disk galaxies and the formation of a galaxy in a fully cosmological simulation. It is found that the sticky particle model does a good job of reproducing many of the observed properties of interacting galaxies, including the properties of the ISM in the resulting elliptical galaxy.

Contents

List of Figures

List of Tables

Declaration

The work described in this thesis was undertaken between 2003 and 2006 while the author was a research student under the supervision of Dr. Tom Theuns in the Department of Physics at the University of Durham. This work has not been submitted for any other degree at the University of Durham or any other University.

Chapter 3 and 4 of this thesis have been published in the form of a paper

- Booth C. M., Theuns T., Okamoto T., "Simulating Molecular Cloud Regulated Star Formation in Galaxies", MNRAS, 376, 1588

The simulations from chapter 2 have been used in the following paper

- Brooks A.M. , Governato F., Booth C. M., Willman B., Gardner J.P., Wadsley J., Stinson G., Quinn T., "The Origin and Evolution of the Mass-Metallicity Relationship for Galaxies: Results from Cosmological N-Body Simulations", ApJL, 655, L17

Acknowledgements

My time in Durham surely ranks amongst the happiest periods of my life and for this I am indebted to a great many people.

This thesis is dedicated firstly to Tom Theuns, who has had a profound effect on my development over the past three and a half years. I could not imagine working alongside a better advisor and teacher. Secondly to my officemates – and hopefully still friends after the stresses of the thesis writing process! – Greg Davies, John Helly, Mark Swinbank and Kristen Coppin who have always been ready with helpful words and stimulating discussion. Between them they have made life in the office an absolute pleasure.

Many thanks must also go to my friends, who never fail to brighten a dull day, and whose company has made even the most testing times at work enjoyable. In alphabetical order particular credit must go to: Rob Crain, Claudio Dalla Vecchia, Jim Geach, Geraint Harker, Noam Libeskind, Jim Mullaney, Mark Norris, Chris Power, David Radburn-Smith, Nic Ross, John Stott and Dave Wake.

It is, perhaps, inevitable that I have neglected somebody in this list so if you stumble over this thesis and feel deeply upset that you are absent try not to hold it against me. It wasn't personal, I promise.

Nothing I have done over the past few years would have been possible without my family, who have patiently supported me at all stages of this long journey and from the youngest age have nurtured in me an attitude of playful scientific discovery and love of learning. Finally – and most of all – this thesis is for Gemma Harrison, who makes the universe worth studying.

Thank you!

Chapter 1 | *Introduction*

1.1 Background

The main thrust of this thesis is to obtain an understanding of the physics that is important to the formation, evolution and dynamics of galaxies by using large-scale computer simulations. In order to understand galaxy formation it is necessary that we first obtain a basic knowledge of the cosmological framework in which we are working, both in order to understand the physical conditions in which galaxies are thought to form and so that we can assess the impact of galaxies on the surrounding universe. In this chapter we will therefore outline the basic features of the hot Big Bang (BB) model and the physical mechanisms by which the observable structure in the universe today came to be formed. We will see that although it is possible to summarise the properties of the universe at very early times using only a few equations and constants, the evolution of these initial conditions exhibits an inexorable march from simplicity to complexity, until the universe we see today is an immeasurably intricate and complex place.

We begin by sketching some of the notable turning points in the history of the study of the universe, before reviewing the current state of the Hot BB theory. Finally we address in some detail the features of galaxies that are most relevant to this thesis. Notably, the properties of the interstellar medium in galaxies, and the process of star formation.

1.1.1 The Development of the Hot Big Bang Model

The universe is the sum of all matter that exists and the space in which all events occur or could occur. Cosmology, taken as a whole, is the study of the origin and evolution of the universe. The study of cosmology has a long history involving science, philosophy, and religion and is amongst the oldest of humanity's pursuits. We are concerned with *physical cosmology*, the application of the principles of physics to the universe at large. The first application of modern physics to cosmology occurred with Isaac Newton's 1687 publication of *Principia Mathematica* and his use of the theory of gravity to

explain the motions of celestial bodies. One fundamental difference between Newton's cosmology and those preceding it was the application of the Copernican principle (no 'special' observers should be proposed and so bodies both on and off the earth should be subject to the same physical laws). Newton believed that the Universe must be both infinite and static. If the distribution of matter did not extend forever, he realised, then it would inevitably collapse inwards due to its own self-gravity. One major objection to this model of the universe was popularised by Heinrich Wilhelm Olbers in 1824 (although first proposed by Kepler in 1610) and is now known as *Olbers' paradox*

Olbers argued that if we live in an infinite, transparent universe filled with stars, then in any direction one looks in the night sky, one's line of sight will fall on the surface of a star. This implies that the sky should have a uniform brightness, equal in luminosity to the surface of a star. This fact is in obvious disagreement with the fact that the night sky is dark. This argument was so strong that it puzzled scientists for over 75 years. Surprisingly, the first essentially correct solution to this paradox came from the author and poet Edgar Allan Poe in his 1847 poem 'Eureka':

> *"Were the succession of stars endless, then the background of the sky would present us an uniform luminosity, like that displayed by the Galaxy – since there could be absolutely no point, in all that background, at which would not exist a star. The only mode, therefore, in which, under such a state of affairs, we could comprehend the voids which our telescopes find in innumerable directions, would be by supposing the distance of the invisible background so immense that no ray from it has yet been able to reach us at all. That this may be so, who shall venture to deny?"*

Poe argues that since light has a finite speed and the universe is not infinitely old, the light from the most distant sources has not yet reached us. This solution was put forward independently on a firmer scientific basis by Kelvin (1901). These first arguments against the idea of an infinite, static universe marked the beginnings of an investigation into to the properties and dynamics of a constantly evolving universe, governed by the laws of physics.

Modern scientific cosmology is usually considered to have started with Albert Einstein's publication of the theory of general relativity (Einstein (1916)), in which he wrote down the field equations that describe the relationship between space-time and matter-energy. The most fundamental assumption of cosmology from the days of Einstein through to the 1980's was that the universe is both *homogeneous* and *isotropic* on large

scales, this assumption became such a necessary part of virtually all cosmological models that it is known as the cosmological principle (however, see section 1.1.2, for a discussion of inflationary theory, which may provide a physical explanation for the observed isotropy and homogeneity of the universe)

In 1935 A. G. Walker and H. P. Robertson independently found a metric that determines the space-time interval between two events in a dust filled universe that obeys the cosmological principle. These models were first studied in detail by A. Friedmann in 1922 (and independently by G. Lemaitre in 1927) who solved Einstein's field equations for an isotropic, homogeneous universe to obtain what are now known as the Friedmann equations

$$H^2 \equiv \left(\frac{\dot{a}}{a}\right)^2 = \frac{8\pi G}{3}\rho + \frac{\Lambda}{3} - \frac{kc^2}{a^2} \tag{1.1}$$

$$\frac{\ddot{a}}{a} = \frac{4\pi G}{3}(\rho + 3p) + \frac{\Lambda}{3}\,. \tag{1.2}$$

In these equations the matter in the universe is described as a fluid with density ρ and pressure p. The universe has curvature k and expansion factor $a = a(t)$ is normalised such that a at the present epoch is unity. c represents the speed of light and Λ represents a constant arbitrarily added by Einstein to his original formulation of General relativity in order to allow that the Universe is static. H is the Hubble constant that characterises the rate of expansion of the Universe

The Friedmann equations reveal the astonishing fact that there is a connection between the density of the universe and its geometry. Assuming that the cosmological constant is zero then for any given expansion rate there is a corresponding critical density, ρ_c, that will yield $k = 0$, given by

$$\rho_c(t) = \frac{3H(t)^2}{8\pi G}\,. \tag{1.3}$$

The ultimate behaviour of the universe depends on its mean density. If $\rho < \rho_c$, then the universe is unbound and a can continue to increase to infinity. If $\rho > \rho_c$ then the universe is bound and a inevitably collapses to 0. The ratio of the average density to the critical density is an often used quantity so we define

$$\Omega_X = \frac{\rho_X}{\rho_c}\,, \tag{1.4}$$

where ρ_X represents the density of a particular component of the universe (e.g. baryons (b), cold dark matter (c), radiation (r) or dark energy (Λ)). The total density parameter is represented by Ω_0.

Despite this theoretical work on the evolution of an isotropic, homogeneous universe, observational results about the distribution of matter in the universe were still few and far between. In 1916, when Einstein published the theory of general relativity the phrase 'the large-scale distribution of matter' was generally taken to mean the distribution of stars in the Milky Way galaxy (Peebles (1981)). The nature and distribution of 'spiral nebulae' was uncertain, as was whether or not they were associated with the Milky Way or if they were 'island universes' completely decoupled from our galaxy (Kant (1798)) . It was not until the pioneering work of Hubble (1929b) who, following the discovery of a relation between the periodicity of a pulsating Cepheid variable star and its magnitude, was able to use Cepheid variables as sources of known luminosity and discovered that the distance to the nearby galaxy M31 was approximately 275kpc, and therefore external to the Milky Way, which was known to be less than 100kpc across. This marked the first time that any object had been conclusively proven to lie outside of our galaxy.

It was in the same year that Hubble proved conclusively that at least one spiral nebula was of extragalactic origin that he also demonstrated a linear relationship between the redshift of the emission lines in the spectra of other galaxies (Hubble (1929a)), defined as

$$z = \frac{\lambda_{obs} - \lambda_{lab}}{\lambda_{lab}} = \frac{\Delta\lambda}{\lambda}, \tag{1.5}$$

where z is the redshift, λ_{obs} is the wavelength at which a feature is observed and λ_{lab} is the wavelength the same feature has in the laboratory. It is natural to interpret redshifts as being due to the Doppler shift of the light from the galaxy due to the motion of the galaxies away from us. Hubble's law is written

$$v = Hd, \tag{1.6}$$

where v represents the recessional velocity of other galaxies and d represents their distance from us. H, the constant of proportionality, is the Hubble constant as first introduced in equation 1.1. This discovery indicated that the universe was expanding, providing evidence for the usefulness of the Friedman solutions.

The Hubble law also fits with the concept of homogeneity, it is easy to show that if the Hubble law holds for some observer, A, moving with the Hubble flow it must also hold for all other observers moving with the same flow, this is consistent with the Copernican principle. To demonstrate this consider figure 1.1. Each of the three points represents a different observer. If the observer at position $\mathbf{r}_a$ observes the Hubble law to be true, that

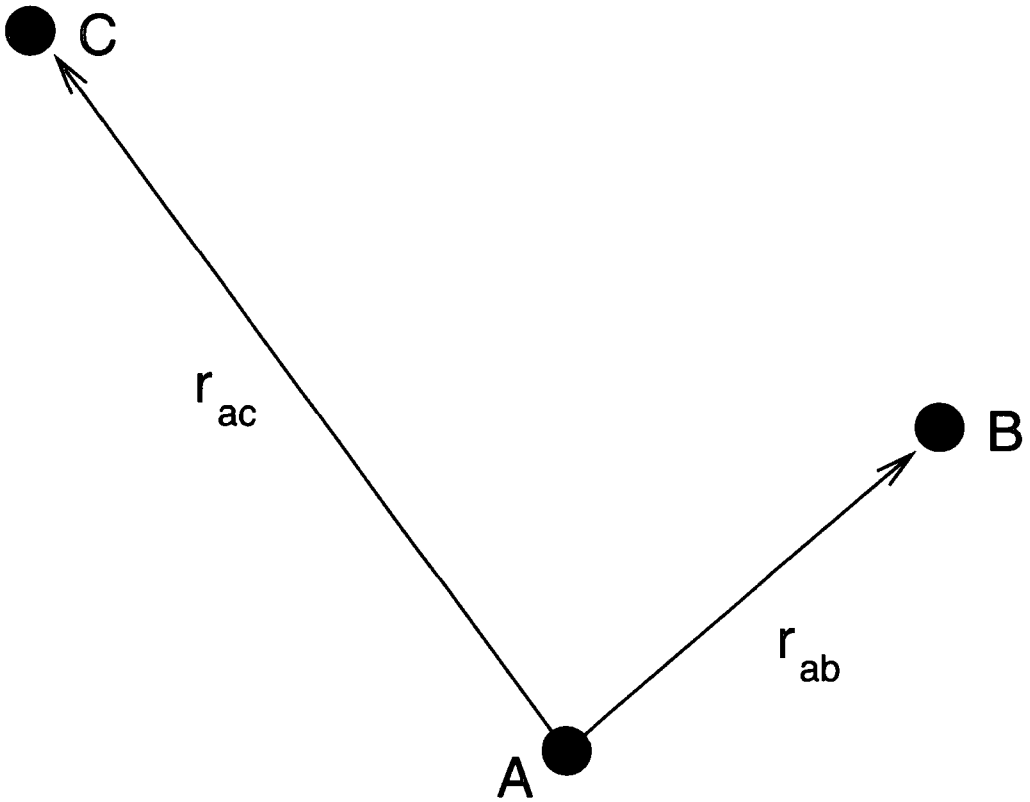

Figure 1.1: Demonstration of the Hubble law. Considering three observers, A, B and C we can show that if the Hubble law holds for any one of the observers then it must necessarily hold for the others.

is

$$\mathbf{v}_{ab} = H\mathbf{r}_{ab}\,, \tag{1.7}$$

and

$$\mathbf{v}_{ac} = H\mathbf{r}_{ac} \tag{1.8}$$

where $\mathbf{v}_{ab}$ is the relative velocity between observer A and observer B. By a simple piece of vector addition we can see that the Hubble law also holds between points b and c,

$$\mathbf{v}_{bc} = H\mathbf{r}_{ab} - H\mathbf{r}_{ac} = H\mathbf{r}_{bc}\,. \tag{1.9}$$

The Hubble law is therefore consistent with the concept of homogeneity.

The ideas of homogeneity and isotropy, when coupled with Einstein's theory of general relativity provide a coherent picture of the universe in which at early times the Universe was small, dense and hot and has expanded and cooled through to the present day. In the following sections we will flesh out the BB paradigm by working chronologically from very early times (10^{-32}s after the BB) to the present day, highlighting some of

the physical mechanisms that operated to form the rich variety of structure we observe today.

1.1.2 The Early Evolution of the Universe

In the following two sections we will detail some of the major features of the evolution of the Universe in a chronological order. The cutoff between the 'early' evolution of the universe and the 'late' evolution is somewhat arbitrary, and has been chosen to correspond to a time shortly after the time at which the cosmic microwave background was formed. This roughly represents the boundary between the parts of the evolution of the universe we can treat analytically (early times) and those that we are forced to treat with numerical tools (late times). In our discussion of the early evolution of the Universe we will consider three different physical processes, each of which represents a fundamental change in the makeup of the Universe. These processes are inflation, nucleosynthesis and decoupling.

Inflation

Despite the great successes of the BB theory in explaining the relative abundances of chemical elements and the existence of the CMB (see the rest of this section), in the early 90's BB theory was plagued by a number of serious problems. In this section we will discuss three of these problems and introduce a period of *inflation* as a possible solution.

The Flatness Problem: It has been known for a long time that the present day mean density of the Universe – parameterised by Ω_0 – is at least to order of magnitude, unity. However, the $\Omega_0 = 1$ universe is unstable. In its very early history, an Ω_0 only very slightly above 1 would have resulted in a very rapid big crunch, while with an Ω_0 only very slightly below 1, the universe would have expanded so fast that stars and galaxies could not have formed. The fact that approximately 13.7 billion years after its formation, the universe still has a value of Ω_0 so close to unity indicates that Ω_0 must have been within one part in 10^{22} (Peacock (1999)) of unity at early times. We can demonstrate this by substituting an expression for Ω_0 into the Friedman equations to obtain

$$\Omega(t)_0 - 1 = \frac{kc^2}{\dot{a}^2}\,. \tag{1.10}$$

Dividing this into the result at the present epoch we obtain

$$\Omega(t)_0 - 1 = \frac{\dot{a_0}^2}{\dot{a}^2}\,. \tag{1.11}$$

Putting in numbers here (Assuming $a \propto t^{1/2}$, i.e. the Universe is dominated by radiation) at this epoch we obtain that $\dot{a}_0^2/\dot{a}^2 < 10^{-48}$. In other words $|\Omega_0 - 1|$ is extremely finely tuned to zero. The problem is that a simple BB theory cannot explain how an Ω_0 so close to unity could arise, the fine tuning of this parameter is indicative of hidden physics.

The Horizon Problem: This problem relates to the uniformity of the CMB (Partridge and Wilkinson (1967); Misner (1968); section 1.1.2). In a BB with only matter and radiation, two widely separated regions (e.g. the regions probed by two patches of the CMB separated by 180 degrees on the sky) will never have been in causal contact (that is, at no point in the history of the Universe will it have been possible for a photon to travel from one region to the other). If two regions cannot have interacted at any point in the past then they should not have been able to smooth out any irregularities in the CMB. This is in contradiction with the observation that the CMB is isotropic and homogeneous to better than one part in 100000 (Smoot et al. (1992))

The Magnetic Monopole Problem: Grand unified theories (GUT) predict the existence of topological defects and massive relic particles, notably magnetic monopoles ('t Hooft (1974)). These particles are expected to form at around the GUT scale ($t \sim 10^{-35}$s). If no more than one monopole forms per horizon scale then the mean density of the Universe would be so high that it would recollapse within $\sim 10^5$ years (Narlikar and Padmanabhan (1991)). Inflation was suggested as a solution to these problems by Guth (1981). According to Guth the BB picture is essentially correct, but with the addition of an *inflationary phase* during which the Universe expands exponentially (as in the classical de Sitter (1917) model) for a short period of time.

The theory of inflation posits that the universe underwent a period of exponential growth ($a \propto e^{Ht}$) within the first 10^{-32}s. This exponential expansion was theorised to occur due to the presence of a quantum scalar field in the early universe (the *inflaton*). In the original models of Guth this scalar field, ϕ, has a potential, $V(\phi, T)$, that depends upon temperature such that at $T \gg T_c$ (where T_c is some critical temperature), the field has one minimum at $\phi = 0$. As the temperature of the Universe decreases the shape of the potential changes until at $T = T_c$ the potential has two minima, and at $T \ll T_c$ the minimum potential is actually at some finite value of ϕ. When this happens, the system is in a state of 'false vacuum', and over the course of time, thermal fluctuations and quantum tunnelling will move the scalar field from $\phi = 0$ to the new, lower potential state, For the time during which the universe is in the 'false vacuum' state, the potential difference between the true vacuum and the false vacuum is the dominant energy

density in the universe and it behaves like a de Sitter universe.

A thorough calculation reveals that Guth's original model does not work (Guth (1983b)), since if the false vacuum is stable for long enough to inflate the universe, the phase transition will proceed in a patchy manner and lead to an inhomogeneous universe incompatible with observations.

Many improvements on the standard model of inflation have been suggested, from changes in the form of the potential (e.g. Linde (1982a,b)), to chaotic inflation whereby the initial value of the potential is slightly different from zero and it slowly 'rolls' to the zero potential (Linde (1983)).

A period of inflation can solve each of the three problems presented so far. The horizon problem is solved because regions outside of each others horizon at the time of CMB emission ($z \sim 1000$) are in contact during the inflationary, de Sitter period and so can thermalize. A period of inflation also has the effect of smoothing out any regions of curvature, forcing that $\Omega_0 \approx 1$.

The temperatures at which magnetic monopoles and other exotic relics would be expected to be produced are greater than $T \sim 10^{27}$K ($t \sim 10^{-34}$s), inflation occurs after this time and is thought to double the Universe in size roughly 60 times (Peacock (1999)) from a size of $\sim 10^{-25}$m to around $\sim 10^{-7}$m, diluting the density of relic particles so that we would never expect to observe them.

Probably the most compelling feature of inflation theory is that it provides a natural mechanism for generating tiny fluctuations in the initial density field due to quantum thermal fluctuations present in any de Sitter universe. The form of these fluctuations was first calculated by four groups working independently (Hawking (1982); Bardeen et al. (1983); Starobinsky (1982); Guth (1983a)), who predicted that the spectrum of perturbations laid down by inflation would be that of a *nearly scale-invariant Gaussian random field* (see section 2.4). The properties of Gaussian random fields are discussed in great detail by Bardeen et al. (1986); a Gaussian random field is defined as any random field for which each value is drawn independently from a Gaussian probability density function. The properties of a Gaussian random field are specified entirely by its power spectrum and in the case of cosmological initial conditions the field is thought to have the form

$$P(k) = Ak^{n_s} . \tag{1.12}$$

This prediction has been borne out by the WMAP Cosmic Microwave Background experiment (Spergel et al. (2003, 2006)), which by probing the statistical distribution of density

perturbations at the time of decoupling found that the spectral index, n_s, which is 1 for a scale invariant field, and is predicted to be between 0.92 and 0.98 by simple models of inflation (Steinhardt (2004)), was found to be 0.95. Additionally galaxy surveys (e.g. York et al. (2000)) show galaxy clustering properties consistent with a spectrum of perturbations of this form. These experiments are important confirmations of the theory of inflation and show that the form of the initial density perturbations in the Universe is very close to that predicted by inflation. Other methods of fluctuation generation, for example cosmic strings (Albrecht and Stebbins (1992)) and global textures (Park et al. (1991)) do not make such predictions for the form of the initial density perturbations.

It is worth noting, however, that currently inflation theory is understood principally in terms of its predictions for the initial conditions of the hot, early universe. Despite having passed many observational tests, the physics in inflation theory is still largely *ad hoc* modelling and as such there are open questions about the theory, particularly with regards to the hypothesised inflaton field, which does not currently fit into the standard model of particle physics

Big Bang Nucleosynthesis

The mechanism of stellar nucleosysnthesis (the fusing of primordial hydrogen into heavier elements) was first discussed by Salpeter (1952) and Burbidge et al. (1957), who found that if stellar nucleosynthesis were the only mechanism by which elements heavier than hydrogen could be formed then we vastly under-predict the abundance of Helium, which makes up over 20% of the observable Universe.

The hot, dense universe predicted by the BB model at early times provides an ideal mechanism for generation of the primordial mix of heavy elements we observe. This process is reviewed thoroughly by Boesgaard and Steigman (1985) and sketched only in the barest detail here.

At a temperature of just below 10^{12}K, the universe contained a mixture of photons, electron-positron pairs, and neutrinos. There was also a smaller number of protons and neutrons that were constantly transformed into each other[1]. As long as the rate of the reactions that convert protons and neutrons between each other remains high enough, the neutron-proton ratio will be described by the Boltzmann law. At 10^{12}K this ratio is 0.985. As the universe expands the reaction rates drop rapidly and the neutron-proton ratio becomes 'frozen' at the value it has when $T \approx 10^{10}$K, which was $n_n/n_p = 0.223$.

[1]the following are the important reactions $n \rightleftharpoons p^+ + e^- + \bar{\nu}_e; n + e^+ \rightleftharpoons p^+ + \bar{\nu}_e; p^+ + e^- \rightleftharpoons n + \nu_e$

At this point the universe is still too hot for heavier nuclei to form and the free neutrons continue to decay via the process

$$n \rightleftharpoons p^+ + e^- + \bar{\nu}_e \,. \tag{1.13}$$

This reaction has a half-life of 617s and continues to dominate until the temperature of the universe drops as far as 10^9K. This took approximately 229s, and the neutron-proton ratio becomes 0.213. Below 10^9K protons and neutrons readily combine to form deuterium and then helium via the following reaction chains

$$^2\mathrm{H} + {}^2\mathrm{H} \rightleftharpoons {}^3\mathrm{H} + {}^1\mathrm{H}\,, \tag{1.14}$$

$$^3\mathrm{H} + {}^2\mathrm{H} \rightleftharpoons {}^4\mathrm{He} + n\,, \tag{1.15}$$

and

$$^2\mathrm{H} + {}^2\mathrm{H} \rightleftharpoons {}^3\mathrm{He} + n\,, \tag{1.16}$$

$$^3\mathrm{He} + {}^2\mathrm{H} \rightleftharpoons {}^4\mathrm{He} + {}^1\mathrm{H}\,. \tag{1.17}$$

The buildup of large amounts of heavier elements is blocked by the fact that there are no stable elements with atomic numbers 5 or 8 at these temperatures and so only trace amounts of heavier elements (e.g. ^{7}Li and ^{7}Be) are formed (Dicus and Teplitz (1980)). Detailed calculations of the abundances of the heavier elements were carried out by Yang et al. (1984)

Detailed calculations of the predicted primordial abundances of the elements generated during this period provide a very strong test of BB theory. Although complicated by stellar nucleosynthesis the fraction of ^{4}He observed in the universe agree incredibly well with the BB predictions (see e.g. Izotov et al. (1994)). The abundances of other elements (e.g. Li) are not in such good agreement with the predictions of BBN, but it is unclear whether the origin of this discrepancy is observational, stellar, nuclear or more fundamental (Coc and Vangioni (2005)). The fact that the helium abundance in the universe never drops below 23%, no matter where it is observed is an important confirmation of the theory.

The Cosmic Microwave Background

At the present epoch, we observe a homogeneous background of electromagnetic radiation, well described by a black body with a temperature of 2.73K, which gives it a peak wavelength in the microwave section of the electromagnetic spectrum. The existence of

this cosmic microwave background (CMB) was first predicted qualitatively by Alpher et al. (1948), and observed by Penzias and Wilson (1965).

After nucleosynthesis took place and the primordial mixture of hydrogen, helium and traces of other elements were formed, the universe was made up of a hot plasma of photons, electrons and baryons. Due to the adiabatic expansion of the universe the temperature of this plasma was decreasing. When the temperature of the universe fell to approximately 3000K (redshift of $\sim$ 1100), it became favourable for protons and electrons to combine into neutral hydrogen in a process called *recombination* (Peebles (1968)).

Before this occurrence the photons are kept in thermal equilibrium with the baryons due to the large cross section for the interaction between photons and electrons (Thomson scattering). When recombination takes places this cross section drops to virtually zero and the matter and radiation fields begin to evolve independently (*decoupling* of the photons and baryons). At the moment of decoupling the spectrum of the photons is well described by a black body at a temperature of $\sim 3000K$, by the present day the radiation has been redshifted by a factor a_{dec}/a_0 and has a temperature of approximately 2.73K.

Due to the initial density perturbations put in place by a period of inflation, the CMB is not perfectly smooth, there are small fluctuations in its temperature, these fluctuations are of order one part in 100,000 (Smoot et al. (1992)). These fluctuations arise due to a large variety of physical mechanisms, some of which will be summarised here. *Primary* fluctuations are those that arise due to physical effect before or at the epoch of decoupling. *Secondary* anisotropies arise due to scattering along the line of sight. It is important to note that an accurate calculation of the effect of these perturbations requires a full numerical treatment of the Boltzmann equation (see e.g. Seljak and Zaldarriaga (1996)), so we will discuss them only qualitatively. Primary anisotropies include

- Sachs-Wolfe perturbations. Photons from high density regions at decoupling have to climb out of potential wells and so are redshifted
- Adiabatic perturbations. In high density regions, both the radiation and matter will be compressed and have a higher temperature

These effects are important for perturbations for which only gravity has been important up until the time of recombination, that is: those with wavelengths larger than the horizon size at decoupling. On smaller scales a variety of additional physical processes act on the perturbations.

Radiation pressure tends to erase anisotropies, whereas the gravitational force acts to

make baryons collapse in overdense regions. These two competing effects create acoustic oscillations, which give the CMB its characteristic peak structure. The peaks correspond, roughly, to resonances occurring during recombination when a particular mode is at its peak amplitude. The location of the first acoustic peak in the CMB spectrum depends sensitively upon the total matter density in the universe and thus its location is of crucial importance. Many experiments including Toco (Miller et al. (1999)), Boomerang (Mauskopf et al. (2000)) and Maxima-1 (Hanany et al. (2000)) were designed primarily to determine its location. In the ΛCDM model, the peak shows up right where it would be expected if the curvature of the universe was zero (i.e. $k = 0$).

Secondary anisotropies, which arise due to the interaction between the CMB photons and the intervening medium include:

- The integrated Sachs-Wolfe effect. Photons travel through evolving potential wells and are blueshifted as they fall in to the potential, then redshifted again as they climb back out. If the potential deepens as the photons are travelling through it there will be a net redshift of photons

- The Sunyaev-Zel'dovich effect (see e.g. Sunyaev and Zeldovich (1980)). Photons that interact with high energy electrons (for example those present in the hot diffuse gas of a galaxy cluster), may undergo inverse Compton scattering, in which some of the energy of the electrons is transferred to the photons, leading to an apparent upward shift in CMB temperatures in the directions of galaxy clusters. Some galaxy clusters have been observed via this effect (Birkinshaw et al. (1984))

Other secondary effects including gravitational lensing of the CMB photons can introduce non-gaussianity into the CMB spectrum, this must be carefully controlled for.

See Hu and Dodelson (2002) for a comprehensive recent review of the different mechanisms by which anisotropies are embedded in the CMB.

1.1.3 The Late Stage Evolution of the Universe

After the cosmic background radiation was decoupled from the baryonic component of the universe its subsequent evolution is governed primarily by the effects of gravity, which drives the collapse of objects on all scales, from the largest superclusters down to individual stars. In this section we investigate the process by which galaxies are formed.

Large Scale Structure Formation

Gravity causes the density perturbations laid down by inflation to amplify themselves; overdense regions tend to become more overdense and underdense regions tend to become more underdense. Over time this leads to the collapse of virialised 'haloes' of matter. These haloes continue to interact with each other gravitationally; merging hierarchically to form ever larger structures.

The formation of virialised haloes is a non-linear problem and as such we must resort to numerical tools to investigate it in detail. In section 2.2 we introduce the most widely used numerical tools, and in section 2.4 discuss the generation of the initial conditions that go into one of these codes.

The dynamics of gas in these virialised haloes is a complex and dynamic process. In this section we sketch an outline of how this dense gas is thought to form the wide variety of galaxies we see in the present day universe. In section 1.2 we will discuss the properties of the interstellar medium in present day galaxies, and in chapter 3 will investigate how this system can be simulated.

According to many recent galaxy formation models (Somerville and Primack (1999); Cole et al. (2000); Bower et al. (2006)) diffuse gas that falls into a halo is shock heated to the virial temperature of that halo. When the virial temperature of the halo (White and Rees (1978)) is high enough the gas can cool radiatively (Rees and Ostriker (1977)) and may collapse into the halo. Haloes gain angular momentum from tidal torques operating during their formation (see e.g. Mo et al. (1998)) and so the gas is accreted into the form of a disk. Dense, cold gas in the disk of a galaxy will collapse into stars (see section 1.3.1 for an overview). Various feedback processes from stars regulate the star formation rate in the galaxy (Dekel and Silk (1986)).

The dynamics and evolution of the gas in galaxies is very complex. Stars are thought to form in molecular clouds in a complex interstellar medium (ISM) in which magnetic fields (Safier et al. (1997)), cosmic rays, turbulence (Krumholz and McKee (2005)), relativistic jets (Klamer et al. (2004)), molecules, dust, and radiative transfer may all play some role. Additionally mergers between galaxies can move the gas in the galaxy far from equilibrium.

Reionization

The formation of the first stars and galaxies marks a transition between the smooth universe we have examined at high redshift and the clumpy universe we see at low redshift. It is currently thought that this occurs at redshifts ~ 50 (Reed et al. (2005b); Gao et al. (2005)).

After recombination (see 1.1.2) the hydrogen in the universe is neutral and thus absorbs photons blueward of the Lyman α line very strongly (Gunn and Peterson (1965))[2]. Neutral hydrogen therefore has the effect of efficiently absorbing all UV photons. However, modelling of the transmitted light from observed quasars implies that at least as far back as $z \leq 5.8$ the neutral fraction of hydrogen was less that 10^{-6} (Fan et al. (2000)). We therefore require some mechanism by which the neutral hydrogen that exists from $z \sim 1000$ down to $z \sim 6 - 15$ becomes ionized.

It is thought that this process occurs via the escape of ionizing photons ($h\nu \geq 13.6$eV) from the sites of star formation into the surrounding IGM. In this way each star forming object will ionize a 'bubble'of hydrogen. As the number density of star forming objects increases, ionized bubbles begin to overlap until the intergalactic medium is ionized and reionization is said to be complete.

The redshift at which reionization takes place is still uncertain, additionally reionization is a patchy process, and proceeds by stages (Gnedin (2000)). Studies of quasar spectra have placed the redshift of reionization as low as 6 (Becker et al. (2001)), the WMAP CMB experiment estimated that the redshift of reionization as $\sim 11 - 17$ (Spergel et al. (2003, 2006)), and numerical studies of reionization in ΛCDM simulations place this epoch anywhere in the range $z \sim 7 - 12$ (Haiman and Loeb (1998); Gnedin and Ostriker (1997); Gnedin (2000)).

The end of reionization marks the time at which the universe takes on the characteristics it has at a redshift of zero, with star forming galaxies merging in a hierarchical manner embedded in a highly ionized intergalactic medium.

Many open questions remain about the nature of the sources that reionized the universe. Current best estimates indicate reionization occured at $z \sim 12$ it is known that the observed number counts of high redshift galaxies and quasars could not produce enough ionizing flux to successfully reionize the universe. Other sources therefore become necessary. Some candidate objects have included population III stars and micro-quasars.

[2]This period has become known as the 'cosmic dark ages' a term originally coined by Sir. Martin Rees

21-cm hydrogren emission (Madau et al. (1997)) provides an ideal tool for probing the epoch of reionization and some of the new generation of radio telescopes (e.g. LOFAR (Zaroubi and Silk (2005))) are targeted at discriminating between these different sources and so explaining the process of reionization.

The Existence of 'Dark' Matter

Over the past century a variety of observations have suggested very strongly that a large fraction of the Universe must be in the form of 'dark' matter. That is: matter that does not emit or scatter enough electromagnetic radiation to be directly detectable.

The first evidence for a large fraction of matter in the universe being dark came from two directions almost simultaneously. On large scales it was discovered that when the virial theorem is applied to galaxy clusters (Zwicky (1933)) the observable mass in the galaxy cluster could not account for the random motions of the galaxies. On smaller scales it was found that in our own galaxy the numbers of visible stars fell short by 30-50% of adding up to the amount of matter implied by their velocities. Over the next decades evidence for a large fraction of the matter in the Universe being dark began to stack up. Rotation curves in galaxies were discovered to be flat out to large radii (Ostriker et al. (1974)), and gravitational lensing implies that there is much more mass in galaxy clusters than can be observed directly (Walsh et al. (1979)).

It is still unclear exactly what dark matter is made of. Many candidates have been suggested, these may be broadly classified into baryonic and non-baryonic candidates. Baryonic candidates are mainly classified under the umbrella term MACHOs (massive compact halo objects), a general name for any kind of astronomical body that emits little or no radiation and is present in interstellar space. Candidates for MACHOs have included black holes, neutron stars, brown dwarfs and very faint red dwarf stars. Studies of BBN have indicated that baryons do not make up enough of the universe to explain all of the missing mass. Non-baryonic candidates may be classified as 'cold','warm' or 'hot', differing from each other by the mean velocity the candidate particles have at high redshift. At least one hot dark matter candidate is known, the neutrino,although this particle is not massive enough to account for the missing mass in the universe (Goobar et al. (2006)). Additionally, hot dark matter candidates do not allow gravitational collapse on small scales due to their free-streaming motion out of small potential wells. For this reason at least some of the dark matter content of the universe is thought to be in the form of cold dark matter.

Evidence for dark matter is so strong that it has become an integral part of the modern cosmological paradigm, and has been found necessary in order for large structures to have formed by gravitational collapse over the lifetime of the universe.

The Modern Cosmological Model

Starting from the assumptions of homogeneity and isotropy and applying Einstein's theory of general relativity the BB theory provides a coherent framework within which we can make progress towards understanding the formation and evolution of galaxies.

Shortly after the BB we have seen how a period of inflation, which imprints tiny density fluctuations into the initial density field, solves many problems with the basic BB picture and provides a natural mechanism by which the seeds of the galaxies we see today can be formed. When the temperature of the universe drops enough that it is neutral then we see that the primordial radiation field is decoupled from the matter field and subsequently evolves independently. We observe this relic radiation at the present day at microwave wavelengths and it provides a strong probe of the properties of the universe.

At later times, the perturbations laid down by inflation begin to collapse gravitationally, dragging gas into their potential wells. This gas cools radiatively and some fraction of it collapses into stars. Stellar feedback processes make the resulting structure of galaxies and the ISM very complex, and very many different feedback processes operate in bringing about a stable equilibrium.

In addition to the CMB, many other observations help in constraining the properties of the Universe. These include large scale galaxy surveys (e.g. Colless et al. (2001); York et al. (2000)), which probe the clustering properties of the galaxies at low redshift and hence give us a second, independent probe of the properties of the primordial density field.

The 'Hubble key project' is an attempt to pin down the Hubble constant, H_0, through the use of Cepheid variable stars in nearby galaxies as standard candles in order to make accurate distance determinations for a sample of nearby ($\leq$ 20Mpc) galaxies (Freedman et al. (2001)). H_0 may then be probed by applying the Cepheid calibration to several secondary distance indicators (e.g. Type Ia supernovae and the Tully-Fisher relation) operating further out in the Hubble flow.

Additionally supernovae used as standard candles can tell us about the expansion properties of the universe (Branch (1998); Knop et al. (2003))

Parameter	WMAP Only	WMAP + 2dFGRS
$100\Omega_b h^2$	$2.233^{+0.072}_{-0.091}$	$2.223^{+0.066}_{-0.083}$
$\Omega_m h^2$	$0.1268^{+0.0072}_{-0.0095}$	$0.1262^{+0.0045}_{-0.0062}$
h	$0.734^{+0.028}_{-0.038}$	$0.732^{+0.018}_{-0.025}$
τ	$0.088^{+0.028}_{-0.034}$	$0.083^{+0.027}_{-0.031}$
n_s	$0.951^{+0.015}_{-0.019}$	$0.948^{+0.014}_{-0.018}$
σ_8	$0.744^{+0.050}_{-0.060}$	$0.737^{+0.033}_{-0.045}$

Table 1.1: Cosmological Parameters as derived from the WMAP 3 year results. The middle column shows the results obtained from the WMAP data alone, the right hand column shows the effect of adding the analysis of the 2dFGRS. Data adapted from Spergel et al (2006). Ω_b and Ω_m were defined by equation 1.4, h is the Hubble constant divided by 100km/s/Mpc, τ is the optical depth to the surface of last scattering, n_s is the slope of the initial density perturbation power law (equation 1.12) and σ_8 is the RMS density fluctuation in spheres of 8Mpc.

These many independent observations paint a coherent picture of a universe born in a BB, and well described by the Friedman equations. The most recent experiments to obtain the values of the constants that describe the universe include the WMAP probe (Spergel et al. (2003, 2006))

Assuming a power-law flat ΛCDM model the WMAP experiment along with other experiments as detailed above places tight constraints on the values of the cosmological parameters. Table 1.1 summarises the current WMAP estimates of these numbers, both from data from the WMAP experiment alone, and from a combination of the WMAP and 2dFGRS survey (Colless et al. (2001)), which reduces the error bars on the measurements.

Combining the WMAP results with supernova catalogues allows us to estimate that the Universe is dominated by dark energy. In combination with the Hubble key project (Mould et al. (2000)) the value of the Hubble constant can be measured with great precision.

Now that we have sketched out the primary features of a BB cosmology, the remainder of this introductory chapter will be concerned with a more detailed treatment of the properties of individual galaxies.

1.2 The Interstellar Medium

Thus far we have sketched the main features of the evolving universe from when it was a fraction of a second old down to the present day. We have not, however, looked in much detail at the properties of the gas *internal* to each galaxy. In this section we describe the properties of the interstellar medium (ISM), and the stellar content of galaxies.

1.2.1 The Components of the Interstellar Medium

According to the models of McKee and Ostriker (1977) (hereafter MO77; see also Efstathiou (2000); Monaco (2004); Krumholz and McKee (2005)) the ISM of the MW consists of at least three separate and distinct gas phases: a hot tenuous medium at a temperature of $\sim 10^6 K$; cold, dense molecular clouds at a temperature of $\leq 100K$ and a warm medium that exists at the boundaries between clouds and the hot medium with $T \sim 10^4 K$. In the MW, the hot medium has a filling factor of 70–80% and the cold clouds account for a few percent of the volume (MO77). Different techniques are used to observe these different phases, with radio observations probing roto-vibrational transitions of molecules (mainly CO), the 21-cm line probing atomic hydrogen, and UV- and X-ray observations probing the hot phase, see e.g. Binney and Merrifield (1998) for an overview and further references. The fact that different techniques are used to observe the different gas phases might exaggerate the degree to which these phases are really distinct.

Observations of star formation in the MW show that most form in groups, either as gravitationally bound clusters or unbound associations, in the most massive of the molecular clouds (Giant Molecular Clouds, hereafter GMCs), with masses $\sim 10^6 M_\odot$, and sizes of order 30-50pc, see e.g. Blitz and Thaddeus (1980) and Lada and Lada (2003) for recent reviews. The relatively small sizes of GMCs currently limit detailed observations of such clouds to nearby galaxies, with recent surveys done in the MW (Solomon et al. (1987); Heyer et al. (2001)), M33 (Rosolowsky and Blitz (2004)) and the LMC (Fukui et al. (2001)).

Blitz et al. (2006) present detailed observations of GMCs in five local galaxies. GMCs are excellent tracers of spiral structure to the extent that they are often used to *define* the location of arms, in a similar way as for example HII regions or massive stars are. There is a good correlation between GMCs and filaments of HI, although the reverse is not true, suggesting that clouds form from HI.

Observations in more distant galaxies are currently limited to measuring the mean surface density of molecular gas, with more detailed observations awaiting new instruments such as ALMA[3]. According to Young and Scoville (1991), the fraction of gas in the molecular phase depends on Hubble type, with early-type spirals tending to be predominantly molecular, and late-types atomic . Optically barred spirals show a clear enhancement of CO emission along the bar. This suggests that the large-scale structure of the galaxy affects the formation of clouds, and hence presumably also the star formation rate. A physical implementation of star formation should therefore aim to track the formation and evolution molecular clouds. A recent review of the status of three phase models of the ISM is presented by Cox (2005)

1.2.2 The Atomic Component of the Interstellar Medium

The material that makes up the majority of the volume of the ISM is a diffuse, atomic gas. Typical densities and temperatures for this phase of matter are approximately $n = 10^{-2.5}$ atoms per cubic centimetre and $T = 10^{5.7}$K (MO77). This diffuse gas phase is formed by the heating action of supernovae, and it is this phase which most supernova remnants expand into and so controls the dynamics of SN remnant expansion (for a more complete discussion on this point see section 3.2.6).

One of the major physical processes that controls the thermal properties of the atomic component of the ISM and hence the phase structure of the ISM is radiative cooling (see e.g. Black (1981); Sutherland and Dopita (1993)). The first studies in this area (Cox and Tucker (1969); Tucker and Gould (1966)) concentrated on simple, optically thin plasmas. Since then both our understanding of atomic processes and the available computing power have increased and allowed a full treatment of collisional ionization rates and other atomic processes. Sutherland and Dopita (1993) performed calculations of the radiative cooling rates of a hot astrophysical plasma in collisional ionization equilibrium. Photoionization (Seaton (1958)), electron collision ionization, charge transfer reactions and recombination radiation (Gould (1978)) were all treated in a self consistent manner for a set of 225 species of ion. The resulting cooling rates are shown in figure 1.2. Sutherland and Dopita (1993) noted that non-equilibrium effects can appreciably change the shape of the astrophysical cooling function, but only analysed these effects for a few, idealised, non-equilibrium situations. The cooling function of a primordial gas is of vital importance to the formation of galaxies as it is this cooling that determines the fraction

[3]http://www.alma.nrao.edu/

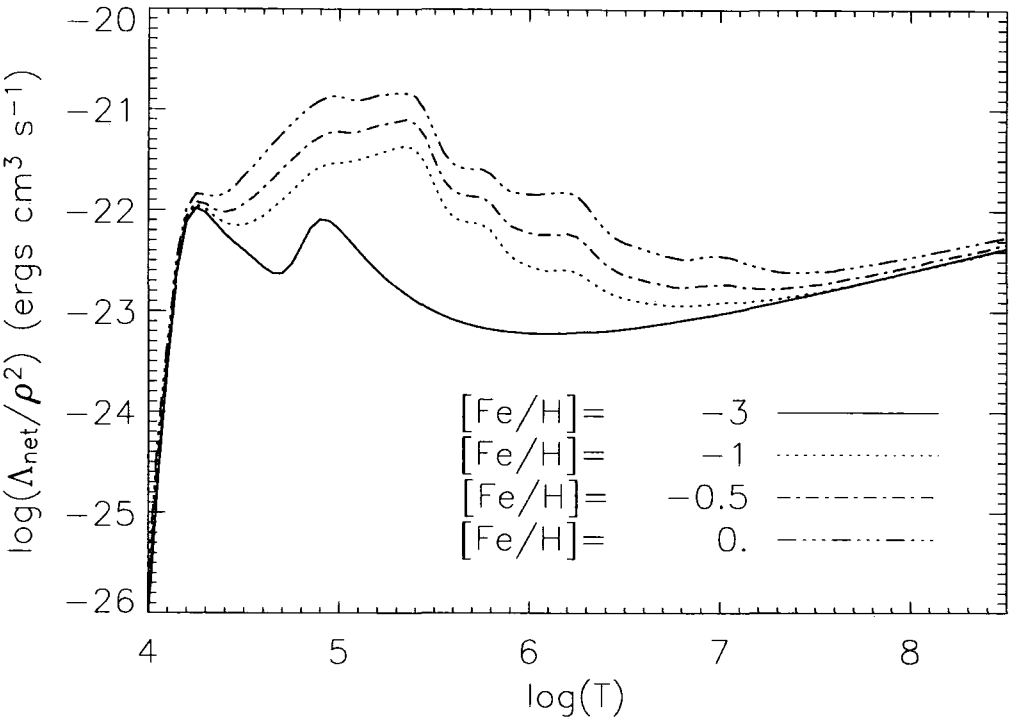

Figure 1.2: Radiative cooling rate of a gas as a function of temperature for a number of different metallicities. Data from Sutherland & Dopita (1993). The ratios between the different metal abundances are assumed to be in solar proportion. The cooling rate falls off below 10^4K due to the lack of molecular hydrogen in these calculations. The mid temperature cooling peaks are due to electron collision ionization (and associated radiation due to recombination) and at high temperatures Bremsstrahlung radiation dominates.

of gas that can cool into galactic disks and controls with great sensitivity the properties of the interstellar medium

1.2.3 The Molecular Component of the Interstellar Medium

It has long been understood that the vast majority of star formation in the Milky Way takes place inside molecular clouds (see e.g. Lada and Lada (2003) and references therein). The study of molecular clouds is therefore of critical importance in our understanding of how galaxies form and evolve. In this section we discuss the formation and properties of

molecular clouds before investigating the mechanism by which they collapse into stars in the next section.

The Formation of Giant Molecular Clouds

Although the early models by Field et al. (1969) assumed that the different phases of the ISM were in pressure equilibrium, modern observations paint a much more complex and dynamic situation, in which the ISM is shaped by turbulence, possibly powered by SNe and the large-scale dynamics of the galactic disk itself, see e.g. Burkert (2006) for a recent review. A galaxy-wide effect seems required to explain the observed Hubble-type dependence of cloud properties.

Yet how GMCs form in this complex environment is not well understood (Blitz and Rosolowsky (2004)). Some authors have suggested that GMCs form by the coagulation of preexisting molecular clouds (Kwan and Valdes (1983); Oort (1954)) while others have argued that GMCs form primarily from atomic gas through instability or large-scale shocks (Blitz and Shu (1980)), a viable mechanism by which this could occur is the formation of convergent flows induced by a passing spiral arm (Ballesteros-Paredes et al. (1999)). Of course, both modes of formation may occur: in high density regions, where the vast majority of hydrogen is molecular it seems likely that molecular clouds form from the coagulation of smaller clouds, whereas in the outskirts of galaxies where the gas is predominantly atomic the compression of gas in spiral density shock waves provides a more plausible formation mechanism.

Observationally, star formation in disks seems to occur only above a given surface-density threshold (Kennicutt (1989)), with star formation dropping abruptly below the threshold even though the gaseous disk may extend far beyond it. Schaye (2004) describes a model in which this threshold arises naturally due to the thermal instability when gas cools from 10^4 K to the cold phase ($\sim$ 100K), rendering the disk gravitationally unstable on a range of scales. This suggests that a combination of thermal instability and large-scale dynamics may be responsible for determining when and where GMCs form.

Elmegreen (2000) discusses observational evidence that GMCs are in fact short lived entities that form, make stars and disperse again on their dynamical time scale. This short time-scale alleviates the need for an internal energy source to sustain the observed internal supersonic turbulence, something that had puzzled astronomers for a long time. Pringle et al. (2001) discuss this assumption in more detail, and suggest that GMCs form from agglomeration of the dense phase of the ISM, already in molecular form, when

compressed in a spiral shock. They envisage the pre-existing molecular gas to be in dense 'wisps', in the inter arm regions, formed from atomic gas by shocks, as simulated by Koyama and Inutsuka (2000).

Recent numerical simulations support the view that when clumpy gas is overrun by a density wave, it produces structures that resemble GMCs. Wada et al. (2002) present high-resolution two-dimensional simulations of the evolution of perturbations in a cooling, self-gravitating disk in differential rotation. They show that the disk develops stationary turbulence, even without any stellar feedback. Bonnell et al. (2006) and Dobbs et al. (2006) perform three dimensional simulations of the passage of clumpy cold gas through a spiral shock. Their simulations produce dense clouds, with large internal velocity dispersion reminiscent of the 'supersonic turbulence' seen in GMCs. They note that the velocity dispersion is generated on all scales simultaneously, in contrast to what is usually meant by turbulence where energy cascades from large to small scales. Mac Low and Klessen (2004) review the current state of the art in simulations and models of GMC formation, including references to more recent work. In this picture of clouds, GMCs are temporary structures formed and dissolving in converging flows, do not require an internal source of energy, are not in virial or pressure equilibrium, and need not even be gravitationally bound. They point-out that the relative contribution of galactic rotation and stellar sources to driving the observed turbulence is not clear.

The Properties of Giant Molecular Clouds

As implied by the name, molecular clouds are dense regions consisting primarily of molecular hydrogen that forms via interaction with interstellar dust grains (Cohen (1976b)). Molecular clouds have a small spatial extent and as such are very hard to resolve. Over recent years, however, surveys of molecular clouds have been undertaken in the MW and various nearby galaxies. When it became possible to spatially resolve individual molecular clouds it was found that they do not have a simple structure, but are instead complex and dynamic objects. The study of the structure of molecular clouds is very much an active research area today. Hierarchical temperature and density peaks are known to exist within molecular clouds, with dense cores embedded within larger, less dense, molecular clumps. These less dense clumps are, in turn, embedded in larger and less dense clumps (Dickman et al. (1990); Elmegreen and Falgarone (1996)). Densities decrease by approximately an order of magnitude going from clump to clump (Cesaroni et al. (1994)). This has led to molecular clouds being described as having a 'fractal' struc-

ture (see Elmegreen and Elmegreen (2001) and references therein)

1.3 The Stellar Content of Galaxies

In this section we discuss the formation, properties and observations of the stellar content of galaxies. We first introduce the mechanism by which most stars are thought to form; the collapse of turbulent molecular clouds (section 1.3.1). We then describe the ways in which star formation can be observationally probed in distant galaxies (section 1.3.2). Finally we talk about how massive stars end their lives as supernovae (section 1.3.3). This process is of critical importance in the energetics and dynamics of galaxy evolution and additionally supplies the vast majority of the heavy elements in the universe (1.3.4).

1.3.1 Star Formation in Molecular Clouds

In the older picture of cloud formation, GMCs were long-lived, gravitationally bound, virialised objects. The presence of supersonic turbulence ensures that clouds do not immediately collapse to form stars, as this would predict a star formation rate for the MW which is far higher than observed. Locally unstable clumps collapse to form proto-stars, which built-up their mass to produce the initial mass function (IMF) through competitive accretion (e.g. Bonnell et al. (1997)).

However simulations show that the energy contained in supersonic motions is quickly dissipated even in the presence of magnetic fields (see references in Mac Low and Klessen (2004)). To sustain the turbulence hence requires an energy source, for example from star formation, yet some clouds have turbulence but no current star formation.

The modern picture is one in which clouds are short-lived structures and the turbulence results from the same process that formed the cloud in the first place. Observationally, GMCs turn a small fraction $\epsilon_\star \approx 0.1$ of their mass into stars before they disperse again. This low star formation efficiency of clouds may be due to the fact that they are short lived. The short life times of (star forming) clouds also follows from the small age spread in star clusters (see e.g. Gomez et al. (1992)), and indicates that star formation in a given cloud only lasts for a few million years. The short life-times of GMCs then also suggests that competitive accretion (e.g. Bonnell et al. (1997)) is less important in shaping the IMF (Padoan and Nordlund (2002)).

Turbulence generates a range of substructures inside a GMC, and Padoan and Nordlund (2002) suggest that such 'turbulent fragmentation' builds a mass spectrum of protocores, some of which will collapse under their own gravity to form stars. The resulting IMF is a power-law due to the self-similar nature of the turbulence. Only cores dense enough so that self gravity can overcome their magnetic and thermal energy can collapse. This consideration flattens the IMF at low masses, and prevents very low-mass cores from forming stars. They also argue that the maximum mass is a fraction of the overall cloud mass.

A young stellar population does of course dump a lot of energy into its surroundings through stellar winds, ionisation, and SN explosions. Even if these do not drive the observed turbulence, they may contribute to the destruction of the cloud, and prevent further star formation. Most simulations use such feedback from star formation to regulate the star formation rate.

1.3.2 Observations of Star Formation Rates

In all but the closest galaxies individual stars remain unresolved even with the most modern telescopes. Most information on the star formation properties of galaxies comes from integrated light measurements in the ultra-violet (UV) and far-infrared (FIR) and from observation of the strength of recombination lines, for example Hα. We will now discuss each of these methods, highlighting both the advantages and disadvantages of each one.

Ultraviolet Continuum: Young stars dominate the emission at ultraviolet wavelengths so the luminosity scales almost linearly with SFR (Kennicutt (1998)). The conversion between UV flux in a given band and the SFR can be derived using stellar synthesis models (see e.g. Bruzual and Charlot (1993)). The optimal wavelength range to make UV observations is $1250 - 2500$ angstroms, which is longward of the Lyman alpha forest but still short enough to remove most contamination from older stellar populations. These wavelengths cannot be observed from ground based telescopes for redshifts $z < 0.5$ but are visible from redshifts $1 - 5$. For this reason the most complete UV studies of nearby galaxies have been carried out by balloon, rocket and space experiments.

Far-Infrared Continuum: Interstellar dust in galaxies will absorb a significant fraction of the stellar luminosity. This heats the dust, which then re-emits photons with a black body spectrum characterised by the temperature of the dust. In real galaxies the situation is somewhat complicated by the fact that the dust exists at at least two discrete

temperatures (e.g. Cox et al. (1986)), and so any analysis must take into account contributions from a 'warm' component associated with dust around star-forming regions and another 'cool' component, which is emitted by the diffuse dust throughout the rest of the galaxy. This makes the calibration of the conversion factor between FIR luminosity and SFR a somewhat controversial subject, and only relatively recently have the calibrations used by different authors (Hunter et al. (1986); Lehnert and Heckman (1996); Meurer et al. (1997)) begun to agree to within better than a few tens of percent.

Recombination Lines: Hydrogen atoms that interact with high energy photons can be ionized, and then at a later time recombine with the electrons, emitting photons at specific frequencies. Stars with masses $> 10M_{\odot}$ and lifetimes of < 20Myr contribute significantly to the flux of these ionizing photons, so measuring the strength of the recombination lines provides an estimate of the instantaneous star formation rate. The most commonly used line is Hα, which is both very strong and exists in a part of the spectrum visible from the ground (at least for $z < 0.5$). Calibrations between Hα flux and SFR have been provided by a number of authors (Kennicutt (1983); Leitherer and Heckman (1995)). The Hα line is used very commonly as an SFR indicator due to its high sensitivity. Additionally SFRs measured by this method are very sensitive to the slope of the IMF, and as such provide a good way of constraining its properties (Kennicutt (1983))

At high redshift the Hα line is redshifted outside of the visible window and therefore must be investigated with space-based experiments. There is therefore a lot of interest in using higher order lines as SFR tracers. The integrated strengths of the other hydrogen recombination lines is very low, and they are strongly influenced by absorption in stellar atmospheres. However, the [OII] forbidden-line doublet is sufficiently strong and sufficiently well behaved that it is possible to calibrate between SFR and [OII] luminosity (Gallagher et al. (1989)). SFRs measured by this line are somewhat more uncertain than similar ones calculated using the Hα line, but the [OII] line is visible up to a higher redshift.

Many large surveys of the global SFRs of galaxies have been carried out using all of the techniques summarised above. Hα(Cohen (1976a); Young et al. (1996)), UV(Deharveng et al. (1994); Buat (1992)), FIR(Colless et al. (2001); Moshir et al. (1992)). The absolute SFRs in galaxies (usually expressed in units of $M_{\odot}$/yr, show an enormous range, from virtually zero in gas-poor elliptical, S0, and dwarf galaxies to $20M_{\odot}$/yr in gas-rich spiral galaxies and $100M_{\odot}$/yr in high redshift starburst galaxies, although these figures are

somewhat uncertain due to the as yet poorly constrained shape of the stellar initial mass function, which although measured for our own galaxy (Salpeter (1955); Kroupa (1998); Chabrier (2001)), is still unknown in high redshift objects, where the physics of the ISM may be significantly different to the low redshift universe.

1.3.3 The Physics of Supernova Explosions

A supernova event marks the end of life for some stars. There are a variety of different mechanisms by which SN can occur. These include accretion of matter from a companion star (Type Ia) or exhaustion of its own fuel supply (Types Ib, Ic, and II). Each of these mechanisms can take a star to the point where it can no longer support itself against gravity and thus collapses, throwing off its outer layers in a burst of energy that outshines an entire galaxy. This discussion is divided into sections on Type I supernovae and Type II supernovae (see e.g. Woosley and Weaver (1986) for a review). The distinction between supernova types is based on the presence or absence of hydrogen lines in the spectrum. The two types of supernova are almost totally distinct phenomena, the only relations being the approximate equality of the explosion energy (10^{51} erg) and the fact that both produce heavy elements.

Type II supernovae are estimated to occur once every 44 years in our galaxy, and Type I's every 36 years (Tammann (1982)). In this section we will discuss the physics of both Type I and Type II supernovae before summarising the behaviour of the resulting supernova blast wave, and describing the metal yields from different types of supernova.

Type 1 Supernovae

Supernovae that do not show prominent hydrogen lines are classified as Type I. Type I supernovae are not a homogeneous set and following Elias et al. (1985) we will consider Type I supernovae to be split into three subgroups, Type Ia (strong Si II line), Type Ib and Ic (characterised by an absence or presence of a Helium line)

Type Ia supernovae are generally considered to be due to an accreting white dwarf in a binary system that grows to a critical mass (Whelan and Iben (1973)), and ignites carbon or helium. The energy from the burning disrupts the star at high velocity. In general no neutron star or black hole remnant would be expected from this type of explosion.

Type Ib and Ic supernovae are thought to be associated with massive stars (Wheeler and Levreault (1985)), and perhaps represent the collapse of a star massive enough to

have blown away its outer hydrogen envelope. The supernova explosion in this case would proceed in a way similar to the iron core-collapse supernovae discussed in the following section.

Type 2 Supernovae

Type II supernovae are generally believed to be a consequence of gravitational collapse of massive stars ($M > 8M_{\odot}$). Type II supernovae are characterised by the presence of hydrogen lines in their spectra (Branch et al. (1981)). The fate of massive stars depends sensitively on their mass and composition (metallicity) at birth. See e.g. Heger et al. (2003) for a recent review.

The mass range for stars that undergo supernova events fitting our description of a Type II supernovae is bounded on the lower end by the largest mass of star that can become a white dwarf and on the upper end by the most massive stars that will keep an appreciable hydrogen envelope. For isolated stars, this mass can be estimated in a number of ways: by finding the mass of the progenitors of the largest white dwarfs (Iben and Renzini (1983)), with statistical arguments on the occurrence of supernovae (Tammann (1982)) and theoretical models for white dwarf formation (Iben (1985)). The values obtained by each of these techniques are in good agreement at $8M_{\odot}$.

The mass of the most massive star that maintains a hydrogen envelope is uncertain and depends strongly on metallicity, and varies from approximately $30M_{\odot}$ in solar metallicity stars to hundreds of solar masses in metal free stars (Heger et al. (2003)). Stars with masses greater than $8M_{\odot}$ and with a hydrogen envelope will undergo what we observe as Type II supernovae. More massive stars may undergo a violent instability

Stars in the mass range $8 - 11M_{\odot}$ (Barkat et al. (1974)) form, in their later stages of evolution, a core of Oxygen, Neon and Magnesium (Miyaji et al. (1980)). According to the models of Barkat et al. (1974) these O-Ne-Mg cores grow through a complicated series of shell burnings, until two competing effects *electron capture by Ne and Mg* (acting to allow the core to collapse gravitationally) and *Oxygen deflagration* (acting to cause the star to explode) begin to act against each other. Miyaji et al. (1980) found that electron capture is the dominant effect and stars in this mass range have cores that collapse into neutron stars.

More massive stars undergo supernovae via a different mechanism. These stars are massive enough to ignite all six nuclear burning stages (hydrogen, helium, carbon, neon, oxygen and silicon) until an iron core is formed. As the iron core grows its temperature

and density increase until photons have enough energy to destroy heavy nuclei, a process known as photodisintegration. Most importantly:

$$^{56}_{26}\mathrm{Fe} + \gamma \rightarrow 13\,^{4}_{2}\mathrm{He} + 4n\,, \tag{1.18}$$

and

$$^{4}_{2}\mathrm{He} + \gamma \rightarrow 2p^{+} + 2n\,. \tag{1.19}$$

Photodisintegration can, in a very short time, undo what the star has been trying to do its entire life, namely produce elements more massive than H and He. This process of stripping iron down to protons and neutrons is highly endothermic and the core begins to collapse. Under the extreme conditions that now exist the free electrons that had assisted in supporting the core through electron degeneracy pressure are captured by heavy nuclei and the protons that were produced through photodisintegration

$$p^{+} + e^{-} \rightarrow n + \nu_{e}\,. \tag{1.20}$$

Most of the core's support is now gone and it begins to collapse rapidly until supported by neutron degeneracy pressure, at which point it rebounds. The outer layers of the star collapse inwards on the core and rebound, sending shock waves outward. This is a Type II supernova.

The late stage evolution of stars massive enough to shed their hydrogen-envelopes is more complex still and depends upon the rotation speed, metallicity and mass of the star. Depending on mass and metallicity different instabilities become important, including the 'pair instability' (Fowler and Hoyle (1964)). The resulting supernova events can have a large range of effects on the supernova remnant from complete disruption of the star (Heger and Woosley (2002)) to the formation of a massive black hole (Fryer et al. (2001)).

Main sequence stars with masses greater than $8M_{\odot}$ are short lived so Type II supernovae are observed only in regions that have recently formed stars and therefore rarely in elliptical galaxies (Tammann (1974)).

The Evolution of a Supernova Remnant

In the classical model of Supernova Remnant (SNR) evolution (Chevalier (1977); Gull (1973); Woltjer (1970)) there are four main stages or phases through which a SNR passes: Free Expansion, Adiabatic, Snowplough and Dispersal. We simplify the discussion of SNR evolution by treating a supernova as an injection of some amount of energy, ϵ_0, to an amount of mass M_0, which acquires an initial velocity, v_0. At time t the resulting blast

wave has a radius R_s. We treat the system as spherically symmetric and consider how it interacts with the surrounding ISM of density n_{ism} hydrogen atoms per cubic centimetre (Woltjer (1972)) we can treat each of these phases in turn:

I. Free Expansion: The supernova ejecta will sweep up gas from the ISM as it travels. As long as the mass swept up is very much less than the mass in the ejecta:

$$\frac{4\pi}{3} n_{ism} m_H R_s^3 < M_0 \,, \tag{1.21}$$

then the expansion of the remnant will be essentially free and much of the development will depend on the initial conditions.

II. Adiabatic: The swept up mass will increase until it exceeds M_0, we then enter the phase where the behaviour of the expanding shock wave can be described by the self similarity solution of Sedov (see section 3.2.6 for a more detailed discussion of this phase). During this phase the shock wave has a radius $\propto t^{2/5}$, other properties of the shock wave are discussed more fully in section 3.2.6. This solution for the behaviour of the shock wave assumes that the gas is adiabatic. In reality, a hot gas will cool radiatively so this regime is valid whilst

$$\int \left(\frac{d\epsilon}{dt}\right)_{\rm rad} dt < \epsilon_0 \,. \tag{1.22}$$

By assuming that all of the mass internal to the shock wave is contained in a thin shock wave it can be shown (Woltjer (1972)) that the time at which the integrated radiative energy loss equals $\frac{1}{2}\epsilon_0$ is

$$t_{\rm rad} = 1.1 \epsilon_0^{4/17} n_{ism}^{-9/17} \,, \tag{1.23}$$

and assuming that the adiabatic relation for the velocity still holds:

$$v_{\rm rad} = 2.0 \times 10^7 n_{ism}^{2/17} (\epsilon_0 / 1 \times 10^{50})^{1/17} {\rm cm/s} \,. \tag{1.24}$$

This evaluates to 200km/s and depends only very weakly on the parameters of this particular supernova. This velocity is taken to mark the end of phase II and the beginning of phase III.

III. Snowplough: When the radiative losses become dominant the behaviour of the shock wave will change. Matter passing through the shock wave cools rapidly and the density becomes high. In this phase we can consider the shock wave to be a thin, dense shell ploughing through the ISM. Pressure forces are no longer important and the shock moves with a constant radial momentum. The equation of motion simply becomes (Chevalier (1977)):

$$(4\pi/3) n_{ism} m_H R^3 v = C_1 \,, \tag{1.25}$$

where C_1 is a constant. Integrating with respect to time we obtain that

$$R = R_{\rm rad}\left(\frac{8}{5}\frac{t}{t_{\rm rad}} - \frac{3}{5}\right)^{1/4}, \tag{1.26}$$

where the subscript rad represents the values at the transition from stage II to stage III.

IV. Dispersal: After the shell has slowed down for some time its velocity becomes comparable to the random thermal motions of the ISM (around 10km/s). The shell disperses and loses its identity. The matter in the shell is mixed in with the material in the surrounding ISM, depositing the heavy elements that formed during the supernova explosion in the ISM.

The model as introduced so far neglects a number of important physical processes, including the presence of magnetic fields in the swept up shell, the pressure of cosmic rays within the shell, the inhomogeneity of the ISM and thermal conduction between the hot gas of the supernova remnant and the surrounding cold molecular clouds (this process is discussed in section 3.2.7). These additional physical processes mean that the problem of understanding the evolution of a SNR is not yet closed and is still an active area of research.

1.3.4 Metal Enrichment

As discussed previously in this section, stellar nucleosysnthesis and supernova explosions create elements heavier than the H and He formed by BB nucleosysnthesis (see section 1.1.2).

In astronomy any elements heavier than helium are described as 'metals'. The fraction of metals in a sample of gas is usually quantified using its 'metallicity', defined for Iron as

$$\left[\frac{\rm Fe}{\rm H}\right] \equiv \log_{10}\left(\frac{N_{\rm Fe}}{N_{\rm H}}\right) - \log_{10}\left(\frac{N_{\rm Fe}}{N_{\rm H}}\right)_{\odot}, \tag{1.27}$$

Where N represents the number density of a particular species, and the subscript $\odot$, is the value for the sun. A star with a metallicity equivalent to that of the sun therefore has a metallicity of 0. The observed range of metallicities in the MW is -4.5 (old, extremely metal poor stars) to +1 (very young, metal rich stars).

Calculating the expected metal yield from a supernova explosion is not an easy task, and is a function of the mass, metallicity and rotational speed of the star. Additionally each of the different supernova mechanisms will produce different proportions of metals. There is still uncertainty about the precise metal yields from all types of supernovae.

Various authors have investigated the yields from Type II supernovae (Woosley and Weaver (1995); Thielemann et al. (1996); Limongi et al. (2000)) and although much work has been performed in this area, the resulting supernova yields are still somewhat uncertain (Travaglio et al. (2004)) due to our only approximate understanding of the precise mechanism by which core collapse supernovae are triggered. The dominant product from these supernovae are thought to be the α elements, defined as the $Z > 22$ multiples of He (e.g. Mg, Si, S, Ca), which are synthesised by alpha capture during SNII.

The nucleosysthesis expected in type I supernovae has been calculated by several groups (e.g. Nomoto et al. (1984)). The dominant products from these supernovae are the iron peak nuclei (elements with an atomic number near that of iron, and high binding energy per nucleon).

The differing yields from different supernova types may, therefore, be used to probe the star formation history of the universe. Since Type II supernovae occur on a very short timescale, the relative abundances of the α and Fe elements can provide clues as to the history of star formation in a given object (Tissera et al. (2002))

1.4 Motivation for This Thesis

In this section we provide a brief overview of the contents of each chapter.

1.4.1 Computational Cosmology

Cosmological structure formation is a complex and non-linear process, therefore a thorough understanding of both simulation algorithms and their shortcomings is of crucial importance in carrying out scientific investigation in this field. This chapter is primarily concerned with numerical issues affecting cosmological simulation. We begin by providing an overview of the simulation techniques used in cosmological structure formation simulations, before carrying out numerical tests of two simulation codes. We then introduce the process by which cosmological initial conditions are created and using this knowledge probe the numerical effects that alter the properties of a halo as a function of its mass resolution.

1.4.2 Statistical Modelling of the Interstellar Medium

Most computational models of star formation and supernova feedback are crude at best and rely on straight fits to empirical laws. In this chapter we introduce in detail a novel,

physically motivated prescription for the simulation of a multiphase ISM on galactic scales. This model could find many applications, two of which are discussed in the following two chapters.

1.4.3 The Interstellar Medium in Isolated Galaxies

In chapter 4 we investigate the properties of the interstellar medium in an isolated disk galaxy using the model introduced in chapter 3. We find that the model described in chapter 3 can reproduce many of the observed properties of quiescent galaxies, and we undertake a short investigation into the effects of changing some of the physics of the ISM.

1.4.4 Simulating Galaxy-Galaxy Interactions

Mergers and other gravitational interactions between galaxies are an essential part of hierarchical galaxy formation scenarios, and it is likely that the vast majority of galaxies in the observable universe have been shaped by collision events (Toomre (1977)). This suggests that in order to understand the properties of present day galaxies we require a thorough investigation of the dynamics and energetics of galaxy-galaxy interactions. In this chapter we analyse the properties and behaviours of previously quiescent disk galaxies as they undergo gravitational interactions with one another. It is found that many of the properties of the resulting remnant, including density and brightness profiles, the age gradient and the makeup of the ISM match very well with the corresponding properties in local early-type galaxies. Additionally during the merger strong star formation is observed in the tidal features of the interacting galaxy pair.

Chapter 2

Computational Cosmology

2.1 Introduction

The past few decades have seen huge advances in our understanding of the formation and evolution of cosmic structure. Recent galaxy surveys (see e.g. Colless et al. (2001); York et al. (2000)) have allowed us to quantify the structure of the local Universe and theoretical models have allowed us to explain how these structures grew from the first few moments of the Universe's existence to the present day. Due to the huge timescales involved in the formation of large scale structure, computer simulation has become one of the most important methods for the investigation of the formation and evolution of the largest scale cosmic structure. In order to perform reliable simulations is important that we understand the relative strengths and weaknesses of different simulation algorithms. In adition it is also important that we have a reliable way of generating the initial conditions for large scale structure simulations. This chapter is concerned with all of these things and is split broadly into two sections.

In the first section we introduce and describe the most common cosmological simulation techniques before performing a series of tests of the reliability of simulation codes by carrying out a comparison of the results obtained by two different simulation techniques against one of the standard cosmological tests, the Santa Barbara cluster comparison test (Frenk et al. (1999))

In the second half of this chapter we discuss the techniques by which cosmological initial conditions can be generated and introduce a code for the generation of high resolution cosmological initial conditions in which additional small scale power can be added to large scale modes. We use this code to present a detailed study of the effects of mass resolution on a set of simulated galactic haloes.

2.2 Simulation Techniques

In cosmological simulation the matter in the universe is usually modelled in two seperate components: firstly a collisionless fluid that represents dark matter or stellar material and secondly a baryonic component (primarily hydrogen and helium). Both of these phases feel the gravitational force, the gas phase is in addition subject to hydrodynamic forces. In order to turn the problem of the solution of the hydrodynamics equations into one that can be represented numerically we need to discretize the fluid properties that we wish to calculate. Broadly speaking hydrodynamic simulation codes may be broken down into two classes 'Eulerian' (discretize space and represent gas properties on a grid) and 'Lagrangian' (discretize mass and represent fluid properties in individual particles).

Hydrodynamic forces may be evaluated in a large number of different ways. The most commonly used Lagrangian codes employ the Smoothed Particle Hydrodynamics (SPH) (Gingold and Monaghan, 1977; Monaghan, 1992) method, and the most common Eulerian codes use the Piecewise Parabolic Method (PPM), first developed by Colella and Woodward (1984) (see also Woodward and Colella (1984)). Lagrangian simulation codes have been implemented in a cosmological framework by various authors, first on a static grid (Cen (1992)) and later on a deformable grid allowing a spatially variable mass resolution Bryan et al. (1995); Fryxell et al. (2000); Teyssier (2002); Quilis (2004). Although not discussed further in this thesis it is worth noting that other hydrodynamic methods do exist, including HPM, and the smoothed lagrangian hydrodynamics codes due to Gnedin (1995).

Most simulation codes calculate the gravitational forces (through solution of the Poisson equation) in one of a limited number of ways: either through the use of fast Fourier transforms on grids (PM methods). see e.g. (Klypin and Shandarin, 1983; White et al., 1983; Efstathiou and Eastwood, 1981); hierarchical trees (Barnes and Hut (1986); Jernigan and Porter (1989)); mesh relaxation methods (Brandt (1977)), or direct summation of the pairwise forces (see, e.g. (Aarseth et al., 1979; Frenk et al., 1983)). Each of these methods has its own advantages and disadvantages. PM codes are extremely fast but spatial resolution is limited by the size of the spatial grid. Other methods are more computationally expensive but allow forces to be resolved on much smaller scales. Hybrid codes, for example P^3M (Efstathiou and Eastwood, 1981; Couchman et al., 1995; Wadsley and Bond, 1997) or Tree-PM (Wadsley et al., 2004; Springel, 2005) can combine the best features of each of these schemes. As in the case of the hydrodynamic calculation we will

discuss only the most commonly used methods of calculating the gravitational force, neglecting interesting but rarely used techniques such as the approach due to Widrow and Kaiser (1993) of reformulating the Schroedinger equation to describe the dynamics of collisionless matter.

In the remainder of this section we will discuss in more detail a few of the methods by which the gravitational and hydrodynamic forces may be calculated for arbitrary distributions of matter.

2.2.1 The Gravity Calculation

For any continuous density field $\rho(\mathbf{r})$, we can calculate the associated gravitational potential via the Poisson equation

$$\nabla^2\Phi(\mathbf{r}) = 4\pi G\rho(\mathbf{r}), \tag{2.1}$$

where Φ represents the gravitational potential and G is Newton's gravitational constant. The gradient of the potential as obtained from 2.1 can then be obtained to calculate the gravitational acceleration at any point. In cosmological comoving coordinates the Poisson equation becomes (Peebles (1981))

$$\nabla^2\Phi(\mathbf{r}) = 4\pi G a^2[\rho - \bar{\rho}]\,. \tag{2.2}$$

General relatavistic effects can be neglected in cosmology due to the fact that the Newtonian limit is applicable on scales smaller than the Hubble length (c/H) and larger than the Schwartzchild radii of any collapsed objects. In order to approximate a continuous field computationally we need to discretise the phase space distribution of matter, $f(x, y, z, v_x, v_y, v_z)$. This is usually achieved by subsampling the true phase-space distribution and representing it with enough discrete particles to capture the important features of the underlying phase space distribution.

In this section we will discuss four different ways of calculating the gravitational force: The direct summation, using Fourier transforms on a regular grid, using a hierarchical tree and finally using iterative methods on a (possibly irregular) grid. Finally these four techniques are compared and contrasted.

Particle Particle Methods

The most conceptually simple way of calculating the gravitational force on a point mass due to a system of other point particles is the particle-particle (PP) direct summation method. This method, used in the first ever simulations of cosmic structure formation (Aarseth (1963); Hénon (1964), works by explicity summing the gravitational force exerted on each particle by each other particle directly via Newton's law of gravitation

$$\vec{F} = \frac{GMm}{(r^2 + \epsilon^2)^{3/2}}\vec{r}, \tag{2.3}$$

where ϵ represents a gravitational softening term, which acts to flatten off the gravitational force at small radii ($r < \epsilon$) and so diminish the effect of two-body relaxation.

PP codes solve exactly for the gravitational force on each particle, the disadvantage of these codes is that the number of computations to calculate the gravitational force on N particles scales as N^2, so these codes are unfeasible for use in even moderately large simulations.

Particle Mesh Methods

One method of cutting down the number of operations needed to calculate the gravitational force is to calculate potentials on a regular mesh and then interpolate the forces back to the particles.

The process of using a mesh to calculate the gravitational forces on a series of discrete mass elements consists of three seperate steps:

1. Mapping the discrete particle masses on to a uniform grid
2. Solution of equation 2.1 to obtain the potential on the grid
3. Differencing of the potential on the uniform grid at the location of each particle to obtain the gravitational force.

In this section we will discuss each of these processes in turn. For the sake of simplicity we will assume that we have a cubic volume of side length L, which contains N_p discrete particles. The mass of the ith particle is m_i. The mass distribution at any given three dimensional coordinate, $\mathbf{r}$ may then be described by

$$m(\mathbf{r}) = \sum_{i=0}^{N_p} m_i \delta(\mathbf{r} - \mathbf{r}_i)\,. \tag{2.4}$$

If we place a uniform cubic grid over the volume then using equation 2.4 we can calculate the mass density at a gridpoint with coordinate $\mathbf{r}_p$ by

$$\rho(\mathbf{r}_p) = \frac{1}{\Delta^3} \sum_{i=0}^{N_p} m_i W(\mathbf{r}_i - \mathbf{r}_p), \tag{2.5}$$

where Δ represents the grid spacing and W is a function that represents the charge assignment scheme that is in use. In order to simplify the mathematics we will demonstrate a number of charge assignment functions in one-dimension but note that multidimensional versions of the assignment functions can be obtained by multiplying together the corresponding one-dimensional functions for each component. The simplest solution is to assign all of a particle's mass to its nearest grid point (NGP), mathematically this is represented by

$$W(\mathbf{x}) = \begin{cases} 1 & \text{if } |x| < \frac{\Delta}{2}; \\ 0 & \text{otherwise}, \end{cases}$$

where $x = x_i - x_p$. The NGP scheme introduces lots of noise on small ($< \Delta$) scales, where the assigned charges will flip from 0 to their maximum value as particles cross grid boundaries. A more accurate solution is obtained by using the cloud in cell (CIC) scheme, which spreads a particle's mass over the nearest two grid points in each direction. This scheme may be described

$$W(\mathbf{x}) = \begin{cases} \left(1 - \frac{|x|}{\Delta}\right) & \text{if } |x| < \Delta \\ 0 & \text{otherwise}. \end{cases}$$

This is more computationally expensive than the NGP scheme but the resulting mappings are more accurate. More complex still is the triangular shaped cloud (TSC) scheme, where each particle's mass is spread over even more grid points and the resulting density is even less noisy. TSC is described by

$$W(\mathbf{x}) = \begin{cases} \frac{3}{4} - \left(\frac{|x|}{\Delta}\right)^2 & \text{if } |x| \leq \frac{\Delta}{2}; \\ \frac{1}{2}\left(\frac{3}{2} - \frac{|x|}{\Delta}\right)^2 & \text{if } \frac{\Delta}{2} < |x| \leq \frac{3\Delta}{2}; \\ 0 & \text{otherwise}, \end{cases}$$

where the values of the coefficients are determined by requiring that the function and its derivative are continuous and that it integrates to unity. Figure 2.1 shows the difference between the three mass assignment schemes in one dimension. The choice of a charge assignment scheme, therefore, depends upon a number of factors. High order schemes are more computationally expensive to calculate, but reduce the amount of noise in the

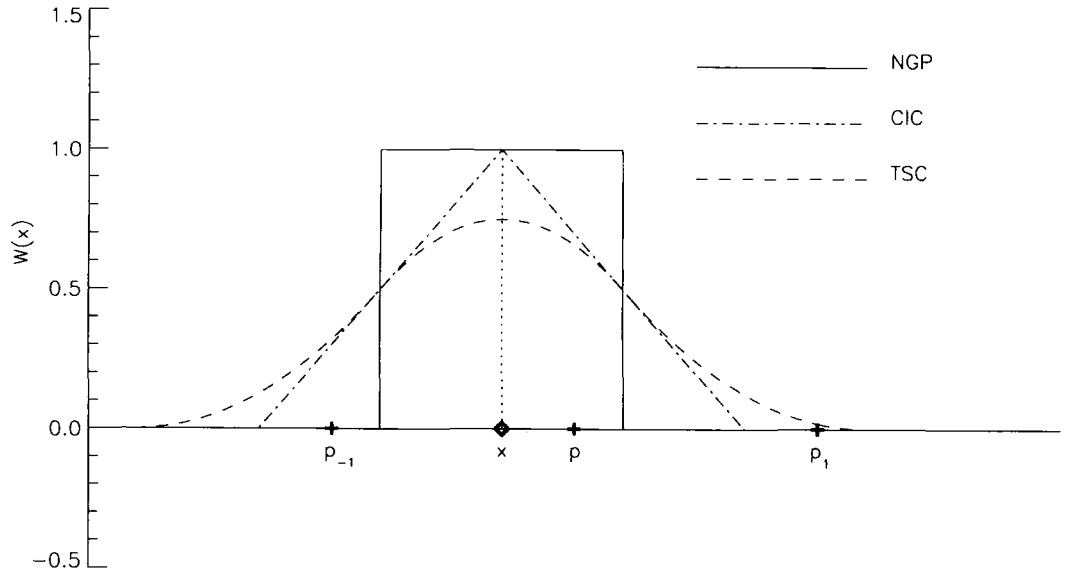

Figure 2.1: The weighting functions for three mass assignment schemes in one dimension. The amount of mass that is assigned to each gridpoint is proportional to the value of the assignment function at the gridpoint. Considering a particle at point x with neighbouring grid points p_{-1}, p and p_1 the NGP method assigns all mass to gridpoint p, CIC assigns to the nearest two points (p and p_1). TSC assigns mass to the nearest three points.

resulting solution. Low order schemes require few operations to calculate, but increase the amount of noise in the result.

The second step in computing the gravitational force is to solve equation 2.1 on the uniform grid. With the advent of rapid methods for performing Fourier transforms in the 1960s (Cooley and Tukey, 1965), fast Fourier transform (FFT) methods, the most computationally efficient method of solving this equation became to work in k-space.

To begin we need to note that the Poisson equation is linear, that is, the potential at any mesh point (p, q, r) can always be written as the sum of contributions from all other source points (p', q', r'), or

$$\phi_{p,q,r} = \sum \mathfrak{G}_{p-p',q-q',r-r'} \rho_{p',q',r'} \,. \tag{2.6}$$

Equation 2.6 expresses the potential as the convolution of the source distribution ρ with some function that describes the interaction, usually called the Green's function, $\mathfrak{G}$.

Now, via the convolution theorem, the statement that (see e.g. Boas (1983))

the Fourier transform of a convolution is equal to the piecewise products of the Fourier transforms of the quantities involved

we can rewrite equation 2.6 in the form

$$\hat{\phi}_{k,l,m} = \hat{\mathfrak{G}}_{k,l,m}\hat{\rho}_{k,l,m} \,. \tag{2.7}$$

In order to solve the Poisson equation we therefore need to identify the form of the Green's function that describes the interaction. To do this we note that the Greens function for a particular differential equation is defined to be its solution under the influence of a delta function (Boas (1983)). That is:

$$\nabla^2 \mathfrak{G}(t,t') = \delta(t'-t)\,, \tag{2.8}$$

where $\delta(t-t')$ represents a Dirac delta function centered at t'. Using the Green's function we can then try to find a solution to the Poisson equation for a real density field by adding up the contributions from point sources at each gridpoint. The Green's function in this case is described by(Hockney and Eastwood (1988))

$$\hat{\mathfrak{G}}_{p,q,r} = -1/\Big[\pi(p^2+q^2+r^2)\Big]\,. \tag{2.9}$$

The form of the Green's function changes when we define the density only on a grid. The Green's function of the seven-point finite-difference approximation to the laplacian is

$$\hat{\mathfrak{G}}_{p,q,r} = -\frac{\pi}{\Delta^2}\frac{1}{\left(\Big[\sin^2(\pi p\Delta)+\sin^2(\pi q\Delta)+\sin^2(\pi r\Delta)\right)}\,. \tag{2.10}$$

See appendix B for details on how this form of the Green's function is derived. Substituting equation 2.10 into equation 2.7 allows us to obtain the potential at every point in space by Fourier transforming the density field, multiplying with $\mathfrak{G}_{p,q,r}$ and then taking an inverse Fourier transform. The gradient of the potential at the position of each mass element may then by approximated by finite differencing of the potential

$$\left.\frac{\partial\phi}{\partial x}\right|_{i,j,k} = \frac{1}{2\Delta}(\phi_{i+1,j,k}+\phi_{i-1,j,k}-2\phi_{i,j,k})\,, \tag{2.11}$$

which is accurate to first order. The spatial resolution available through FFT methods is limited by the spatial size of the FFT grid (as demonstrated in figure 2.2). To obtain gravitational forces on scales below that of the FFT grid we need to apply additional methods.

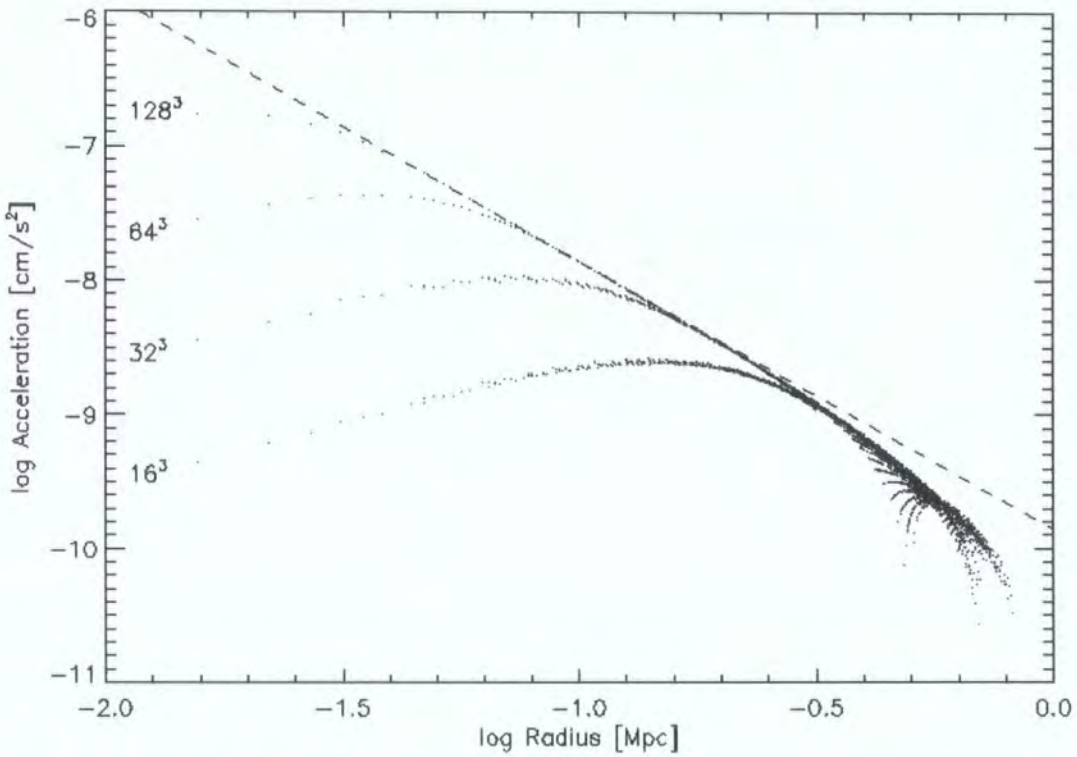

Figure 2.2: Gravitational acceleration of a series of test masses ($m = 0$) due to a single point mass in the centre of a periodic box. The dashed line shows the potential from a point mass, ignoring the periodic images of the massive particle (GM/r^2). Each series of black points represents the gravitational acceleration of a single particle as performed with a different number of PM cells (as marked on the graph). The deviations from a pure $1/r^2$ law at high radii are due to the gravitational influence of the periodic images of the point mass. The deviations at low radii are due to the finite PM grid size. The higher the resolution of the PM mesh, the more accurate the gravitational force at small scales.

Tree Methods

As an alternative to Fourier techniques are the so-called tree methods. In these schemes, the particles are arranged in a hierarchy of groups. In order to cut down on the number of computer operations when compared to a PP code, distant particles in the tree are then treated in groups. The process by which a tree is constructed and then used to calculate the gravitational force is discussed in this section.

There are a multitude of different ways of organizing the particles in a volume into a hierarchy, including the Barnes and Hut octree (Barnes and Hut (1986)), trees based on nearest-neighbour pairings (Jernigan and Porter (1989)) and binary trees. The methods by which two different types of tree-structure can be unambiguously created is discussed here.

Constructing a Barnes-Hut tree: In this scheme, starting with the entire computational domain, the volume is recursively partitioned into a sequence of cubes. Each time a cube is found to contain more than one particle it is split into eight equal volume children. This process is demonstrated for two-dimensions in figure 2.3.

Constructing a Jernigan-Porter tree: (Jernigan (1985)) Given a list of N particles the two which are closest together in physical space are joined together to form a node. These two particles are replaced by a single centre of mass node. This process is repeated indefinitely until only one centre of mass node remains.

The detailed shape of the hierarchical tree affects only the storage requirements and efficiency of the gravitational calculation, the actual mathematical details are independent of which tree construction method is used, so the following presentation of techniques for calculating the gravitational force given a hierarchical tree structure is independent of precisely which tree is used.

The gravitational force on a single particle is calculated via the following method: Starting from the largest node we apply the criterion

$$r > \frac{l}{\theta}, \tag{2.12}$$

where r is the distance between the particle we are considering and the current node of the tree. l is the spatial extent of the node and θ is an accuracy parameter. If this inequality is satisfied then the tree node is distant enough that the tree walk along this branch may be terminated and the force from this node added to the total force on the particle. If, on the other hand, the inequality is not satisfied, the node is opened up and its child nodes are evaluated. This process is repeated recursively until every particle

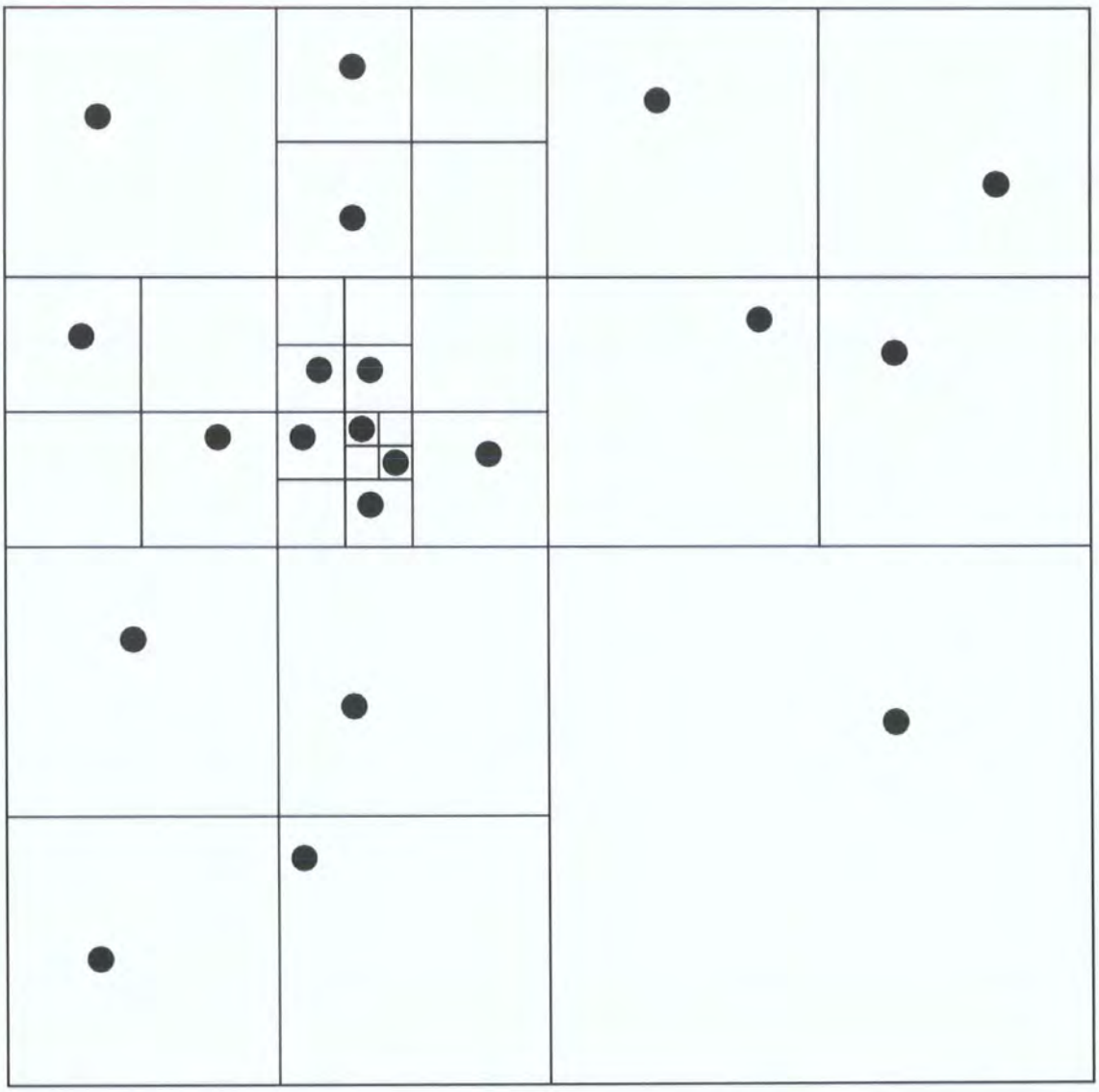

Figure 2.3: Simple depiction of a two dimensional version of an octree, the quadtree. Each black circle represents a single particle and each square represents a node on the tree. The quadtree is constructed by starting with the entire computational volume contained within one node and then recursively splitting each node into four equal pieces if it contains more than one particle. Here we see six different levels of the tree.

has been allowed to contribute to the gravitational force.

The force on a particle from any node can be calculated to first order by

$$\vec{F} = \frac{GMm}{(\mathbf{r}^2 + \epsilon^2)^{3/2}}\vec{r}, \tag{2.13}$$

where r is the distance between the centre of mass of the node and the particle. M and m are the mass of the node and the particle respectively and ϵ is the Plummer softening of the gravitational potential. More accurate forces can be obtained at the cost of more computations per node by including higher order corrections to the gravitational force.

Consider the distribution of matter inside any node of volume $\mathfrak{V}$, its effect on the potential and acceleration field outside $\mathfrak{V}$ is given by

$$\phi(r) = \int_{\mathfrak{V}} \mathfrak{G}(\mathbf{r} - \mathbf{x})\rho(\mathbf{x})d^3x\,, \tag{2.14}$$

where ρ is the mass density of matter in the volume and $\mathfrak{G}$ is the Green's function of the interaction. In the case of gravity we use the Green's function of the Laplacian, equation 2.9. The analytic form of the high order corrections for the gravitational force has been described in detail by Salmon and Warren (1994), who derived the analytic forms of the high order corrections all the way up to the hexidecapole.

It is worth noting that by this method we obtain only an approximation to the true force. However, the discrepancy between the calculated force and the actual force obtained by direct summation may be made arbitrarily small by tuning the tree opening criterion, θ (how deeply through the tree we walk when doing the calculation), and altering the order to which the gravitational potential is calculated for each cell (how accurately we evaluate the acceleration due to each node).

There is currently disagreement between various authors about the most efficient way to evaluate a tree force. In the original treecodes of Springel et al. (2001) the potential was expanded out to the quadrupole term, however in the more recent versions Springel (2005), it was found to be more efficient to use only the monopole term, and to walk deeper into the tree. In contrast the treecode of Wadsley et al. (2004) used the hexadecopole moment for each node, and found it more computationally efficient to use relatively few tree nodes. Hernquist (1987) and Barnes and Hut (1989) both find that the use of the quadrupole moment may increase the efficiency of the tree calculation.

Mesh Relaxation Methods

As an alternative to using Fourier methods for solving the Poisson equation on a grid, iterative methods may be used. These methods are of great use in eulerian codes (e.g.

FLASH Fryxell et al. (2000)) and have definite advantages when used in conjunction with adaptive mesh refinement (AMR) (see section 2.2.2), in which gravity needs to be solved on a grid that is not necessarily uniform in space.

The solution of the Poisson equation on a mesh via relaxation method proceeds in three steps

1. Map the discrete particles to the mesh
2. Iterate to find the correct gravitational potential
3. Difference the potential and map back to the particles to obtain the gravitational force.

The first of the three steps proceeds in an identical manner to that discussed in section 2.2.1. The particles are mapped on to the grid using usually either the NGP, CIC or TSC schemes. Considering a two-dimensional grid (grid spacing Δ), we can write that

$$\frac{\partial^2\phi}{\partial x^2} + \frac{\partial^2\phi}{\partial y^2} \approx \frac{\phi_{i+1,j} - 2\phi_{i,j} + \phi_{i-1,j}}{\Delta^2} + \frac{\phi_{i,j+1} - 2\phi_{i,j} + \phi_{i,j-1}}{\Delta^2} = \rho_{i,j}\,. \tag{2.15}$$

This equation can be rearranged into a form we can work with iteratively

$$\phi_{i,j} \approx \frac{1}{4}\left(\phi_{i-1,j} + \phi_{i+1,j} + \phi_{i,j-1} + \phi_{i,j+1} + \Delta^2\rho_{i,j}\right). \tag{2.16}$$

Equation 2.16 forms the basis for the Jacobi method of solving for the gravitational potential on a grid. The full method is as follows: Take a guess at the gravitational potential, usually this takes the form of the gravitational potential calculated on the last timestep, or if no potential is known it can be zeroed out. Now loop over every gridpoint applying equation 2.16 to obtain an improved estimate of the gravitational potential at that coordinate. Keep on iterating until the solution has converged to the correct potential. It should be noted that it is hard to define exactly what is meant by convergence. One commonly used measure of the error in the potential is the residual, defined as

$$R(\mathbf{x}) = \nabla^2\phi(\mathbf{x}) - \nabla^2\phi(\mathbf{x}) = \rho(\mathbf{x}) - \nabla^2\phi(\mathbf{x})\,, \tag{2.17}$$

where ϕ represents our current best estimate of the gravitational potential, as obtained by iteration. When $\sum R(\mathbf{x})^2$ drops below some critical tolerance parameter then the potential is said to be converged.

One improvement to the Jacobi method is to use Gauss-Seidel iteration. Computationally Gauss-Seidel iteration proceeds in exactly the same way as Jacobi iteration,

except the values are updated as soon as they are calculated. It can be shown (Hockney and Eastwood (1988)) that this leads to a large reduction in the number of computer operations needed to converge the solution.

An additional improvement comes about when we consider the parallelisation of the iteration problem. As presented so far, the standard Gauss-Seidel scheme cannot be run easily in parallel since each calculation depends upon the results obtained from the previous one. One way to get around this is to use the so-called 'red-black' ordering of points. This ordering is demonstrated in figure 2.4. The advantage of red-black ordering with regards to parallelisation is that the calculation as performed on each black point is independent of what happens to every other black point. Therefore in a massively parallel code, each processor can calculate the potential on some subset of the black points, before communicating once, and then working independently again on the red points.

The major disadvantage of relaxation techniques is that due to the fact that each gridpoint interacts only with its immediate neighbour every timestep that large scale perturbations take very many iterations to travel the length of the grid, and convergence is very slow. This problem will be addressed when discussing hybrid codes in section 2.2.1.

Comparison of Methods of Solving the Poisson Equation

So far in this section we have described four different methods of solving the Poisson equation for a system of discrete particles. Each of these methods has its own advantages and disadvantages. In this section we will compare each of the different methods and introduce some examples of hybrid codes, which combine the best features of two or more computational methods.

Particle-Particle Codes: PP codes have the advantage that they are conceptually the simplest codes to understand, and they obtain the gravitational force on any particle to within machine precision. The big problem with PP codes is that as the number of particles N increases, the number of calculations increases as $\sim O(N^2)$, making PP codes computationally prohibitive for large numbers of particles. Specialised hardwave, for example GRAPE (Sugimoto et al. (1990)) can be employed to allow the rapid evaluation of the gravitational sums, but PP codes are still limited in their application to large simulations.

Particle-Mesh Codes: PM codes solve exactly for the gravitational force on a series

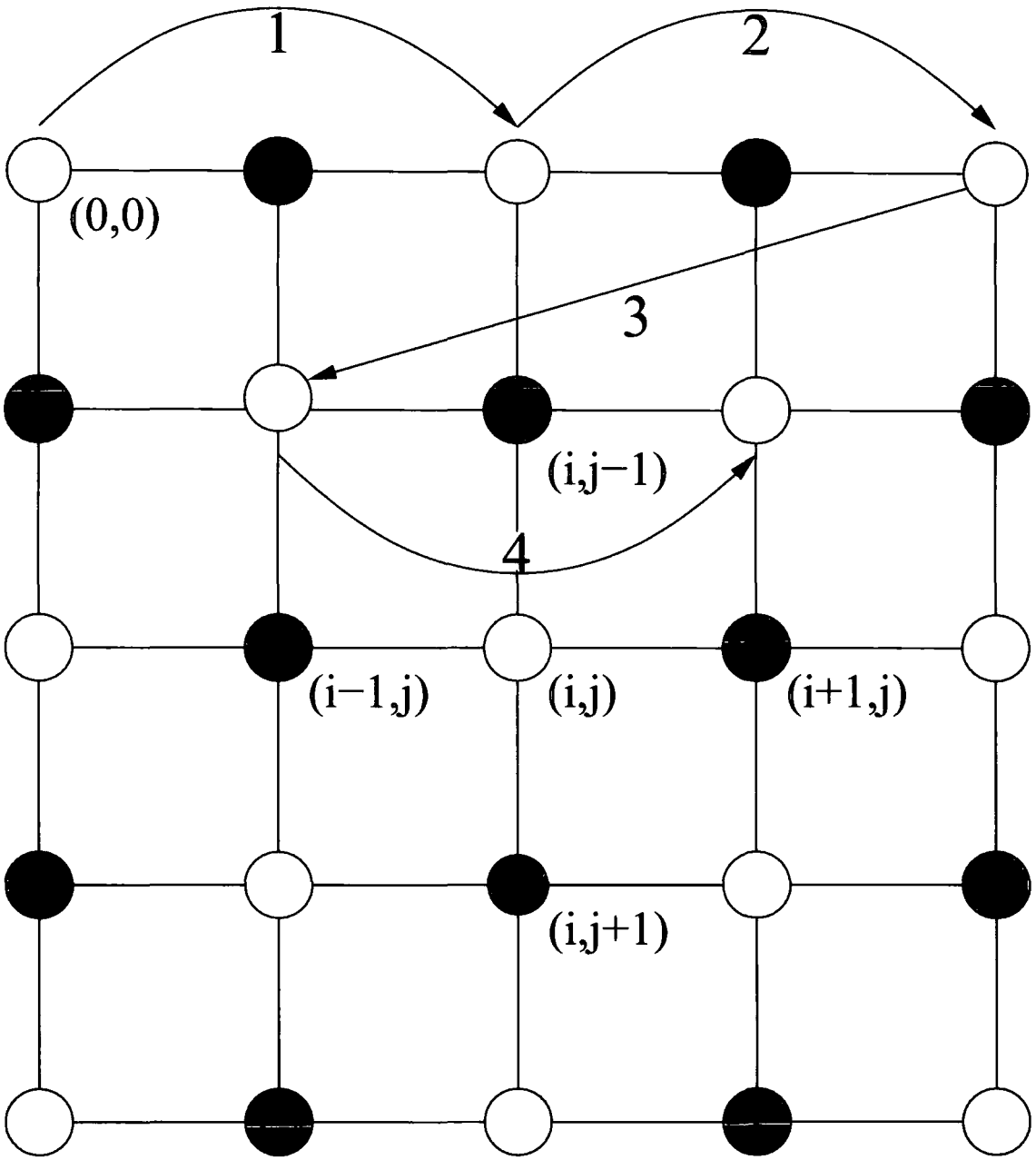

Figure 2.4: Red-Black ordering. Each circle represents a point on the computational grid, specified by two indices i and j. When iterating to solve the gravitational potential, we first loop over all white points (as labelled by arrows 1,2,3,4), updating the solution as we go. Then we do a second loop over all black points, using the updated values of the white points to obtain the new solution.

of gridpoints, the only errors introduced are due to the interpolation from particles to gridpoints and back. The major drawback of a PM code is that the gravitational force cannot be represented below the scale of a couple of grid spacings, and a hard limit is placed on the size of a PM grid by memory considerations. To achieve a factor of two in the grid spacing, the total number of gridpoints must be increased by a factor of 8. The number of calculations needed for a PM code scales as $O(N_g \log_2 N_g)$ (Hockney and Eastwood (1988)), where N_g represents the number of gridpoints in the simulation domain, making the PM calculation one of the most efficient methods of obtaining a gravitational potential.

Tree Codes: Tree codes solve for the gravitational potential at the point of each particle to within any desired accuracy. The number of calculations required to evaluate the gravitational potential in a system of N particles scales as $O(\mathrm{N}\log N)$ (Springel (2005)). Although not as efficient as a PM code, tree codes do not suffer from the resolution limit imposed by a finite grid size.

Mesh Relaxation Codes: Mesh relaxation techniques (e.g. Gauss-Seidel iteration) can solve the Poisson equation to within any required tolerance. On a uniform grid, pure Gauss-Seidel iteration is unworkable due to the large number of iterations required to communicate information over very many gridpoints. These techniques become more useful in combination with adaptive grids. In these codes the large scale perturbations are first solved on a coarse grid and then sampled up to a finer grid, with the Gauss-Seidel iterations used only to perform corrections on small scales.

Hybrid Techniques: Various authors have either extended these techniques or combined two or more of them in order to make use of the best features of each method. The large drawback to using a PM code is that the forces on small scales are strongly supressed. The simplest extension to a plain PM code is to explicitly sum the forces from nearby particles (the PP calculation), and use the mesh to calculate long range forces. This is a $\mathrm{P^3M}$ code (Hockney and Eastwood (1988); Efstathiou and Eastwood (1981)). Efstathiou et al. (1985) compared the relative accuracy of $\mathrm{P^3M}$ and PM codes in a cosmological context. $\mathrm{P^3M}$ codes can resolve the gravitational force down to any required scale but the number of operations needed to calculate the gravitational force scales as $O(N_n \log(N))$ (Springel (2005)), where N represents the number of particles in the simulation and N_n represents the average number of neighbours (defined as particles close enough to be calculated using the PP bit of code). If the particle resolution is significantly higher than the resolution of the PM grid then the PP calculation begins to dominate and

the calculation slows down. A further extension to the P^3M code is to adaptively place high resolution PM grids over high density parts of the volume Adaptive-P^3M (Couchman et al. (1995)). This cuts down on the amount of work that the PP calculation has to do inside the refined regions. Care must be taken, however, as the memory requirements for the storage of many high resolution PM grids are large.

The numerical technique that is currently most commonly employed in cosmological simulation is the Tree-PM (Xu (1995)) method. In a similar way to the P^3M method, the short range part of the gravitational interaction is replaced with a tree code. This simulation technique is very computationally efficient, allows the gravitational force to be resolved to arbitrarily small scales and as such has become the technique of choice for most of the current generation of lagrangian codes.

2.2.2 The Hydrodynamic Calculation

In order to describe the behaviour of an ideal gas we need to define both the equations of motion and the equation of state. The equation of state of an ideal gas is given by

$$p = A\rho^{\gamma}\,, \tag{2.18}$$

where γ is the ratio of the specific heats. There are then three equations that describe the behaviour of the gas. The continuity equation

$$\frac{\partial \rho}{\partial t} + \nabla \cdot (\rho \mathbf{v}) = 0\,, \tag{2.19}$$

the Euler equation,

$$\frac{\partial \rho \mathbf{v}}{\partial t} + \nabla \cdot (\rho \mathbf{v}^2) + \nabla p = \rho \mathbf{g}\,, \tag{2.20}$$

and the energy evolution equation:

$$\frac{\partial \rho E}{\partial t} + \nabla \cdot [(\rho E + p)\mathbf{v}] = \rho \mathbf{v} \cdot \mathbf{g}\,. \tag{2.21}$$

Here p represents the gas pressure, ρ represents its density and γ is the adiabatic exponent. A is assumed to be constant in both space and time and is related to the specific entropy of the gas. v and g represent the velocity and gravitational acceleration vectors and E is the internal energy per unit mass of the gas. These equations also need to be coupled to the Poisson equation as described in section 2.2.1.

In the remainder of this section we will discuss how these equations can be modelled both by a system of particles and by a regular mesh.

Particle Methods

The most popular Lagrangian (mass quantised) hydrodynamics method is Smoothed Particle Hydrodynamics (SPH; (Gingold and Monaghan, 1977; Monaghan, 1992)) in which the fluid is represented by some number of discrete point particles, and the fluid properties at any point can be calculated by taking the weighted mean of the properties of nearby particles.

The main advantages of SPH are that it does not need any sort of spatial grid in order to calculate spatial derivatives and that by its lagrangian nature areas of interest (usually high density regions) are well represented due to the flow of particles into that area. This is in contrast to grid based hydrodynamic methods where great effort must be spent in setting up grids so that areas of interest are simulated in high detail (see section 2.2.2).

The essentials of the SPH method can be expressed with two concepts. Firstly we need to assume that the phase space distribution of a gas can be adequately represented by some discrete distribution of particles. Secondly the properties of the gas fluid at any point can be estimated by taking a weighted average of those properties over the surrounding particles.

The value of some hydrodynamical quantity, A, can be calculated at any point in space via the following equation

$$\widetilde{A}(\mathbf{r}) = \int A(\mathbf{r}')W(\mathbf{r}-\mathbf{r}',h)\mathbf{dr}', \tag{2.22}$$

where the integration is over all space. A represents some property of the fluid, with $\widetilde{A}$ representing an estimated value at coordinate $\mathbf{r}$. $W(r,h)$ is an appropriately chosen smoothing function, the SPH kernel, which must obey two properties. Firstly it must be normalised,

$$\int W(\mathbf{r}-\mathbf{r}',h)\mathbf{dr}' = 1\,, \tag{2.23}$$

secondly, in the limit that we have an infinite number of particles (and therefore h tends to zero), the kernel must tend toward becoming a delta function

$$\lim_{h\to 0} W(\mathbf{r}-\mathbf{r}',h) = \delta(\mathbf{r}-\mathbf{r}')\,. \tag{2.24}$$

The original kernel chosen by ((Gingold and Monaghan, 1977)) was a Gaussian,

$$W(x,h) = \frac{1}{h\sqrt{\pi}}e^{-(x^2/h^2)}\,, \tag{2.25}$$

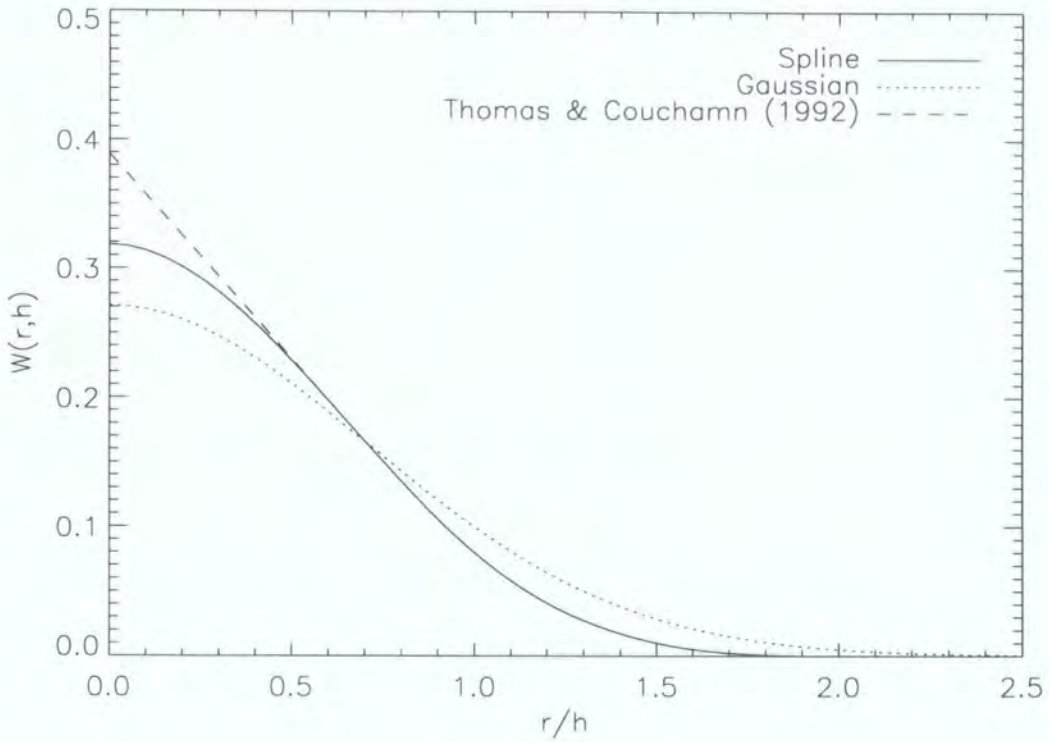

Figure 2.5: A comparison of SPH kernels as used in the literature. The spline kernel falls off to precisely zero ar $r/h = 2.0$, the Gaussian kernel is small but nonzero at high radii. The Thomas & Couchman (1992) kernel is identical to the spline kernel at $r/h > 0.5$, but is modified such that it is linear at smaller radii

an improvement to the Gaussian kernel comes in the form of a spline kernel

$$W(\mathbf{r}, h) = \frac{1}{\pi h^3} \begin{cases} 1 - \frac{3}{2}\frac{r}{h}^2 + \frac{3}{4}\frac{r}{h}^3 & \text{if } 0 \leq \frac{r}{h} < 1; \\ \frac{1}{4}(2 - \frac{r}{h})^3 & \text{if } 1 \leq \frac{r}{h} \leq 2; \\ 0 & \text{otherwise}. \end{cases}$$

The spline kernel has a continuous second derivative, the dominant error term in the integral interpolant falls off as h^2, and for $r > 2h$ the kernel is precisely zero. Figure 2.5 shows three different SPH kernels used in the literature.

When working with a finite number of particles the integral in equation 2.22 is approximated by a summation

$$\widetilde{A}(\mathbf{r}) = \sum_i m_i \frac{A_i}{\rho_i} W(\mathbf{r} - \mathbf{r_i}, h)\,. \tag{2.26}$$

Where i represents a unique particle label for each particle in the simulation. It is important to note that although the summation in equation 2.26 is formally done over

all particles, in reality the choice of $W(r,h)$ will mean that only those particles within a distance $2h$ of the point we are considering are important in the calculation. Derivatives of the interpolant can be obtained by ordinary differentiation; no need for finite differencing or grids. For example ∇A may be written

$$\nabla \widetilde{A}(\mathbf{r}) = \sum_i \frac{A_i}{\rho_i} \nabla W(\mathbf{r} - \mathbf{r}_1, h)\,. \tag{2.27}$$

Using these ideas the equations of motion of an ideal gas may be obtained. Consider an ideal gas with no heat sinks or inputs, decoupled from the gravitational force. The momentum (or Euler) equation is then described by

$$f = -\frac{1}{\rho}\nabla p + \nabla \phi_G = \frac{\partial v}{\partial t} + (v \cdot \nabla)v\,. \tag{2.28}$$

For the purposes of demonstrating how SPH represents the equations of motion of an ideal gas we will consider rewriting the $\nabla P/\rho$ term in a form suitable for integration with an SPH code. The simplest approach is to use the fundamental equation of SPH (equation 2.26) along with equation 2.27 and the identity

$$\nabla P = [\nabla(\rho P) - P\nabla\rho]/\rho\,, \tag{2.29}$$

to write

$$\rho_a \nabla P_a = \sum_i m_i (P_a - P_i)\nabla_i W(r_i - r_a, h)\,, \tag{2.30}$$

where $\nabla_i W(r_i - r_a, h)$ represents the gradient of $W(r_i - r_a)$ taken with respect to the coordinates of particle a. However, with this equation of motion, linear and angular momentum are not conserved exactly (Monaghan (1992)). It is therefore better to make the equation symmetric between a and i by using the identity

$$\frac{\nabla P}{\rho} = \nabla(\frac{P}{\rho}) + \frac{P}{\rho^2}\nabla(\rho)\,, \tag{2.31}$$

we can write that

$$\frac{\nabla_a P_a}{\rho_a} \approx \sum_i \frac{m_i}{\rho_i^2} P_i \nabla_i W(r_i - r_a, \bar{h}) + \frac{P_a}{\rho_a^2}\sum_i m_i \nabla_i W(r_i - r_a, \bar{h})\,;$$

$$\frac{\nabla_a P_a}{\rho_a} = \sum_i m_i \Big(\frac{P_a}{\rho_a^2} + \frac{P_i}{\rho_i^2}\Big)\nabla_i W(r_a - r_i, \bar{h})\,, \tag{2.32}$$

where $W(r_a - r_i, \bar{h})$ is a symmetrized kernel (Hernquist and Katz (1989)), which ensures that the force between two particles is precisely symmetric.

$$W(r_a - r_i, \bar{h}) = \frac{1}{2}|W(r_i - r_j, h_i) + W(r_i - r_j, h_j)|\,. \tag{2.33}$$

Equations 2.32 and 2.33 provide the basis for reconstructing the equations of motion of an ideal gas in a form suitable for use in SPH. Using these techniques the momentum of particle i can be integrated forward in time using (Springel and Hernquist (2002))

$$\frac{dv_i}{dt} = -\sum_a m_a \Big(\frac{P_a}{\rho_a^2} + \frac{P_i}{\rho_i^2} + \Pi_{ia} \Big) \nabla_a W(r_a - r_i, \bar{h}) \,. \tag{2.34}$$

Where Π_{ia} represents an artificial viscosity force between particles i and a. The artificial viscosity is introduced in order to damp the unphysical oscillations that occur after strong shocks, and also has the effect of allowing shocks to occur. The artificial viscosity term was originally introduced by Monaghan and Gingold (1984) and took the following form, known as the Monaghan-Gingold tensor

$$\Pi_{ij} = \begin{cases} -\frac{\alpha c_{ij} \mu_{ij} + \beta \mu_{ij}^2}{\rho_{ij}}, & \text{if } (r_i - r_j) \cdot (v_i - v_j) < 0; \\ 0 & \text{otherwise} \end{cases}$$

$$\mu_{ij} = \frac{h_{ij}(r_i - r_j) \cdot (v_i - v_j)}{r_{ij}^2 + \eta^2}, \tag{2.35}$$

where c_{ij}, h_{ij} and ρ_{ij} are the arithmetic means of the sound speed, smoothing length and density of particles i and j. α and β are free parameters that are used to tune the strength of the artificial viscosity term. Steinmetz (1996) found that values of $\alpha = 0.5$ and $\beta = 1$ worked well. For problems with strong shocks, these values were increased to $\alpha = 1$ and $\beta = 2$, but it is noted that an increased artificial viscosity has the effect of smearing out shocks.

It was noted (Hernquist and Katz (1989); Katz and Gunn (1991)) that this form of the artificial viscosity does not vanish in pure shear flows ($\nabla \times v \neq 0$, $\nabla \cdot v = 0$), and may lead to unphysical angular momentum transport in the formation of disks, particularly in the case of low resolution galaxy simulations (Steinmetz (1996)). This problem can be almost completely prevented by using the form of the articifial viscosity due to Balsara (1995)

$$\bar{\Pi}_{ia} = \Pi_{ia}(f_i + f_a) \,, \tag{2.36}$$

where the function f is an order-of-magnitude estimate of the irrotational fraction of the flow. Described by

$$f_i = \frac{|\nabla \cdot v_i|}{|\nabla \cdot v_i| + |\nabla \times v_i| + 0.0001 c_i / h_i} \tag{2.37}$$

The final term in the denominator prevents divergences. In the case of a purely compressive flow ($\nabla \times v = 0$, $\nabla \cdot v \neq 0$) $f = 1$, and the artificial viscosity is identical to the Monaghan-Gingold viscosity. In a purely rotational flow ($\nabla \times v = 0$, $\nabla \cdot v \neq 0$) the

viscosity is completely supressed. Steinmetz (1996) found that in a simple simulation of a gas disk containing 280 particles and using the Monaghan-Gingold artificial viscosity the half-angular-momentum velocity grew by a factor of 2 to 3 within 3Gyr. Using the modified artificial viscosity the half-angular-momentum radius varied by less than 10% over a Hubble time.

Grid Methods

The basis of most grid based hydrodynamics codes is to split the simulation volume into a discrete set of gridpoints, for which the gas properties are known. The evolution of this system can then be evolved by solving for the behaviour of a gas at the boundaries between each of these cells. This problem may be described in the following way,

$$\mathbf{u}(x,0) = \begin{cases} u_{\mathrm{L}}^0 & \text{for } x < 0\,, \\ u_{\mathrm{R}}^0 & \text{for } x \geq 0\,, \end{cases}$$

where subscripts denote spatial positions and superscripts represent time. Such a problem is called a *Riemann problem* and represents a discontinuity in the gas properties. The usual way of incorporating the Riemann problem into the numerical solution is to take (u_i^n, u_{i+1}^n), for each i in turn, that is to treat the boundary between each grid cell in the simulation as a separate Riemann problem, which are then thought of as providing information about the solution in each interval $(i, i+1)$. The precise workings of the Riemann solver are beyond the scope of this thesis but include random choice methods (Glimm (1965); Chorin (1976)) and Newton iteration (Colella and Glaz (1985); van Leer (1979)).

Godunov (1959) assumed that the initial data could be replaced by a piecewise constant set of states with discontinuities at $x_{i-1/2}$ and $x_{i+1/2}$, this simplified problem can then be solved exactly. Godunov then replaced the exact solution with a new set of piecewise constant approximation, preserving the integral properties of the exact solution. The first major extension to this approach was made by van Leer (van Leer (1979)), who approximated the data by piecewise linear segments, allowing discontinuities between the segments. This approach required the solution to a more complex problem but raises the accuracy of the resulting solution substantially.

The piecewise parabolic mesh (PPM) method (Colella and Woodward (1984); Woodward and Colella (1984)) extends this concept to higher orders and uses parabolic solutions to the Riemann problem, allowing for much more accurate solutions. PPM codes are now used in a wide variety of current mesh codes (e.g. Fryxell et al. (2000); Bryan

et al. (1995)) due to the high order accuracy of the scheme and the fact that PPM can resolve strong shocks much more readily than the lower order piecewise codes.

Uniform mesh codes run into the same problems as pure PM gravity codes, the spatial resolution of the resulting solution is limited by the size of the largest uniform mesh that can fit in memory. For this reason adaptive mesh refinement (AMR) codes have been developed (e.g. Fryxell et al. (2000)). Here the spatial resolution of the grid is allowed to vary with position. This is demonstrated in figure 2.6, which depicts the density field around a simulated galaxy cluster (see section 2.3.1 for details of the simulation).

In most AMR codes, the actual structure of the adaptive mesh takes one of two forms: *block structured,* in which the computational volume is filled with identical 'blocks' that may be split apart or combined together to change the spatial resolution at a point., or *structured grids* in which rectangular grids of different sizes and resolutions are placed in regions of interest. Figure 2.6 shows an example of a block structured code (FLASH). Each square in the image represents $8 \times 8 \times 8$ grid points. It is clear that the regions of interest (the centre of the galaxy cluster) are simulated with greater precision than the surrounding gas. One challenge in writing a block structured AMR code is to find some measure of when it is necessary to refine a block up to a higher refinement level. FLASH uses the Löhner (1987) estimator. In one dimension if we have some discrete function u, defined at gridpoints seperated by an amount Δ then we can approximate the second derivative as:

$$\frac{\partial^2 u}{\partial x^2} \approx \frac{u_{i+1} + u_{i-1} - 2u_i}{\Delta^2}. \tag{2.38}$$

The Löhner estimator, which is a modified version of the second derivative, normalised by the average of the gradient over one computational cell, is then given by

$$L = \frac{|u_{i+1} - 2u_i + u_{i-1}|}{|u_{i+1} - u_i| + |u_i - u_{i-1}| \epsilon \Big[|u_{i+1} - 2|u_i| + |u_{i-1}| \Big]}, \tag{2.39}$$

where u_i is the refinement test variable's value in the ith cell. The last term in the denominator of this expression acts as a filter, preventing the refinement of small ripples. By default the constant ϵ is given a value of 0.01, although this can be tuned in the code. In addition to this refinement criterion it was found that forcing refinement in regions of high density provided very good results.

At the expense of more complex coding, AMR codes allow Eulerian hydrodynamics codes to compete with Lagrangian codes, both in terms of spatial resolution and the computational resources required to evolve a system (see e.g. O'Shea et al. (2005) for a recent comparison)

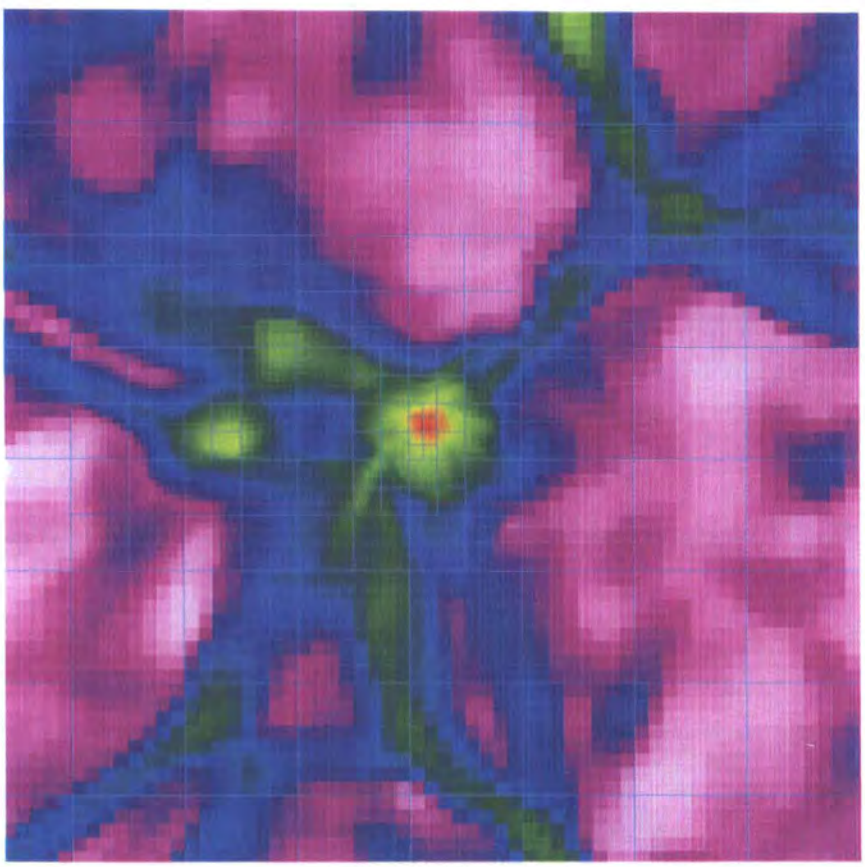

Figure 2.6: Baryonic density slice around a simulated galaxy cluster at redshift 0. The image is 20Mpc across. Blue lines represent the location of blocks in the adaptive AMR mesh, each square contains 8×8 gridpoints. It is clear that the mesh has a higher spatial resolution in the higher density regions so the properties of the cluster are simulated more exactly than those of the surrounding low density gas. The blocks in this image were refined using the local gas density to flag when it becomes necessary to increase the level of refinement.

2.2.3 Time Stepping

The final numerical detail we will consider is the role of timestepping in cosmological simulation.

The naive choice for a system of timestepping is just to update the velocity and position at the start of each timestep and then make linear increments over the length of each timestep. This may be denoted by

$$r_{i+1} = r_i + v_i \Delta t\,, \tag{2.40}$$

$$v_{i+1} = v_i + a_i \Delta t\,, \tag{2.41}$$

where r, v and a are positions, velocities and accelerations respectively. The subscript i represents the value at the beginning of timestep i, and $i+1$ represents its value at the end. This timestepping method is only first-order accurate. A simple improvement on this simple timestepping scheme is the so called *leapfrog* scheme (see e.g. Hockney and Eastwood (1988)), which is second-order accurate, but still only requires one costly force evaluation per timestep

$$r_{i+\frac{1}{2}} = r_i + \frac{1}{2} v_i \Delta t\,, \tag{2.42}$$

$$v_{i+1} = v_i + a_i t\,, \tag{2.43}$$

$$r_{i+1} = r_{i+\frac{1}{2}} + \frac{1}{2} v_{n+1} \Delta t\,, \tag{2.44}$$

More complex timestepping algorithms are discussed by Quinn et al. (1997). Other than the time integration method we need to be careful with the length of timesteps. If timesteps are too short then the simulation will take an unfeasable amount of time to run. If they are too long then the system being simulated may become unstable

For baryonic matter the fundamental timestep limiting factor is given by the Courant-Friedrich-Lewy (CFL; Courant et al. (1928)) condition, which qualititatively states that the timestep must be less than the time for 'some significant action' to occur, and preferably considerably less. For baryonic matter this is usually set using the time it takes for a 'signal', say, a sound-wave to propagate across one resolution element, or

$$\Delta t_{\mathrm{cfl}} = \frac{H\ \mathrm{cfl}}{c} = \frac{H \rho\ \mathrm{cfl}}{\gamma p}\,, \tag{2.45}$$

where cfl is a parameter, set significantly lower than unity in order to guarantee stability, c is the local sound speed. H is the size of a single resolution element corresponding to either the smoothing length of a particle or the size of a grid cell depending on the type of simulation code in use. Other timesteps used in simulations include limits controlled by the radiative cooling rate of a gas and the maximum particle displacements per timestep.

2.3 Code Validation

In sections 2.2.1 and 2.2.2 we discussed a large number of different simulation algorithms, all of which make different assumptions and calculate forces in widely differing ways. It is reasonable, therefore, to ask how similar the behaviour of the different codes is in a physically relevant situation. In this section we investigate the accuracy of results produced by two different simulation codes (FLASH Fryxell et al. (2000) and Gadget Springel (2005)), which operate using two very different algorithms (PPM on an adaptive grid & Mesh relaxation in FLASH versus SPH and Tree-PM in Gadget).

The full physics of galaxy formation and evolution is a very complex problem (see chapter 3), and is not yet fully understood. For this reason we restrict our studies to physics that is relatively well understood: gravitational dynamics and adiabatic[1] gas dynamics. Although vastly simplified, this model has immediate relevance to the simulation of various astronomical objects including the hot component of X-Ray clusters.

Inclusion of more complex physical processes including cooling and heating, metal production, supernova feedback and reionization is still something that differs wildly between different authors and a comprehensive comparison between different author's implementations of additional physics still remains to be done.

Various code comparison projects have been undertaken in the literature. O'Shea et al. (2005) compare two codes, simulating dark matter and adiabatic gas in a large cosmological volume. The most comprehensive comparison project undertaken so far is probably the Santa Barbara (SB) comparison project of Frenk et al. (1999). The initial conditions for the SB cluster are publically available[2], making the SB cluster an ideal way to verify the accuracy of our simulation codes.

2.3.1 The Santa Barbara Test

The SB cluster (Frenk et al. (1999)) represents the formation of an X-Ray cluster in a CDM universe, and was originally simulated independently by 12 different groups. The codes compared in the paper span the full range of techniques discussed in this chapter and include both parallel and serial simulation codes, and have resolution lengths from 5kpc all the way up to 960kpc.

[1] Although technically these simulations do contain non-adiabatic shocks and should perhaps better be termed 'non-radiative'simulations, we continue to follow the convention found in the Santa Barbara paper and refer to them as adiabatic simulations

[2] http://star-www.dur.ac.uk/~csf/clusdata

The cosmology of choice for the SB study used the parameters $h_{100} = 0.5$, $\sigma_8 = 0.9$, $\Omega = 1.0$, $\Omega_b = 0.1$. The size of the simulated volume at redshift 0 was 64Mpc. The power spectrum for the simulation was obtained from Bardeen et al. (1986). The initial conditions were made available in the form of 256^3 grids of linear theory displacements in the x, y, and z directions (see 2.4), and each author in the original SB paper used these displacement files to generate initial conditions in their own format. The recommended starting redshift for each simulation is 20.

Simulation Details

We ran the SB cluster initial conditions with both Gadget and FLASH. The initial conditions were subsampled down to a 64^3 mesh, then one particle was placed in the centre of each gridcell. The minimum allowed adaptive gridcell size allowed in FLASH is 0.125Mpc, the gravitational softening allowed in Gadget is 0.1Mpc. The minimum SPH smoothing length is constrained to be a minimum of 0.1 times the gravitational softening.

At redshift zero the centre of mass coordinates of the haloes agreed very well, [33.308, 34.45, 33.53] in FLASH versus [33.418, 34.36, 33.26] in Gadget. The dark matter properties at redshift zero lie in all cases within the range of scatter investigated in the SB paper. The dark matter density profiles are shown in figure 2.7. Outside of the resolution length, each density profile agrees very well. Inside of one resolution length the results become very uncertain. The same behaviour was found with the dark matter velocity dispersion profiles (figure 2.8). Plots of the positions of individual dark matter particles in each halo show that although the overall position of the halo remains unchanged between simulations, the locations of the very non-linear small scale structure is significantly different between the two runs. Once again this is in good agreement with the differences between different codes found in the original SB paper.

In common with the SB paper we find that when looking at the baryonic component of the matter in the halo agreement between the different codes is less good. The gas density profile in the halo (figure 2.10) is in good agreement down to roughly the resolution length of each code. The AMR codes, which specify gas properties on a grid have a constant density below the grid spacing.

The temperature profile of the galaxy clusters are plotted in figure 2.10. Additionally plotted in this graph are the results from the code of Bryan and Norman (1995), an AMR code that solves the hydrodynamic equations in a similar way to FLASH. Once again up

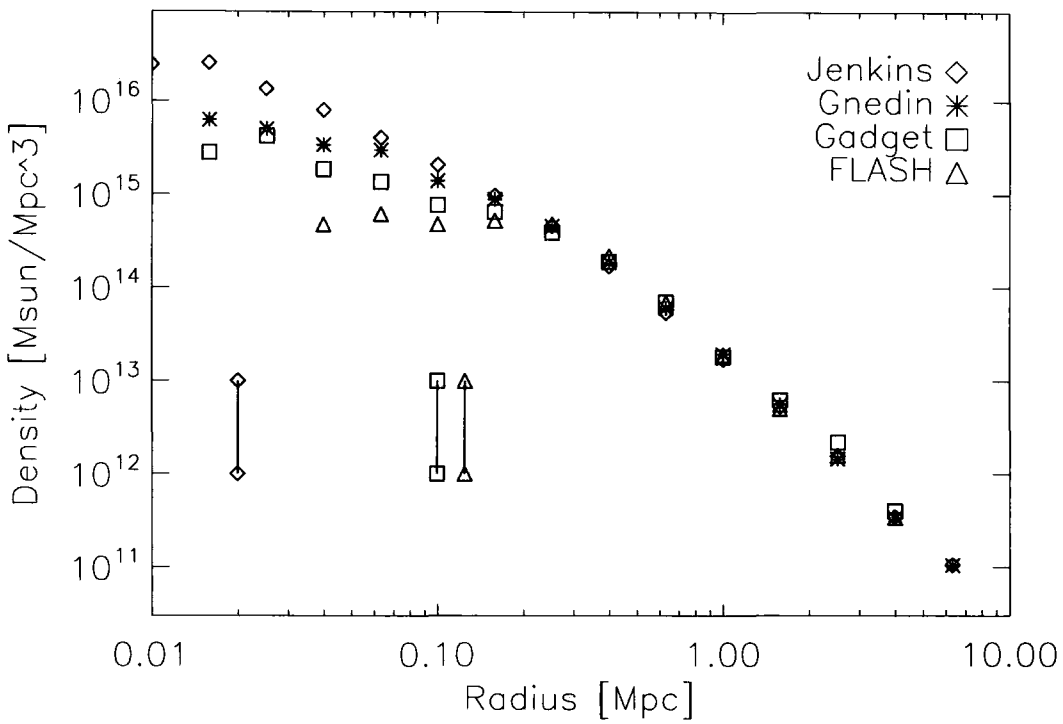

Figure 2.7: Dark matter density profile of the z=0 halo from both the FLASH and Gadget simulations alongside the results of Jenkins and Gnedin from the Santa Barbara paper. The three vertical lines represent the resolution limit in each of the simulations. The FLASH resolution limit is set to the size of the smallest cells in the cluster. Flash obtains a constant density on scales below the grid spacing. The Gadget softening was chosen to match closely with the FLASH grid spacing. The softening of Jenkins is 20kpc, the softening of the Gnedin simulation is equal to the softening of the Gadget simulation.

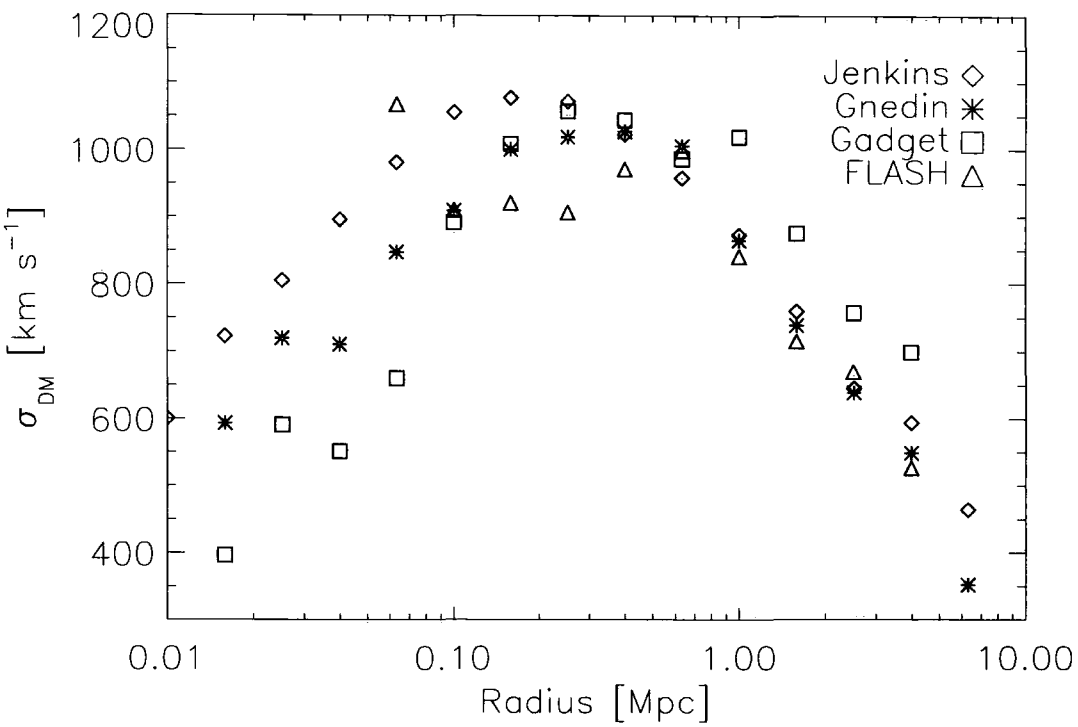

Figure 2.8: Dark matter velocity dispersion profile of the z=0 halo from both the FLASH and Gadget simulations alongside the results of Jenkins and Gnedin from the Santa Barbara paper. The quantity shown in the plot is the one-dimensional velocity dispersion, calculated from the three dimensional velocity dispersion by $\sigma_{1d} = \sigma_{3d}/\sqrt{3}$. In common with Frenk et. al. (1999) we find that agreement between all codes is to within 20% outside of the resolution limit of the code.

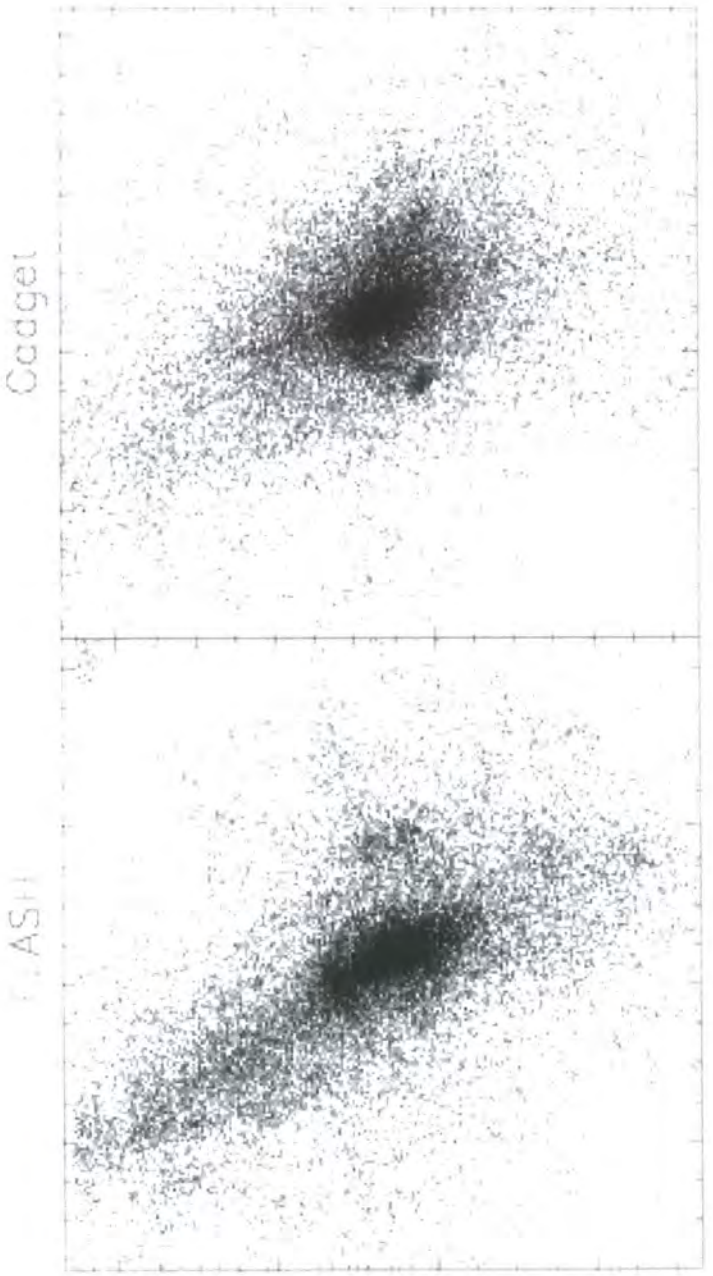

Figure 2.9: Dark matter particles in an 8Mpc cube centered on the centre of mass of each halo. The shapes of the haloes between the FLASH and Gadget runs differ by a small amount, but are both well within the spread of shapes observed in the original Santa Barbara study.

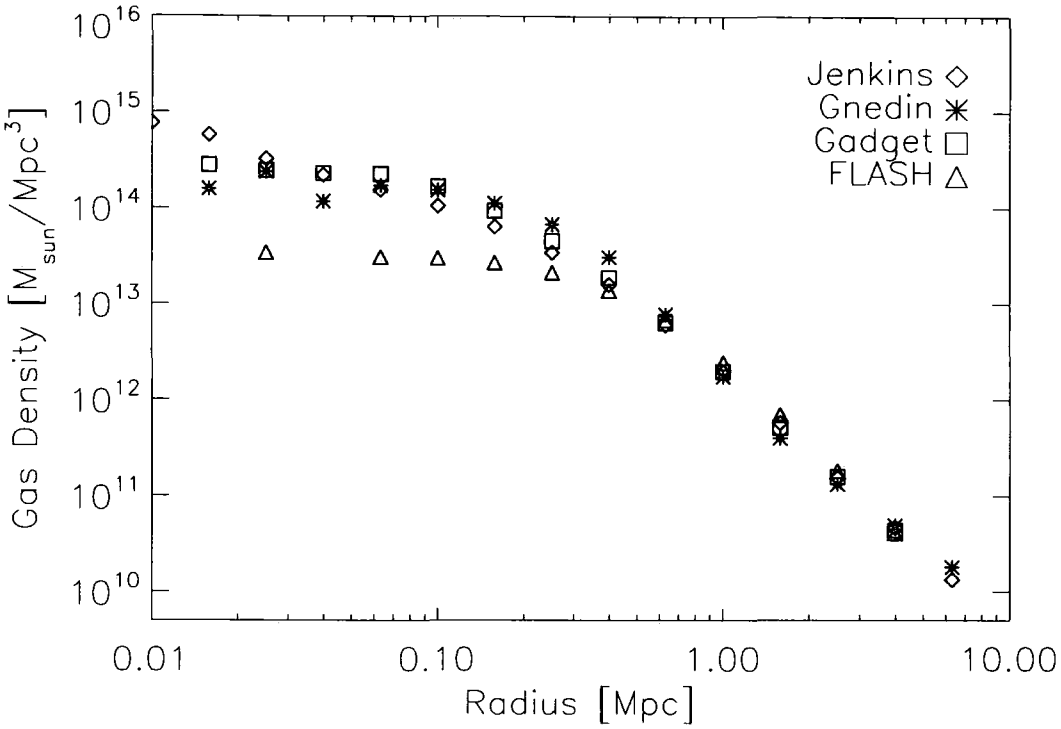

Figure 2.10: Gas density profile of the SB cluster from various runs. Agreement outside of the resolution length is good between all codes. Inside of one resolution length the density of the AMR run flattens off due to the finite cellsize.

to the resolution length of the simulation the results are very similar.

These results suggest that both codes can reliably simulate a complex, non-linear situation and despite the wildly different numerical effects and methods applied in each code the overall results are remarkably similar. This suggests that both codes are solving both the gravitational evolution and hydrodynamics accurately in this fully cosmological scenario.

2.4 Initial Conditions

The generation of correct and accurate initial conditions for cosmological simulation is of crucial importance. The problem is one of representing a nearly scale-invariant Gaussian random field with a given power spectrum using a discrete set of particles. In this section we introduce methods of generating the initial, uniform distributions of particles, before discussing methods of imposing a given power spectrum on this particle distribution,

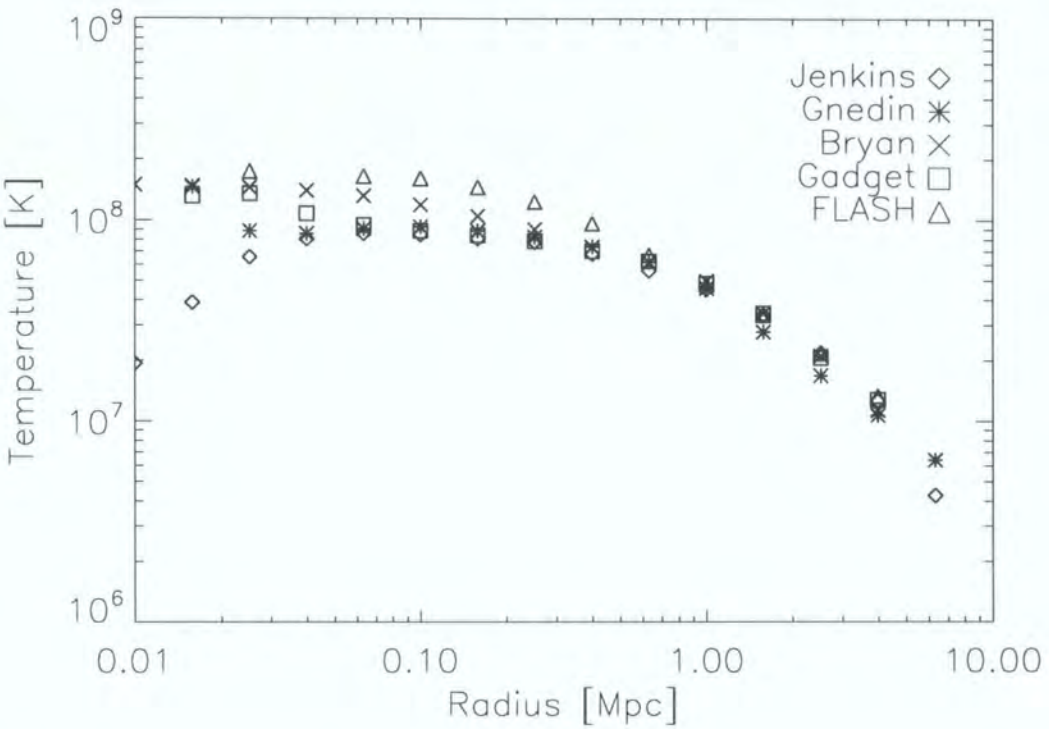

Figure 2.11: Temperature profile of the SB cluster. Agreement at the outskirts of the cluster is good. Additionally plotted in this graph are the results from the code of Bryan & Norman (1995), an adaptive mesh refinement code similar to FLASH. It appears that the temperatures near the centre of the halo diverge depending upon the simulation method used. It should be noted, however that the cellsize in the FLASH simulation is 0.125Mpc so we cannot trust results below this radius.

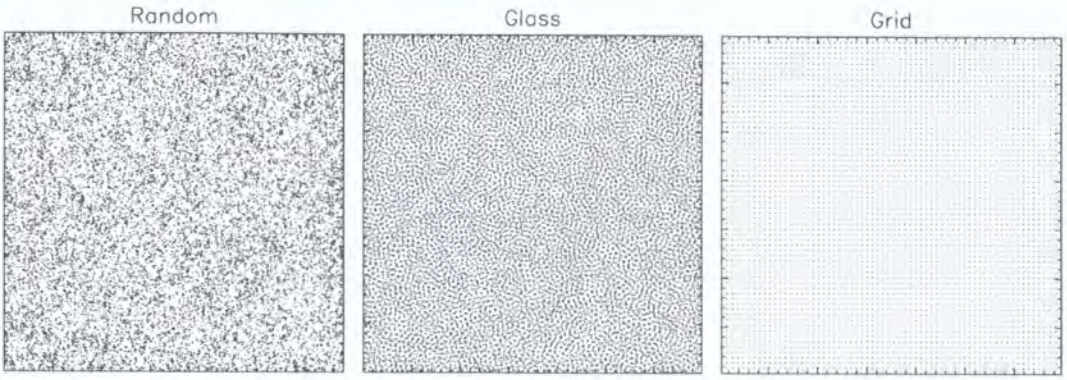

Figure 2.12: Different types of pre-initial particle distribution. Each panel shows particles from a thin slice from the pre-initial conditions of a 262144 particle simulation. The random distribution is unsuitable for any sort of simulation, both the grid and glass distributions are used by various authors.

and then discussing techniques for resimulation of individual objects. A code developed using the techniques in this section is used in section 2.5 to quantify the numerical effects of mass resolution on simulated galaxy haloes.

2.4.1 Pre-initial Conditions

Before generating cosmological initial conditions it is important that we are able to create a set of 'pre-initial conditions'; which represent the state of the system before the cosmological perturbations are imposed. This has been investigated in detail by White (1994), who discussed three choices for initial particle positions: randomly placed particles, particles on a grid and particles in a *glass* distribution. An example of each of these three configurations is shown in figure 2.12

The first type of particle distribution, random placing of particles suffers strongly from Poisson noise and initially has a white noise power spectrum. If a simulation filled with randomly distributed particles is evolved, non-linear objects will form, even if other fluctuations are not imposed.

The usual approach to get around this is to place particles on a grid, the problem with this is that the initial grid structure introduces strongly preferred directions along each axis on the scale of a few grid spacings. Simulations with very little small scale power (e.g. hot dark matter simulations) will therefore develop spurious features along the grid axis.

The optimal solution, as first proposed by White (1994) is to take an initially random distribution of particles and evolve it as an Einstein-de Sitter universe for many expansion factors, with the sign of the gravitational force reversed, making it repulsive. This has the effect of smoothing out the particle distribution and removing all large scale perturbations and preferred directions.

2.4.2 Generation of Uniform Volume

As mentioned at the beginning of section 2.4 the problem we wish to solve is that of representing a primordial spectrum of density fluctuations using a discrete ensemble of particles. As discussed in section 1.1.2 in the inflationary scenario these density fluctuations are thought to take the form of a Gaussian random field. This is defined as a field where in real space each data element is chosen from a Gaussian probability distribution. Equivalently we can represent this in k-space by choosing for each k-value normally distributed amplitudes (with variance equal to $P(k)$) and random phases.

The properties of a Gaussian random field may be described completely by its power spectrum, $P(k)$, which in the case of most inflation models is of the form

$$P(k) = Ak^{n_s}\,, \tag{2.46}$$

where A and n_s are the amplitude and slope of the primordial power spectrum. Cosmological initial conditions are generated at significantly lower redshift than the epoch of inflation and so we have to take into account their early linear evolution. This is usually accomplished by multiplying the initial fluctuation spectrum by a transfer function representing the later evolution of the fluctuations

$$P(k) = Ak^{n_s}|T(k,t)|^2\,, \tag{2.47}$$

Transfer functions have been published by many authors, Holtzman (1989) provides a listing of early examples and describes how such transfer functions are calculated. These analytic examples have been superseded by numerical codes that compute matter transfer functions accurately (e.g. Ma and Bertschinger (1995); Seljak and Zaldarriaga (1996)). For the rest of this chapter we will assume that reliable transfer functions have been provided. We now introduce the methods by which initial conditions can be generated by two different methods; working in k-space and real-space.

In k-space

Our starting point is to describe the density at a given space and time, using the density contrast, defined as

$$\delta(x,t) = \frac{\rho(x,t) - \bar{\rho}(t)}{\bar{\rho}(t)}, \tag{2.48}$$

where $\bar{\rho}(t)$ is the mean density of the universe at time t. If we assume that the simulation volume we are interested in is periodic then we may obtain the k-space representation of the density field via a Fourier transform,

$$\delta(k) = \frac{1}{(2\pi)^3} \int e^{-i\mathbf{k}.\mathbf{x}} \delta(x) d^3x \,. \tag{2.49}$$

In k-space we may measure the power spectrum, $P(k)$, of the Gaussian random field by noting that

$$P(k) = \delta(k)\delta^*(k) \,. \tag{2.50}$$

Where $*$ represents the complex conjugate. In order to generate a random field with a desired power spectrum we initially specify the k-space density fluctuation field, $\delta(k)$. The k-space fluctuation is a complex value with random phase and a gaussian distribution of amplitudes. We pick a random amplitude for each k-vector from a distribution with variance $P(k)$. These random numbers are the k-space representation of the density field, the real space initial density field may be then recovered by an inverse Fourier transform

$$\delta(x) = \int e^{i\mathbf{k}.\mathbf{x}} \delta(k) d^3k \,. \tag{2.51}$$

This provides a conceptually simple way of generating random fields with any desired power spectrum, but it does have some drawbacks, notably that only a discrete number of wavevectors can fit a whole number of wavelengths across the simulation volume. These wavevectors are given by

$$k = \frac{2n\pi}{L}, \tag{2.52}$$

where L is the size of the simulation volume. This suggests that the power spectrum is only sampled at a series of discrete values, and so any features in the power spectrum that lie between these points are not modelled. This effect is particularly serious at small values of k, where only very few wavelengths fit across the box. Secondly the finite size of the simulation volume means that wavelengths larger than that of the simulation box are not included in the simulations. Gelb and Bertschinger (1994) showed that in a CDM cosmology a simulation volume of size 50Mpc would underestimate σ_8 by over

40% due to the truncation of the power spectrum at long wavelengths. Simulations of the Lymanα forest are particularly strongly affected by the loss of this large scale power (see Rauch et al. (1997)). We shall see in later sections how some of these difficulties may be overcome.

Given a pre-initial distribution of particles and an associated density field the final step in calculating the initial particle distribution is to perturb the initial particle positions to give them the the same power spectrum as the density field generated above. This procedure is calculated using the Zel'Dovich approximation (Zel'Dovich (1970))

$$\mathbf{r}(t, \mathbf{q}) = a(t)[\mathbf{q} - b(t)s(\mathbf{q})]\,, \tag{2.53}$$

where $\mathbf{q}$ represents the unperturbed position of each particle, $\mathbf{r}(t, q)$ is the perturbed position of a particle initially at position $\mathbf{q}$, $b(t)$ is the growth rate of linear density fluctuations in the expanding universe and $s(q)$ may be written as the gradient of a potential, $s(q) = \nabla\Phi(q)$ (Shandarin and Zeldovich (1989)), given suitable normalisation.

The form of the growth rate for density perturbations depends upon the cosmology we are using, and are calculated by rewriting the continuity, Euler and Poisson equations in terms of the density contrast (Peebles (1981)), and then assuming that in the early universe both δ and $\dot{\delta}$ are small. In the case of an Einstein-de Sitter universe ($\Lambda = 0, \Omega_0 = 1$, dust-dominated) then two solutions are permitted; a growing mode with $\delta \propto t^{2/3} \propto a$ and a decaying mode $\delta \propto 1/t \propto a^{-3/2}$. In the case of universes with lower matter densities or a cosmological constant the solution is more complex but some situations still lend themselves to analytic solution (see e.g. White (1994))

Once positions have been assigned, it is necessary to generate initial velocities for the particles. At times corresponding to the start of the simulation the peculiar velocity at a point can be derived immediately from equation 2.53

$$\dot{r}(t, q) = -\dot{b}(t)s(q)\,. \tag{2.54}$$

The full procedure for generating a uniform set of initial conditions is therefore to

- Generate a random field in k-space with variance $P(k)$ at each k vector
- take the inverse fourier transform of this field, to obtain a uniform mesh of densities with the required power spectrum
- generate a 'pre-initial' distribution of particles

- displace the particles using the Zel'Dovich (1970) approximation, set velocities using equation 2.54

In the following sections we will examine how initial conditions may be generated by a different method and then how non-uniform initial conditions may be created.

In Real Space

It was pointed out by Salmon (1996) that any Gaussian random field sampled on a lattice can be written as the convolution of white noise with a function that we will call the transfer function, or

$$\delta(\mathbf{x}) = \int T'(k)N(k)e^{i\mathbf{k}.\mathbf{x}}d^3k\,, \tag{2.55}$$

Where $T'(k)$ represents the transfer function. Note that the transfer function defined above is not the same as that defined in section 2.4.2. $N(k)$ is Gaussian white noise with autocorrelation

$$\xi(r) = \langle N(x)N(x+r)\rangle = \delta_D(0)\,, \tag{2.56}$$

where δ_D represents a Dirac delta function. The transfer function may be shown to be related to the desired power spectrum of our density field by (Salmon (1996))

$$T'(k) = [P(k)]^{1/2}\,. \tag{2.57}$$

Thus we may construct a random field with any desired power spectrum via the following steps:

1. Generate an uncorrelated gaussian white noise sample, $N(x)$, for each real space gridpoint
2. Take the Fourier transform of this white noise
3. Multiply the noise by the transfer function as given previously
4. Inverse Fourier transform this result to obtain the real space density contrast field

This method is very similar to the k-space approach to generating Gaussian random fields, but with the addition of an extra Fourier transform (step 1). This makes the generation of single level Gaussian random fields more computationally expensive than the k-space approach , but is absolutely critical when the algorithm is extended to multiple levels.

2.4.3 Generation of 'Zoomed' Initial Conditions

As discussed in section 2.4.2 in order to obtain the correct clustering statistics of haloes in a cosmological setting we require the use of large simulation volumes. However, in order to simulate an individual galaxy in a realistic manner we require a spatial resolution better than 1kpc and a mass resolution better than $10^6 M_\odot$. This consideration has led to many authors performing 'zoomed' simulations, where most of the particles are concentrated in regions of interest, and other regions are represented only by relatively few particles. Generating initial conditions of this form provides additional challenges on top of those required to generate a uniform volume. In this section we will discuss how zoomed initial conditions can be generated, both in real and k-space.

In k-space

To make random fields on multiple levels of refinements an approach followed by many workers is that due to Katz et al. (1994). Here the Gaussian random field is first generated at the coarsest level, then again at a higher resolution ensuring that all of the random numbers chosen for long wavelength power match up exactly with the coarse data. These density fields are then overlaid onto each other and the high resolution data is then thrown away in the regions where it is not needed.

This approach has the advantage that it is simple to code, but the maximum resolution of any region in the simulation is limited by the largest FFT that can be performed as in order to generate even a small region at high resolution the high resolution data for the entire simulation volume is generated by direct FFT and then most of it is thrown away. This fact limits the maximum resolution of any initial conditions generated by this method on today's computers to around 2048^3 (holding a single 2048^3 array of single precision real numbers in memory takes 32Gb of RAM). For this reason alternative approaches to the generation of Gaussian random fields have been implemented, we will now discuss one of these.

In Real Space

Pen (1997) and Bertschinger (2001) extended the real-space techniques of Salmon (1996) to multiple levels of refinement. In this section we will discuss the generation of initial conditions on two levels of refinement, as represented in figure 2.13. In figure 2.13 the coarse level has M vertices, the subvolume has $M_s = 3$ vertices and refinement factor,

$r = 2$. We can then describe any gridpoint using two indices, m for the coarse grid and n for the refined grid. The first step in generating a refined set of initial conditions is to create an additional sample of white noise on the refined grid, N_1, which maintains the same large-wavelength structure as the white noise on the coarse grid, N_0. This may be accomplished by (Hoffman and Ribak (1991)) the process

$$N(m,n) = N_1(m,n) + N_0(m) - \bar{N}_1(m)\,. \tag{2.58}$$

This just represents that each coarse gridpoint has its value propagated to its associated r^3 refined points, then a high frequency correction $N_1 - \bar{N}_1$ is added. Given this white noise we now need to calculate the corresponding density field, which is considered to be split up into long and short-wavelength components,

$$\delta(m,n) = \delta_0'(m,n) + \delta_1(m,n)\,, \tag{2.59}$$

where $\delta_0'(m,n)$ represents the contribution of the coarse density field, $\delta_0(m)$, to the high resolution density field. $\delta_1(m,n)$ is the additional short wavelength contribution from the refined region.

The *short-wavelength contribution* may be calculated simply from

$$\delta_1(m,n) = [N_1(m,n) - \bar{N}_1(m)] \star T'\,, \tag{2.60}$$

where $\star$ represents a convolution. It was shown by Bertschinger (2001) that it is possible to carry out this convolution using only $(rM_s)^3$ gridpoints and as such the full $(rM)^3$ calculation is avoided.

The *long-wavelength contribution* could, in principle, be evaluated by resampling the coarse grid at every point up to the full resolution of the refined region (i.e. an entire r^3M^3 points), and then explicitly carrying out the convolution over the entire volume. This is impractical and runs into exactly the problem we are trying to avoid through working in real space as we would be forced to carry out convolutions over the entire $(rM)^3$ volume. One solution to this problem is to write $\delta_0'(m,n)$ as a convolution of the coarse density field with some filtering function:

$$\delta_0'(m,n) = \sum_{m',n'} \delta_0(m')W(m-m',n-n')\,. \tag{2.61}$$

This equation has a simple interpretation. The coarse grid density is spread to the fine grid by mapping each value of $\delta_0(m)$ to r^3 grid points. This leads to aliasing effects due to each bunch of r^3 gridpoints having exactly the same value, and in k-space this leads to

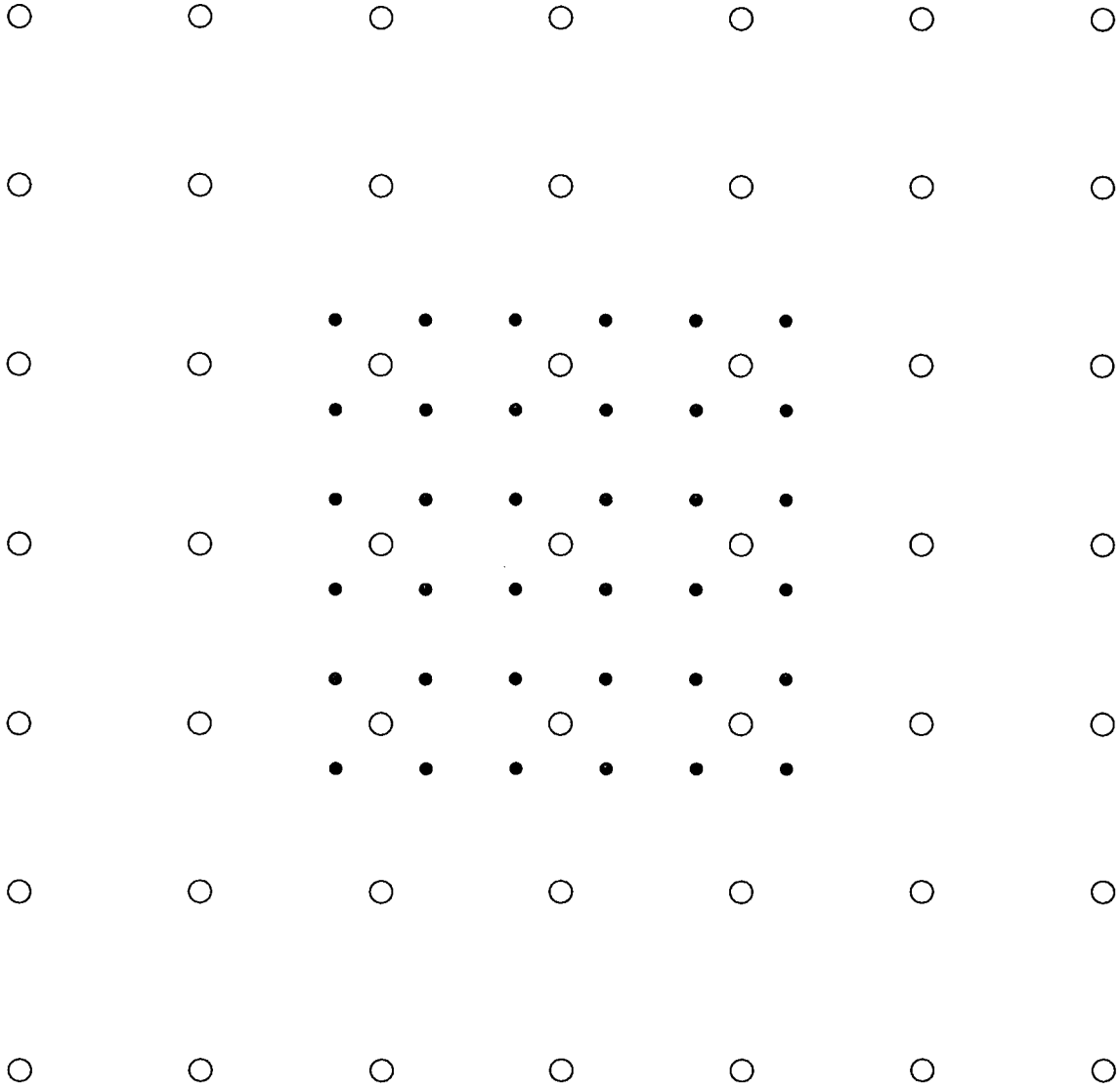

Figure 2.13: Simple depiction of a nested, hierarchical grid. The hollow points represent a coarse grid, with size $M = 7$, the filled points represent a refined region with refinement factor, $r = 2$ and the size of the refined region is $M_s = 3$

high frequency distortions, thus just setting $\delta'(m,n) = \delta_0(m)$ leads to an incorrect power spectrum. Bertschinger (2001) showed that this problem can be avoided through the use of an *aliasing filter*, which for certain forms of $W(m,n)$ is exactly equivalent to carrying out the full convolution.

Figure 2.14 shows a typical CDM overdensity field with two different levels of refinement generated by the methods described above. The refined density fields in each of the panels was generated without resorting to carrying out the full $(rM)^3$ calculation, and as such grids at much higher levels of refinement can be generated without

prohibitive memory and computational costs. This section contains a simplified sketch of the method by which the real-space refinement technique works, more detail is contained in Pen (1997) and Bertschinger (2001)

2.4.4 An Initial Conditions Toolkit

Generating a zoomed set of initial conditions consists of very many separate and distinct steps, we need to: generate the transfer function and initial particle distribution. Create density and velocity fields for each different mass resolution. Finally the particles on each level of refinement must be displaced according to the Zel'Dovich (1970) approximation.

In order to facilitate this process an interactive toolkit has been developed, which allows interactive selection of cosmological parameters and refinement positions (figure 2.15).

In addition to generating cosmological density fields using the real space techniques of Bertschinger (2001) the package facilitates the easy resimulation of haloes. Two features of the code that make this process easy are the method of particle refinement, and the way in which noise samples are generated so that their large scale properties remain the same regardless of the resolution of the sample. The methods by which each of these processes is carried out is detailed in the following section

Particle Refinement on Individual Haloes

When creating the initial particle distributions for the simulation of an individual halo it is important that we both minimize the number of high resolution particles in the simulation (in order that it remains computationally cheap to run), and ensure that the halo itself remains uncontaminated by low resolution particles. These two constraints are sometimes difficult to satisfy at the same time. We will now describe the process by which our code marks out individual haloes and ensures they remain uncontaminated until redshift zero. Figure 2.16 shows the steps required to identify and recursively refine a region of a simulation. Each panel represents a different part of the process

top-left: A low resolution simulation is run, all particles that are within the halo at redshift zero are marked, and their positions in the low resolution initial conditions are noted. This defines the region of the early universe that will collapse into the halo at redshift zero

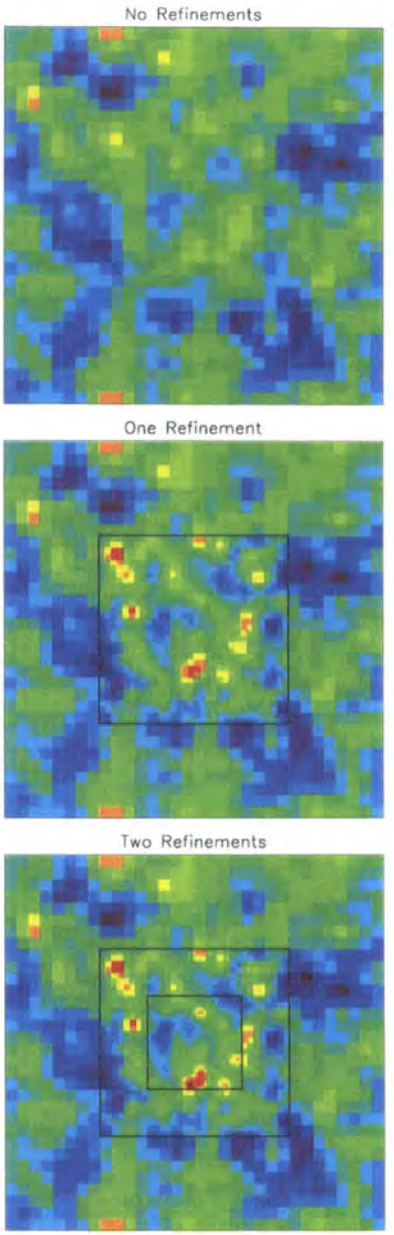

Figure 2.14: Slice through a typical overdensity field for a CDM set of initial conditions. The upper panel shows an unrefined density field with $M = 32$. The central plot depicts the same field with an additional subgrid ($r = 2$, $M_s = 16$), and the lowest grid shows a second, nested refinement ($r = 4$, $M_s = 8$). Note that in each case the large scale features of the field agree well, but additional small-scale power is added to the simulation volume.

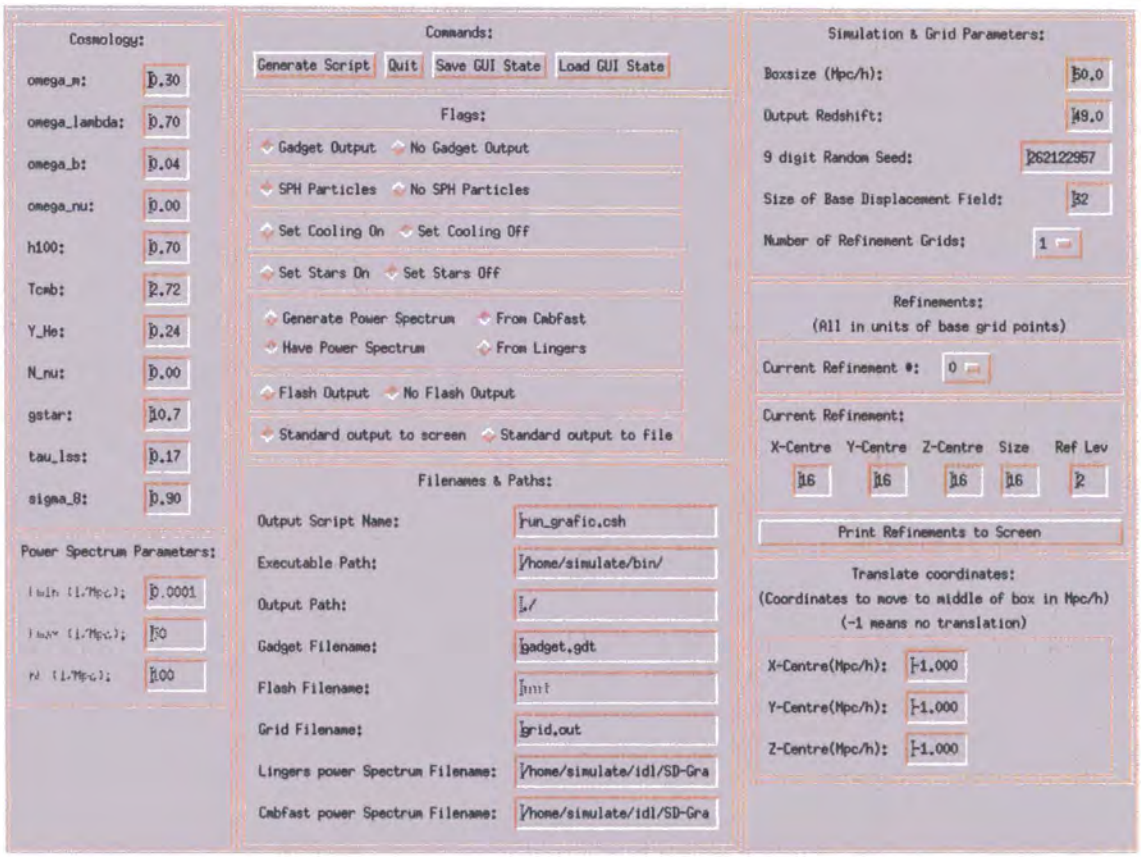

Figure 2.15: Grapical User Interface for the initial conditions toolkit, allowing for simple, interactive input and design of cosmological initial conditions.

top-right: It is important that particles that end up in the halo are completely surrounded by other high-resolution particles, in order that their properties are self consistently calculated and no spurious numerical effects are introduced. The first step of ensuring this is the case is to map the low-resolution halo particles to a three dimensional grid, note that there are holes in the grid, and some particles are disconnected from the rest of the region.

bottom-left: The grid is convolved a number of times with the three-dimensional version of the following kernel

$$\mathbf{X} = \begin{pmatrix} 0 & 1 & 0 \\ 1 & 1 & 1 \\ 0 & 1 & 0 \end{pmatrix}.$$

This has the effect of filling in holes in the marked region, and expands the region so that previously unlinked regions are now linked.

bottom-right: All low resolution particles lying within the expanded grid are marked and then split into 8 lower mass particles. Particles that interact with the halo should now be part of one contiguous region, and should be surrounded by other particles of the same mass. Figure 2.17 shows an example of this process being carried out recursively. At redshift zero The resulting halo is uncontaminated by high resolution particles out to a few times r_{200}, and there are a minimal number of particles in the initial conditions. If, at any point, it is found that the halo is contaminated, it is easy to mark additional particles, and so extend the high resolution region, until the halo does not become contaminated by redshift zero.

Resolution Independent White Noise

One disadvantage of generating noise samples in real-space is that it is very difficult to increase the resolution of a uniform grid whilst maintaining the same large scale power. In order that our initial conditions toolkit can, for a given random seed, *always* reproduce the same large scale structure we require a more sophisticated method of generating white noise samples. We choose to work in k-space and generate numbers such that the lowest k-vectors are always filled in first with zero-mean gaussian deviates. The noise sample is then obtained by performing an inverse FFT on this field. If we require the same noise field at a different resolution this process is repeated, with higher frequency modes incorporated, the underlying low frequency structure will, however, remain unchanged.

Putting together the real-space refinement techniques with a simple, interactive initial condition design package and the halo resimulation techniques discussed in this section allows us to rapidly and easily construct catalogues of resimulated haloes in any cosmology, and to scale up and down the mass resolution of any one of these haloes without affecting the large scale properties of the simulation. In the next section we use this code to probe the effects of mass resolution on the properties of simulated haloes.

2.5 Resolution Studies

The effects of numerical resolution on the properties of simulated galaxies is numerically complex, hard to quantify, especially in the presence of complex physical processes for instance SN feedback and radiative cooling. In this section we attempt to quantify the effects of particle number on the properties of individual MW sized haloes.

Early galaxy formation simulations (e.g. Navarro and White (1994)) reported a huge loss of angular momentum in galaxies, leading to the formation of galaxies strongly dominated by a central concentration of cold gas. Governato et al. (2004) and Kaufmann et al. (2006) have shown that the angular momentum problem is due to poor mass and spatial resolution, which may lead to significant angular momentum loss in baryonic disks embedded in dark matter haloes.

Additionally Governato et al. (2006) found that as the number of particles in the halo approached several million, the resulting galaxy became increasingly less centrally concentrated. It is clear that a thorough understanding of the effects of resolution on the properties of simulated galaxies is a non-trivial problem but is necessary in order to fully understand galaxy formation.

The work described in this section represents preliminary work in this direction, comparing a set of MW sized haloes generated using the initial conditions code of section 2.4.4 at a variety of mass resolutions.

2.5.1 The Simulation Set

In order to identify suitable candidates for resimulation a uniform volume of size 50Mpc containing 192^3 dark matter particles was evolved from redshift 99 to redshift zero (using $\Omega_0 = 0.3$, $\Omega_b = 0.044$, $h_{100} = 0.7$, $\sigma_8 = 0.9$). From this volume MW mass haloes ($\sim 10^{12} M_\odot$) were selected and resimulated at a variety of mass resolutions. Table 2.5.1 contains details of the mass resolutions in different simulations. The highest mass reso-

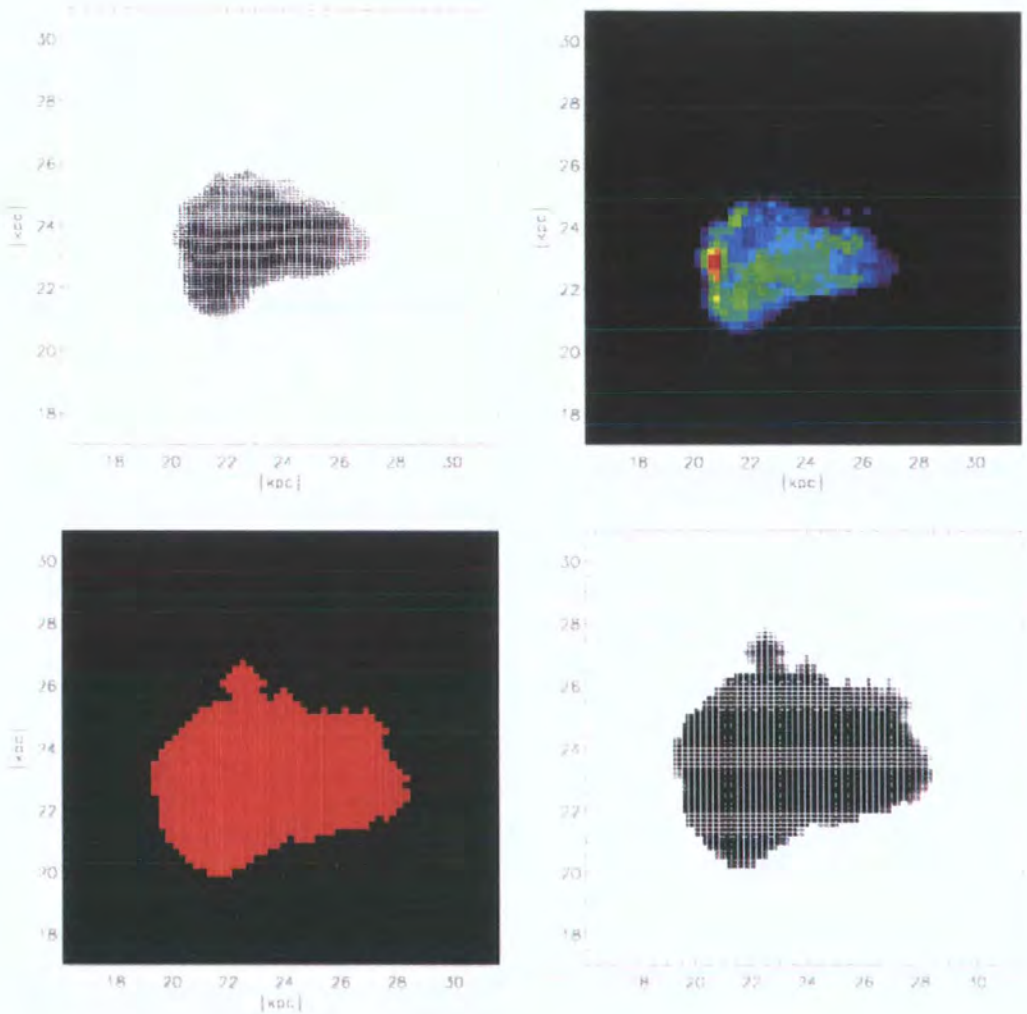

Figure 2.16: The process by which individual haloes are marked out in a zoomed simulation. The process is described in detail in the text and will be summarized here. *top-left:* a low resolution simulation is run, and the particles that end up in the halo are traced back to the initial conditions. *top-right:* these particles are mapped to a grid. *bottom-left:* this grid is then convolved with a kernel (equation 2.4.4), which ensures that the halo remains uncontaminated. *bottom-right:* particles in the marked region are split into eight lower mass particles.

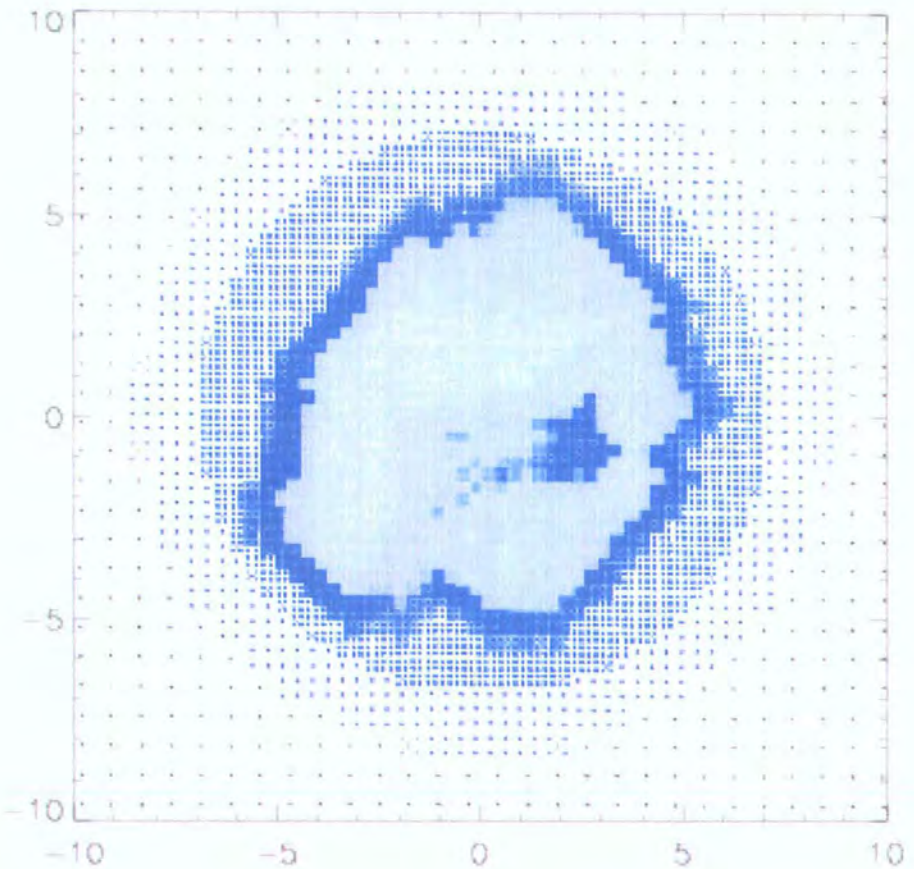

Figure 2.17: Thin slice through the initial ($z = 99$) particle distribution in a zoomed galaxy simulation. The darker the colour of a point the more massive the particle it represents. The ratio of masses between the largest and smallest particles in this simulation is ~ 5000

Name	Mass Resolution ($M_\odot$)	Gravitational Softening (kpc)
Uniform	7.21×10^8	9.11
X0X2	9.01×10^7	4.61
X0X3	2.67×10^7	3.03
X0X4	1.12×10^7	2.27
X0X5	5.76×10^6	1.82
X0X6	3.34×10^6	1.52

Table 2.1: Details of the initial particle masses in each of the simulations. The naming convention followed is that the numbers represent one-dimensional spatial resolutions ($\propto N_{part}^{1/3}$), as a multiple of the resolution used in the uniform simulation. The mass represents the smallest dark matter particle mass in the refined region.

lution haloes have a dark matter mass resolution of $2.84 \times 10^6 M_\odot$, corresponding to of order a few million dark matter particles within the virial radius of the halo. The lowest mass resolution simulations contain only a few tens of thousands of particles within the virial radius of the halo. The gravitational softening length of each simulation was chosen to be consistent with that used in Reed et al. (2005a), scaled with the linear spatial resolution ($\propto N^{1/3}$) of our simulations.

Each simulation was run with dark matter only, again with dark matter and adiabatic gas and then finally with dark matter, and full physics (star formation, feedback, radiative cooling, as described in Stinson et al. (2006)). In this section we discuss only the dark matter simulations.

2.5.2 The Basic Properties of Haloes

Some global properties of the haloes are plotted as a function of mass resolution in figure 2.19. For each halo the virial radius, r_{200}, defined as the radius at which the mean density contrast of the halo falls to 200 times the critical density of the universe was calculated and in addition each halo was fitted with the universal density profile due to Navarro et al. (1997)

$$\frac{\rho(r)}{\rho_c} = \frac{\delta_c}{\left(\frac{r}{r_s}\right)\left(1+\frac{r}{r_s}\right)^2}. \tag{2.62}$$

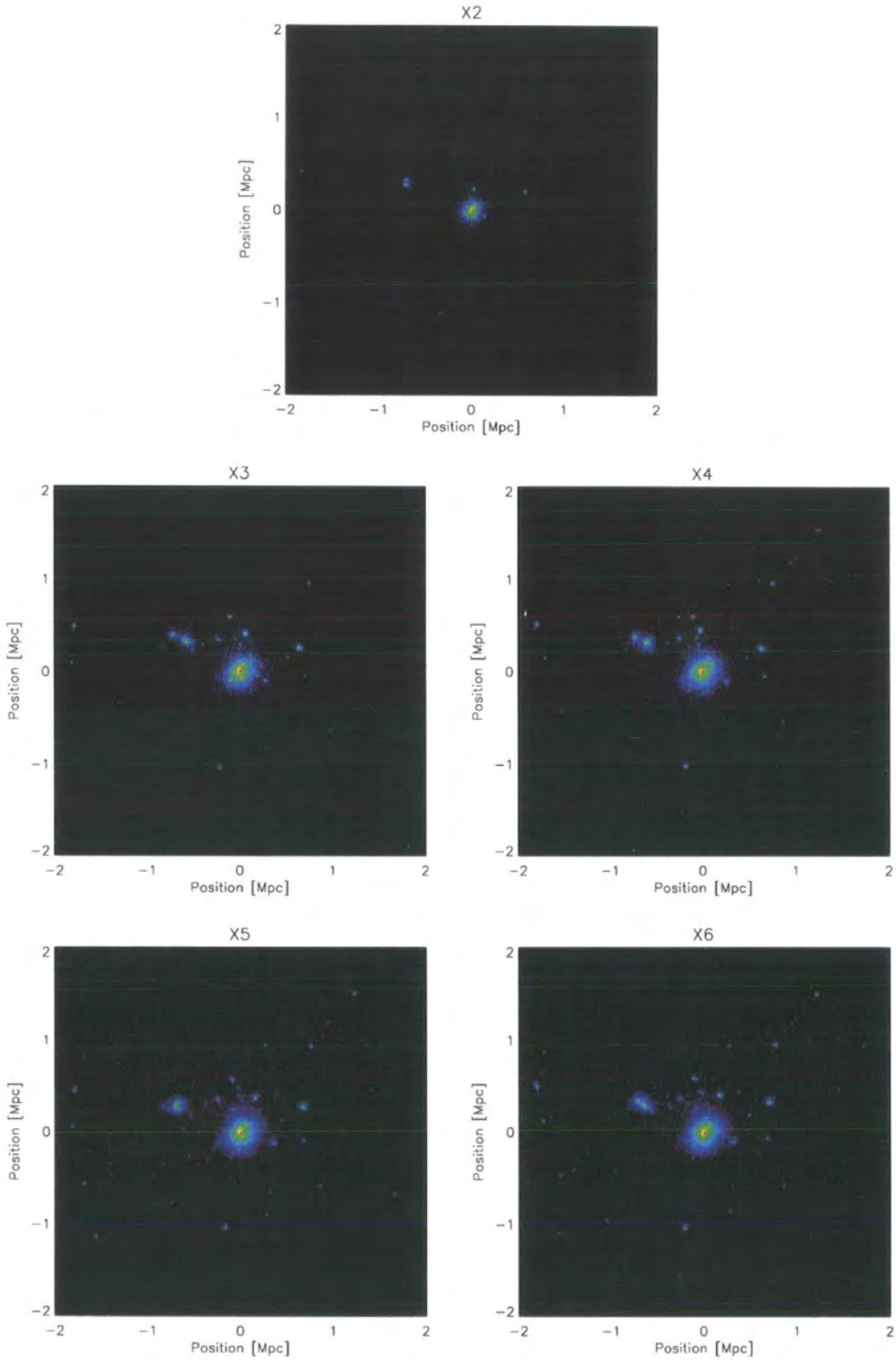

Figure 2.18: Dark matter particles in each of the haloes. It is clear that dark matter substructure in each of the simulations is in almost exactly the same place.

This profile fits the densities of dark matter haloes using two parameters, a central density, δ_c, and a scale radius, r_s. Additionally the *concentration* of a halo may be defined as the ratio of its virial radius to its scale radius. This number measures the shape of the halo (Łokas and Mamon (2001))

Figure 2.19 shows some of these parameters plotted as a function of the mass resolution of the simulation. One encouraging result is that the concentration parameters of the haloes remains approximately constant across all mass resolutions, indicating that the halo shape is independent of resolution. σ_{DM}, the three dimensional dark matter velocity dispersion decreases as the mass resolution in the halo is degraded. As would be expected the central overdensity of the halo, δ_c, decreases as the particle mass is increased. This is due to the effects of larger softening lengths.

Figure 2.20 shows the dark matter density profile of the halo for each mass resolution. The diagonal lines are power laws with slopes -3 and -1.5, as would be predicted from the universal halo fitting formula of Navarro et al. (1997). Figure 2.21 shows the three dimensional dark matter velocity dispersion of each halo, again agreement between the various simulations is very good, especially at large radii, where the features corresponding to individual pieces of substructure match up well.

Figure 2.22 shows the mean radial velocity as a function of radius for all of the different resolutions. It is clear that despite the vastly different refinement sizes and resolutions between the different simulations, the large scale flow velocities of the simulations are always recovered.

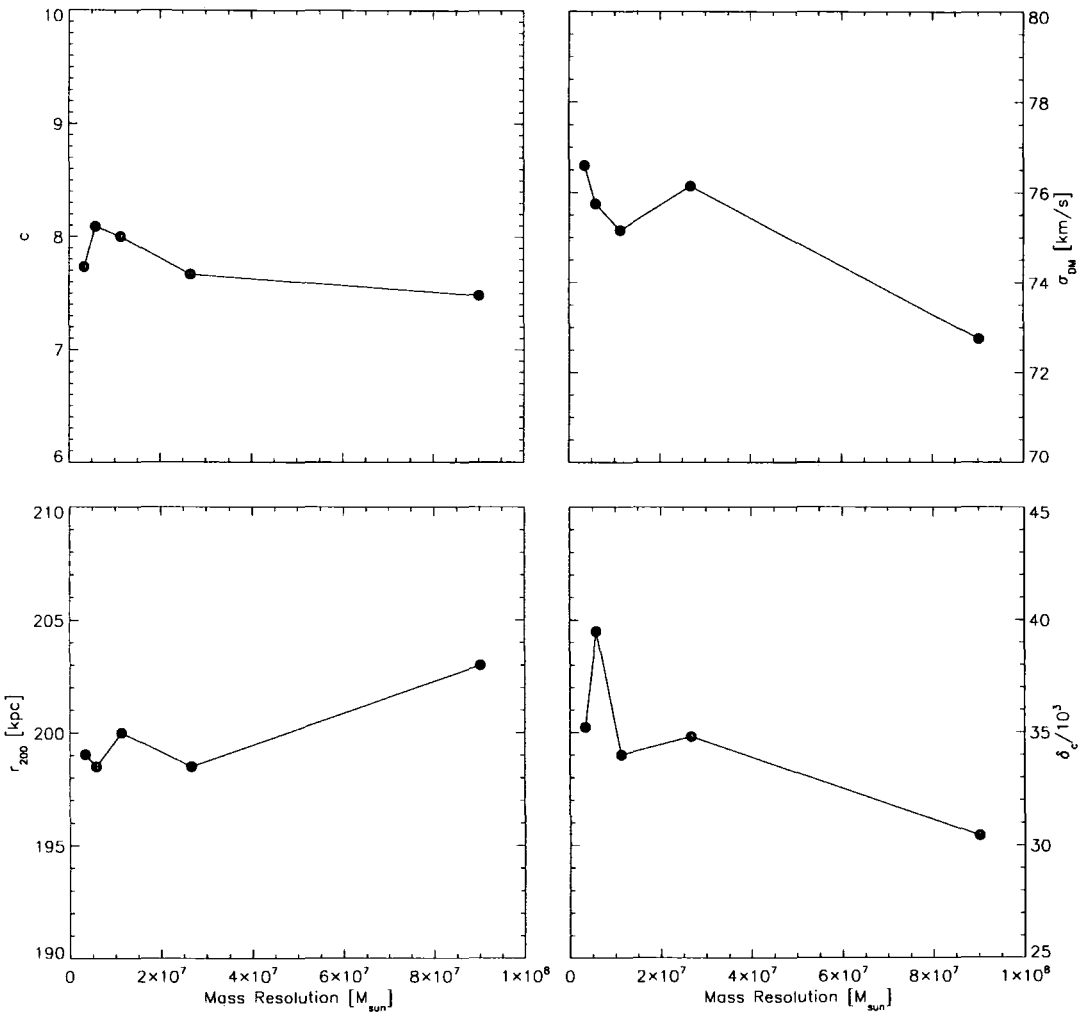

Figure 2.19: The global properties of the dark matter halo as a function of particle mass. *top-left* Halo concentration, *top-right* mean three dimensional velocity dispersion within r_{200}, *bottom-left* virial radius, *bottom-right* galaxy central overdensity as determined from a fit to the NFW profile.

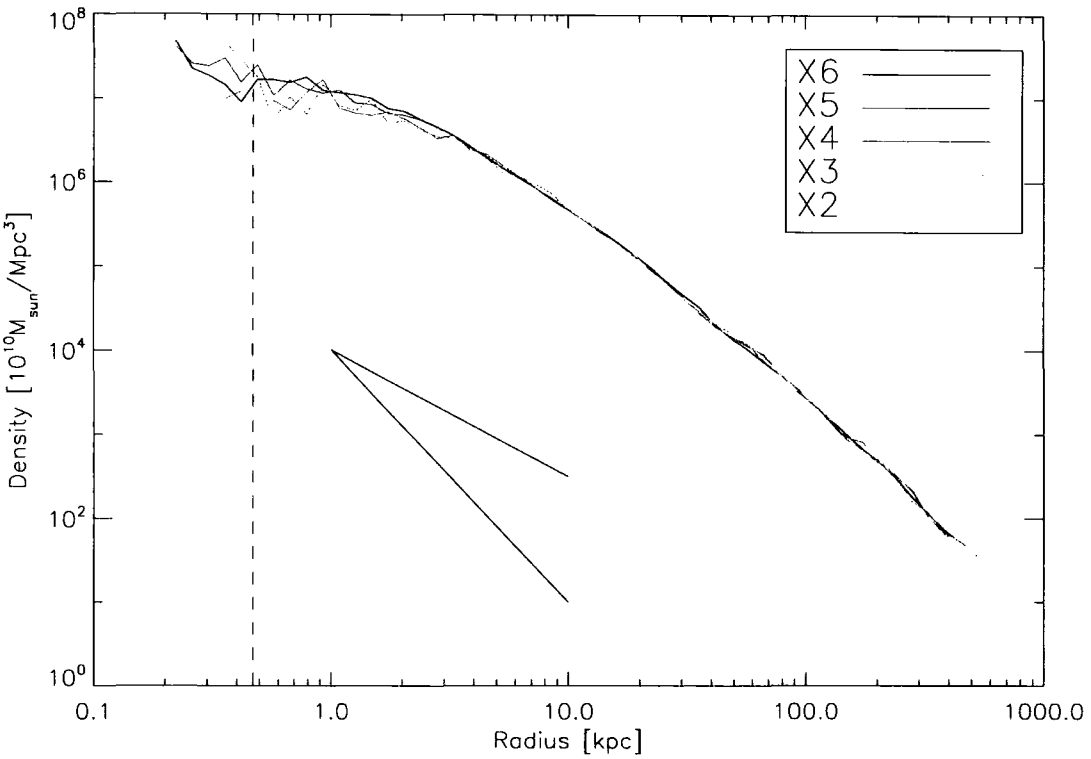

Figure 2.20: Dark matter density profiles. The vertical lines represent the softening length in simulations X2 and X6. The diagonal lines represent power laws with slopes -1 and -3, which are the inner and outer slopes prediced by the NFW density profile. The agreement between the different simulations is good up to the resolution length of each simulation.

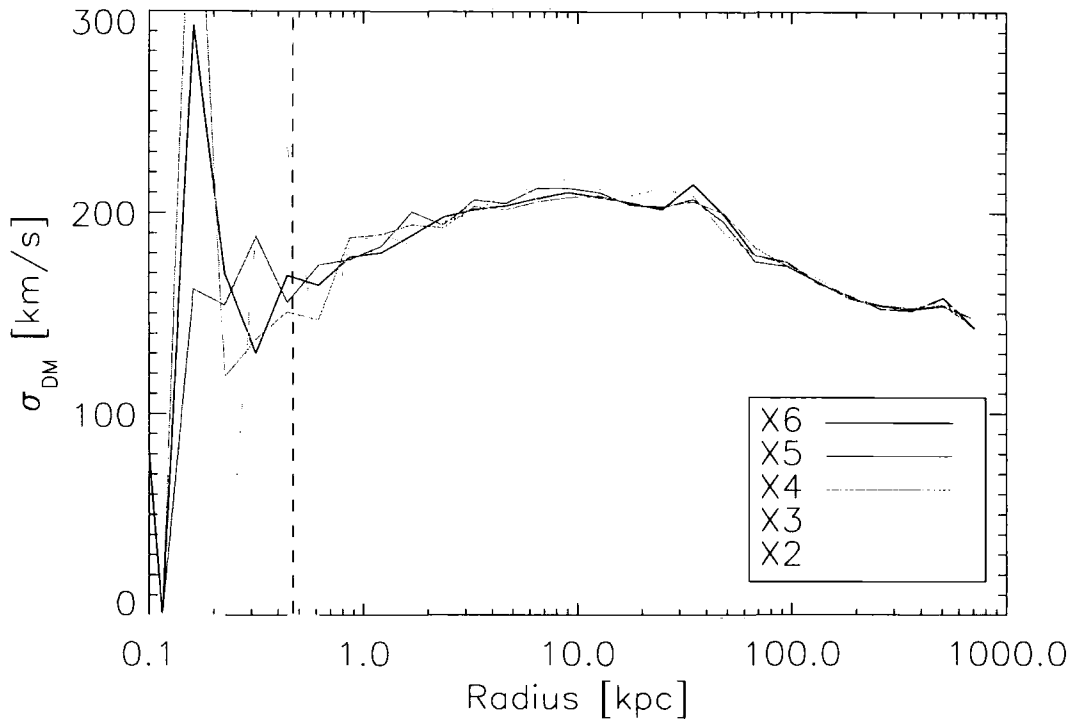

Figure 2.21: Dark matter velocity dispersion profiles, computed by taking the variance of all of the dark matter particles in a series of concentric shells. The vertical lines represent the softening lengths of simulations X2 and X6. The agreement between the different simulations is good up to the resolution length of each simulation.

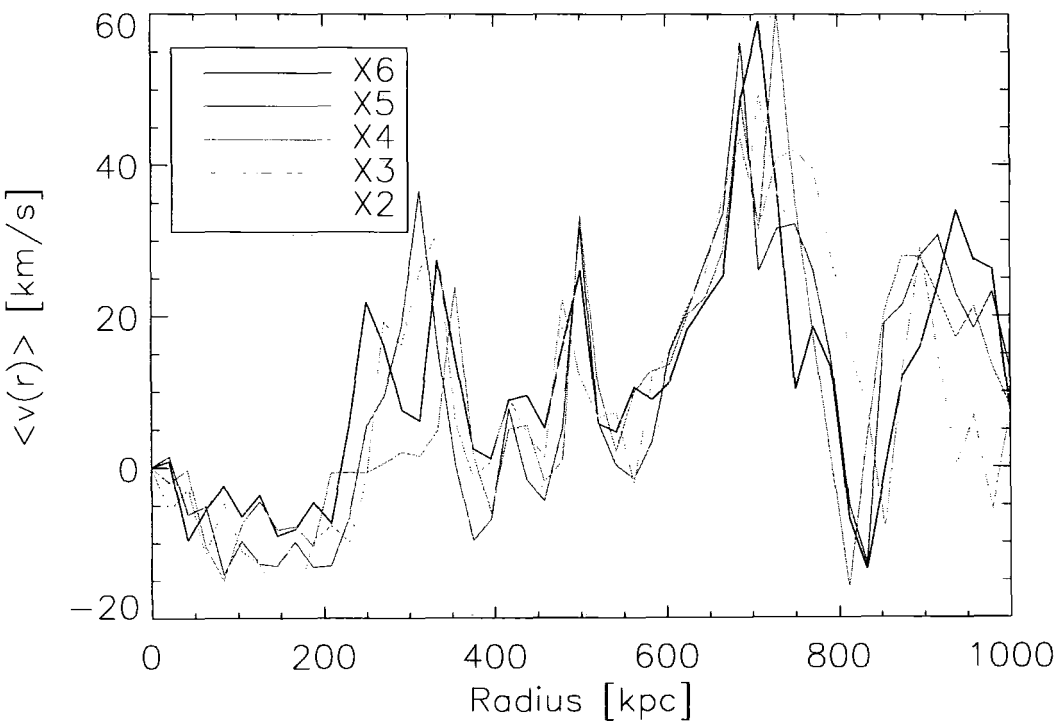

Figure 2.22: Dark matter infall velocity as a function of radius. It is clear that the large scale flow properties are preserved between the simulations, although the mean radial velocity is a very noisy statistic

Chapter 3

Statistical Models of the Interstellar Medium

3.1 Introduction

The problem of modelling star formation in large scale simulations is a difficult one for a number of reasons. Firstly, the detailed process of star formation is not fully understood even in our own galaxy and additionally we expect that young galaxies in the high redshift Universe will have wildly differing properties from those of our own quiescent disk. Secondly, on the scales of interest in Cosmological simulations (tens of Mpc and upwards) we can not achieve the required spatial or mass resolution to resolve the actual formation of stars. Most star formation prescriptions in the literature today approach this in one of two ways. Either by creating a set of rules that govern when a 'gas unit' (be that particle or grid cell) may change into a star particle, then converting them in a stochastic manner (Kay et al. (2002)) or by describing the interstellar medium (ISM) in a statistical manner (Springel and Hernquist (2003); Yepes et al. (1997)). In the following chapter we introduce examples of the first generation of star formation models before discussing the major problems with them. We then describe in detail our own implementation of the physical processes that are important in star formation and the evolution of the ISM.

3.1.1 Models of Star Formation Using a Single Phase

The basic empirical law that most numerical models either use explicity or try to fit by the adjustment of free parameters is the Kennicutt law (Schmidt (1959)):

$$\Sigma_{SFR} = C\Sigma_{gas}^{N} \tag{3.1}$$

Where Σ denotes a density per unit area. This simple power law relation between star formation rate density (SFR) and gas density was found to hold over many orders of

magnitude by Kennicutt (1988), who constrained the exponent to be $N = 1.4 \pm 0.2$.

The basic process by which star formation is then modelled is to, at each timestep, apply some sensible criteria that describe whether or not a particular gas unit is eligible to turn into a star. Some criteria that have been used in the literature include (X represents a free parameter in each rule):

1. The minimum overdensity: $\delta > X$
2. The minimum physical density: $\rho > X$
3. The maximum temperatute: $T < X$
4. Converging flow: $\nabla.v < 0$
5. Jeans instability: $\tau_J < \tau_{dyn}$
6. Cooling instability: $t_{cool} < t_{dyn}$

Rules 1 and 2 prevent underdense material from collapsing and forming stars, rule 3 prevents material that is too hot to collapse gravitationally from turning into stars. Rule 4 represents the local estimate of the divergence of the gas flow, for example in an SPH simulation this is given by

$$\nabla.v_i = -\frac{1}{\rho_i}\sum m_j v_{ij}\frac{1}{2}\left[\nabla_i W(r_{ij}, h_i) + \nabla_i W(r_{ij}, h_j)\right] + \frac{H_i - \Lambda_i}{\rho_i}, \tag{3.2}$$

where $W(r, h)$ is the SPH kernel so $\nabla.W(r, h)$ is the direction of the gradient of the SPH kernel at a given point. A negative divergence represents a net flow of baryonic material into this mass unit.

Rule 5 forces that only material that is Jeans unstable (that is: it is unstable to any perturbations and cannot diffuse away density fluctuations as sound waves) to collapse. In a Lagrangian simulation a particle may be considered Jeans unstable if

$$\frac{h_i}{c_i} < \frac{1}{\sqrt{4\pi G\rho_i}}. \tag{3.3}$$

Here, h_i represents the SPH smoothing length of the gas particle, c_i is the sound speed in that particle.

The final rule represents the fact that as a gas cloud collapses it heats up. If the time it takes for a gas cloud to radiate away this extra heat is less than the characteristic timescale on which it can collapse then it can continue to collapse unimpeded; otherwise it will become pressure supported.

Table 3.1: Star formation criteria used by different authors

Author(s)	Star Formation Rules
Pearce et al. (1999) (see Kay et al. (2002))	$\delta > X \; ; T < X$
Summers (see Kay et al. (2002))	$\delta > X \; ; T < X \; ; \rho > X$
Navarro and White (1993)	$\rho > X \; ; \nabla.v < 0 \; ; t_{cool} < t_{dyn}$
Steinmetz and Mueller (1994)	$\nabla.v < 0 \; ; t_{cool} < t_{dyn} \; ; \delta > X$
Katz (1992)	$\tau_J < \tau_{dyn} \; ; \nabla.v < 0 \; ; t_{cool} < t_{dyn}$
Cen and Ostriker (1992)	$\delta > X \; ; \nabla.v < 0 \; ; \tau_J < \tau_{dyn}$
Katz et al. (1996)	$\delta > X \; ; \rho > X \; ; \nabla.v < 0$
Mihos and Hernquist (1994b)	$\delta > X \; ; \nabla.v < 0$

A selection of the particular criteria chosen by a number of authors is included in table 3.1.1. When some gas unit has been labelled as eligible to form stars by whatever set of rules its author has chosen then its SFR is calculated by the Schmidt law (equation 3.1), and then depending upon its SFR has some probability of either

- being converted into a collisionless star particle representing millions, or hundreds of millions of stars, or

- spawning a new collisionless star particle with a mass in direct proportion to the SFR of the gas particle and decreasing the mass of the gas particle by an equivalent amount

The first approach has the advantage that it is both simple to implement and actually cuts down on the amount of computational work that needs to be done on each timestep as more stars are formed (star particles do not feel hydrodynamic forces). On the other hand, the minimum amount of star formation that can be resolved is equal to the mass resolution of the simulation. The second approach has the advantage that smaller amounts of star formation can be resolved but it can be computationally very expensive to calculate gravitational forces after spawning a lot of new collisionless particles in high density regions.

A comparison of different star formation methods (including most of those in table 3.1.1) was recently undertaken by Kay et al. (2002) who found that although each prescription agreed well in most ways that some fundamental physical properties, such as the fraction of baryons in stars, in each simulation could vary greatly between star for-

mation treatments. The star formation histories for each method also showed significant differences in shape.

One of the largest problems with the modelling of star formation in this manner is that these star formation recipes are chosen purely phenomenologically and although they may mirror the large scale behaviours of star forming regions they offer no insights into the actual dynamic processes that go into the formation of stars.

Additionally feedback from core collapse (type II) SNe, described as an extra source of thermal or kinetic energy in these single phase models, was found to have little effect in the early models. This is because the gas in the surroundings of star formation sites is at high density and so is very efficient at just radiating away the added energy. As a consequence, too much gas cooled in dense knots, producing galaxies much more concentrated than those observed (Navarro and Benz (1991); Weil et al. (1998)).

3.1.2 Multiphase Star Formation

In response to these problems with the simplest star formation and feedback criteria several authors have introduced 'multiphase' models for star formation in which the ISM is treated as a number of distinct phases. These schemes take various forms including modification of the simulation algorithm (Ritchie and Thomas (2001); Croft et al. (2000)), treating the multiphase medium implicitly by formulating differential equations that model the interactions between the phases(Yepes et al. (1997); Springel and Hernquist (2003); Okamoto et al. (2005)), or by decoupling the cold molecular phase from the hot phase by means of 'sticky particles' (Semelin and Combes (2002); Harfst et al. (2006)), removing 'cold' particles from the SPH calculation (Hultman and Pharasyn (1999); Pearce et al. (1999, 2001); Marri and White (2003)), or by explicit modification of the SPH routines to decouple cold, molecular gas from the hot phase (Scannapieco et al. (2006)). The decoupling of the hot and cold ISM phases allows thermal heating from SN feedback to become more efficient (due to the much lower density of the hot phase), and also allows one to follow the properties of the cold molecular phase of the ISM. In this chapter we describe how the physical processes integral to the evolution of the ISM may be modelled computationally.

3.2 Details of the Sticky Particle Model

In typical simulations of galaxy formation we can resolve the Jeans length of the ambient gas phase and so can treat its hydrodynamic properties consistently. However, we cannot yet resolve the properties of the cold molecular phase of the ISM. We therefore follow the evolution of the ambient gas phase using a hydrodynamic simulation code, whereas we treat the cold phase using a statistical model that encapsulates the physics relevant to the formation and evolution of molecular clouds. In this section we introduce the properties of the sticky particle model and describe the physics we have implemented.

Following Efstathiou (2000) we consider the ISM to consist of warm and hot ambient materials, and cold molecular clouds. We additionally treat the properties of SN remnants. Throughout this chapter the properties of the ambient medium will be represented with the subscript h, the properties of the molecular clouds with the subscript c, and the properties of the gas internal to SN remnants, or hot bubbles, with the subscript b.

The ambient gas phase is represented using the entropy conserving, parallel Tree-SPH code GADGET2 (Springel (2005); Springel et al. (2001)). The properties of SPH simulation codes were introduced in some detail in chapter 2. We will refer to the gas component treated using SPH interchangeably as ambient, warm or hot, to distinguish it from the cold molecular gas. We will see that in galaxy formation simulations, this ambient (i.e. non-molecular) medium naturally develops three relatively well-defined phases: a warm ($T \sim 10^4$K) component in a galactic disk, a hot ($T \sim 10^6$K)) tenuous component of shock-heated gas in the halo, and a similarly hot component resulting from gas heated by SN. The fourth, cold ($T \sim 100$K) and molecular cloud phase is represented with sticky particles, which interact gravitationally with all other material in the simulation and are allowed to stick together forming more massive sticky particles. Stars and dark matter are both treated as collisionless particles by GADGET2.

The different phases of the ISM may interact with each other as follows: thermally unstable ambient gas may collapse into molecular clouds via thermal instability (section 3.2.1). Molecular clouds can interact with each other to form GMCs (section 3.2.2). GMCs then collapse into stars (section 3.2.5). Stars disrupt the cloud they formed from and may, via SN feedback, return energy (section 3.2.6) to the ambient phase. Hot bubbles blown by SNe can evaporate cold clouds (3.2.7) and heat the ambient medium.

Fig 3.1 contains a summary of all of the physics implemented in our model. Arrows

represent a transfer of mass and/or energy from one phase to another. The distinction between clouds and GMCs is somewhat arbitrary; they are separated in the figure to allow an easy pictorial representation of mass and energy transfer within a single phase. Appendix A contains a list of frequently used symbols and their meaning.

Each physical process will be treated in turn in the remainder of this section. We first introduce the physics relevant to each physical process before discussing the numerical implementation. We will also give our preferred physical values for the various parameters that occur. How we choose these is discussed in section 3.3.

3.2.1 Radiative Cooling And The Formation of Molecular Clouds

Begelman and McKee (1990) show that under appropriate physical conditions, a thermal instability may operate in hot gas which causes a fraction of the gas to condense into much colder molecular clouds. The sticky particle star formation prescription contains a basic representation of this process, based on a detailed treatment of baryonic radiative cooling.

Relevant Physics

The radiative processes that we take into account are Compton cooling off the microwave background, thermal Bremsstrahlung cooling, line cooling and photo-ionization heating from Hydrogen, Helium and metal species in the presence of an imposed ionising background. These routines were developed for a different project and will be described elsewhere[1]. Briefly, they use tabulated rates for radiative cooling and photo-ionization heating for many species and ionization states computed assuming ionization equilibrium using CLOUDY (version 05.07 of the code last described by Ferland et al. (1998)) with a UV background given by Haardt and Madau (2001). The rates are tabulated element by element and we will assume solar abundance ratios and specify a fixed metallicity of the gas in solar units. We do, however, note that the behaviour of the system may depend upon precisely which value of the metallicity we choose, and investigate this in section 4.4

Other processes such as cosmic ray heating, and cooling by dust and atomic lines that affect the molecular gas in clouds are not treated explicitly since we do not model the internal properties of the clouds themselves.

[1]We would like to thank our colleagues J Schaye, C Dalla Vecchia and R Wiersma for allowing us to use these rates.

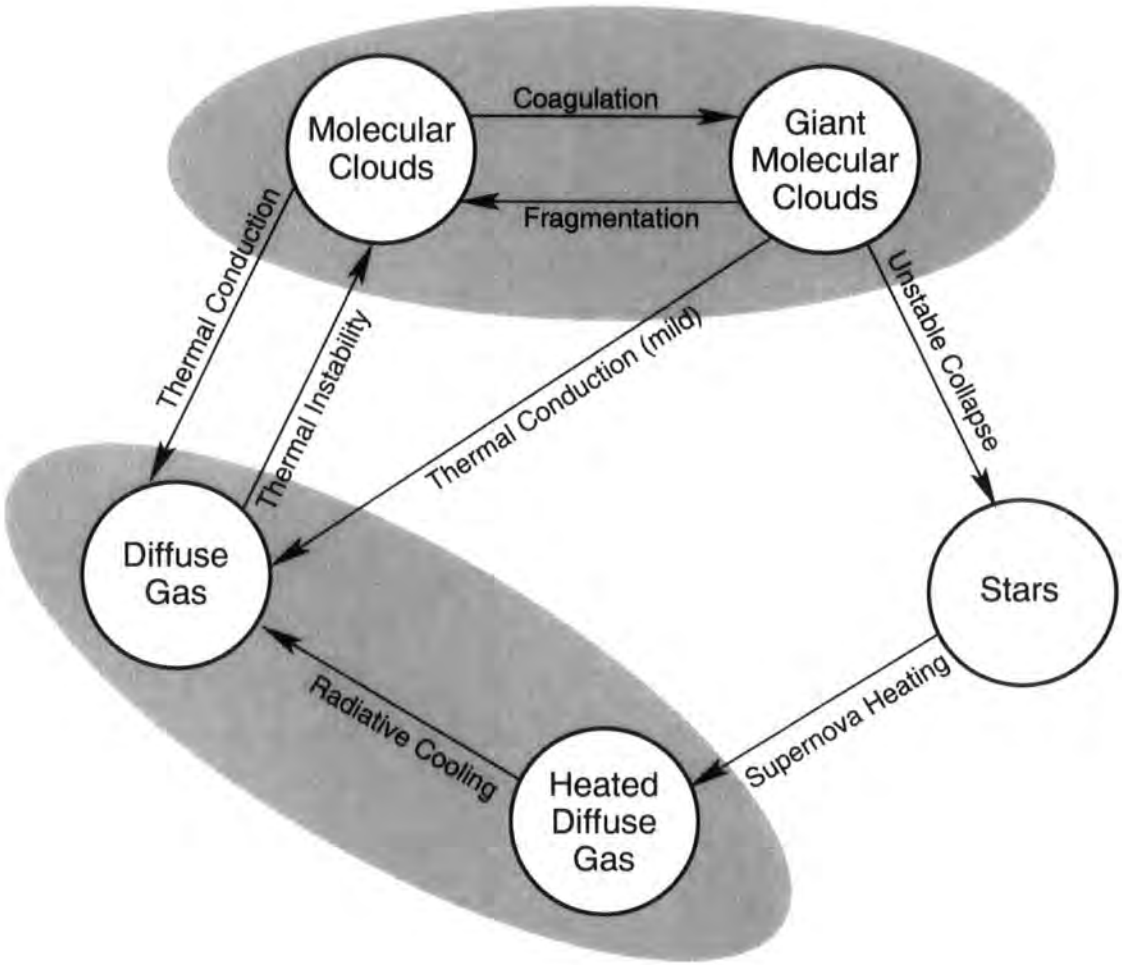

Figure 3.1: Summary of the physical processes that operate in our model of a two phase interstellar medium. The boundaries between molecular and giant molecular clouds and between heated and non-heated diffuse gas are somewhat arbitrary and they are separate out in this figure only to highlight the different physical mechanisms that are operating at any given time. Each arrow represents the transfer of mass and/or energy from one phase to another.

We include a simple model to determine the rate at which the ambient gas forms molecular clouds. When we identify ambient gas that is thermally unstable (Begelman and McKee (1990)) we allow it to collapse into molecular clouds. The rate at which this process occurs is goverened by the rate at which the gas is losing thermal energy by radiative cooling.

Numerical Implementation

Following Yepes et al. (1997) we define a density threshold, $\rho_{\rm th}$, to determine when gas becomes thermally unstable. Gas with $\rho < \rho_{\rm th}$ undergoes ordinary radiative cooling. Gas with density above the threshold becomes thermally unstable and begins to be converted to molecular clouds. In addition to the density criterion we add a maximum temperature ($T_{\rm th}$) for gas to be called thermally unstable which has the effect of preventing SN heated gas in dense regions from collapsing straight to the cold phase.

When gas has been identified as thermally unstable it begins to form molecular clouds at a rate controlled by the rate at which the gas can lose thermal energy by radiative cooling

$$\frac{d\rho_c}{dt} = -\frac{d\rho_h}{dt} = \frac{1}{u_h - u_c}\Lambda_{\rm net}(\rho_h, u_h), \tag{3.4}$$

where u_h and u_c represent the internal energies per unit mass of the ambient phase and cold phase respectively and $\Lambda_{\rm net}$ is the cooling rate of the ambient gas (ergs cm^{-3} s^{-1}). We assume that the cold clouds remain at a fixed temperature of $T_{\rm c} = 100$K hence their thermal energy $u_{\rm c}$ is a constant as well.

In practice, each ambient gas particle is identified as either thermally unstable, or non-thermally unstable. Non-thermally unstable gas undergoes radiative cooling; thermally unstable ambient gas forms molecular clouds at a rate controlled by the radiative cooling rate, as described by Eq. 3.4.

In this way each ambient gas particle can keep track of what fraction of its mass is in the form of molecular clouds. Gas in the molecular phase is ignored for the purposes of the SPH calculation. When the amount of mass in the molecular phase in a particle reaches the resolution limit of the simulation a seperate 'sticky particle', representing many sub-resolution molecular clouds is created. This process decouples the molecular clouds from the associated ambient phase. Since we cannot resolve the individual molecular clouds in each sticky particle we work with the mass function of clouds. Initially we assume that the molecular clouds formed through instability are all in the smallest mass

bin, that is that the clouds formed by thermal instability are very small, and will interact to form more massive clouds. In the following section we describe the behaviour and evolution of the sticky particles in the simulation.

3.2.2 Cloud Coagulation and GMC Formation

Molecular clouds are typically many orders of magnitude more dense than the medium they form in (MO77), and their behaviour is governed by a different set of rules than the ambient medium. This section describes the physics of the simplified molecular clouds in the sticky particle model and how it is implemented.

Relevant Physics

We assume that clouds may be treated as approximately spherical objects that obey a power law relation between mass (M_c) and radius (r_c)

$$\begin{aligned} r_c &= \left(\frac{M_c}{M_{\rm ref}}\right)^{\alpha_c} r_{\rm ref} \\ &= 36 \left(\frac{M_c}{10^5 M_\odot}\right)^{0.3} {\rm pc}\,. \end{aligned} \tag{3.5}$$

Here, α_c describes how clouds grow as mass is added to them (if they remain at constant density then $\alpha_c = 1/3$), and $M_{\rm ref}$ and $r_{\rm ref}$ are a reference mass and radius used to fix the normalisation of this relation. The example phyical values used in this equation are discussed fully in section 3.3.1. The lower bound on molecular cloud masses is typically calculated to be $100 M_\odot$ (Monaco (2004)) due to the efficient destruction of smaller molecular clouds by photoionization. We introduce an upper limit by converting molecular clouds with large masses into stars (see section 3.2.5 for discussion). In order to facilitate easy estimates of the relative importance of various effects we have substituted typical numbers and units into most of the equations in this section.

Numerical Implementation

Each sticky particle represents numerous cold clouds. Sticky particles are hydrodynamically decoupled from the ambient SPH phase of the gas and interact only gravitationally with the other phases in the simulation. However, when two sticky particles collide they may coagulate to form a more massive sticky particle. The mass of the smallest molecular clouds is typically orders of magnitude below the mass resolution in a cosmological simulation. We represent an entire mass spectrum of clouds statistically inside of each

sticky particle. Our formalism to treat the evolution of the mass function of clouds internal to each of the 'multiple cloud' particles will start from the Smoluchowski equation of kinetic aggregation (Smoluchowski (1916)), which describes the behaviour of a system consisting of ballistic particles that can interact via mergers. The coagulation behaviour of this system is driven by a coagulation kernel, $K(m_1, m_2)$, that represents the formation rate of clouds of masses $m = m_1 + m_2$,

$$K = \langle \Sigma v_{\rm app} \rangle_v, \tag{3.6}$$

where $v_{\rm app}$ is the relative velocity of the clouds and Σ is the collision cross section. For a Maxwellian distribution of velocities with three-dimensional dispersion σ we have $\langle v_{\rm app} \rangle = 1.3\sigma$ (Monaco (2004)). The product of the approach velocity and the collision cross section is averaged over the distribution of relative velocities. The cross section is

$$\Sigma \approx \pi (r_c + r_c')^2 \left(1 + 2G \frac{M_c + M_c'}{r_c + r_c'} \frac{1}{v_{\rm app}^2}\right), \tag{3.7}$$

where the first term represents the collision geometric cross section and the second term represents the effect of gravitational focusing (Saslaw (1985)). The focused term becomes significant when the approach velocity is not much larger than the internal velocity dispersion of the system. In most cases of interest the geometric term will dominate so the focused term is neglected. In these calculations we need to assume that molecular clouds, although transient and turbulent, are stable for long enough for coagulation to take place. This is reasonable because the cloud velocity dispersion is typically larger than the sound speed of the cold cloud gas (Monaco (2004)).

To model the cooling of sub-resolution molecular clouds via gravitational interaction it has been assumed that when molecular clouds with relative velocities, $v_{\rm app}$, greater than $v_{\rm stick}$ (a parameter in our simulations) collide they do not merge, but rather bounce back with relative velocity a fraction, η, of the initial approach velocity. Clouds with relative velocities less than $v_{\rm stick}$ merge. For simplicity it has been assumed that the velocity distribution of clouds is Gaussian with a velocity dispersion that is a function of cloud mass, $\sigma = \sigma(m)$.

The upper and lower bounds on the molecular cloud mass function are set such that the smallest mass bin is comparable with the smallest observable clouds, and the largest molecular clouds are approximately the same mass as the largest clouds in the MW. The mass function is discrete. All clouds are assumed to form at the lowest mass, M_{min},

and then the mass of each bin is a multiple of this value. This discrete mass function is neccessary when working with the Smoluchowski equation.

In order for us to be able to hold a mass function with a large number of bins internal to every single sticky particle without the requirement to store one number for each mass bin we parameterize the mass function as a third order polynomial, and store only the four coefficients between timesteps.

As these sub-resolution clouds interact and merge, the one dimensional velocity dispersion $\sigma(m)$ changes, which affects the rate of evolution of the cloud mass function, $n(m)$. Let $E_{\rm m} = (3/2)m\sigma^2(m)$ denote the random kinetic energy of clouds with mass m. $E_{\rm m}$ may change due to three distinct processes:

- Clouds with masses m' and $m - m'$ merge to form extra clouds of mass m, increasing $E_{\rm m}$ at a rate $\dot{E}_{\rm gain}$
- Clouds with masses m may merge with clouds of any other mass decreasing the number of clouds of mass m. This process decreases $E_{\rm m}$ at a rate $\dot{E}_{\rm loss}$
- Clouds with mass m may interact collisionally with clouds of any other mass and so lose kinetic energy. This process decreases $E_{\rm m}$ at a rate $\dot{E}_{\rm cool}$

The net change in kinetic energy for particles of mass m during some timestep Δt is given by

$$\Delta E_m = \frac{dE_m}{dt}\Delta t = \left[\dot{E}_{\rm gain} - \dot{E}_{\rm loss} - \dot{E}_{\rm cool}\right]\Delta t\,. \tag{3.8}$$

And for this change in kinetic energy, the corresponding change in velocity dispersion is given by

$$\dot{\sigma} = \frac{2\dot{E} - \dot{M}\sigma^2}{2M\sigma}\,. \tag{3.9}$$

Details of the equations used to model these processes are given in Appendix 3.2.3, and the method by which they are solved numerically in Appendix 3.2.4.

The same processes (cooling and merging) are followed explicitly for the individual sticky particles in our simulations, which can interact in the same two ways as the unresolved sub resolution clouds. Following the same rules should allow us to remove much of the resolution dependence of the star formation. As the mass resolution of a simulation is degraded, more massive clouds will be treated with the sub-grid physics; our implementation should ensure that the large scale results are approximately the same. This is demonstrated in section 3.3.1.

3.2.3 Energy Transfer Through Coagulation

In this section the numerical methods by which the equations governing molecular cloud behaviour are discussed in detail. The starting point is the Smoluchowski equation of kinetic aggregation (Smoluchowski (1916))

$$\frac{\partial n}{\partial t} = \frac{1}{2V}\int_0^\infty n(m',t)n(m-m',t)K(m',m-m')dm' \\ -\frac{1}{V}n(m,t)\int_0^\infty n(m',t)K(m,m')dm', \tag{3.10}$$

where $n(m,t)$ represents the number of clouds with masses between m and $m+dm$ contained within a volume, V and $K(m,m')$ represents the kernel for aggregation of clouds with masses m and m', as defined by Eq (3.6)

In one dimension, the fraction of collisions between clouds of masses m_1 and m_2 that lead to mergers is given by

$$f_m(\sigma_1,\sigma_2) = \frac{1}{\sigma_1\sqrt{2\pi}}\int_{-\infty}^{\infty} e^{-\left(\frac{v_1}{\sqrt{2}\sigma_1}\right)^2}\left[\mathrm{erf}\left(\frac{v_1+v_{\mathrm{stick}}}{\sqrt{2}\sigma_2}\right)-\mathrm{erf}\left(\frac{v_1-v_{\mathrm{stick}}}{\sqrt{2}\sigma_2}\right)\right]dv_1\,. \tag{3.11}$$

Figure 3.2 shows for two populations of particles with different velocity dispersions the fraction of collisions that will lead to a merger, this demonstrates the symmetry between σ_1 and σ_2 in equation 3.11. Using this definition of f_{m} the Smoluchowski equation becomes

$$\frac{\partial n}{\partial t} = \frac{1}{2V}\int_0^\infty n(m',t)n(m-m',t)K(m',m-m')f_m(\sigma_{m'},\sigma_{m-m'})dm' \\ -\frac{n(m,t)}{V}\int_0^\infty n(m',t)K(m,m')f_m(\sigma_m,\sigma_{m'})dm'\,. \tag{3.12}$$

As discussed in section 3.2.2, clouds of mass m may gain or lose kinetic energy in three ways: clouds of mass m' and $m-m'$ may merge to form extra clouds of mass m. Clouds of mass m may merge with clouds of any other mass to decrease the number of clouds of mass m. Finally clouds of mass m can interact gravitationally with any other clouds, thus losing kinetic energy. These three processes are termed gain, loss and cooling.

Gain processes may be represented in the following way, where we have integrated over m' such that the two particles that merge have masses that sum to m

$$\dot{E}_{\mathrm{gain}} = \int_0^\infty\int_{v_1=-\infty}^{v_1=\infty}\int_{v_2=v_1-v_{\mathrm{stick}}}^{v_2=v_1+v_{\mathrm{stick}}}\Big[P(v_1)P(v_2)n(m',t) \\ n(m-m',t)K(m',m-m')f_m(m',m-m')E_f\Big]dv_2dv_1dm'\,. \tag{3.13}$$

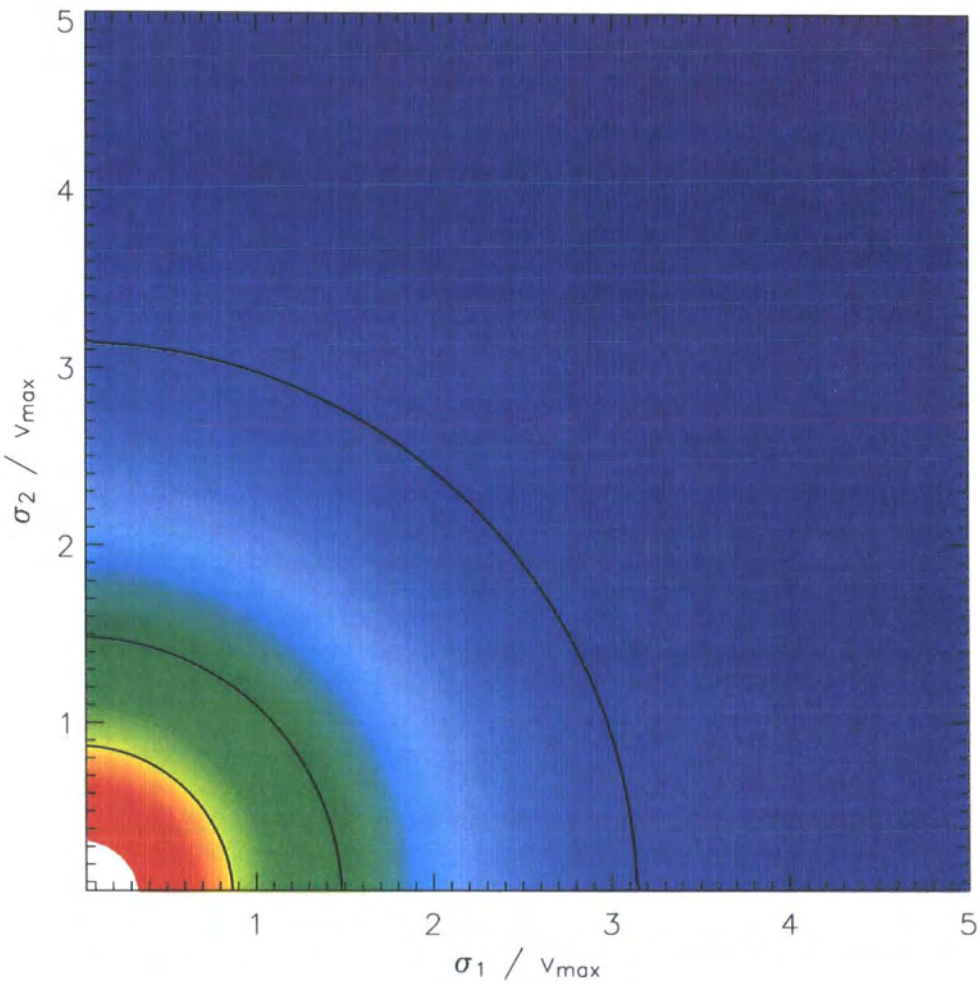

Figure 3.2: The merging fraction as a function of σ_1 and σ_2. White represents a merging fraction of 1.0, dark blues represent low merging fractions. The solid black lines show merging fractions of 0.75, 0.5 and 0.25.

$P(v_1)$ and $P(v_2)$ are the probability distributions velocities v_1 and v_2 and are assumed to be gaussian with standard deviation σ_1 and σ_2 respectively. E_f represents the final kinetic energy of a collision between particles of masses m' and $m - m'$. E_f is evaluated by considering conservation of momentum,

$$E_f = \frac{1}{2}\frac{(m'v_1 + (m - m')v_2)^2}{m}. \tag{3.14}$$

Eq (3.13) then becomes

$$\begin{aligned}\dot{E}_{\text{gain}} = \frac{n(m',t)}{2\pi}\int_0^\infty n(m-m',t)K(m',m-m')\\ \int_{-\infty}^{\infty}\int_{v_1-v_{\text{stick}}}^{v_1+v_{\text{stick}}}\frac{1}{\sigma_{m'}\sigma_{m-m'}}e^{-\left(\frac{v_1}{\sqrt{2}\sigma_{m'}}\right)^2}e^{-\left(\frac{v_2}{\sqrt{2}\sigma_{m-m'}}\right)^2}\\ \frac{1}{2}\left(\frac{(m'v_1+(m-m')v_2)^2}{m}\right)dv_2dv_1dm',\end{aligned} \tag{3.15}$$

and Eq (3.15) may be written

$$\begin{aligned}\dot{E}_{\text{gain}} = \frac{n(m',t)}{2\pi}\int_0^\infty n(m-m',t)K(m',m-m')\int_{-\infty}^{\infty}\frac{1}{\sigma_{m'}\sigma_{m-m'}}e^{-\left(\frac{v_1}{\sqrt{2}\sigma_{m'}}\right)^2}\\ \int_{v_1-v_{\text{stick}}}^{v_1+v_{\text{stick}}}e^{-\left(\frac{v_2}{\sqrt{2}\sigma_{m-m'}}\right)^2}\frac{1}{2}\left(\frac{(m'v_1+(m-m')v_2)^2}{m}\right)dv_2dv_1dm'\end{aligned} \tag{3.16}$$

The total kinetic energy of particles of mass m may also be decreased by mergers between particles of mass m and any other mass (the second process in the list). Similarly to Eq (3.15), the rate of energy loss may be written

$$\begin{aligned}\dot{E}_{\text{loss}} = \frac{n(m,t)}{2\pi}\int_0^\infty n(m',t)K(m,m')\int_{-\infty}^{\infty}\frac{1}{\sigma_m\sigma_{m'}}e^{-\left(\frac{v_1}{\sqrt{2}\sigma_m}\right)}\\ \int_{v_1-v_{\text{stick}}}^{v_1+v_{\text{stick}}}e^{-\left(\frac{v_2}{\sqrt{2}\sigma_{m'}}\right)^2}\frac{mv_1^2}{2}dv_2dv_1dm'.\end{aligned} \tag{3.17}$$

Finally, the total energy of particles with mass m may be decreased by collisions between particles of mass m and particles of any other mass that occur at relative velocities greater than v_{stick}. In this case, the velocity of both particles is decreased by a factor η relative to the centre of mass. For a collision between particles of masses m_1 and m_2 (velocities v_1 and v_2) the final velocity of particle 1 (denoted v_1') is evaluated by conservation of momentum

$$v_1' = \eta(v_1 - v_{\text{com}}) + v_{\text{com}}$$

$$v_{\text{com}} = \frac{m_1v_1 + m_2v_2}{m_1 + m_2}$$

$$\Delta E = \frac{1}{2}m_1 v_1'^2 - \frac{1}{2}m_1 v_1^2, \tag{3.18}$$

Using these definitions, the change in energy of a particle of mass m_1 by gravitational cooling with a particle of mass m_2, denoted ϵ is given by

$$\epsilon = \frac{m_1}{2}\Big[v_1^2(1-\alpha^2) - v_2^2\beta^2 - v_1 v_2 \alpha\beta\Big], \tag{3.19}$$

where

$$\alpha = \eta + \frac{m_1}{m_1+m_2}(1-\eta) \tag{3.20}$$

$$\beta = \frac{m_2}{m_1+m_2}(1-\eta). \tag{3.21}$$

In a similar way to Eq (3.15) the energy loss via this process may be written

$$\dot{E}_{\rm cool} = \frac{n(m,t)}{2\pi}\int_0^\infty n(m',t)K(m,m') \int_{-\infty}^{\infty}\frac{1}{\sigma_m\sigma_{m'}}e^{-\left(\frac{v_1}{\sqrt{2}\sigma_m}\right)^2}\int^{|v_1-v_2|>v_{\rm stick}}\epsilon e^{-\left(\frac{v_2}{\sqrt{2}\sigma_{m'}}\right)^2}dv_2 dv_1 dm'. \tag{3.22}$$

3.2.4 The Solution of the Coagulation Equations

In our simulations we solve the discrete versions of Eq (3.12), Eq (3.8) and Eq (3.9). By assuming that cloud mass is quantised into N bins characterised by an index, i, where $M_i = iM_0$ we can write

$$\dot{n}_k = \frac{1}{2V}\sum_{i+j=k} K_{ij} f_{ij}^m n_i n_j - \frac{n_k}{V}\sum_{j=1}^{jmax} K_{jk} f_{ij}^m n_j, \tag{3.23}$$

$$\dot{E}_k = \dot{E}_{\rm gain} - \dot{E}_{\rm loss} - \dot{E}_{\rm cool}, \tag{3.24}$$

$$\dot{\sigma}_k = \frac{\dot{E}_k - \frac{1}{2}\sigma_k^2 M_k \dot{n}_k}{\sigma_k n_k M_k}, \tag{3.25}$$

where subscripts represent different mass bins. $K_{ij} \equiv K(M_i, M_j) \equiv K(iM_0, kM_0)$. The superscript m represents that f is a cross section for particle mergers

To demonstrate the technique for solving these equations we will consider the numerical solution of the simple Smoluchowski equation (Eq (3.10)), which when written in a discrete form takes on the following form

$$\dot{n}_i = \frac{1}{2V}\sum_{j=1}^{i-1} n_j n_{i-j} K_{ij} - \frac{n_i}{V}\sum_{j=1}^{N} n_j K_{ij}. \tag{3.26}$$

Following Benson et al. (2005) Eq (3.26) can be rewritten in the form of a matrix equation

$$\dot{\mathbf{n}} = \mathbf{B} \cdot \mathbf{k}, \tag{3.27}$$

the vector k has $N \times N$ elements corresponding to $K(m_i, m_j)$. The kernel matrix, B has $N \times N \times N$ elements and may be written more explicitly as

$$\dot{n}_i = \sum_{jk} B_{ijk} k_{jk}, \tag{3.28}$$

where

$$B_{ijk} = \frac{n_j n_k}{V}\Big(\frac{1}{2}\delta_{i,j+k} - \delta_{ik}\Big) \tag{3.29}$$

δ represents a Kronecker delta function. We solve Eq (3.27) implicitly using an iterative method.

The solution of the equations that govern energy exchange between clouds (Eq (3.16), Eq (3.17) and Eq (3.22)) is the same as for the solution of the Smoluchowski equation in that we will write the equations in the form of the linear multiplication of two matrices and then solve this equation implicitly. In order to simplify the notation in this section we will denote the terms in the three equations that are inside of the integrals over velocity as ξ. Explicitly for the case of the equation for energy gain (Eq (3.16)):

$$\xi^G(m, m') = \frac{1}{2\pi}\int_{-\infty}^{\infty} \frac{1}{\sigma_m \sigma_{m'}} e^{-\left(\frac{v_1}{\sqrt{2}\sigma_m}\right)^2} \int_{v_1 - v_{\text{stick}}}^{v_1 + v_{\text{stick}}} \frac{1}{2} e^{-\left(\frac{v_2}{\sqrt{2}\sigma_{m'}}\right)^2} \Big(\frac{(mv_1 + m'v_2)^2}{m}\Big) dv_2 dv_1 \tag{3.30}$$

The corresponding terms in the equations for energy loss(3.17) and cooling (3.22) are denoted $\xi^L(m_1, m_2)$ and $\xi^C(m_1, m_2)$ respectively. Note that the definitions of ξ include the factors of 2π and $\frac{1}{\sigma}$ from throughout the equations.

The equation for the total evolution of the energy of a system of coagulating and cooling particles may be written in terms of these new functions as:

$$\begin{aligned}\dot{E}(m) = &\int_0^{\infty} n(m', t) n(m - m', t) K(m', m - m') \xi^G(m', m - m') dm' \\ &- n(m, t) \int_0^{\infty} n(m', t) K(m, m') \xi^L(m, m') dm' \\ &- n(m, t) \int_0^{\infty} n(m', t) K(m, m') \xi^C(m, m') dm'\end{aligned} \tag{3.31}$$

Which when discretized and rearranged becomes

$$\dot{E}_i = \sum_{j=1}^{i-1} n_i n_j K_{ij} \xi_{ij}^G - n_i \Big(\sum_{j=1}^{N} n_j K_{ij} \left(\xi_{ij}^C + \xi_{ij}^L\right)\Big) \tag{3.32}$$

The subscripts represent different mass bins ($n_j \equiv n(jM_0)$). Our goal is to rewrite Eq (3.32) in the form of a linear multiplication of two matrices

$$\dot{\mathbf{E}} = \mathbf{C} \cdot \mathbf{k}, \tag{3.33}$$

where $\mathbf{k}$ is defined in the same way in the solution of the Smoluchowski equation, that is: $k_{ij} \equiv K(m_i, m_j)$. The form of $\mathbf{C}_{ijk}$ that is consistent with Eq (3.32) is given by:

$$C_{ijk} = n_j n_k \Big(\delta_{i,j+k} \xi^G_{jk} - \delta_{ik} \big(\xi^C_{jk} + \xi^L_{jk} \big) \Big) \tag{3.34}$$

This form for $\mathbf{C}_{ijk}$ is functionally equivalent to $\mathbf{B}_{ijk}$ (Eq (3.29)) so the solution may proceed in exactly the same way as for the Smoluchowski equation, the only difference is the form of the matrix $\mathbf{B}$

The calculation of the quantities ξ^G, ξ^C and ξ^L is computationally very expensive so they are initialised once into a lookup table at the start of every simulation and obtained by bilinear interpolation thereafter

3.2.5 Cloud Collapse and Star Formation

The vast majority of stars form in Giant Molecular Clouds. This process is described in the sticky particle model by allowing the most massive clouds in the galaxy to collapse into stars.

Relevant Physics

We follow the process of star formation in our simulations by waiting for star forming clouds to be created by the coagulation process described in section 3.2.2. We define star forming clouds to be clouds of a mass similar to the most massive clouds observed in the MW ($\sim 10^6 M_\odot$). When one of these star forming clouds is created it is assumed to collapse on a short timescale and approximately $\epsilon_\star \sim 10\%$ of its mass is converted into stars, whilst the remainder is disrupted by stellar feedback processes including stellar winds, SN feedback and photoionization. This process reflects that although stars may form in less massive molecular clouds, it is not until the relatively rare, massive O and B stars are created that the cloud is destroyed (Elmegreen (1983)).

We assume that each cloud collapse forms a single stellar population with an IMF of the standard Salpeter (1955) form

$$N(M)\, dM \propto M^{-(1+x)} dM\,, \tag{3.35}$$

where x is the slope of the IMF and takes the usual value of 1.35. The masses of stars are assumed to lie between well defined minimum and maximum values, $M_{\star,\min}$ and $M_{\star,\max}$.

Numerical Implementation

The treatment of star formation adopted in most simulations is to identify gas that is likely to be star-forming and impose a star formation rate given by the Schmidt law,

$$\dot{\rho}_\star = C\rho_{\rm gas}^{N_{\rm SF}} . \tag{3.36}$$

Here, $\dot{\rho}_\star$ and $\rho_{\rm gas}$ denote the rate of star formation per unit volume and the gas density respectively. This power law relation between star formation rate (SFR) and gas density was found to hold over many orders of magnitude by Kennicutt (1988), who constrained the exponent to be $N_{\rm SF} = 1.4 \pm 0.2$.

We take a different approach: unstable molecular clouds are identified in the simulations as any cloud with a mass greater than $M_{\rm sf}$. We identify the formation of these massive clouds by using the cloud mass function, as stored internally to every single sticky particle. These unstable clouds are assumed to collapse on a very short timescale, forming stars.

As soon as a cloud of mass $M_{\rm sf}$ forms, it is assumed to be disrupted by OB stars on a timescale of $\sim$10Myr (Matzner (2002)), the rest of the massive cloud is broken down into smaller clouds and the coagulation process begins all over again as described in section 3.2.2. This process is modelled by taking the fraction of the cloud's mass that does not turn into stars, $1-\epsilon_*$, and assuming that the net effect of the stellar feedback processes is to fragment the GMC into the smallest clouds represented in the sticky particle internal mass function. This has the net effect of steepening the cloud mass function.

Each star particle formation event represents the formation of a single stellar population of stars that are all assumed to have the same age, and to be drawn from the Salpeter IMF. Each stellar particle is therefore formed with a mass approximately equal to ϵ_* times the mass of a starforming cloud. If this particle mass is not allowed by the mass resolution of a given simulation then we either store up unresolved stars internal to a sticky particle (if the star mass is too small to be allowed), or split it into multiple, equal mass particles (if the star mass is too large to be allowed).

3.2.6 Supernova Feedback

Our simulations include only energy feedback from type II SN. These events return energy from the stars to the ambient phase. We note that it is not currently computationally feasible to resolve the properties of SN remnants so we treat them with a simple, analytic prescription. The mechanism by which SN feedback is implemented in our model is discussed here.

Relevant Physics

Each star of mass greater than $8M_{\odot}$ releases $10^{51}E_{51}$ ergs in thermal energy when it undergoes a SN event. The lifetime, t, of a star of mass M (where $M > 6.6M_{\odot}$) is given by (Padovani and Matteucci (1993))

$$\frac{t}{\mathrm{Gyr}} = 1.2\left(\frac{M}{M_{\odot}}\right)^{-1.85} + 0.003\,. \tag{3.37}$$

Each SN explosion can be approximated as the injection of energy at a single point in space. If we assume that the ambient density on scales of interest is approximately homogeneous, with density ρ_h, then each SN explosion can be modelled as a Sedov blast wave (Sedov (1959)). According to this solution, if at time $t = 0$ we release an amount of energy E_b, then after time t the resulting blast wave will have reached a radius r_b given by

$$\begin{aligned} r_b &= \left(\frac{E_b}{\rho_h}\right)^{1/5} t^{2/5} \\ &= 292\left(\frac{E_b/10^{51}\mathrm{ergs}}{\rho_h/0.1\,\mathrm{cm}^{-3}}\right)^{1/5} (t/10\mathrm{Myr})^{2/5}\,\mathrm{pc}\,. \end{aligned} \tag{3.38}$$

These hot SN bubbles have two main effects. Firstly, as they expand and decelerate the SN heated gas will get mixed in with the surrounding ambient medium; the net result of this process is the heating of the ambient medium. Secondly, as discussed in section 3.2.7, any cold clouds caught inside a SN bubble will undergo evaporation.

There are two main assumptions that must hold for the Sedov solution to be valid, the pressure of the ambient medium, and the cooling rate inside the bubble, must both be negligible. Often at least one these assumptions is invalid. If the ambient medium has a low density and is very hot, for example due to a previous set of explosions, then its pressure is no longer negligible and the Sedov solution breaks down. If the ambient medium is dense then radiative cooling becomes an important process. In the remainder of this section we describe various modifications to the standard Sedov solutions, which allow us to model SN remnants in a wider variety of conditions.

In the case of a hot, tenuous medium the radius of each blast wave is increased (Tang and Wang (2005)). These authors derive a fitting formula for the velocity of a SN blast in a hot medium, which is accurate to within 3%

$$r_b(t) = \int_0^t c_h \Big(\frac{t_c}{t'} + 1\Big)^{3/5} dt', \tag{3.39}$$

$$= 156 \int_0^{t/\mathrm{Myr}} \Big(\frac{t_c}{t'} + 1\Big)^{3/5} dt' \ \mathrm{pc}, \tag{3.40}$$

where c_h is the sound speed of the ambient medium. We assumed a temperature of $T_h = 10^6$K, mean molecular weight of $\mu = 0.58$, blast wave energy of 1×10^{51} ergs and an ambient density of 0.1 atoms per cm^3 in order to illustrate the order of magnitude of r_b. t_c is a characteristic time,

$$t_c = \left[\Big(\frac{2}{5}\xi\Big)^5 \frac{E_b}{\rho_h c_h^5}\right]^{1/3}$$

$$= 0.012 \left[(\xi/1.14)^5 \frac{E_b/10^{51}\mathrm{erg}}{(\rho_h/0.1\,\mathrm{cm}^{-3})(T_h/10^6\mathrm{K})^{5/2}}\right]^{1/3} \mathrm{Myr}\,. \tag{3.41}$$

where ξ equals 1.14 for a gas with adiabatic index $\gamma = 5/3$. This solution matches the standard Sedov evolution, $r_b \propto t^{2/5}$, closely until $t \sim t_c$, after which the shell's velocity becomes constant, $r_b \propto t$. This modification allows us to take into account that the majority (~90%) of SNII happen in preheated SN bubbles (Higdon et al. (1998)) and, therefore, the approximation that the pressure of the ambient medium is negligible is often incorrect. Fig (3.3) shows the difference between an adiabatic gas SPH simulation of a SN induced shock-wave, the pure Sedov solution and the blast wave radius as predicted by the hot medium-modified Sedov solution from Tang & Wang (2005).

Situations where radiative cooling are important may be taken into account using the prescription of Thornton et al. (1998), whose high resolution simulations of SN explosions expanding in an ambient medium with temperature $T_h = 10^3$K, provide the total thermal energy in SN bubbles as a function of time, ambient density and metallicity. We perform bilinear interpolation on the results in tables 2 and 4 of Thornton et al. (1998) to obtain the SN bubble radius and thermal energy at any given time.

Neither of these solutions treats the more general case of SN remnant expansion in a porous ISM, which may have regions of both high and low ambient density, and so we are not able to include the effects of SNe in a fully self-consistent manner. In most of our simulations we use the simple Sedov solution for the evolution of the SN blast waves, but

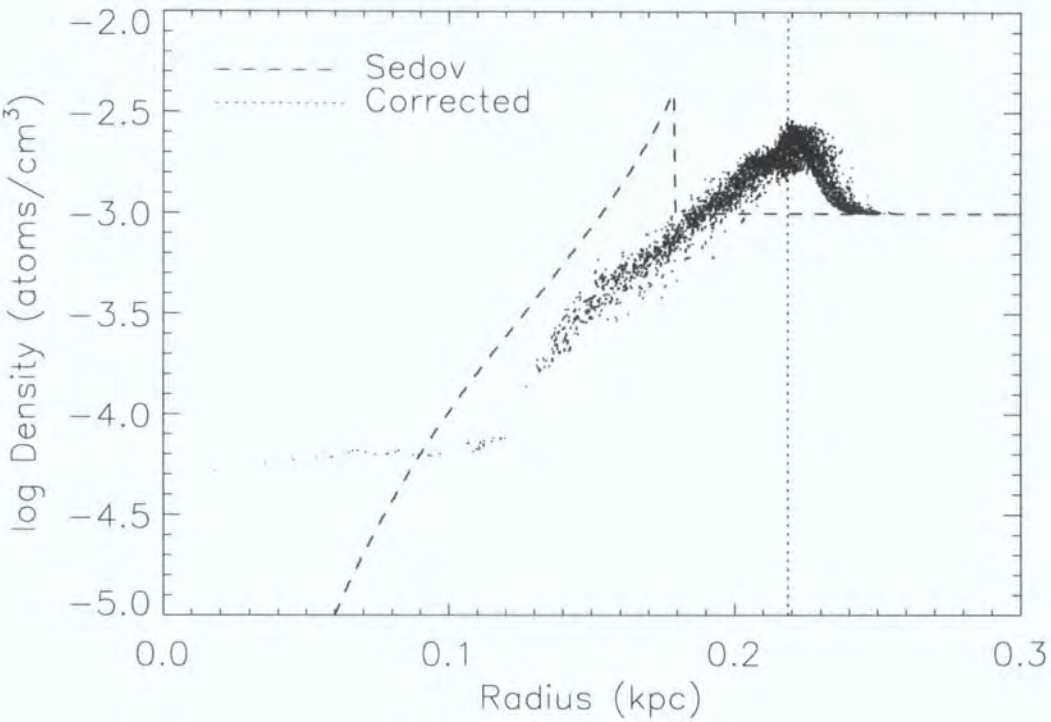

Figure 3.3: Comparison between SPH simulation of a Sedov blast, the Sedov solution and the hot medium correction of Tang & Wang (2005). The points represent individual SPH particles, the dashed line is the Sedov solution and the dotted line is the blast wave radius as calculated with the hot medium correction. The initial condition had a density of 0.001 atoms per cm^3 and a temperature of 10^6K. 10^{51}ergs were injected to the central 32 particles at t_0. This plot was made after the blast wave had evolved for 0.3 Myr.

note that the details of our prescription are uncertain. In section 4.4 we investigate the effects of using different implementations of the physics of SN blast waves to estimate how important the details of the behaviour of SN remnants are to the overall properties of the galaxy. Both the radiative cooling and blast wave velocity physics are varied.

Numerical Implementation

By assuming that each stellar particle in the simulation represents an entire population with the same age we can calculate the minimum and maximum masses of stars that undergo supernova events over any given time period using Eq (3.37). Each of these supernovae is assumed to go off in a neighbouring gas particle (*i.e.* one for which the distance, r, to the star is smaller than its smoothing length, h, in the SPH formalism). We chose this particle randomly from the neighbours, with a weight computed from the solid angle, Ω, it subtends on the sky as seen from the position of the star particle,

$$\Omega = 2\pi \left(1 - \frac{r}{\sqrt{(r^2 + h^2)}}\right). \tag{3.42}$$

This weighting forces that nearby hot, diffuse gas (which tends to have larger h, hence larger weight) is heated more frequently than cooler, denser parts of the ambient medium (which are dense, hence have smaller h).

We do not transfer all SN energy to gas particles each timestep. Assuming that SN explosions are distributed evenly in time and space we can calculate for every ambient gas particle a 'porosity' of SN bubbles, $Q = V_{\rm B}/V_{\rm A}$. For the volume associated with a gas particle we use $V_{\rm A} = (4\pi/3)\,h^3$, and $V_{\rm B} = (4\pi/3)\sum r_b^3$ is the total volume of all the SN bubbles in this particle. When Q is greater than a critical value, $Q_{\rm crit} \approx 1$, the ambient phase is heated, else the available SN energy is carried over to the next time step. This ensures that the ambient phase is only heated when hot supernova bubbles make up a significant fraction of the volume. There are two motivations for this, firstly a given SPH particle cannot represent more than one phase at a given time. Secondly simulations usually do not limit the timestep to be a fraction of the cooling time. Consider a warm, $T \sim 10^4$K, SPH particle in the disk. If a small amount of SN energy is injected into this dense particle, it will cool very efficiently since the cooling rate is very high. It is only when the particle is heated to $T \gg 10^6$K that the reduced cooling may affect the particle dynamically, so that it will move into lower density gas, further decreasing its cooling rate, and becoming part of the hot, tenuous gas. Storing the available heating until the SN bubbles fill a significant fraction of the particle is a way of easing the transition from

warm to hot and makes the outcome less dependent on the timestep.

To determine the porosity Q, we need to know the current radii, r_b, of SN bubbles. The radius r_b depends on the ambient gas properties and also on the available energy, E_b, as discussed in section 3.2.6. Typically a single stellar particle will undergo multiple SN events over a single timestep. Using Eqs. (3.37) and (3.38) and obtaining the SPH estimate of the ambient gas density at the position of the star particle we can estimate the average radius of all supernova bubbles blown by a given star particle at any time. Working under the assumption that the porosity of the ISM is low we calculate the radiative loss from each bubble separately. When the porosity of the ISM becomes $Q > Q_{\rm crit} \sim 1$, the SN bubbles are overlapping significantly and all coherent structure is assumed to be wiped out. The ambient gas particles are heated by the remaining thermal energy in the supernova bubbles and they are considered to disperse. The porosity is set back to zero. Note that using the Sedov solution implies we neglect radiative cooling in the remnants to determine the porosity, Q. However to determine how much energy is in the bubbles once we decide to heat the particle, we do use the tables of Thornton et al. (1998) to account for radiative cooling in the SN shells. We believe that even though this treatment is not fully consistent, it does capture the main physics.

3.2.7 Thermal Conduction

Thermal conduction between the ambient and cold gas in the simulation is an important ingredient in the self-regulation of the star formation rate in our model of the ISM.

Relevant Physics

Thermal conduction has two primary effects. The first is to smooth out the temperature and density profiles inside SN remnants. In the strong explosion solution of Sedov, where thermal conduction is neglected, the temperature of the blast wave increases sharply towards the centre of the blast. This is due to the fact that the gas near the origin was heated by a stronger shock than that at the edges and thereafter evolves adiabatically. The effect of thermal conduction is to efficiently transport heat from the centre of the blast to the outer cool regions. The temperature of the interior of the supernova blast, T_b, is then approximately constant and equal to the mean temperature of the blast(Chevalier (1975); MO77):

$$\left(\frac{T_b}{10^8\mathrm{K}}\right) = 1.2\left(\frac{r_b}{10\mathrm{pc}}\right)^{-3}\left(\frac{n_b}{0.1\,\mathrm{cm}^{-3}}\right)^{-1}\left(\frac{E_b}{10^{51}\mathrm{erg}}\right), \tag{3.43}$$

where n_b and T_b are the mean density and temperature inside the bubble, respectively. We assume r_b to be described by Sedov's self-similar solution. The density n_b is also approximately constant and is given in terms of the ambient density, n_h, as

$$\frac{n_b}{n_h} = 1 + x^{-5/3} \tag{3.44}$$

$$x \equiv 0.65\left(\frac{r_b}{10\mathrm{pc}}\right)\Sigma_{\mathrm{con}}^{1/5}\left(\frac{n_h}{\mathrm{cm}^{-3}}\right)^{3/5}\left(\frac{E_b}{10^{51}\mathrm{erg}}\right)^{-2/5}. \tag{3.45}$$

The dimensionless number Σ_{con} represents the effectiveness of evaporation,

$$\Sigma_{\mathrm{con}} = \frac{\alpha_{\mathrm{con}}}{3}\left(\frac{r_c}{\mathrm{pc}}\right)^2 f_{\mathrm{cl}}^{-1}\phi^{-1}, \tag{3.46}$$

(McKee and Cowie (1977)), and depends on $\alpha_{\mathrm{con}} = \dot{r}_b/c_h$ (the ratio of the velocity of the supernova blast wave to the sound speed of the medium), the cloud's radius, r_c, the volume filling factor of the cold clouds, f_{cl}, and the efficiency of thermal conduction, ϕ (see MO77 for details). For a pure Sedov blast wave $\alpha_{\mathrm{con}} = 1.68$. The presence of magnetic fields and turbulence may decrease ϕ below its maximum value of $\phi = 1$. We compute f_{cl} for each sticky particle from its current cloud mass spectrum given the assumed cloud mass-radius relation, Eq. (3.5).

The second effect of thermal conduction is to evaporate cold clouds. According to (McKee and Cowie (1977); Cowie (1977)), the evaporation rate is well described by:

$$\left(\frac{\dot{M}_c}{\mathrm{M}_\odot\mathrm{Myr}^{-1}}\right) = -0.44 \times \left(\frac{T}{10^6\mathrm{K}}\right)^{5/2}\left(\frac{r_c}{\mathrm{pc}}\right). \tag{3.47}$$

Numerical Implementation

Since we store the mass function of molecular clouds internal to each sticky particle explicitly (Sect. 3.2.2), we can apply Eq. (3.47) along with Eq. (3.5) to each cloud mass bin to calculate the total mass loss of a cloud over one timestep. The evaporation rate of the cloud depends on the temperature of the ambient gas, which is represented with SPH particles. However, as we discussed above, some fraction Q of the volume of each SPH particle may be filled by hot SN bubbles, in which the evaporation rate of clouds may be much higher. Since we have computed Q, we can take this important effect into account.

Consider a single molecular cloud in thermal contact with an ambient medium of (constant) temperature T. The mass of a cloud at the end of a timestep (M_f) is related to its mass at the start of the timestep (M_i) by:

$$M_f = \left[M_i^{1-\alpha_c} - (1-\alpha_c)\frac{0.44T^{5/2}r_{\mathrm{ref}}}{M_{\mathrm{ref}}^{\alpha_c}}\Delta t\right]^{1/(1-\alpha_c)}, \tag{3.48}$$

where T is in units of 10^6K, masses are in $M_\odot$, lengths are in pc and times are in Myr.

Eq (3.48) represents the mass loss rate for a single cloud in contact with a medium of temperature T. More generally in a porous medium a single cloud of mass m has a mean mass loss rate described by:

$$\dot{M}_{\rm cloud} = -Q\dot{M}_{\rm bubble} - (1-Q)\dot{M}_{\rm ambient}, \tag{3.49}$$

where $\dot{m}_{\rm bubble}$ and $\dot{m}_{\rm ambient}$ represent the rate of mass loss for a cloud inside a supernova bubble and situated in the ambient medium respectively.

Eq. (3.48) can be applied directly to the evaporation of a cloud in the local ambient medium ($\dot{m}_{\rm ambient}$). However to apply the same formula to the evaporation of clouds inside of supernova bubbles we need to account for the fact that although the temperature inside the bubbles remains uniform, due to conduction, it is not constant in time, but decreases as the bubble expands. We therefore make the additional assumption that the mean temperature of the supernova remnant is constant over a timestep (a good approximation after a short transient phase). Under this assumption Eq. (3.48) can be applied successfully to the more general case of evaporation in a porous medium. Eq (3.47) and Eq (3.5) are used to show that the total mass loss rate for clouds of mass m in a volume V_A is given by

$$\left(\frac{\dot{M}}{\rm M_\odot Myr^{-1}}\right) = -0.44\left(\frac{M_c}{M_\odot}\right)_c^{\alpha}\left(\frac{r_{ref}}{\rm pc}\right)\left(\frac{M_{ref}}{\rm M_\odot}\right)^{-\alpha_c}\left(Q\left(\frac{T_b}{10^6{\rm K}}\right)^{5/2} + (1-Q)\left(\frac{T_a}{10^6{\rm K}}\right)^{5/2}\right). \tag{3.50}$$

Under the assumption that T_b, the mean temperature of supernova remnants, and T_a, the mean ambient temperature, are constant over any single timestep we can write

$$\left(\frac{\dot{M}}{\rm M_\odot Myr^{-1}}\right) \equiv \lambda\left(\frac{M}{M_\odot}\right)^{\alpha_c}, \tag{3.51}$$

In order to calculate the constant of proportionality, λ, we use an estimate of the mean temperature and density inside of a supernova remnant. These estimates were obtained by noting that by definition $Q \equiv V_B/V_A$. (V_B and V_A represent the total volume in bubbles and the ambient phase respectively). The mean radius of a supernova remnant is then

$$r_b = \left(\frac{3QV_A}{4\pi N_{SN}}\right)^{1/3}, \tag{3.52}$$

where N_{SN} is the total number of supernova explosions that have affected the local ambient medium (calculated from equations 3.37 and 3.35). The mean density inside the

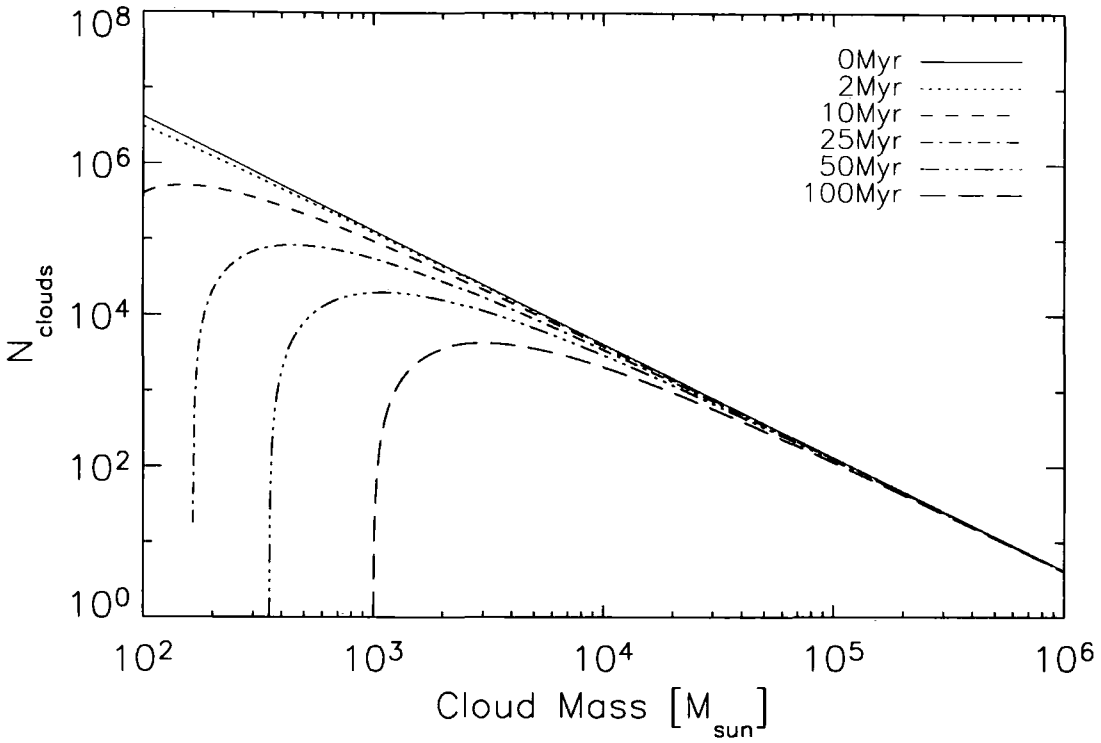

Figure 3.4: Evolution of a population of molecular clouds as they are evaporated by a hot ambient medium. The initial cloud mass function is a power law. The temperature of the ambient medium is assumed to be 10^5K, the porosity of the medium is assumed to remain constant at 0.2, and the temperature of the supernova remnants is $\approx 10^6$K. Thermal conduction acts to preferentially destroy the smaller clouds.

supernova remnants, n_b, may then be calculated from Eq (3.44) and Eq (3.45) and the mean temperature from Eq (3.43).

Over a period of time Δt a cloud with mass M_I will evaporate to a mass of M_F, given by:

$$M_F = \left(M_I^{(1-\alpha_c)} - \lambda \Delta t\right)^{1/(1-\alpha_c)} \tag{3.53}$$

Thermal conduction efficiently destroys smaller clouds, but its effects are far less dramatic on larger clouds. Fig (3.4) shows the evolution of an initially power law mass spectrum of clouds in a hot medium. The energy used to evaporate a mass $M_F - M_I$ of cold clouds is removed from the supernova remnants.

3.2.8 Mass Resolution Limits

The sticky particle model allows particles of all types to change their mass via processes including merging, thermal conduction and star formation. For this reason it is necessary for us to introduce numerical minimum and maximum masses on all particle types. We define at the initial time a characteristic mass resolution for our simulation, $M_{\rm char}$, typically this is set equal to the mass of the ambient gas particles in the initial conditions. Where more than one mass of ambient particles is present (for example in the model galaxies discussed in section 4.1) we use the mass of the gas particles that will be forming most stars. We then define minimum and maximum particle masses relative to this characteristic mass scale.

Ambient gas particles may have their mass decreased by the formation of molecular clouds. If the total mass of a gas particle becomes less than $0.1M_{\rm char}$ then it is converted entirely into a cloud particle. The ambient gas particles may also have their mass increased by the process of thermal conduction. If a gas particle becomes more massive than $4M_{\rm char}$ then it is not allowed to grow any more, and the evaporated cloud mass is given to a different particle. In practice this limit is rarely, if ever, reached as evaporating cold clouds effectively cools the ambient gas particles so they become inefficient at thermal conduction.

Sticky particles may decrease their mass by star formation and evaporation. If the mass of a sticky particle drops below $0.1M_{\rm char}$ then it is either completely evaporated or completely converted into stars. Coagulation may drive the mass of a sticky particle to be very large. In practice this is not a real concern since when a sticky particle becomes very massive the rate at which its internal clouds coagulate also increases, causing it to form stars very rapidly.

Stars have a maximum and minimum mass of $4M_{\rm char}$ and $0.1M_{\rm char}$. If a star forms with a mass greater than the maximum allowed mass it is split into a number of smaller star particles. A sticky particle may not form a star with a mass lower than the minimum allowed mass. In this eventuality then the mass of the 'unresolved' stars is tracked internally by the sticky particle and added into the next star formation event until the total mass of stars formed reaches the resolution limit of the simulation.

These particle mass limits keep all particle masses in the range $0.1M_{\rm char}$ to $4M_{\rm char}$, which both minimises two body effects between very massive and very small particles and also prevents the formation of very many low mass particles, which are computa-

tionally very expensive to evolve.

3.3 Parameter Estimation

The various physical processes in the star formation and feedback models each have associated with them physical parameters. Before we discuss the properties of our model in detail we discuss how its free parameters can be constrained.

The free parameters that control the thermal instability and formation of the molecular clouds are $\rho_{\rm th}$ and $T_{\rm th}$, the physical density and temperature at which thermal instability is allowed to set in and radiative cooling creates molecular clouds. Wolfire et al. (1995) found that a diffuse ISM naturally settles into two stable phases, with a sharp cutoff between the ambient and molecular phases at a density of approximately 1 atom per cm^3. We use this as the value of $\rho_{\rm th}$. A threshold temperature $T_{\rm th} = 10^5$K allows the gas in galaxies which cools radiatively to $\sim 10^4 K$ to collapse into clouds but prevents supernova heated material (typically at temperatures of $10^6 K$) from forming molecular clouds until it has radiated away most of its supernova energy.

The properties of the molecular clouds themselves are contained in four parameters: $r_{\rm ref}$, $M_{\rm ref}$, and α_c as defined in Eq (3.5) and u_c, the internal energy per unit mass of molecular clouds. The first three values are set by comparison with observations of molecular clouds in the nearby galaxy M33 (Wilson and Scoville (1990)):

$$\left(\frac{r_{\rm c}}{\rm pc}\right) = (36 \pm 6)\left(\frac{M}{10^5 M_\odot}\right)^{0.3\pm0.1} \tag{3.54}$$

Thus $r_{\rm ref}$ and $M_{\rm ref}$ are assumed to be 36pc and $10^5 M_\odot$ respectively. This calibration (and an assumed α_c of 0.3) suggest a radius of 122 ± 6pc for the largest clouds observed in the MW ($6 \times 10^6 M_\odot$ (Williams and McKee (1997)).

The properties of the stars and associated feedback are contained within four parameters: x, the slope of the IMF; E_{51}, the energy of each supernova blast in units of 10^{51}erg; $M_{\star,\rm min}$, the minimum star mass; and $M_{\star,\rm max}$, the mass of the largest allowed stars. For E_{51} we use the fiducial value of 1.0 noting, however, that the value of E_{51} is very uncertain and may be significantly higher. The effects of varying E_{51} are investigated in section 4.4. For the purposes of this work uncertainties in the IMF are neglected and x is assumed to take on the standard Salpeter value of 1.35. We follow Kawata and Gibson (2003) in adopting values $0.2 M_\odot$ and $60 M_\odot$ for the minimum and maximum stellar masses, respectively.

The star formation efficiency in a single cloud collapse is also somewhat uncertain and is known to be approximately $\epsilon_\star \approx 11\%$ (Williams and McKee (1997)) in the MW.

The thermal conduction efficiency is characterised by two numbers: $\alpha_{\rm con}$, the ratio of the blast wave velocity to the ambient sound speed and ϕ, the efficiency of thermal conduction. Following MO77, the value of $\alpha_{\rm con}$ is set to 2.5 (for the ideal Sedov blast wave case, $\alpha_{\rm con}$ is 1.68, the presence of thermal conduction changes this value). The thermal conduction efficiency parameter is assumed to be $\phi = 1$. The presence of magnetic fields and turbulence may change ϕ significantly; we investigate the effect of moving away from this value in Sect. 4.4

This leaves $v_{\rm stick}$ (the maximum relative cloud velocity for mergers) and η (the fraction of a cloud's velocity lost per non-merger collision) as free parameters that are hard to constrain via observation. It is noted that the large scale behaviour of a given simulation is largely independent of the value of η. This is because the cold cloud velocity dispersion is always limited by $v_{\rm stick}$. In the following section simple simulations are used in order to calibrate the properties of the physical model.

3.3.1 One Zone Simulations

Simulation Details

A 'one zone model' is a periodic box that represents a fixed mass and volume (i.e. a static, periodic box with no mass outflow). The ambient ISM phase is assumed to be homogeneous. Initially, for a chosen mean density of matter we assume that 50% of the material is initially in the hot phase at a temperature of $T_0 = 10^6$K. The remaining gas is initially in cold clouds with an initial mass function that is a very steep ($N(M)dM \propto M^{-8}dM$) power law. Numerically we represent the different phases as follows: the ambient phase is assumed to be homogeneous and isotropic and so is represented by a single density and temperature throughout the whole periodic volume, molecular clouds are represented by discrete sticky particles that are spawned at a random point in the computational volume with a random velocity, stars are not tracked individually, and are assumed to heat the whole volume evenly when they undergo SN explosions. The mass resolution of the molecular phase is approximately $10^7 M_\odot$, although the effects of varying this figure are investigated later in this section.

This initial situation represents hot, dense gas that has just begun to experience a thermal instability and started forming its first molecular clouds. The volume we sim-

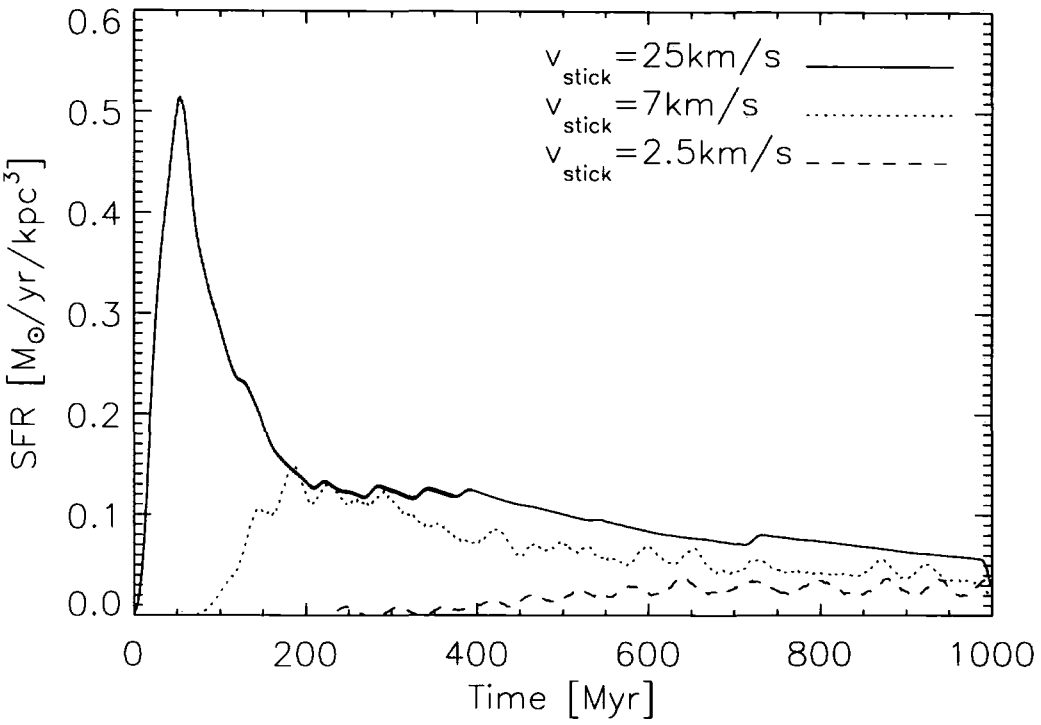

Figure 3.5: Star formation rate as a function of time for a one zone box with three different values of $v_{\rm stick}$. The initial gas density is $n_0 = 2$ cm^{-3} in each case. Each curve follows the same general shape, there is an initial delay during which the first GMCs are forming. The unopposed collapse of the first GMCs causes a burst of star formation, which is quickly regulated by the effects of feedback from stellar winds and supernova explosions. After this initial burst the star formation rate in the simulation settles down and gradually decreases as the gas in the box is used up.

ulate is one cubic kpc. The hot phase will evaporate cold clouds through thermal conduction, and can cool via radiative processes using a simple tabulated cooling function from Sutherland and Dopita (1993) (assuming solar metallicity). Cold cloud particles are scattered randomly throughout the volume and given random velocities. Clouds do not feel gravitational forces. Depending on the parameters, the ambient phase will cool radiatively to form more molecular gas. Clouds will coagulate to form GMCs, which in turn form stars. The associated SNe evaporate smaller clouds, and may heat the ambient medium and quench the star formation. This sequence of events is plotted in Fig (3.5), the same general shape is observed for each value of $v_{\rm stick}$, there is a brief delay as the first clouds coagulate to form GMCs, these clouds then collapse and form stars, which undergo supernovae and quench the star formation. On a longer timescale, the quiescent star formation rate slowly decreases as the available gas is consumed by stars. Since the dynamical equilibrium is reached on a very short timescale, typically a couple of hundred Myr, we assume instantaneous recycling when considering supernova feedback. The role of T_{th} is suppressed in the one zone simulations, due to the fact that energy injected via supernovae cannot escape the volume.

The lack of self gravity does not affect the global properties of the volume significantly. From Eq (3.7) assuming typical cloud properties ($M_c \approx 10^5 M_\odot$, $r \approx 50$pc) and a reasonable velocity dispersion ($\sigma = 7$km/s) the ratio of the geometric part of the cross section to the gravitationally focused part is approximately 0.1, therefore direct collisions between clouds account for the majority of the collisions and gravitational focusing makes for an effect of only 10%. In the following section we will choose a value of $v_{\rm stick}$ by comparing the star formation rates in one zone volumes with the Schmidt law, and also look at the properties of one zone volumes.

As noted in section 3.3 the properties of the simulation are largely independent of η. We assume a value of 0.5 throughout the rest of this thesis.

Calibrating the base model

The one zone model provides a useful sandbox in which we can investigate a wide variety of parameter choices in a relatively computationally inexpensive environment. In the following section we discuss our choices for the values of the different parameters. The effects of moving away from this 'base model' are discussed more fully in later sections.

The parameters that are available for tuning the output of the model are as follows: the cold cloud reference size and radius ($r_{\rm ref}$, $M_{\rm ref}$); the slope of the cloud mass-radius

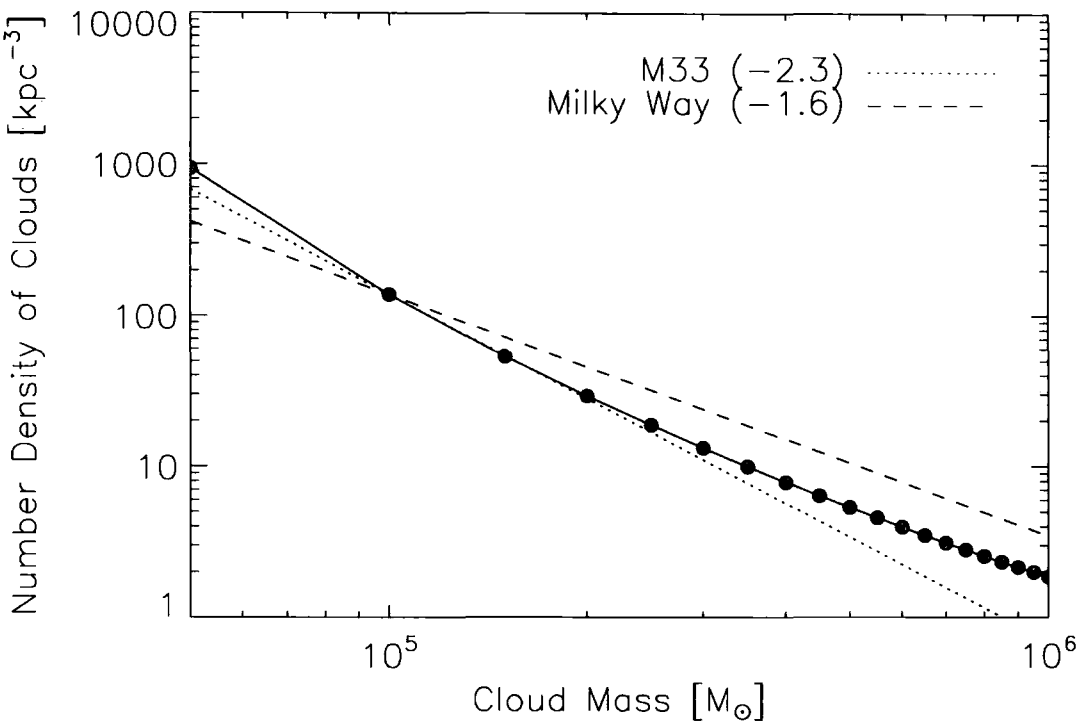

Figure 3.6: Mass function of clouds after 1Gyr in a one zone model. The dashed and dotted lines represent the slopes of the mass functions in the MW (Solomon et al (1987))and M33 (Rosolowsky & Blitz (2004)). The numbers in the legend represent the power law slopes in each of the galaxies. It is clear that we obtain a good agreement between our model and the cloud mass spectrum in real galaxies.

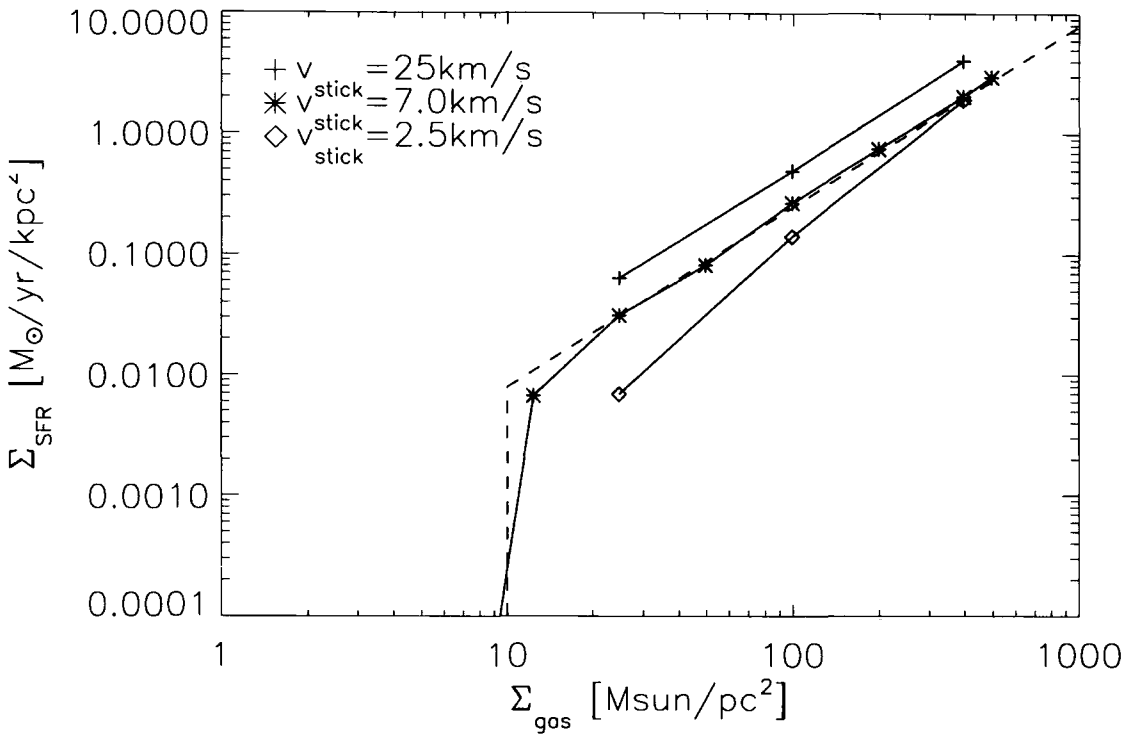

Figure 3.7: Schmidt law. The diagonal dashed line represents the observed star formation law (Kennicutt 1998) and the vertical line represents the observed cutoff in star formation ($10 M_{\odot} \mathrm{pc}^{-2}$; Schaye 2004). Each point represents the star formation rate averaged over a period of 500Myr for a separate one zone simulation. Data is shown for two different values of v_{stick}, the base value used in all subsequent simulations is 7km/s. We calculate star formation rates by averaging the star formation rate in the simulation volume over a 500Myr period. Surface densities were calculated from volume densities by assuming a disk of thickness of 1kpc.

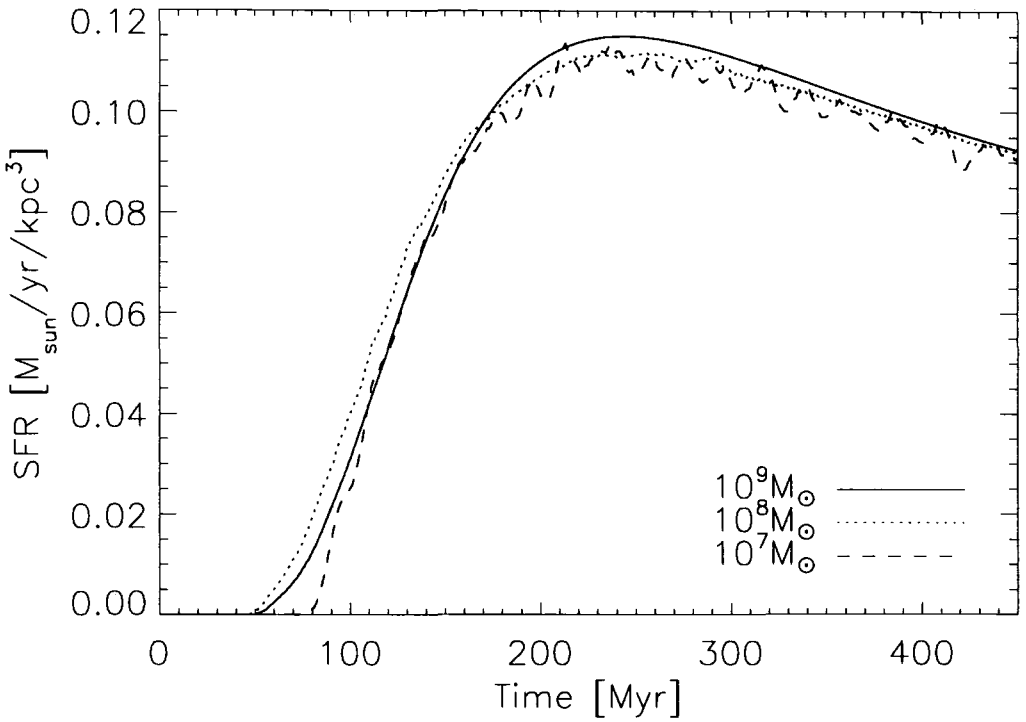

Figure 3.8: Star formation rate as a function of time for one zone models with three different mass resolutions. The star formation rate remains almost unchanged over two orders of magnitude in mass resolution. The coarsest mass resolution of $10^9 M_\odot$ corresponds to the entire one-zone system being represented with a single particle with all clouds interactions modelled with the coagulation equations.

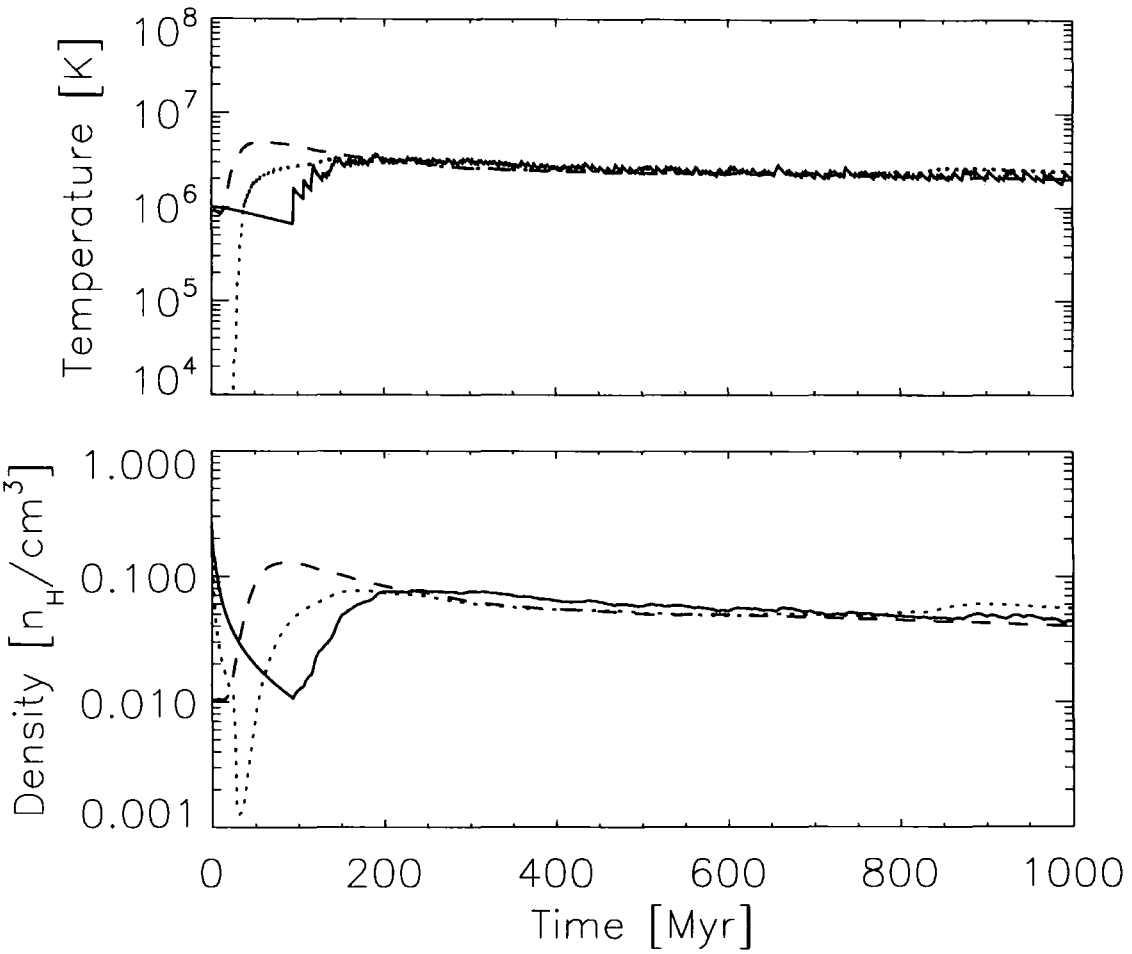

Figure 3.9: Temperature and density of the ambient phase of a one zone model for a variety of different choices of initial temperature and density. The total gas density, ambient gas plus clouds, is always 2 cm^{-3}. The interplay of supernova feedback and radiative cooling quickly brings the system into an equilibrium independent of the initial value. The initial conditions for each of the simulations are as follows: $T = 10^6 K$, 100% atomic (solid line); $T = 10K$, initially 100% atomic (dotted line); $T = 10^6 K$, initially 10% atomic (dashed line).

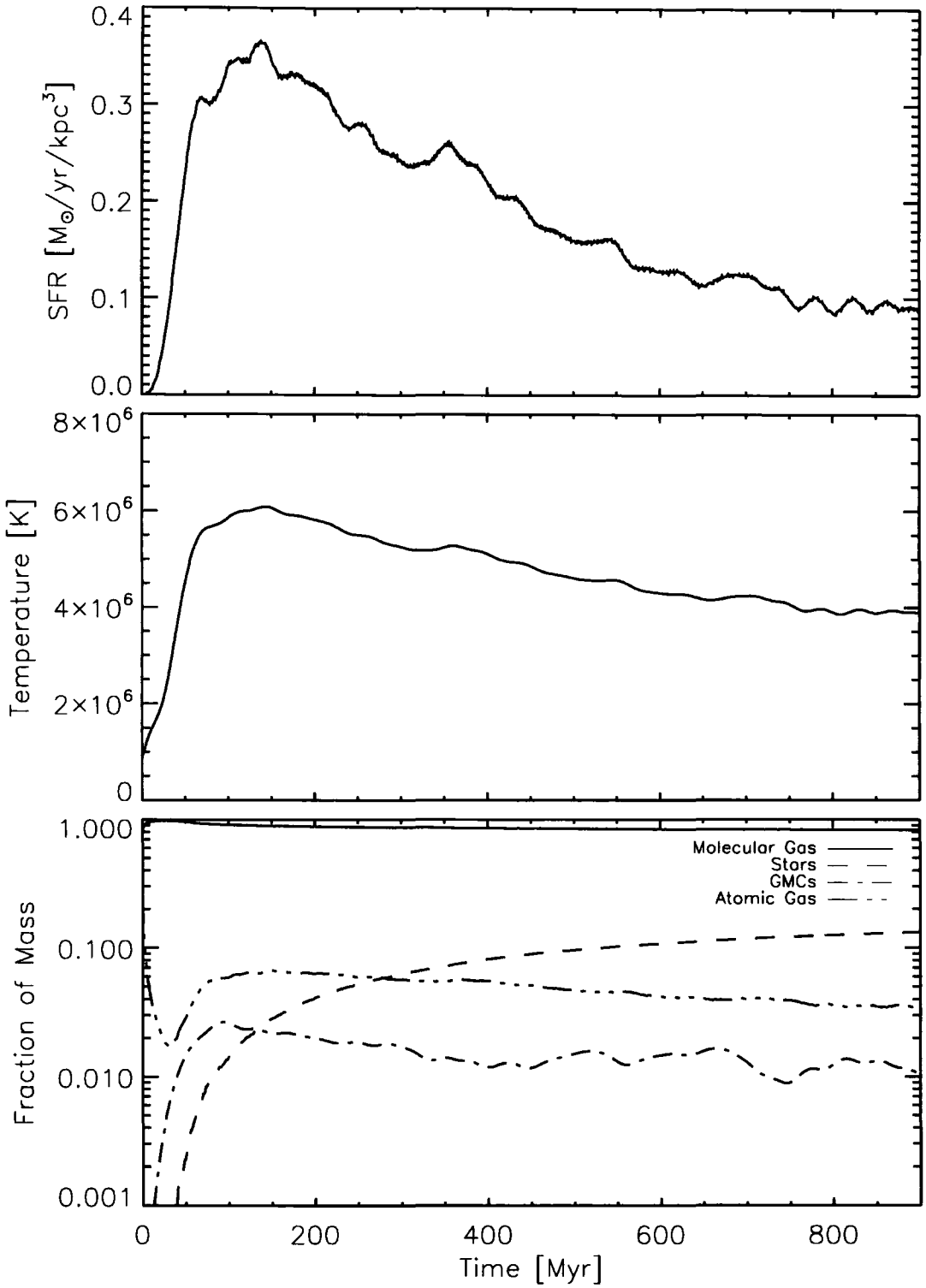

Figure 3.10: The large scale properties of a one zone model with initial density $n_0 = 2\ \mathrm{cm}^{-3}$. The physical parameters used in this model are the same as the base model as discussed in section 3.3.1

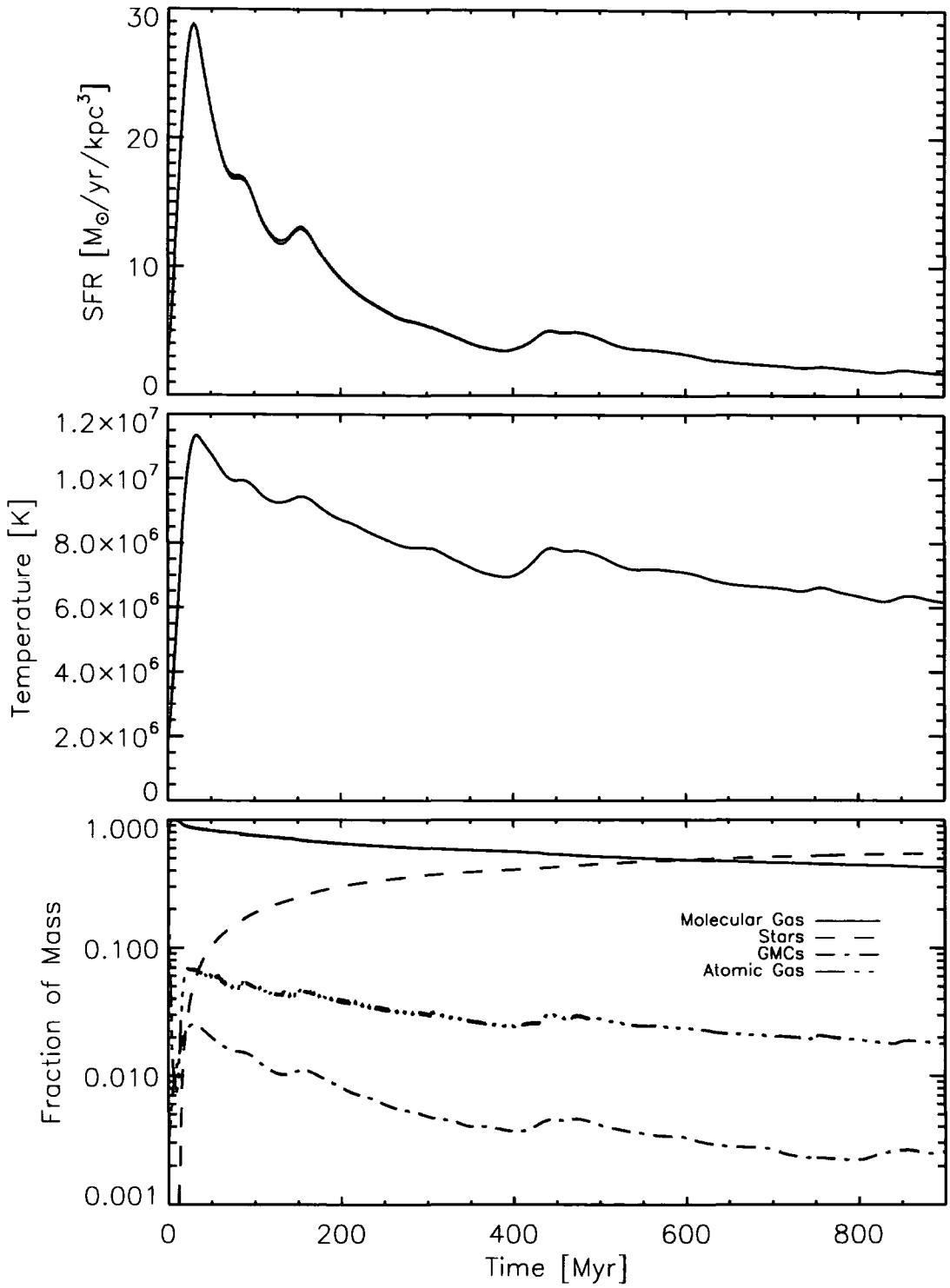

Figure 3.11: Same as Fig (3.10) except with an initial gas density of $n_0 = 16\ \mathrm{cm}^{-3}$

relation, α_c; the efficiency of star formation in any given cloud collapse, $\epsilon_\star$; the maximum relative cloud velocity for merger ($v_{\rm stick}$) and the amount of energy ejected per SNII event (E_{51}).

Even though the initially assumed cloud spectrum, $N(M)dM \propto M^{-8}dM$, is very steep and far from equilibrium, SNe feedback and cloud coagulation rapidly build a mass spectrum $N(M)dM \propto M^{-\alpha}dM$ with $\alpha \approx 2$ (Fig (3.6)), close to what is the observed cloud spectrum in the MW (dashed line) and M33 (dotted lines). This gives us confidence that, although the modelling of cloud formation is simple, it does produce a realistic cloud spectrum.

The ISM model can also reproduce the observed Schmidt law. We find that in our model the interaction between the coagulation of clouds and their destruction by stars leads to a SFR-density relation that is in good agreement with observation (Fig (3.7)) if $v_{\rm stick}$ is set to 7km/s. This represents a reasonable value for the molecular cloud velocity dispersion, as considering theoretical models for the origin of random motion on molecular clouds, we would expect typical velocities in the range 5-7km/s (Jog and Ostriker (1988))

The effect of changing the mass resolution of the simulation over two orders of magnitude is demonstrated in Fig (3.8). Sub-resolution clouds that are simulated only by integrating the coagulation equations are designed to behave in exactly the same way as the resolved cloud particles in the simulation, and so we expect the simulations not to depend strongly on particle number. This is borne out by the good agreement between simulations carried out with only one resolved particle (Fig (3.8), line with mass resolution of $10^9 M_\odot$) where all of the physics is followed by integrating the sub-grid equations in a single particle and simulations with a hundred particles that are followed explicitly.

As stated in previous sections, the behaviour of a one zone model is virtually independent of its initial temperature and the fraction of the gas that starts off in the cold phase. This behaviour is demonstrated in Fig (3.9). A one zone volume with total initial density of $n_0 = 2{\rm cm}^{-3}$ was evolved with a variety of different initial values for the initial temperature and initial fraction of the mass in the hot phase. We observe that regardless of the initial choices for these two quantities the system quickly settles down to its equilibrium state. This process occurs through the opposing actions of thermal conduction and supernova feedback.

Fig (3.10) and Fig (3.11) show the behaviour of the large scale properties of two different one zone volumes as a function of time. The only difference in the initial condi-

tions of the two one zone volumes is their initial density Fig (3.10) shows the evolution of a one zone volume with a total density of 2 atoms/cm^3; Fig (3.11) shows exactly the same plots for a density of 16 atoms/cm^3. The initial temperature of the hot phase in both simulations is 10^6K. In both cases the star formation rate follows the same general shape. There is a small period of time at the beginning of the simulation where small clouds are coagulating and there is no star formation. When GMCs are formed there is a large burst of star formation that is quickly quenched by feedback SN and thermal conduction in SN bubbles. The temperature of the diffuse phase is regulated by a combination of supernova feedback (acting to increase the temperature) and radiative cooling. Due to the fact that we do not allow mass to leave the one zone volume and also assume instantaneous recycling, the temperature profile very closely matches that of the star formation rate. It is noted that in the one zone simulation with the largest density, the temperature of the ambient phase is held at a higher temperature by the action of supernovae. The fraction of the gas in the molecular phase is lower in the high density simulation due to the increased amount of evaporation by thermal conduction in the high temperature ambient phase. In the following chapter the star formation and feedback prescriptions are tested in a more realistic situation, and the properties of the ISM in a simulated galaxy are investigated. In the final chapter we look in detail at the star formation history of a merging galaxy.

Chapter 4

The Interstellar Medium in Isolated Galaxies

4.1 Introduction

In this chapter we apply the physical model developed in chapter 3 to the simulation of isolated galaxies. We perform simulations of both isolated quiescent galactic disks and of the collapse of dark matter/baryonic haloes. We find that the sticky particle model is very successful in reproducing many of the observed properties of disk galaxies, including the molecular cloud mass spectrum, the molecular fraction as a function of radius, the Schmidt law, the stellar density profile and the appearance of a galactic fountain. We find that the ISM created by the sticky particle model is tightly self-regulating and stable; and that simulations of an initially quiescent disk remain stable over many years, with an almost contant SFR, which slowly decreases due to having used up the gas in the disk.

In the second part of this chapter we observe the effects on the galaxy of including differing physics in our implementation.

4.2 Quiescent Disk

One of the fundamental properties that a star formation prescription must be able to reproduce is that in MW like conditions, the resulting behaviour should be similar to that in the MW. In this section we discuss the properties of galaxy simulations set up to approximate the conditions in the MW's quiescent disk.

4.2.1 Simulation Details

We set up a simplified model of a MW type galaxy using initial conditions from GalactICS (Kuijken and Dubinski (1995)). GalactICS generates near equilibrium distributions

Resolution ($M_\odot$)	*Disk*	*Bulge*	*Halo*
Low	6.6×10^6	5.84×10^6	5.6×10^6
Base	8.3×10^5	7.5×10^5	7.1×10^5
High	1.0×10^5	9.2×10^4	1.0×10^5

Table 4.1: Initial particle masses in three different realisations of the model GalactICs galaxy that are used throughout this paper. The disk, bulge and halo consist entirely of baryons, the halo additionally contains dark matter. All masses are in units of $M_\odot$. Baryons are added to the dark matter halo by converting a random 1% of the particles into gas, so the dark matter particle mass in the halo is the same as the gas particle mass.

of collisionless particles consisting of a disk, bulge and halo. These models consist of a spherical bulge component; an approximately exponential disk, which is rotationally supported in the x-y plane and supported by random motion in the z direction; and an approximately spherical halo.

We add baryonic material to this distribution by converting the disk and bulge in their entirety into SPH particles at a temperature of $10^4 K$. 1% of the material in the halo is converted to baryons with a temperature of $10^6 K$. The addition of baryonic material puts the system well out of equilibrium so each simulation is run adiabatically for 250Myr to allow the galaxy to relax closer to its equilibrium state before the additional physics is allowed to operate. The total mass in the disk, bulge and halo are $1 \times 10^{10} M_\odot$, $0.43 \times 10^{10} M_\odot$ and $1.1 \times 10^{11} M_\odot$ respectively. The mass resolution of particles in each of three realisations of this galaxy are summarised in table 4.1. These masses were chosen such that the gaseous particles in each of the three components have approximately the same mass and the dark matter halo particles have masses as close as possible to the gas particle mass. The gravitational softenings for the disk particles (that is: gas, sticky and star) is set to 0.1kpc, 0.05kpc and 0.02kpc in simulations GAL_LORES, GAL_BASE and GAL_HIRES respectively. The dark matter particles have softening lengths ten times larger than the disk particles.

The GalactICS simulations provide a test of the code in a situation somewhat similar to a quiescent MW disk. As discussed in section 3.2, all simulations were performed with the entropy conserving SPH code GADGET2 (Springel (2005)), with all of the physics

Name	Details	$N_{\rm gas}$
GAL_BASE	Base GalactICs model	19330
GAL_LORES	Base model with degraded mass resolution	2450
GAL_HIRES	Base model with improved mass resolution	255000
GAL_BASE_LOSN	E_{51} decreased by factor of 5	19330
GAL_BASE_HISN	E_{51} increased by factor of 5	19330
GAL_BASE_LOCON	Conduction efficiency decreased by factor of 5	19330
GAL_BASE_HICON	Conduction efficiency increased by factor of 5	19330
GAL_BASE_LOZ	Gas metallicity set to 0.5 Solar	19330
GAL_BASE_HIZ	Gas metallicity set to 1.5 Solar	19330
ROT_BASE	Spherical rotating collapse	15000
ROT_LORES	Spherical rotating collapse	4000
ROT_HIRES	Spherical rotating collapse	45000

Table 4.2: Brief table of simulation references and details. $N_{\rm gas}$ shows the number of gas particles in the disk, bulge and halo combined.

discussed in section 3.2 implemented as additional modules. Table 4.2 contains a brief summary of the different simulations. Typical timestep size in one of the base simulations is $\sim 10^4$yr, although this figure is smaller at early times when bursts of supernovae heat gas very strongly.

4.2.2 The Base Simulations

In this section we will discuss simulations run with the base set of physical parameters (section 3.3.1). Most simulations were run at the base mass resolution as defined in table 4.1.

The large scale behaviour of the model galaxy is as follows: Immediately after switching on the additional star formation physics the dense, thermally unstable gas in the disk and bulge collapses into cold clouds, which quickly collapse, causing a large burst of star formation. After approximately 500Myr the galaxy settles down into a quiescent state with a star formation rate of approximately $1M_{\odot}$/yr. The star formation rate gradually decreases as the cold gas in the galaxy is consumed by stars.

It is known that in the MW, most areas of active star formation are concentrated in the

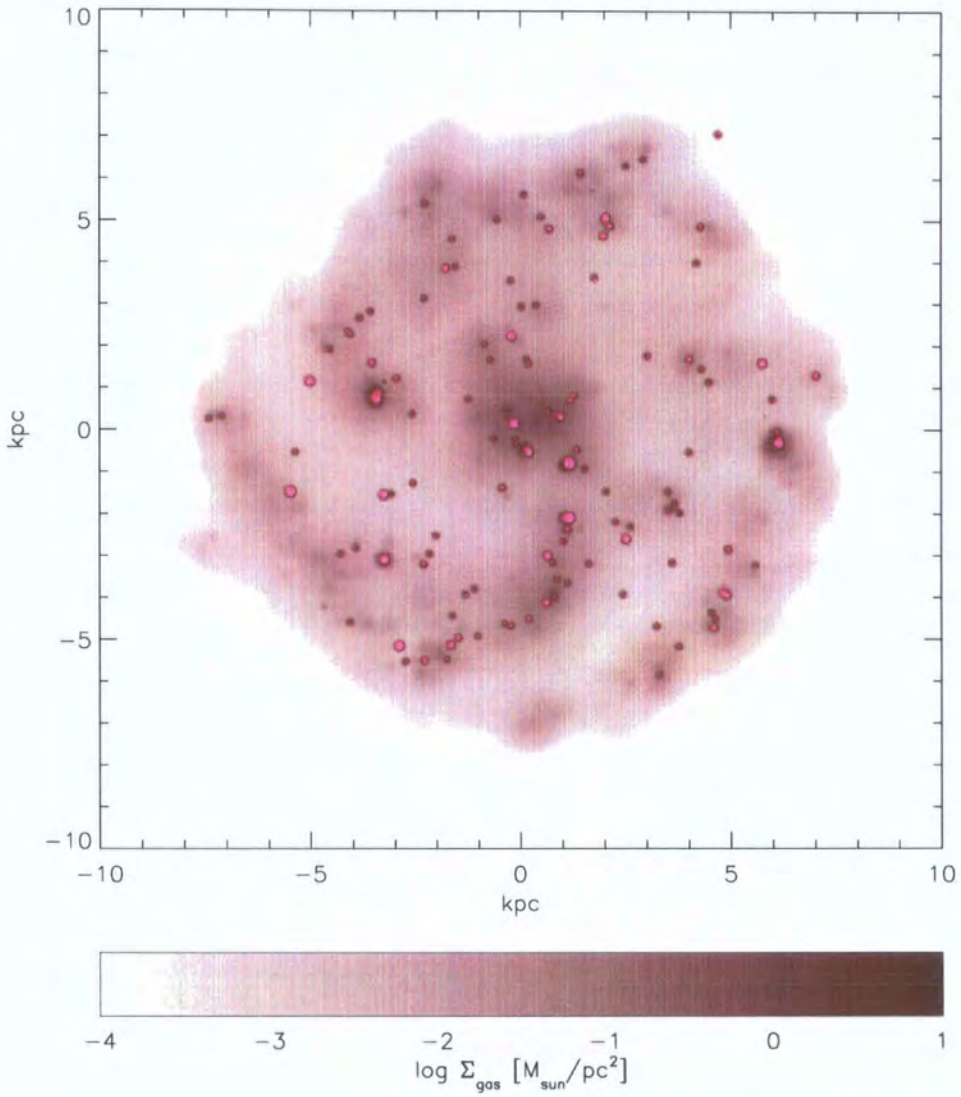

Figure 4.1: Demonstration of the star formation properties of the isolated galactic disk. The continuous field represents the molecular gas surface density of the simulated galactic disk, spiral structure is evident. The circles represent the locations of all stars formed within the last 10Myr. Most star formation events represent the collapse of a single GMC, resulting in the formation of $10^5 M_\odot$ of stars. It is clear that star formation is occurring primarily in the spiral arms of the galaxy.

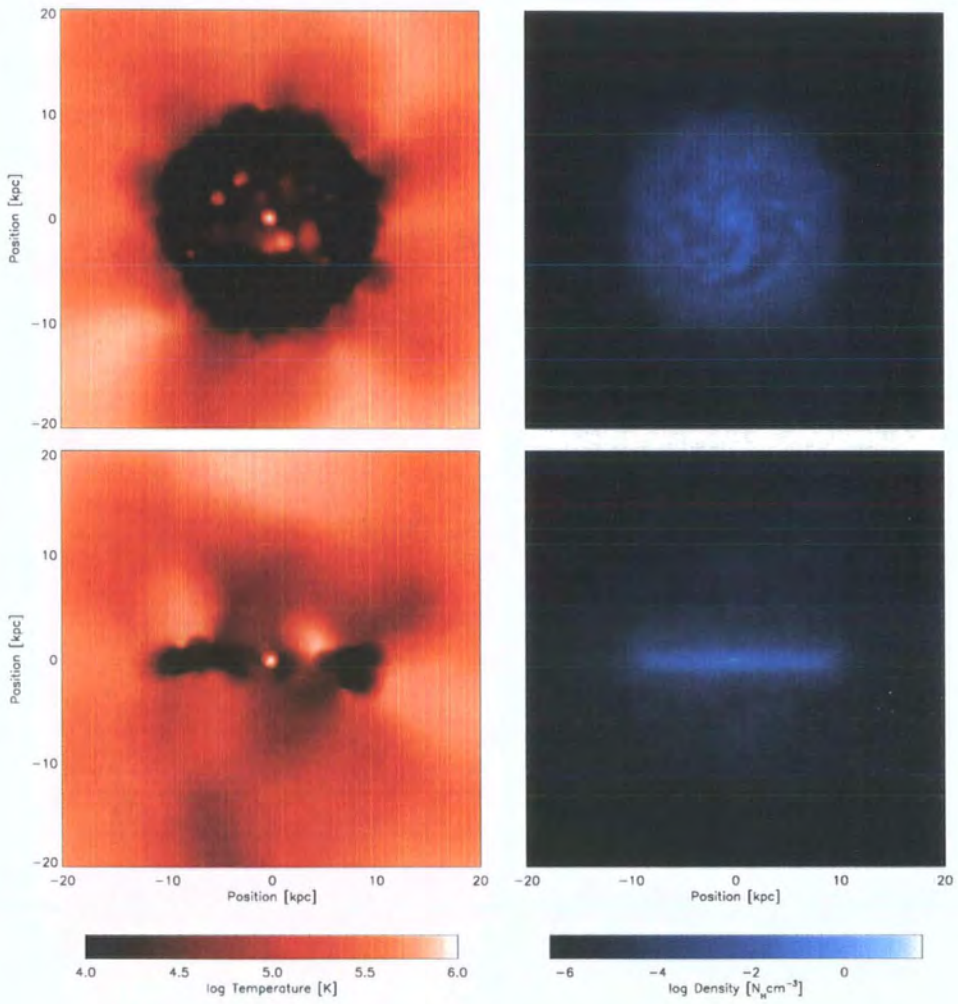

Figure 4.2: A thin slice of the gas temperature and density distributions after 1Gyr in run GAL_BASE. The slice is taken directly through the centre of mass of the stellar disk. The temperature plot clearly shows regions of strongly heated gas, these are areas near to sites of active star formation, where the massive, shortly lived stars are undergoing SNe.

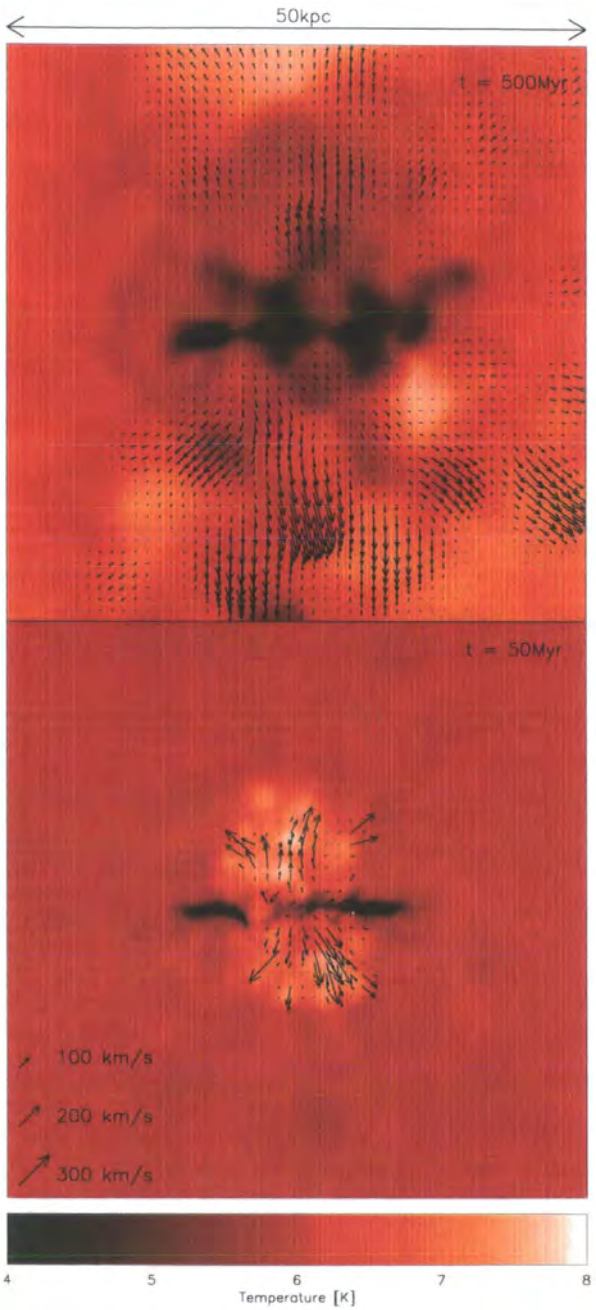

Figure 4.3: A thin slice of the gas temperature field through the centre of a disk galaxy simulation. The arrows represent the gas velocity field, taking into account only gas that has been heated by supernovae. The generation of bipolar outflows from the galactic disk is very clear. The lower plot represents the galaxy after 50Myr, the upper panel is the same galactic disk after 500Myr.

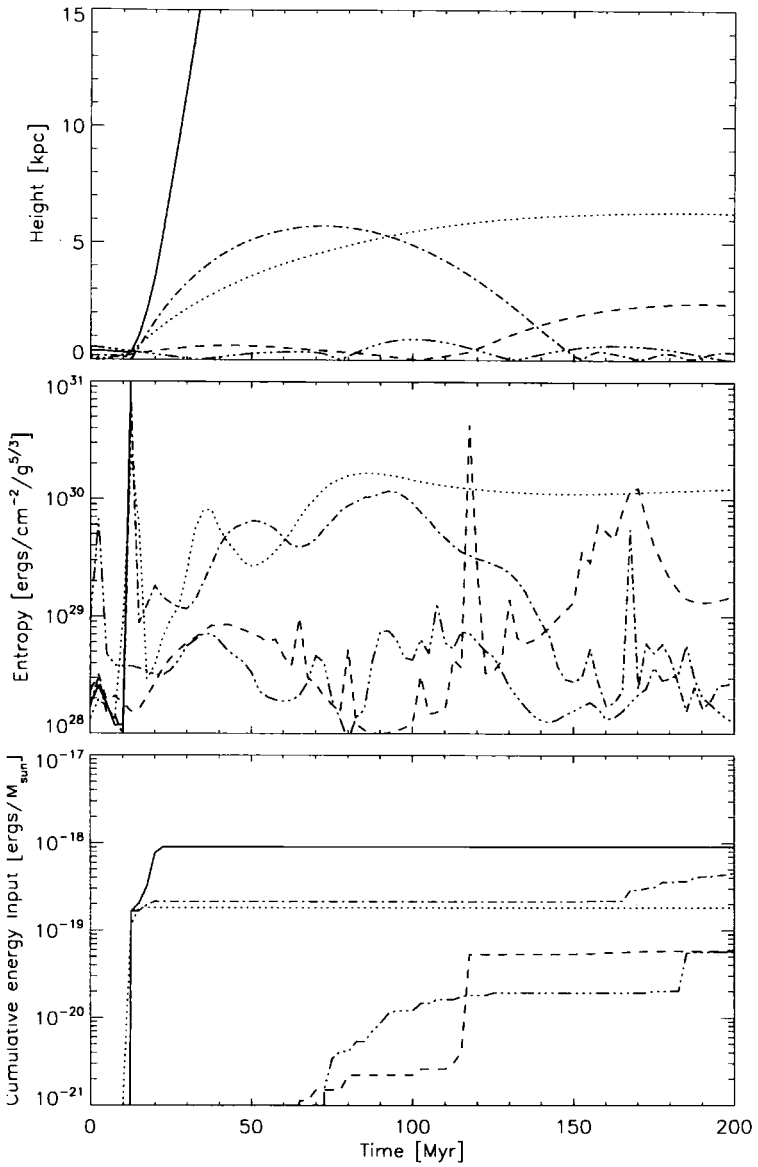

Figure 4.4: Relationship between the number of supernova heatings and the distance from the mid-plane of the disk for a sampling of five particles from the simulated galaxy. Each different linestyle represents a different SPH particle. The top panel shows the perpendicular distance from the centre of the stellar disk, the central panel shows the entropy of each particle and the lower panel the cumulative amount of thermal energy that has been dumped into the particle. It is clear that some particles with a higher entropy are lifted away from the galactic disk where they cool and rain back down on the galactic disk within a hundred Myr of being supernova heated. Other particles are ejected violently from the galaxy, their density becomes very low and they evolve adiabatically.

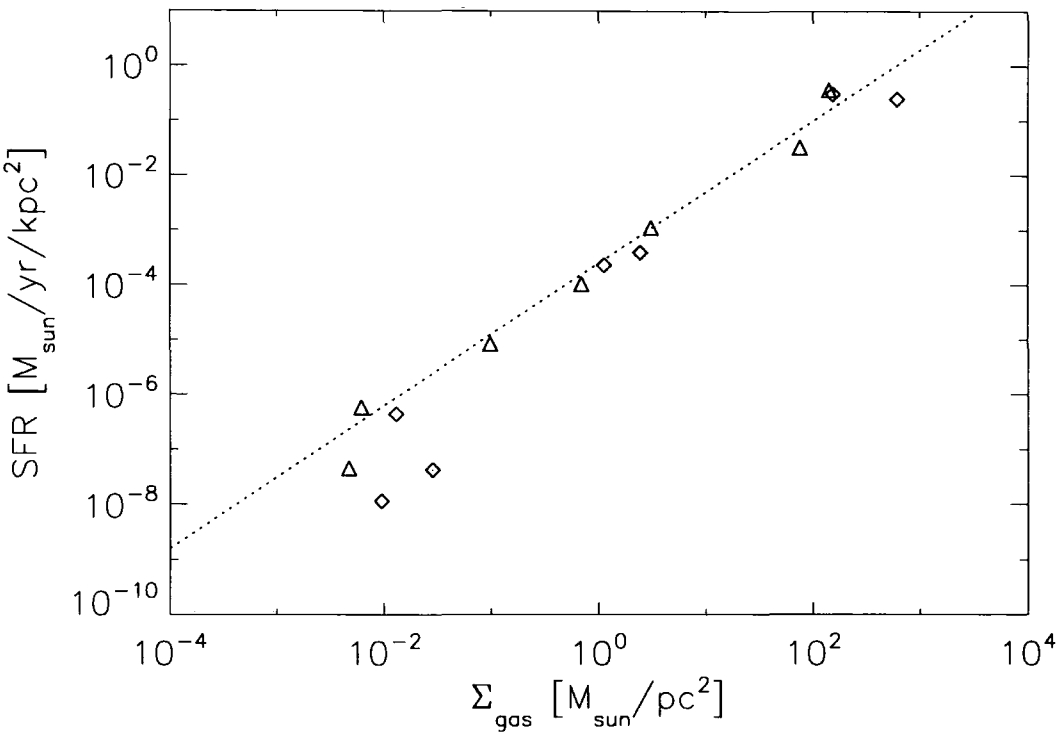

Figure 4.5: The density-star formation rate relationship for our simulated quiescent disk. The diamond shaped points represent the observed star formation rates after 200Myr, and the triangles represent the star formation rates in the same disk after 1Gyr. The dashed line is the observed Schmidt law due to Kennicutt (1998). Our galaxy is in good agreement with the observed Schmidt law throughout its lifetime.

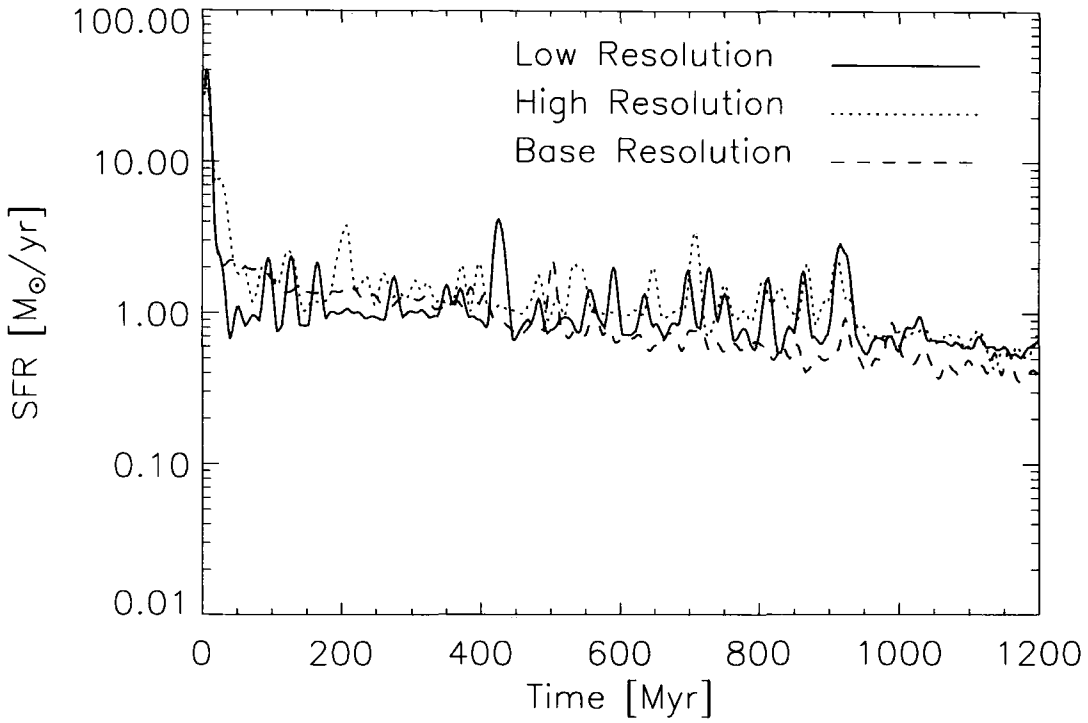

Figure 4.6: Star formation rate as a function of time for isolated galaxy models with different mass resolutions. The mass resolution is 64 times better in the high resolution disk than the low resolution one. The three simulations plotted are GAL_LORES, GAL_BASE and GAL_HIRES. The fact that the star formation rate remains almost unchanged shows that numerical convergence has been achieved.

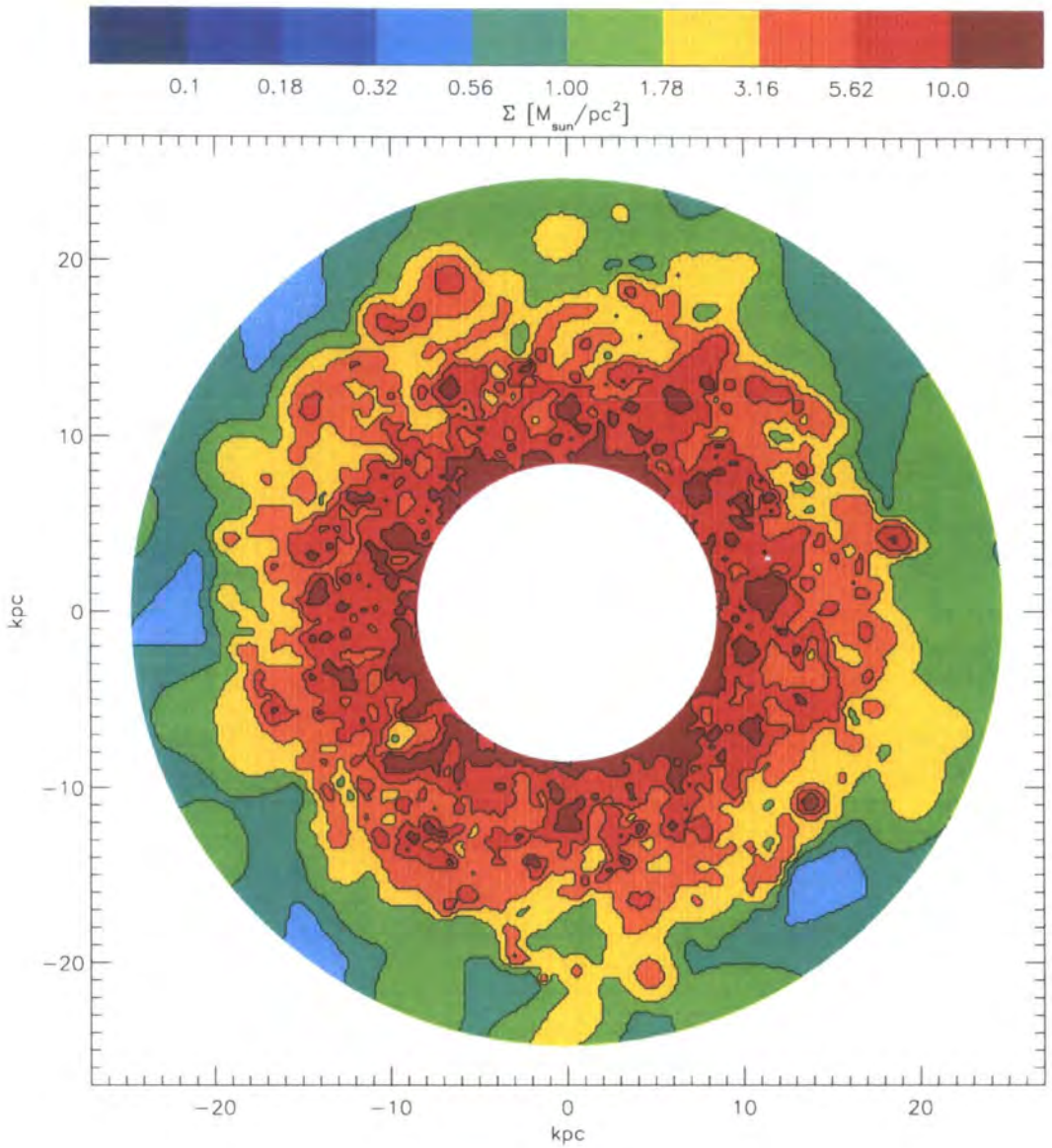

Figure 4.7: Plot of the distribution of atomic gas in a galactic disk. Colours and plot dimensions are matched to those in Levine et al (2006) for easy comparison to observations. The inner circle represents the radius from the centre of the galaxy to the position of the sun. The outer radius is where the observations of Levine et al (2006) are truncated. The simulated MW has a surface density profile in close agreement with that observed by Levine et al.

galactic spiral arms (e.g. Engargiola et al. (2003)). Fig (4.1) shows that our simulations reproduce this behaviour. In the sticky particle model this behaviour occurs naturally as the converging gas flows in galactic spiral arms lead to an increased merger rate and, therefore, to the presence of more star forming clouds. Face and edge on temperature and density plots of the standard resolution galaxy are shown in Fig (4.2). The gas heated by SNII is preferentially situated perpendicular to the plane of the disk, suggesting that the feedback scheme is preferentially heating the low density gas and setting up strong outflows. Fig (4.3) shows the behaviour of the supernova heated gas in a thin slice through the centre of the disk. Initially there is a strong burst of star formation (lower panel of Fig (4.3)), followed shortly by a burst of supernova explosions that heat the gas around the galactic disk as hot at 10^8K. Most of this gas is driven straight out of the halo in a direction perpendicular to the galactic disk. Later on, as the supernova rate dies down, gas is heated more gently and is ejected from the galactic disk in the form of a fountain reminiscent of the galactic fountains present in the MW. This behaviour is demonstrated in figure 4.4, which shows for a random subset of particles from the gas disk the number of times they have been heated as a function of time with their height above the galactic disk. It is clear that upon being strongly heated, some particles are ejected from the galactic disk and fall back down a few hundred Myr later. Others remain in dense regions and cool immediately. Some escape the disk completely in the form of a galactic wind. This behaviour was also observed in the multiphase star formation models of Scannapieco et al. (2006), suggesting that it is a more general feature of multiphase models.

Additionally our simulated galaxies are in good agreement with the observed Schmidt law, Eq (4.5). This behaviour arises due to the self-regulation of the simulated ISM. At higher densities more molecular clouds are formed and so star formation rates are higher. Runaway star formation is prevented by various forms of stellar feedback, which prevent too many clouds from forming. The slope of the Schmidt law in the simulated galaxies may be changed by altering the value of $v_{\rm stick}$. Higher values of $v_{\rm stick}$ lead to clouds coagulating more rapidly, and so low density regions of the galactic disk undergo more star formation. The effect is less severe in the higher density regions of the galaxy as strong feedback from large bursts of star formation can effectively regulate the amount of star formation. Conversely a lower value of $v_{\rm stick}$leads to a steeper Schmidt law with a lower overall star formation rate. This behaviour is demonstrated in Fig (3.5) for the one zone model. The value of $v_{\rm stick}$ used to reproduce the Schmidt law slope

and normalisation in the one zone model also works in the simulated galaxy and the observed galaxy follows the observed Schmidt law very closely throughout its whole lifetime (figure (4.5)). In this figure we do not observe a cutoff in star formation rate at a density of $10\mathrm{cm}^{-3}$ as observed in local galaxies. This anomaly is due to the averaging procedure used when calculating star formation rates and densities. Since we do not store star formation rates on a particle-by-particle basis radial bins were used and star formation rates were calculated from the rate of change of stellar mass in each radial bin. This means that although a given radial bin may have a low density on average it may contain some dense star forming knots.

The resolution independence of the star formation prescription is once again demonstrated by Fig (4.6). The star formation rate between the highest and lowest mass resolution simulations is in remarkably good agreement. The general form followed by all simulations is that there is a strong burst of star formation at the initial time, this is rapidly quenched by supernova feedback, and a self-regulating ISM is set up. The star formation rate slowly increases as the gas in the galactic disk is either used up or ejected in the form of winds.

Recent observations of the gas content of the MW have allowed the construction of maps of its gas surface density (Levine et al. (2006)). In order to compare the properties of our model to observations, another GalactICs model was generated with properties as close as possible to those of the MW. The total mass of the galactic disk was set to $5 \times 10^{10} M_{\odot}$, and the scale radius of the exponential disk to 4.5kpc. This simulation was evolved for 1Gyr. The resulting gas distribution is shown in Fig (4.7). Our simulations are in good agreement with the observations of Levine et al. (2006).

These properties suggest that the star formation and feedback prescriptions behave well in a quiescent disk, a more robust test of how they perform in a more general situation is given by the rotating collapse simulations.

4.3 Rotating Collapse

4.3.1 Simulation Details

The second simulation we investigate is the collapse of a rotating spherical halo (Navarro and White (1993)) with an initial $1/r$ density profile consisting of 90% collisionless dark matter and 10% baryonic material. The mass of the rotating sphere is $1 \times 10^{12} M_{\odot}$ and its initial radius is 100kpc. Velocities are chosen such that the sphere is initially rotating

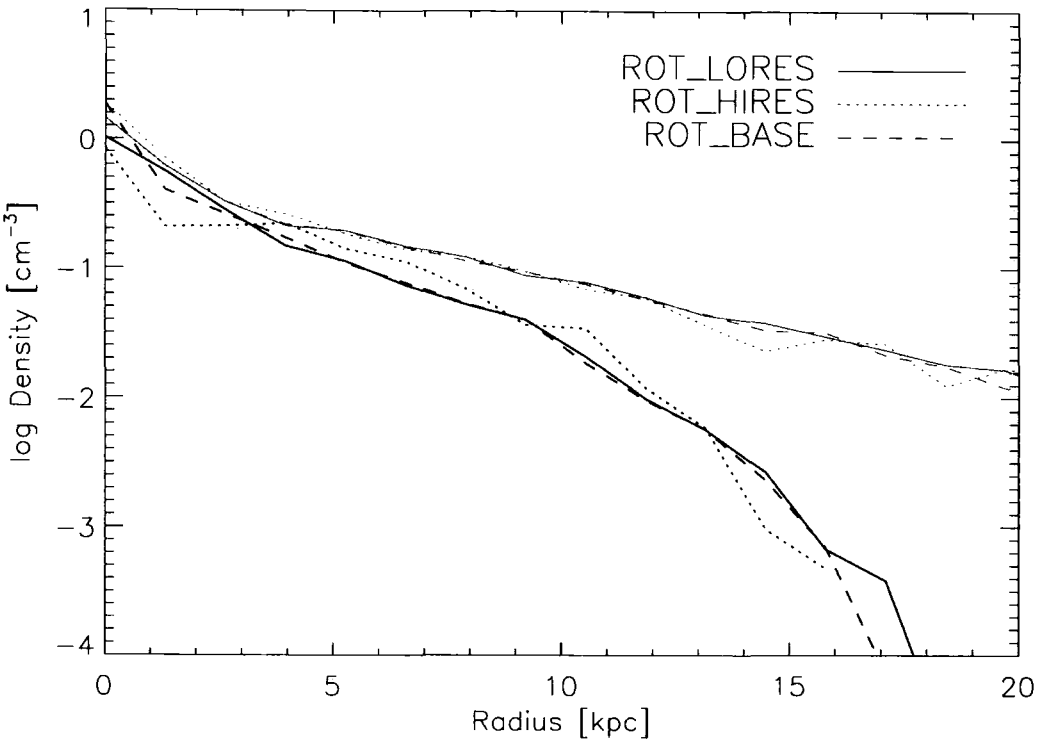

Figure 4.8: Density profiles for the hot, diffuse gas (grey lines) and the cold molecular clouds (black lines). The solid lines represent the low resolution rotating collapse simulations and the dotted lines represent the highest resolution simulations. Agreement between the high and low resolution simulations is very good.

as a solid body with a spin parameter of 0.1. Once again this simulation is created at three different mass resolutions, corresponding to dark matter particle masses of $5.2 \times 10^8 M_\odot$, $5.8 \times 10^7 M_\odot$ and $2.0 \times 10^7 M_\odot$, with corresponding gravitational softenings of 1.93kpc, 0.96kpc and 0.68kpc. The rotating collapse simulations model, in a crude way, the collapse of a protogalaxy, and allow us to investigate how the ISM model behaves when it is initially far from equilibrium and in situations with strong shocks and rapid density changes.

4.3.2 The Base Simulations

After 2Gyr the density profiles of each of the three phases of matter are shown in figure (4.8) and figure (4.9). The density profiles are averaged around the disk; each radial bin represents a ring centered on the centre of mass of the disk. Figure (4.8) shows the radial density profiles of the hot and cold gas. The three different resolution simulations once

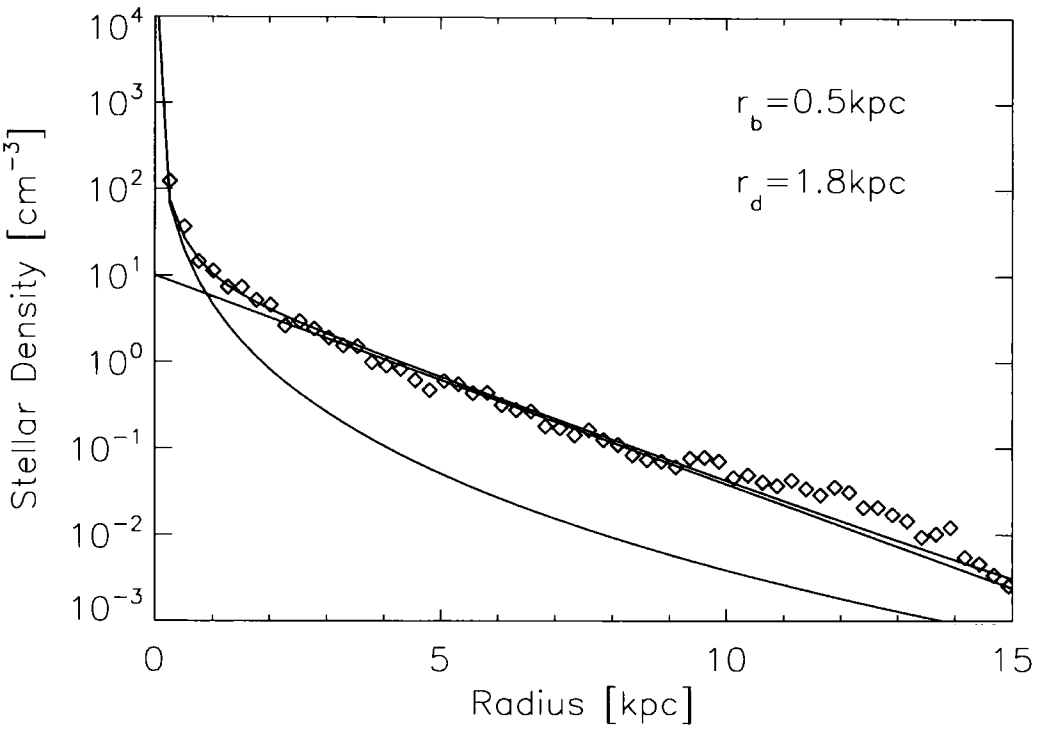

Figure 4.9: Stellar density profile in the base rotating collapse simulation. Solid lines represent the best fit exponential and a de Vaucouleurs profile. The scale radii used in the exponential and de Vacouleurs fits are r_d and r_b respectively. It is clear that even starting from an initial condition far from equilibrium we generate a stellar disk with a surface density profile similar to that in observed galaxies.

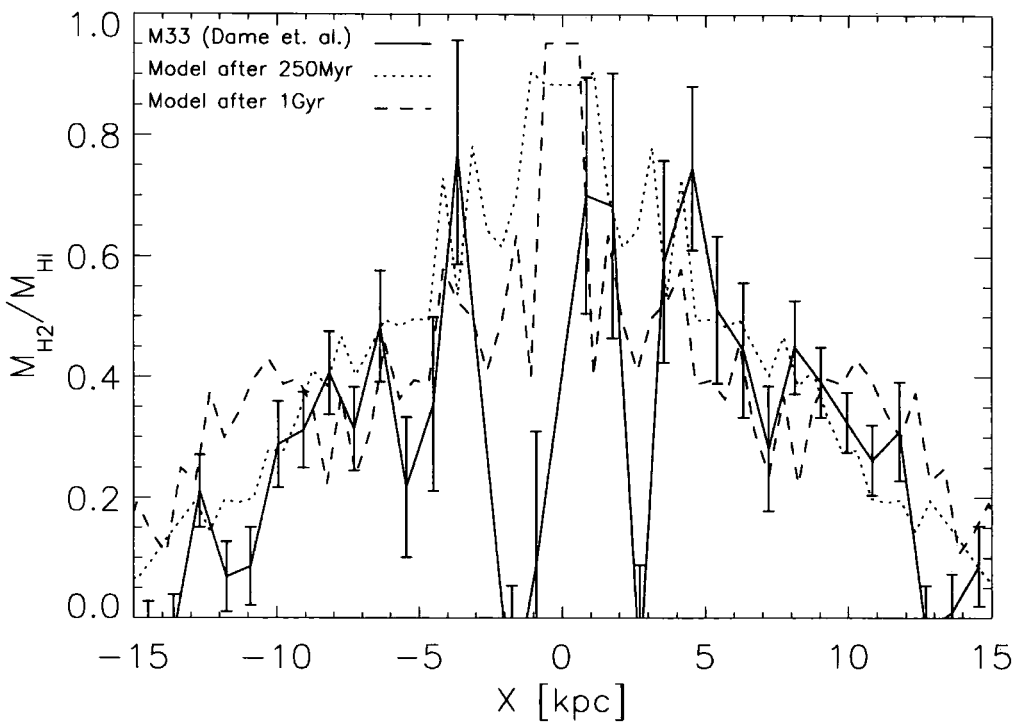

Figure 4.10: Fraction of gas in the molecular phase as a function of distance from the centre of the galactic disk for the rotating collapse model at two different times. The solid line represents the same data as plotted from M33. The simulated galactic disk is in good agreement with observation.

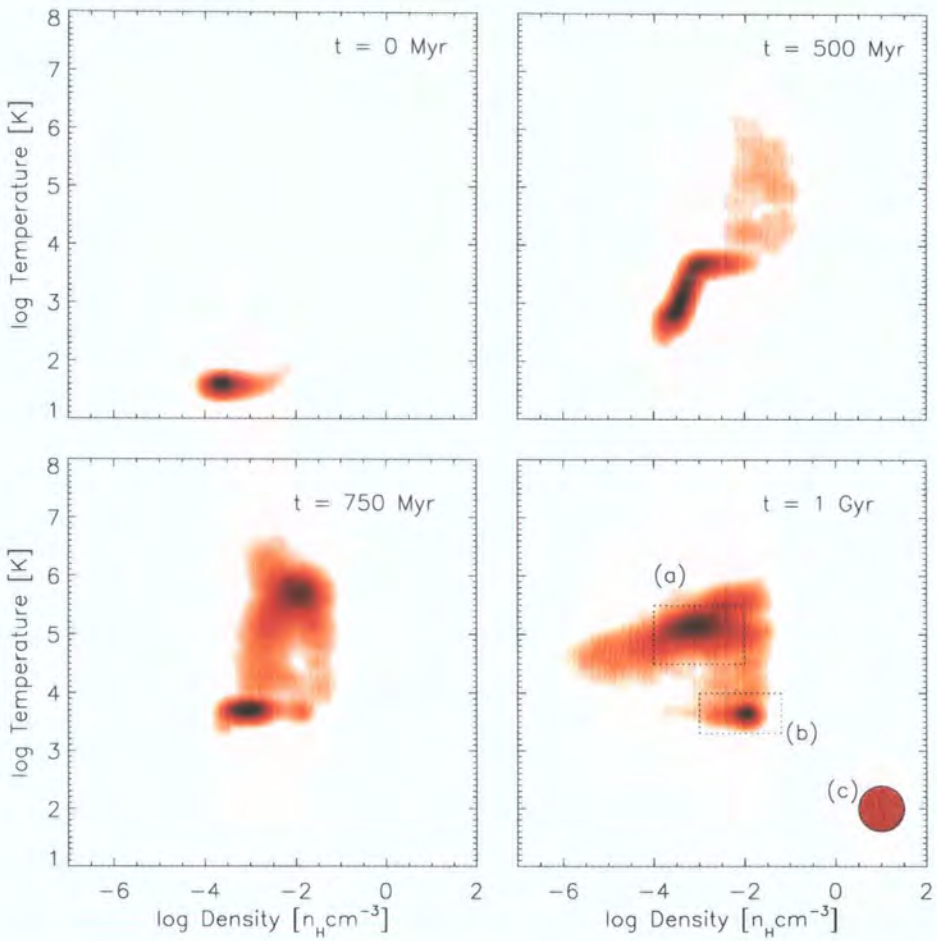

Figure 4.11: Density-Temperature relation for a rotating collapse simulation showing the creation of three distinct components. In the final time plot region *a* contains the supernova heated gas in the halo of the galaxy. *b* is gas contained in the disk of the galaxy, which reaches an equilibrium temperature of $\sim 10^4 K$ and *c* represents the approximate position of the molecular clouds, at an assumed temperature of $100K$. Approximately 45% of the mass is in the hot phase, 40% in the disk and 15% in the cold molecular clouds.

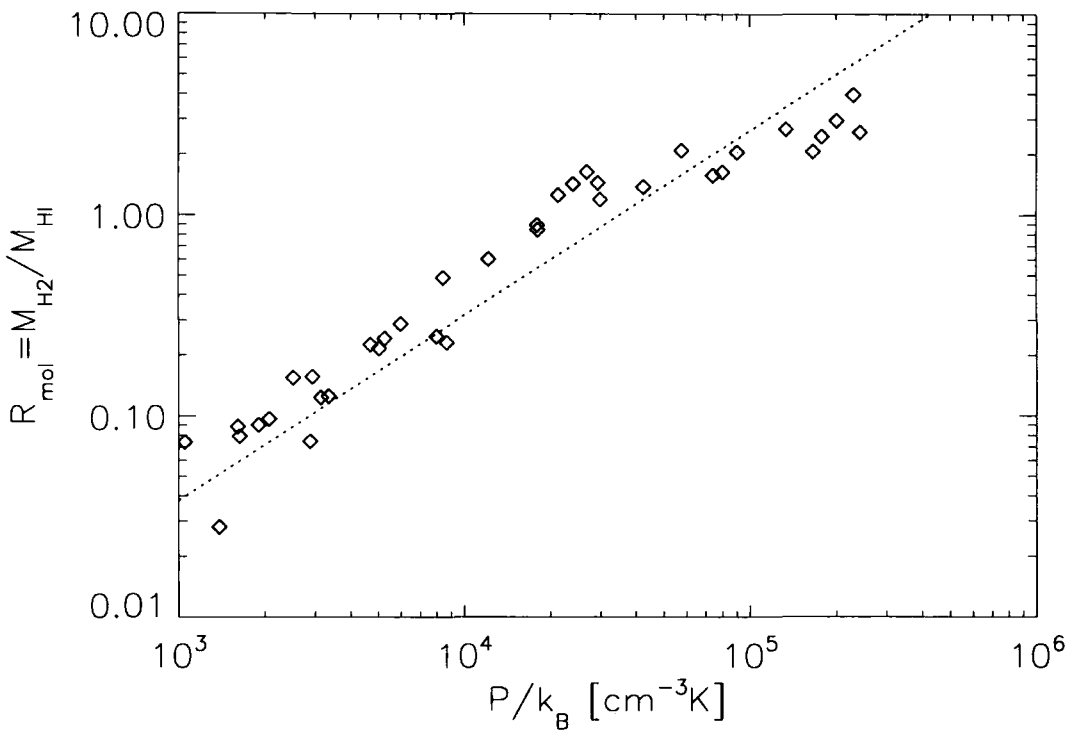

Figure 4.12: The relation between the pressure in the midplane of the galactic disk and the proportion of the gas in the molecular phase, R_{mol}. The dotted line represents the observational result (Eq (4.1))due to Blitz & Rosolowsky (2006). The simulated galaxy is in good agreement with observation.

again behave in very similar ways. Fig (4.9) shows the radial density profile of stellar mass, demonstrating that our star formation prescription gives rise to an exponential disk and a bulge component well fitted by the standard $r^{1/4}$ law.

The rotating collapse simulations are especially interesting because they start far from equilibrium and so features that arise in the final particle distribution are purely an effect of the physics in the simulation and not just set up by hand in the initial conditions. Fig (4.10) shows how the molecular fraction (the ratio of the mass in molecular hydrogen to the mass in atomic hydrogen) varies as a function of distance from the centre. Observational data from M31 (Dame et al. (1993)) is included as a comparison.

The evolution of the thermal properties of the halo are shown in Fig (4.11). In its initial state all the gas in the halo is cold. As the halo collapses it becomes dense and is shock heated. The gas that ends up in the disk comes to an equilibrium between radiative cooling and the heating due to SNe at approximately $10^4 K$ and a halo of hot, SN heated gas at $\sim 10^6 K$ is gradually formed. The addition of the molecular gas ($T \sim$ 100K, $\rho \sim 100-1000\mathrm{cm}^{-3}$) forms an ISM with four phases: shocked halo gas, SNe heated material, cold molecular clouds and warm disk gas. The first two components are hard to distinguish on the $\rho - T$ plot.

Blitz et al. (2006) have argued that the ratio of molecular to atomic gas in galaxies, R_{mol}, is determined by hydrostatic pressure and through observations of nearby galaxies found the following relation:

$$R_{\mathrm{mol}} = \left[\frac{P_{\mathrm{ext}}/k_B}{(3.5 \pm 0.6) \times 10^4}\right]^{0.92\pm0.07}, \tag{4.1}$$

where P_{ext} is an estimate of the mid-plane pressure. R_{mol} is the ratio of mass in the atomic and molecular phases. Fig (4.12) shows the data for the ROT_BASE simulation after 1 Gyr alongside the observed best fit line (Eq (4.1)). We use the SPH estimate of the pressure at $z = 0$. To calculate R_{mol} we use all matter within a vertical distance of 1kpc from the centre of mass of the disk and bin radially. The model of the ISM clearly reproduces the observed behaviour.

4.4 Away From the Base Model

The determination of some of the physical parameters used in our model is somewhat uncertain. In this section we investigate the effect of varying some of the physics included in the models. Large uncertainties are present in the determination of some of the

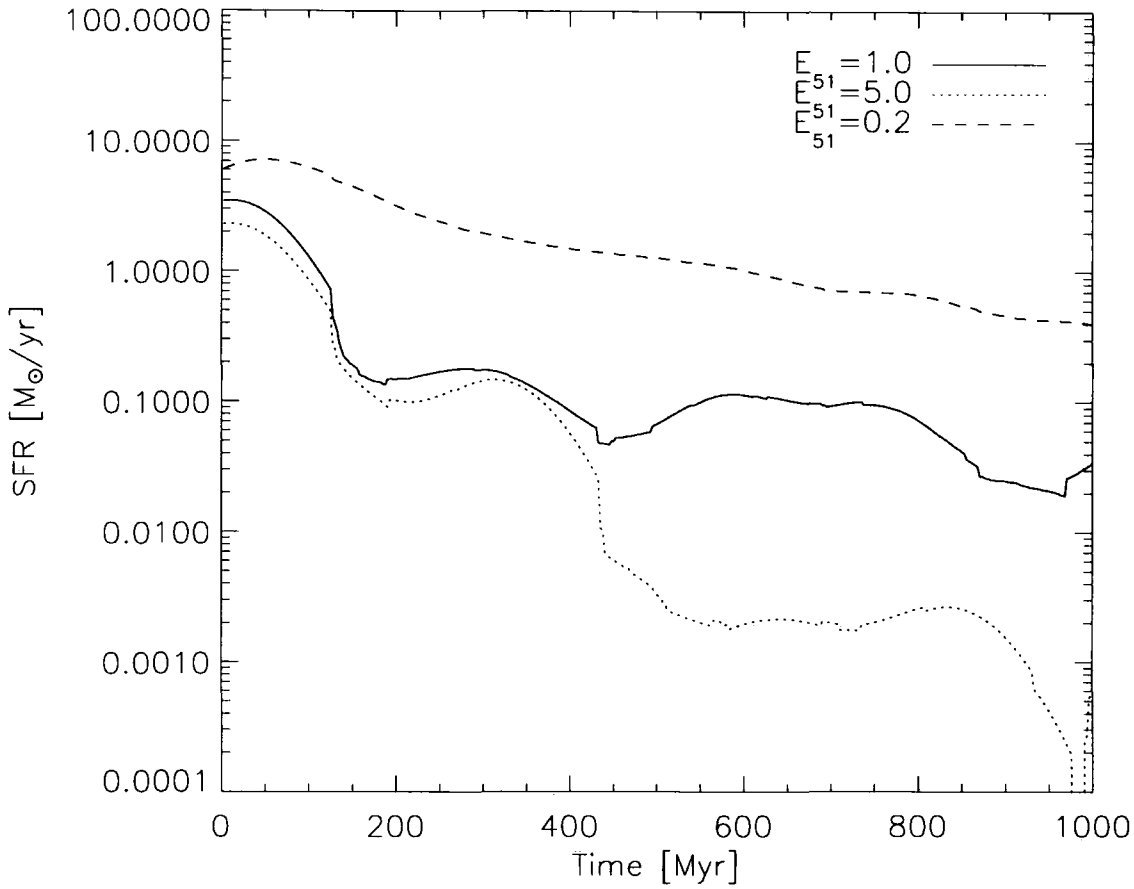

Figure 4.13: The star formation rates in the simulated disks for different values of E_{51}. Higher values of E_{51} effectively quench the star formation by heating and ejecting the ambient gas from the stellar disk.

parameters including E_{51}, the thermal conduction efficiency, and the physics we include in our treatment of supernova explosions. In addition our simulations do not contain a detailed treatment of metals. We demonstrate the effects of changing these parameters on the large scale properties of simulated galaxies.

4.4.1 Supernova Physics

In this section we investigate the effect of changing the parameters that govern the behaviour of supernova remnants. The value of E_{51} is poorly constrained by observation and may differ greatly from unity, for example due to radiative cooling of the supernova remnant. We investigate the effect of moving E_{51} away from unity and also look at changing the physics included in our analytic model for blast wave evolution, firstly

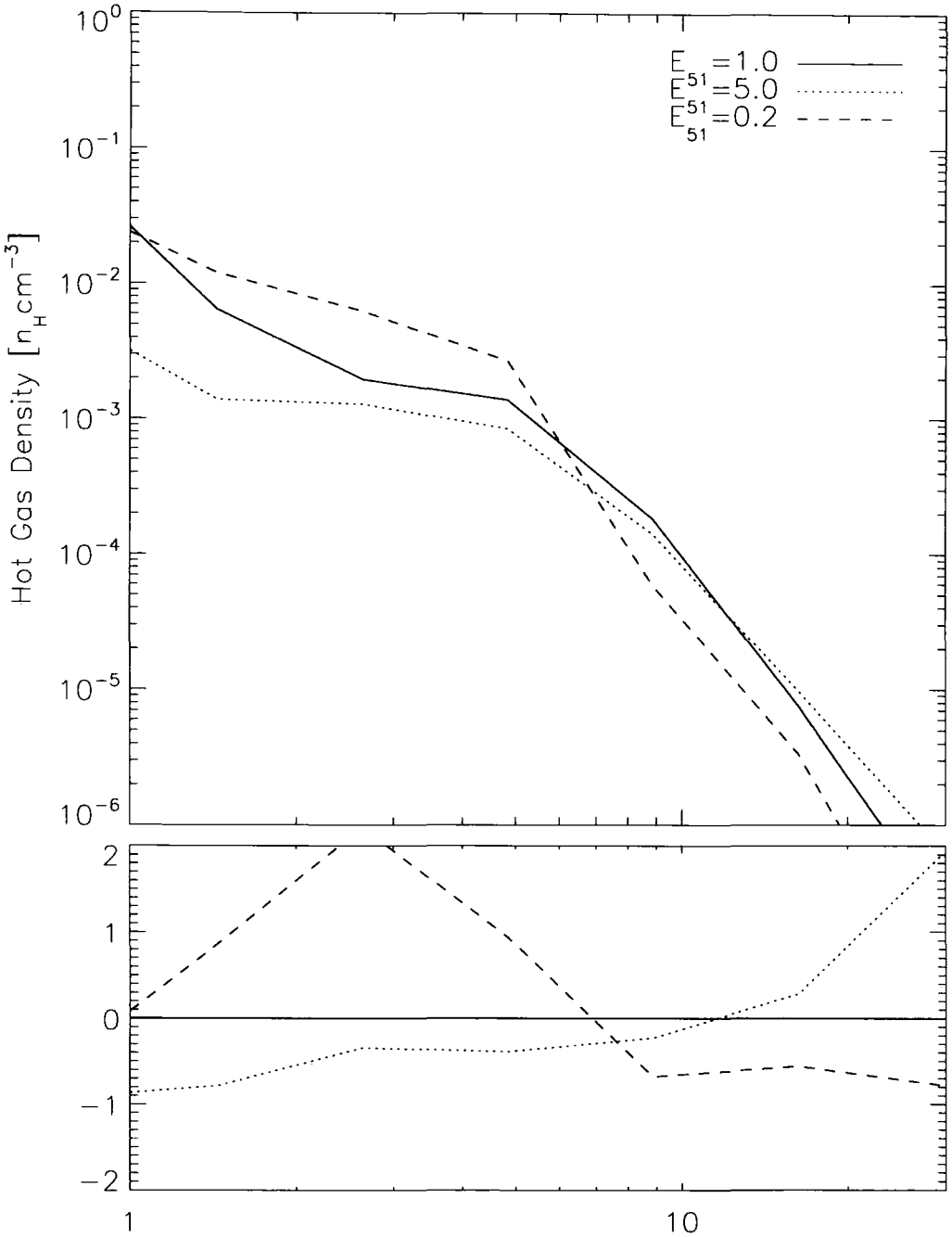

Figure 4.14: The ambient gas density profile in the simulated disks for three different values of E_{51}. The simulations with lower supernova efficiencies lead to more concentrated gas disks.

by extending the simple Sedov solution with the fitting formula due to Tang and Wang (2005) and secondly by investigating the effects of preventing radiative cooling in supernova remnants.

Altering the value of E_{51} has, as expected, two main effects. Firstly an increased supernova efficiency can eject gas from the galactic disk more efficiently and quenches star formation very quickly (fig 4.13). Secondly, the gas disk in simulations with higher supernova efficiency is found to be less concentrated (figure 4.14)

More accurate modelling of the evolution of supernova blast waves (by using the Tang and Wang (2005) fit to the blast wave evolution) does not significantly change the properties of the galaxy. Assuming that a typical supernova remnant expands for approximately $\sim$0.3 Myr before being dispersed, that the mean ambient temperature of the ISM is 10^6 K and the mean density is 10^{-2} atoms per cm^3 then the difference in the blast wave radius between the pure Sedov solution (3.38) and the modified fitting formula due to Tang and Wang (2005) (Eq (3.39)) is never more than 20%. This is demonstrated in Fig 3.3, which shows a pure Sedov blast wave compared with the simulated result from an SPH simulation of a blast wave in a hot ($10^6 K$) medium.

The net result of having larger blastwaves is that the porosity of the ISM increases at a greater rate and the delay between a supernova explosion occuring and its thermal energy being injected into the ambient medium is decreased.

Finally we can switch off the radiative cooling in supernova remnants. The effects here are much more dramatic. In the dense galactic disk a supernova remnant can typically radiate away over 90% of its thermal energy before being disrupted. Switching off radiative cooling in supernova remnants, therefore, has a very severe effect in our galaxy simulations, and leads to the almost immediate suppression of star formation and much of the material in the galactic disk is ejected from the galaxy. This demonstrates that radiative losses from supernova remnants are of crucial importance in our models.

4.4.2 The Effects of Metals

Our simulation code does not contain a detailed description of mass feedback from supernovae, therefore we need to verify that the expected evolution in metallicity over the timescale of the simulation will not substantially affect the properties of the galactic disk.

Following Harfst et al. (2006) we use a simple analytic model to estimate the change in metallicity over the timescale of a typical simulation then run simulations with metallicites bracketing this range. By assuming that stars form at a constant rate of $1 M_\odot$/yr,

that there is one type 2 supernova event per $125M_{\odot}$ of stars formed, and using metal yields due to Woosley and Weaver (1995) we estimate that over the 1Gyr timespan of one of the quiescent disk simulations the average metallicity of the galaxy should not change by more than $0.04Z_{\odot}$.

The base simulations have a metallicity of $1.0Z_{\odot}$, an additional two disk simulations were run with metallicities of $0.5Z_{\odot}$ and $1.5Z_{\odot}$, far outside the metallicity evolution range expected in our quiescent disks. The total amount of stars after 1Gyr in the high metallicity run is 5% higher than in the base run. The low metallicity run contains approximately 5% less stars than the base run. This trend arises because the radiative cooling rate of the ambient phase is related to the ambient gas metallicity. All the properties of the three simulated disks agree to within 10% with the properties of the base simulations.

However, as noted by Harfst et al. (2006) a detailed prescription for the yields from supernovae is necessary if we want to simulate the early evolution of a galaxy.

4.4.3 Thermal Conduction

One of the most poorly constrained parameters is the efficiency of evaporation of molecular clouds through thermal conduction. Magnetic fields and turbulence may affect the amount of thermal conduction by a large amount (MO77). We ran quiescent disk simulations with the efficiency of thermal conduction moved by a factor of five in each direction. The effects of varying thermal conduction on the cloud mass function can be seen in figure 4.15. More efficient thermal conduction leads to a lower density of molecular clouds in the galactic disk, as well as making the cloud mass function more shallow. The star formation rates are affected by a similar amount, in the simulations with a high thermal conduction rate the star formation rate is depressed by a large factor. As discussed in section 4.3 the base value for the thermal conduction efficiency reproduces many of the observed properties of the MW.

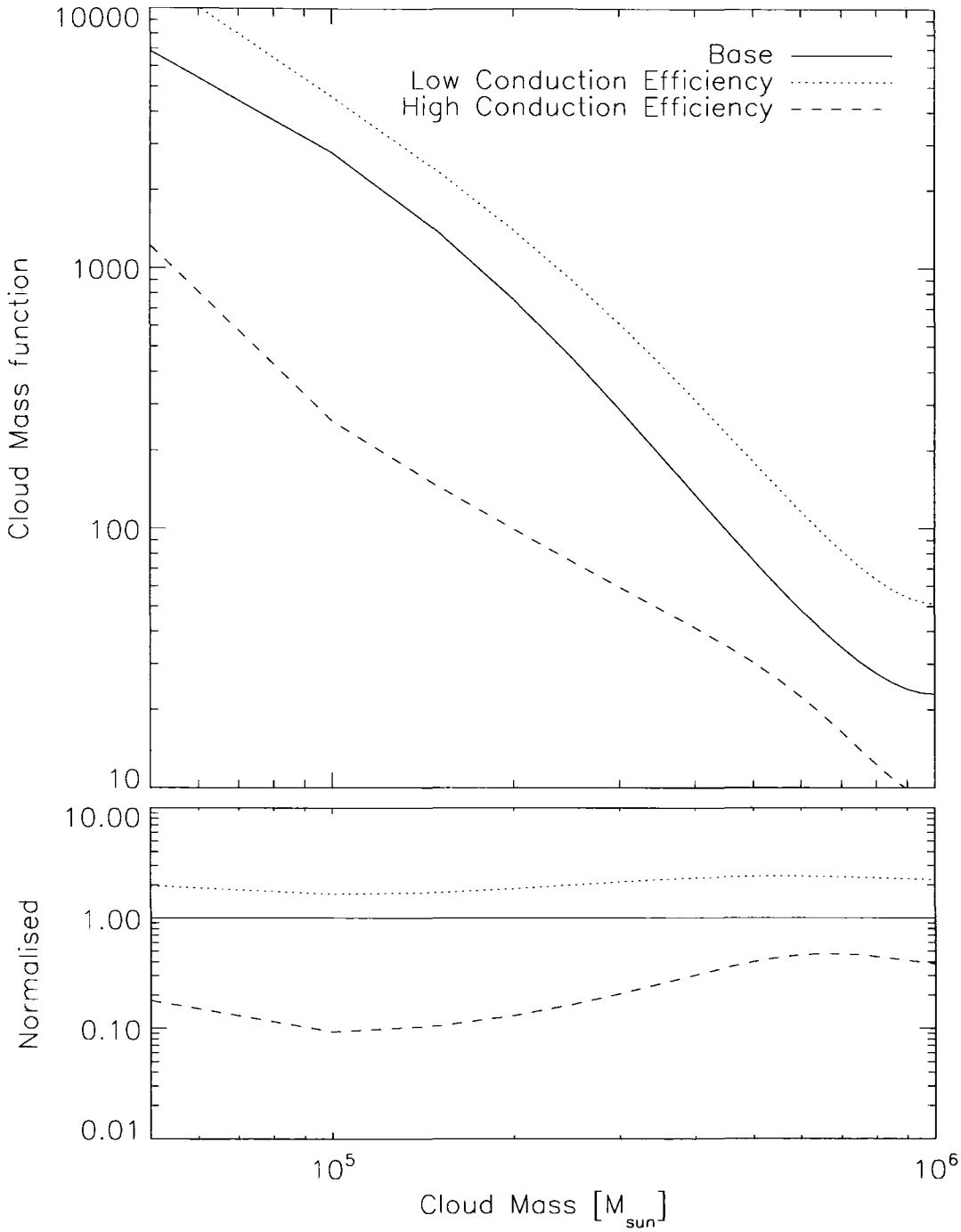

Figure 4.15: The effect of thermal conduction efficiency on the cloud mass spectrum of simulated galaxies. The upper plot shows the cloud mass functions for each galaxy, the lower plot shows the mass functions normalised to that of the base simulation. Higher thermal conduction efficiency leads to a lower density of molecular clouds and also a shallower molecular cloud mass function

Chapter 5

Simulating Galaxy-Galaxy Interactions

5.1 Introduction

Mergers and other gravitational interactions between galaxies are an essential part of hierarchical galaxy formation scenarios (White and Rees (1978)). Mergers can have a dramatic effect on the structure of galaxies. It was first noted by Toomre (1977) that galaxy collisions can drive the evolution of galaxy types by transforming disk galaxies into elliptical galaxies. Additionally galaxy mergers are thought to explain the extremely high levels of star formation seen in high redshift ultra-luminous infrared galaxies (e.g. Sanders et al. (1988))

In this chapter we present simulations of interacting disk galaxies. In section 5.2 we discuss the initial conditions of the simulations. In section 5.3 we introduce the specific simulations that were run and in sections 5.4 and 5.5 we analyse the interacting galaxies in terms of the structure of the tidal tails, and the properties and structure of the resulting remnant. Additionally these simulations provide an ideal way of testing the performance of the sticky particle star formation and feedback model in a more dynamic situation than the isolated galaxies discussed in previous chapters.

We conclude this chapter by simulating the formation of a disk galaxy in a fully cosmological setting.

5.2 Initial Conditions

The most favourable conditions for the creation of tidal tails are interactions in which the angular momentum vectors of the individual galactic disks (spin angular momentum)

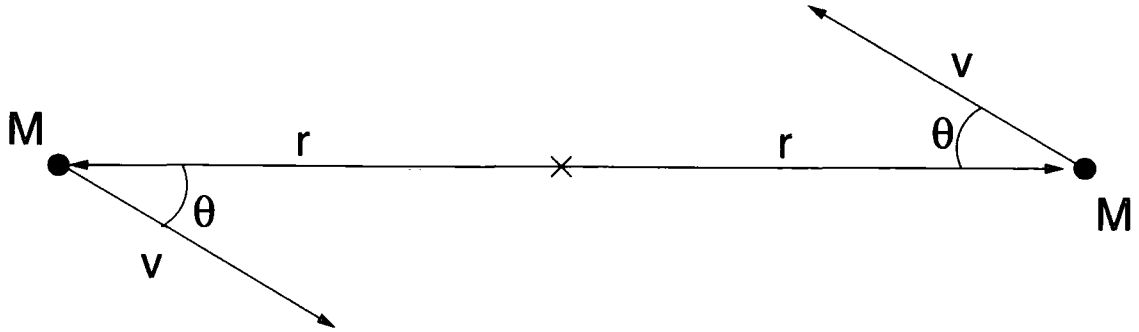

Figure 5.1: Geometry used in the galaxy collision simulations. The circles represent the initial locations of the galaxies. They are separated by an amount $2r$, moving with a velocity v and each has mass M.

are aligned with the angular momentum vector of the orbit (orbital angular momentum) of the galaxies around each other (Springel and White (1999)). Since here we are trying to form prominent tidal tails we usually set up the disk-disk collisions on these types of orbits. The properties of the individual disks are as described in section 4.2.1. The geometry of the initial conditions is described in figure 5.1. We need to specify five numbers to completely define a set of initial conditions: $2r$, the separation between the two disks; 2θ the angle between their velocity vectors; $|v|$, the magnitude of the relative velocities; ψ, the angle between the spin vectors of the two galaxies and M, the mass of each galaxy.

The initial separation of the disks is always set to twice the virial radius of their respective dark matter haloes ($r = r_v$). The magnitude of the velocity is set such that the interaction is 'parabolic' (the total energy of the system is 0). θ is set by considering the 'circularity' of the interaction, which is defined as (Lacey and Cole (1993))

$$\epsilon = \frac{J}{J_c(E)}, \tag{5.1}$$

where J is the orbital angular momentum of the galaxies and $J_c(E)$ is the orbital angular momentum of a circular orbit with the same energy, E. Radial orbits have $\epsilon = 0$ and circular orbits have $\epsilon = 1$. Typical galaxy-galaxy interactions have a circularity of ~ 0.5 (Tormen (1997)). For the collision geometry described above, the circularity of the orbit is given by

$$\epsilon = \sin\theta\,. \tag{5.2}$$

5.3 Simulations

The galaxy collision simulations we ran fall into two main groups; those that are designed to allow us to probe the properties of tidal tails and those that are designed to form an elliptical galaxy to allow us to investigate the properties of the resulting remnant. In all simulations the two galaxies start off separated by 200 kpc, simulations were run with circularities of 0.0,0.2 and 0.5. Initial conditions were set up as described in the previous section.

An additional simulation was run with initial conditions that approximate the interaction between the MW and M31. In this case, properties of the initial conditions are set via observation as possible. The ratio of the galaxy masses is somewhat uncertain and has been estimated as 1:0.7 (Dunn and Laflamme (1993)), 1:0.625 (Klypin et al. (2002)) and 1.25:1 (Seigar et al. (2006)). Due to this uncertainty we assume in our simulations that the galaxies are of equal mass. The initial separation between the galaxies is 780kpc (Holland (1998)) and their initial relative radial velocity is 123 km/s (Dunn and Laflamme (1993)). The galactic latitude of M31 is -21.57 degrees[1], and its disk is tilted at an angle of 77.5 degrees to our line of sight (Schmidt (1957); Ma et al. (1997)). The tangential velocity of the Andromeda galaxy relative to the MW is hard to constrain via observation. It has long been suspected that this tangential velocity must be small, given that there is no other large galaxy in the local group to impart much angular momentum to the M31-Milky Way system (Kahn and Woltjer (1959)). Under the assumption that the Milky Way and M31 have equal but opposite angular momenta Einasto and Lynden-Bell (1982) estimated that the tangential velocity of M31 is 60 ± 30km/s. This is in agreement with studies using the 'least action principle' (Peebles (1989, 1990)). The least action principle assumes that each galaxy can be treated as a point particle and then setting two boundary conditions. Firstly at early times the peculiar velocities of all galaxies are small and secondly that at late times the position of each galaxy is known. It is possible to numerically iterate over trial orbits until we find the one that minimises the 'action' of the system. Recent least action principle studies of the local group suggest that the transverse velocity of M31 is less than 100km/s (Peebles et al. (2001)). We therefore use a value of 60km/s for the transverse velocity of M31.

[1] via NED

5.4 Star Formation in Tidal Tails

Tidal tails are produced during galaxy collisions from the effects of gravitational tides and galactic rotation (Toomre and Toomre (1972)). Tails may be ejected over 100kpc from the merger remnant, and some fraction may become completely unbound from the rest of the system. Evidence for strong star formation in tidal arms comes from the fact that they are often blue (Schombert et al. (1990)), in some tidal features it is possible to detect $H\alpha$ and UV (Neff et al. (2005)) emission, also indicative of strong star formation. The inferred ages of stars forming in tidal arms is much less than the dynamical timescales on which the tidal arms are evolving and so it may be assumed that the stars are forming in the tidal arms themselves (Knierman et al. (2003)). It has been predicted (Barnes and Hernquist (1992); Mihos and Hernquist (1994a)) that the collapse of gas in tidal arms could lead to the formation of 'tidal dwarf galaxies', this has been borne out by observations of star forming clumps in the tidal arms of various interacting galaxies, which are found to have masses in the range $10^{8.3} - 10^{9.8} M_{\odot}$ (Duc and Mirabel (1998)), consistent with the masses of observed dwarf galaxies.

Figures 5.2 and 5.3 show the locations of particles in the stellar disk of the galaxy and the resulting projected temperature structure of the Milky Way/M31 interacting galaxy simulation. The formation of strong tidal features is evident. Gas within the tidal arms cools to $\sim 10^4$K, HII regions due to gas heating by supernovae are also evident. At late times the merger remnant contains very little cold gas, in common with elliptical galaxies observed in the local universe (see next section).

It is hard to objectively quantify either the mass or the extent of tidal arms during an interaction. We follow Springel and White (1999) by using the tidal response, T, defined here as the fraction of the mass of a disk that reaches a distance of more than $3R_D$ from its centre of mass, where R_d is the unperturbed initial truncation radius of the disk. Figure 5.5 shows the evolution of the tidal response of three galaxy interaction simulations as a function of time. There is a clear correlation between the height of the peak in the tidal response and the initial circularity of the orbit, in agreement with the results of Springel and White (1999), suggesting that in order to probe the properties of tidal tails we should be colliding galaxies on nearly circular orbits.

Since stars form from molecular gas, an understanding of the physical properties and kinematics of the molecular phase in tidal arms is very important in the study of the formation of tidal dwarf galaxies. Figure 5.6 shows contours of molecular gas density

on top of a greyscale representation of the atomic gas density in an interacting galaxy pair. The contours of molecular gas density are chosen to match those used by Wilson et al. (2000) in their high-resolution images of molecular gas in the antennae galaxies. In common with Wilson et al. (2000) we find strong peaks in the molecular gas density coincident with the nuclei of each galaxy. Molecular gas is also present in the tidal features around the galaxy and in the region between the two nuclei, which in the case of the antennae galaxies has been named the 'overlap region' Stanford et al. (1990). It has long been known (van der Hulst (1979) that the majority ($> 60\%$) of the molecular gas in typical mergers is found in the tidal arm structures. Our simulations reproduce this, with 62% of the molecular gas being situated further than $3R_d$ from the centre of mass of either of the disks.

In this section we have investigated some of the basic properties of tidal arms and found that our statistical model reproduces very well many of their observed features. It remains as future work (see chapter 6) to apply our model to simulations designed to match the properties of real galaxy mergers.

5.5 Merger Remnants

In this section we compare the properties of the merger remnants left over from the merger of two equal mass disks, the initial configuration of this simulation is as described in the MW/M31 interaction. Results are compared both to other simulations and, where possible, to observational data from local elliptical galaxies.

The total amount of molecular gas in the remnant is $\sim 10^8 M_\odot$, this is in good agreement with observational studies of local early type galaxies (see e.g. Faber et al. (1997))

Previous galaxy merger simulations by Barnes (1992) have concentrated on the kinematics and orbital structure of the resulting galaxy. We find in common with these simulations that the radial density profile of the stellar material in the remnant is well fit by a broken power law with indices -2 toward the interior of the galaxy and -4 towards the outskirts (figure 5.7). The projected brightness profile of the galaxy is well described by the standard de Vaucouleurs law

$$\Sigma(r) = \Sigma_0 e^{[-(r/r_e)^{0.25}-1]}, \tag{5.3}$$

where $\Sigma(r)$ is a surface brightness and the two parameters that control the fit are Σ_0, the central brightness and r_e the effective radius of the galaxy. Magnitudes were calcu-

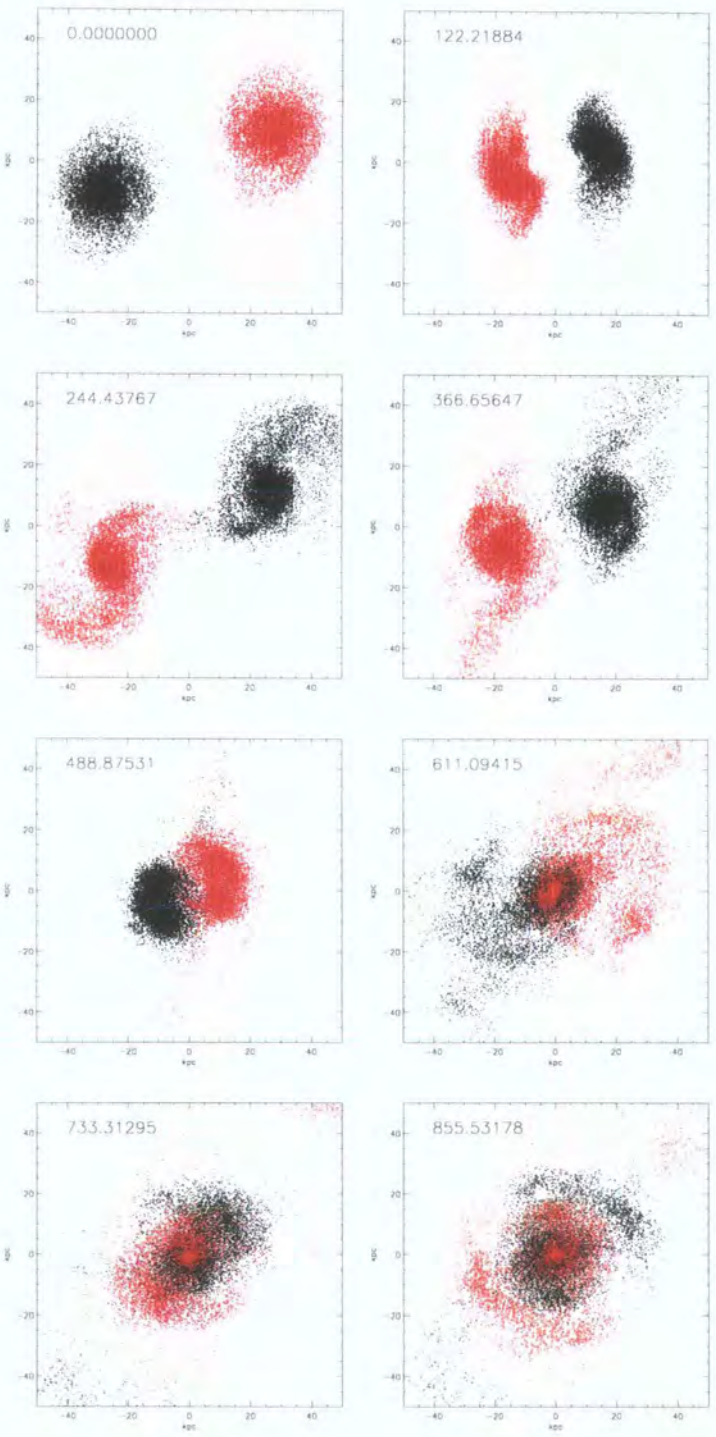

Figure 5.2: Time series showing the location of a random 10% of the particles in the old stellar disk of the galaxies. The numbers represent times in units of Myr

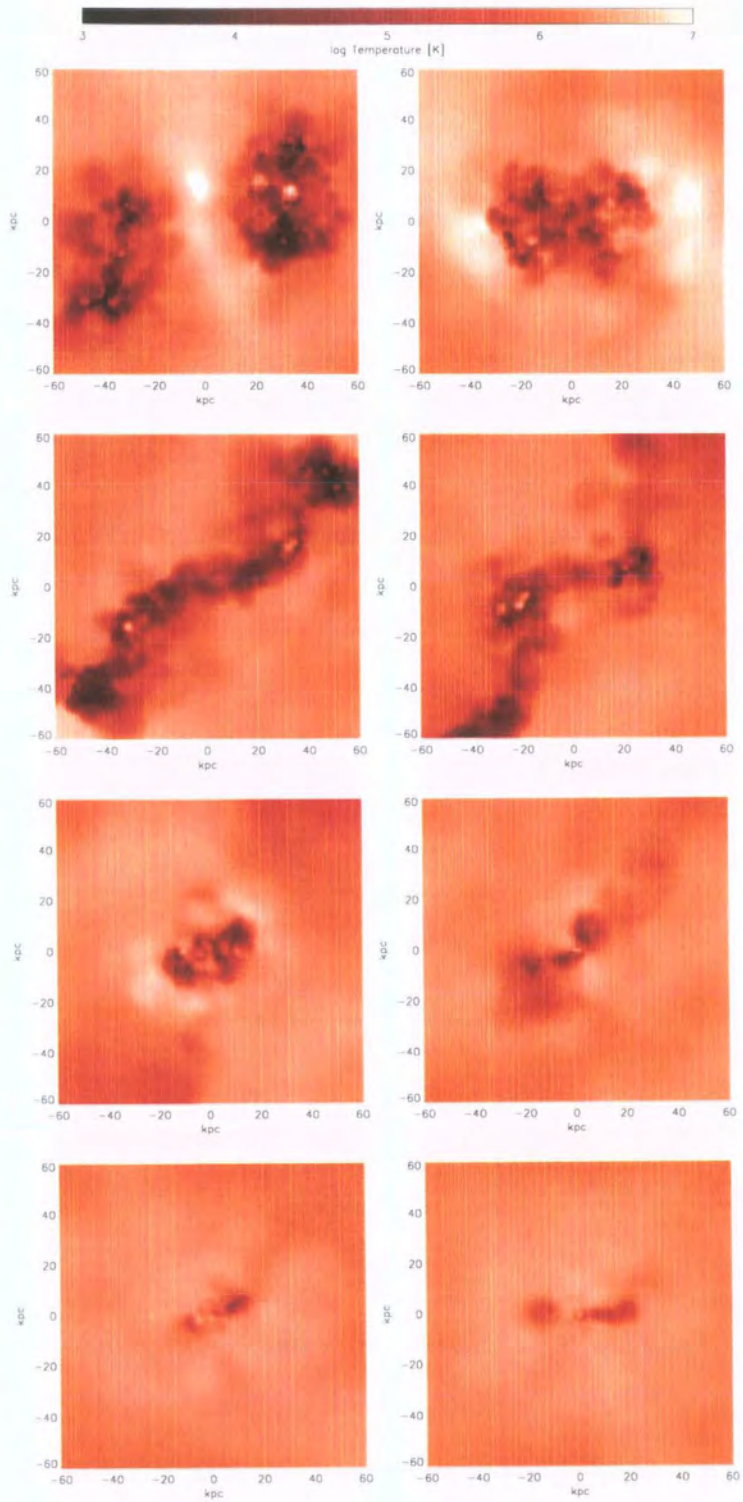

Figure 5.3: Projected mean temperature maps through the merging galaxy. Gas associated with the galaxy is dense enough to allow it to cool to temperatures of $\sim 10^4$K. The times of these snapshots match with those in the previous figure

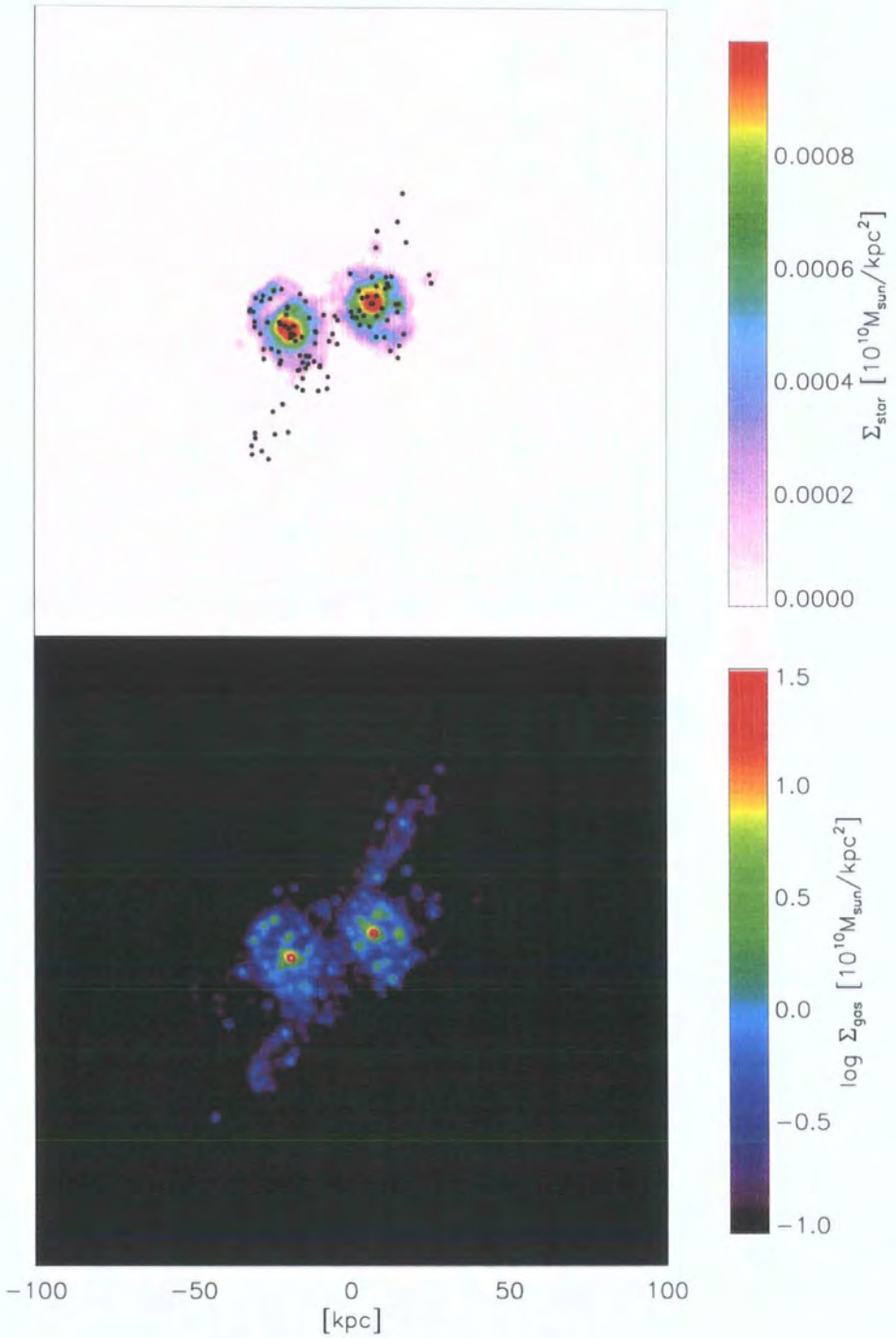

Figure 5.4: Snapshot of interacting galaxies. The upper panel shows contours of stellar density, including all stars. The black points represent sites of star formation within the last 10Myr. It is clear that star formation is occurring in the tidal arms of the galaxy. The lower plot shows the density of gas in the simulation.

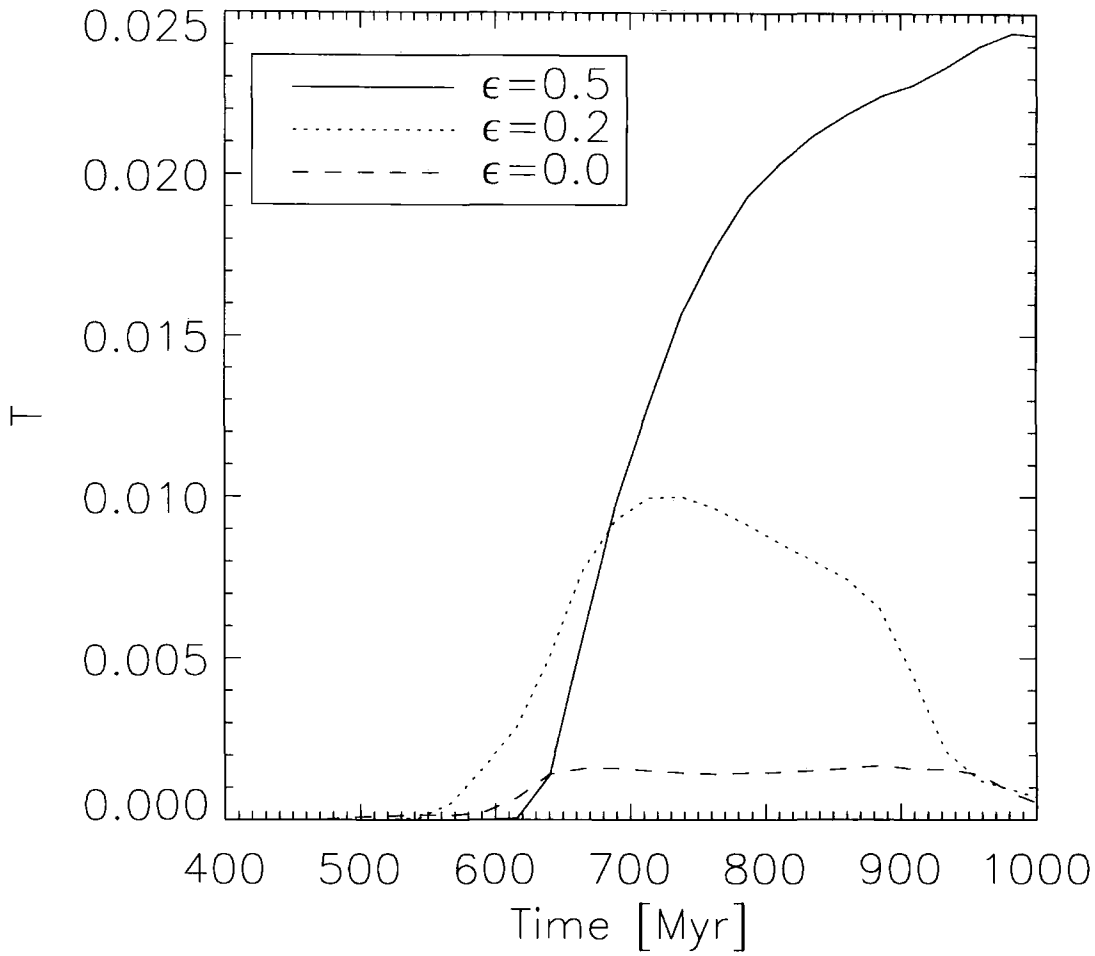

Figure 5.5: The tidal response of the three galaxy collision simulations. The tidal response is defined at the fraction of the mass of a disk that moves to a distance $> 3R_d$ from its centre of mass. There is a clear correlation between the tidal response of a collision and the circularity of the initial orbits.

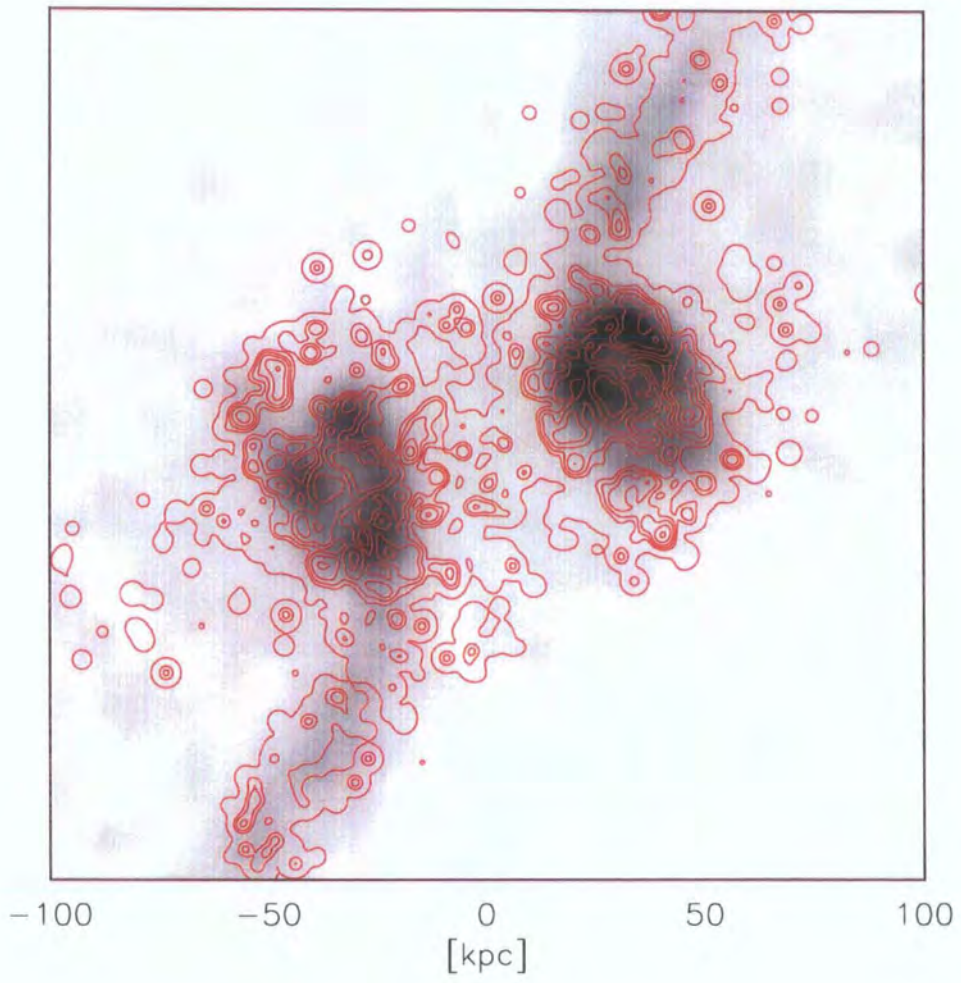

Figure 5.6: The distribution of molecular gas in the interacting galaxy pair. The greyscale image represents the density of atomic hydrogen in the galaxy. The contours show the density of molecular gas. Contours are chosen to match the plots of Wilson et al (2000) and represent 6%, 9.5%, 15%, 23%, 37% and 57% of the peak intensity.

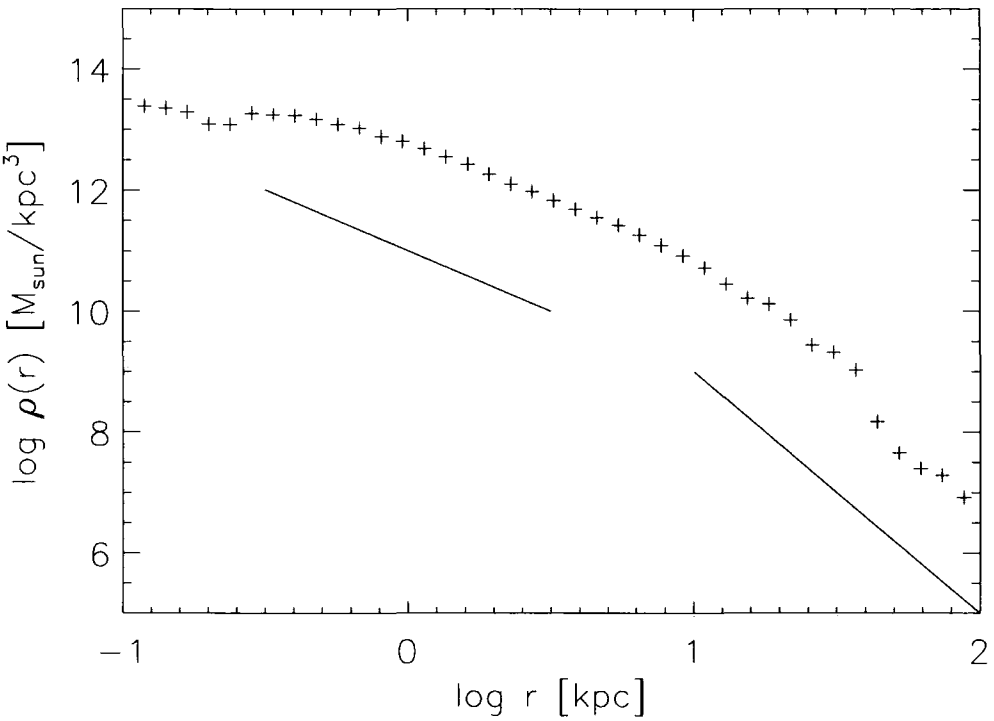

Figure 5.7: The radial stellar density profile of the merger remnant. The diagonal lines are power laws with indices -2 and -4, as observed in the simulations of Barnes (1992)

lated crudely from stellar masses by assuming that the flux from any given particle is proportional to its mass, then calculating the magnitude from $m = -2.5\log(flux)$. This approximation is very crude and it remains as future work (see chapter 6) to include stellar population synthesis models (e.g. Bruzual and Charlot (1993)) in our code in order to provide more accurate observational constraints on the stellar features of our galaxy.

X-ray studies of local early-type galaxies have found evidence for hot gas haloes (see e.g. Forman et al. (1985)) around early type galaxies. The X-ray surface brightness profile was found to closely follow the optical image (Trinchieri et al. (1986)) although closer inspection revealed that the X-ray spectrum consists of both a hard and soft component. The hard X-ray component of the luminosity is found to be proportional to the blue band luminosity of the galaxy (Trinchieri et al. (1986)), suggesting that the origin of this component is due to low-mass X-ray binary stars. The soft component of the X-ray spectrum can be explained in terms of thermal Bremsstrahlung emission from hot gas (Fabbiano et al. (1994)) and as such can be used as a probe of the temperature structure

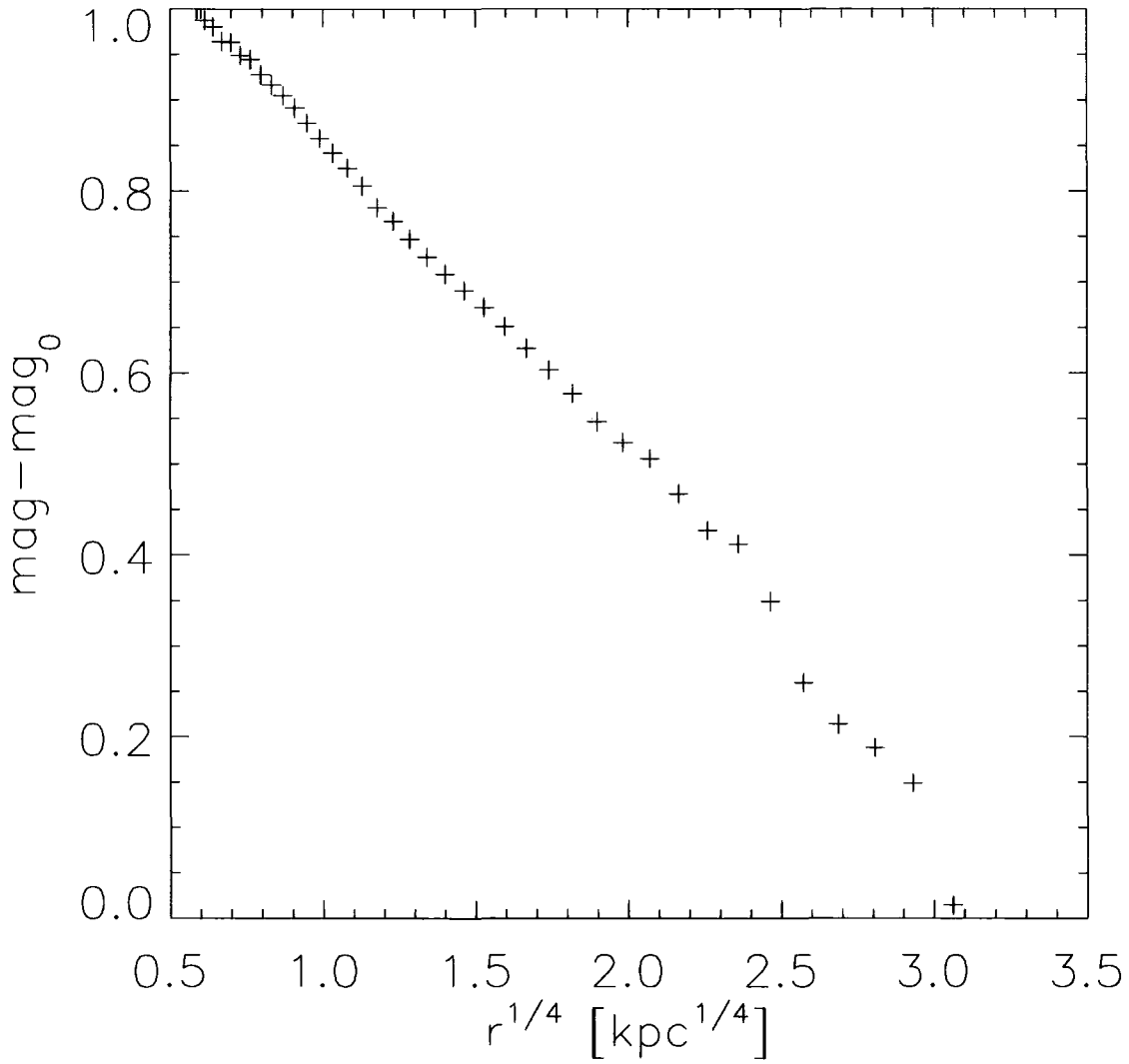

Figure 5.8: Projected surface brightness profile of the merger remnant. Magnitudes were calculated from stellar masses by assuming that the flux from any given particle is proportional to its mass, then calculating the magnitude from $m = -2.5 \log(flux)$.

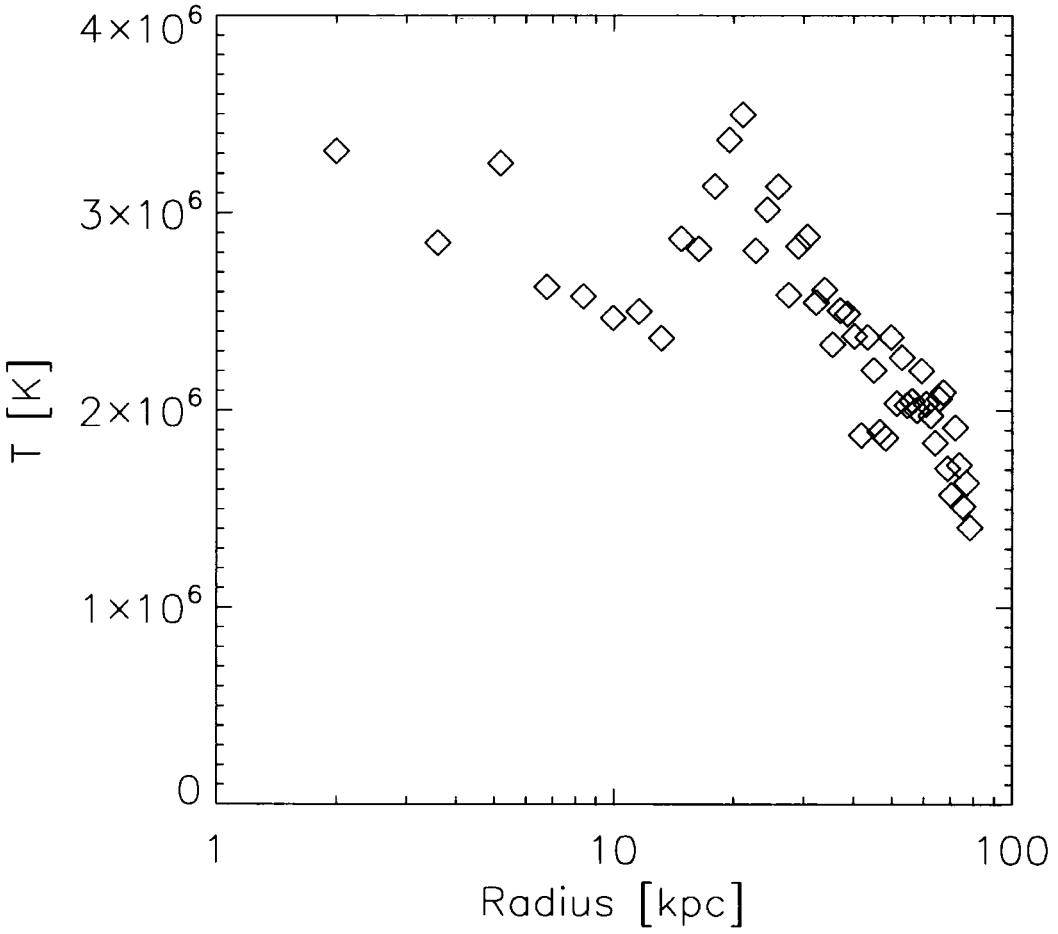

Figure 5.9: Three dimensional temperature profile of the merger remnant, we find a negative temperature gradient in the halo. This is in agreement of recent X-ray observations of local early type galaxies, which have found that in haloes with masses less than $10^{13} M_{\odot}$ there is a negative temperature gradient

of the hot phase of the ISM

Figure 5.9 shows the three dimensional temperature profile of the resulting elliptical galaxy. We find a shallow negative gradient to the temperature profile. This result is in agreement with the observations of Humphrey et al. (2006) (see also Randall et al. (2006); Khosroshahi et al. (2004)), who found that galaxies with halo masses $< 10^{13} M_{\odot}$ tended to have negative temperature profiles

In this chapter we have examined some of the properties of interacting galaxies, we find that we create realistic tidal features and that the resulting merger remnant has many properties in common both with other simulations and the observed properties of early type galaxies in the local universe. These features include density and brightness profiles, the temperature gradient in the galaxy and the appearance of strong bursts of star formation in tidal structures.

5.6 The ISM in a Cosmological Setting

Galaxies do not evolve in isolation and the effects of the surrounding intergalactic medium and mergers with other galaxies play important roles in shaping the properties of the galaxies we observe today. It is therefore important to be able to understand how galaxies form in a fully self consistent cosmological context. As a final test of the code we therefore attempt to simulate a MW-like galaxy picked from a cosmological volume.

In order to facilitate a comparison of our results with those obtained using different codes we use the initial conditions first developed by Okamoto et al. (2005). These initial conditions represent the formation of a single high resolution halo in a volume of 35.325 Mpc/h. The cosmology used is $\Omega_0 = 0.3$, $\Omega_\Lambda = 0.7$, $\sigma_8 = 0.9$, $h_{100} = 0.7$. The gravitational softening for the high resolution parts of this simulation is $\epsilon = 1.4$ kpc.The numerical parameters governing the behaviour of the sticky particle model are exactly the same as those used in the earlier simulations of both isolated and interacting galaxies.

5.6.1 Results

Figure 5.10 shows the projected density of each phase of the ISM at redshift zero. Both the molecular and atomic phases of the ISM are confined to a thin ($\sim$ 1 kpc) disk, whereas the stellar disk has a significantly larger scale height. The radial density profile of the ambient and molecular ISM phases are shown in figure 5.11. It is clear that at the centre of the galaxy the ISM is primarily molecular, and at the outskirts it is almost entirely atomic, qualititatively the shapes of the two density profiles match well with those found in the local universe (e.g. Dame et al. (1993); Binney and Merrifield (1998)). This finding is consistent with the results found in chapter 4 for an isolated model halo, and provides confirmation that our approach towards modeling can provide insight into the properties of the molecular ISM in low redshift galaxies. The molecular fraction in the galaxy ($N(H_2)/(N(H_2) + N(HI))$) as a function of radius also agrees well with that observed

in the local universe (for comparison see figure 4.10).

Figure 5.13 shows the radial density profile of the stellar component of the galaxy. This distribution is well fitted by a Vaucouleurs law, representing a bulge component

$$\Sigma(r) = \Sigma_{0,b} e^{[-(r/r_b)^{0.25}-1]}, \tag{5.4}$$

and an exponential disk

$$\Sigma(r) = \Sigma_{0,d} e^{-(r/r_d)}. \tag{5.5}$$

We find that the values of the scale lengths, r_b and r_d, needed to describe the simulated galaxy are $r_d = 4$kpc, the bulge component has a scale length of $r_b = 0.8$kpc.

Finally the same halo was simulated using different star formation and feedback prescriptions, including the code from Okamoto et al. (2005) and the Gimic code[2], which has been developed to perform large scale simulations of galaxy formation. Comparing the star formation histories of the galaxies generated with each code (figure 5.14) we find that the total mass in stars is very similar between the sticky particle simulation and the run using the Gimic code, differing only by $\sim$ 10% at redshift zero. The Okamoto et al. (2005) code forms more stars by a factor of two. However, we note that at high redshift the sticky particle code forms significantly more stars than the other codes. This is due to its crude treatment of metal production, more specifically the assumption that the metallicity is constant and equal to the solar value at all redshifts. This leads to radiative cooling rates for the gas that are orders of magnitude larger than those for zero metallicity gas and results in an efficient and early collapse of much material.

In this section we have demonstrated that the sticky particle star formation model does a good job of reproducing many of the observed properties of galaxies in the low redshift universe, including: The density profiles of all of the phases of matter, star formation rates over the entire lifetime of the galaxy and the molecular fraction of the galaxy as a function of radius. Possible future directions in which this work may be taken are described in chapter 6.

[2]We thank our colleagues J. Schaye, C. Dalla Veccia and R. Wiersma for allowing us the use of this code, and R. Crain for performing this simulation

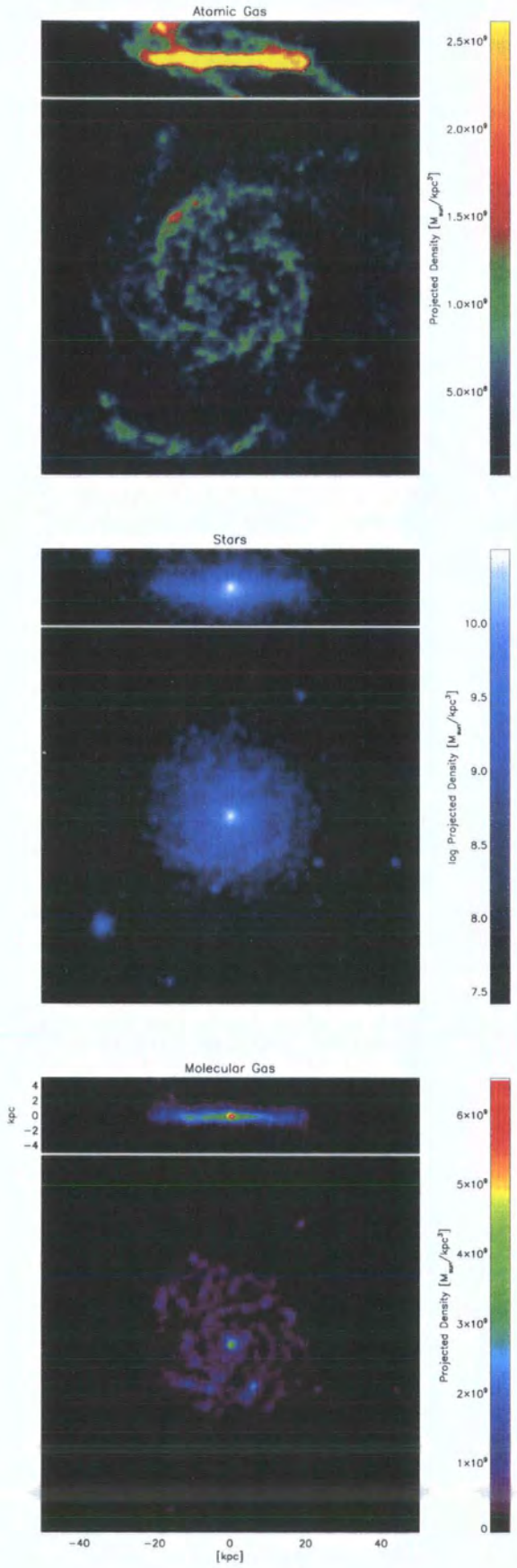

Figure 5.10: Projected density through the redshift zero galactic disk for each of the three baryonic components included in our simulations

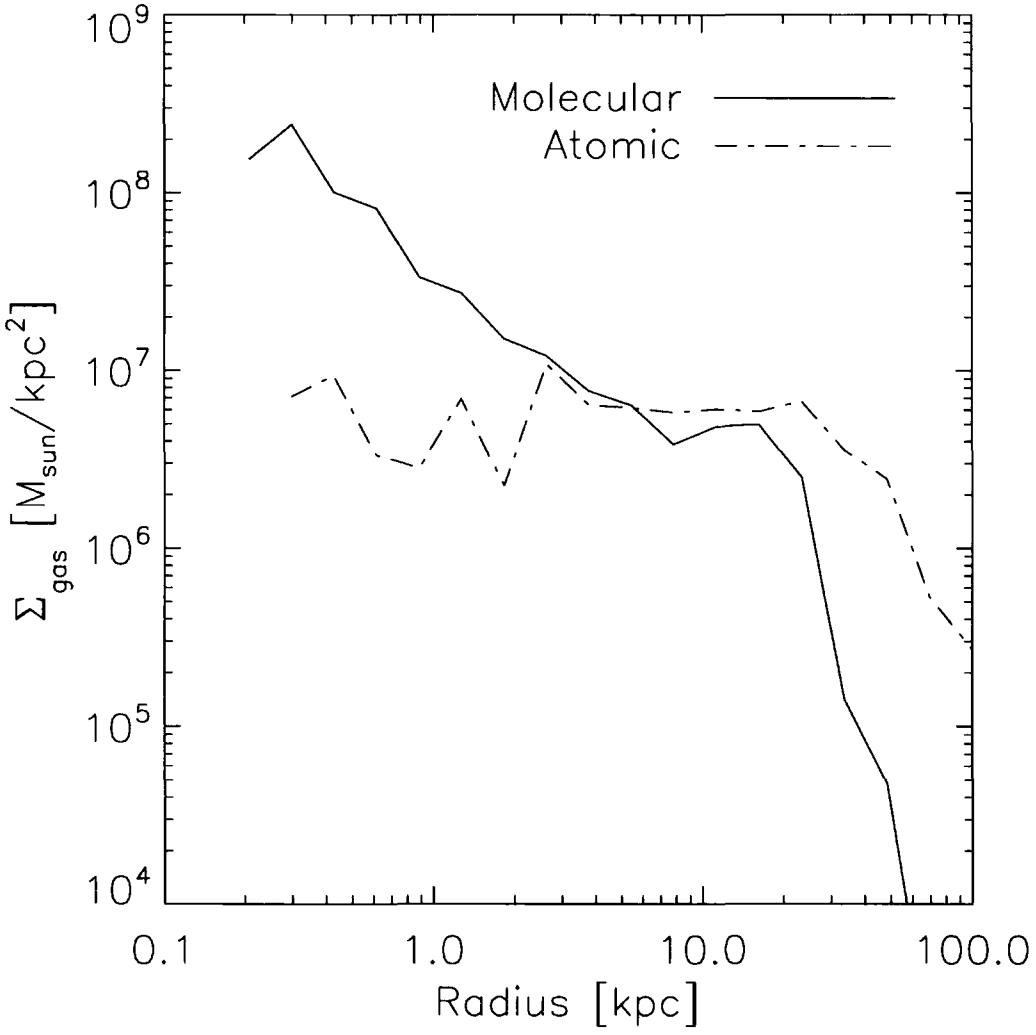

Figure 5.11: Radial density profiles for the hot atomic (SPH) and cold molecular (sticky particle) gas phases in the redshift zero galactic disk. It is clear that near the centre of the galaxy most of the gas is molecular, whereas on the outskirts the galaxy is primarily atomic

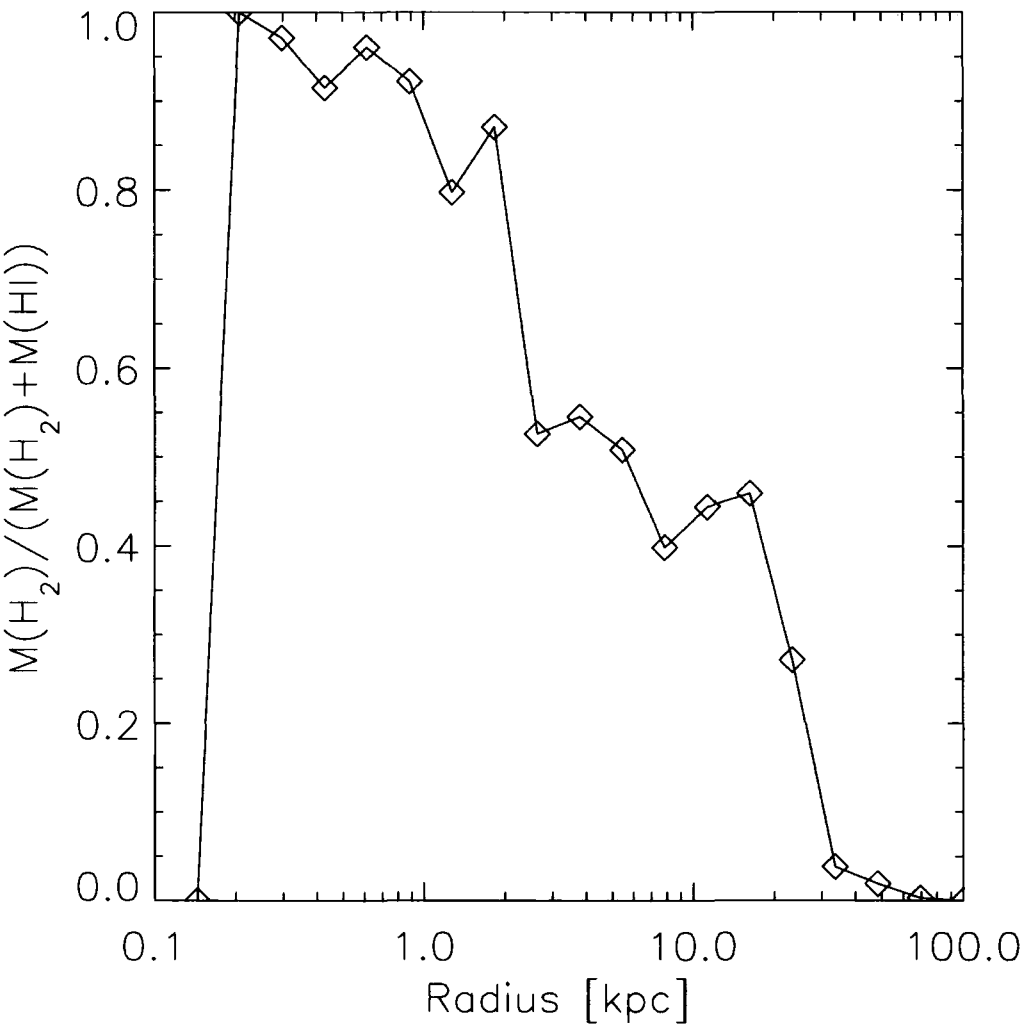

Figure 5.12: Proportion of molecular gas as a function of distance from the centre of the galaxy at redshift zero

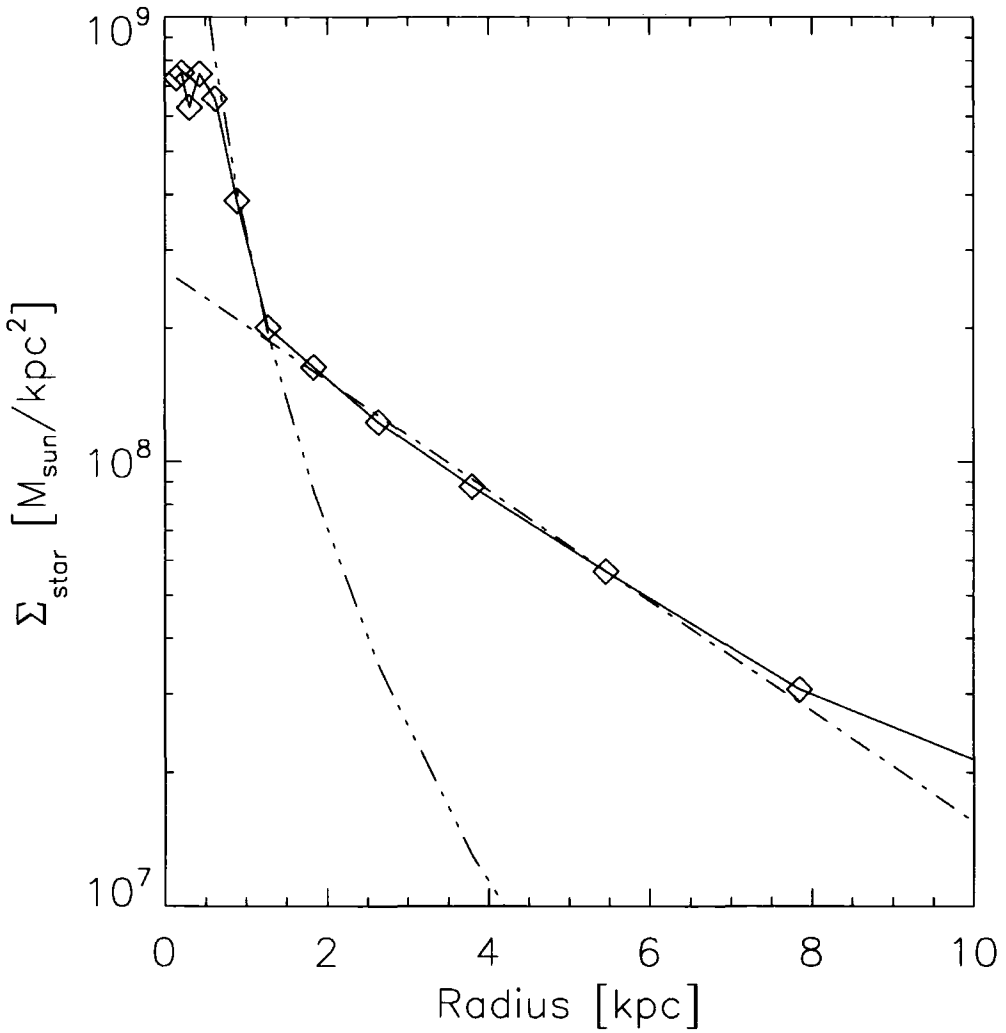

Figure 5.13: Stellar radial density profile of the redshift zero disk. The two dashed lines represent a best fit bulge and disk component for the galaxy.

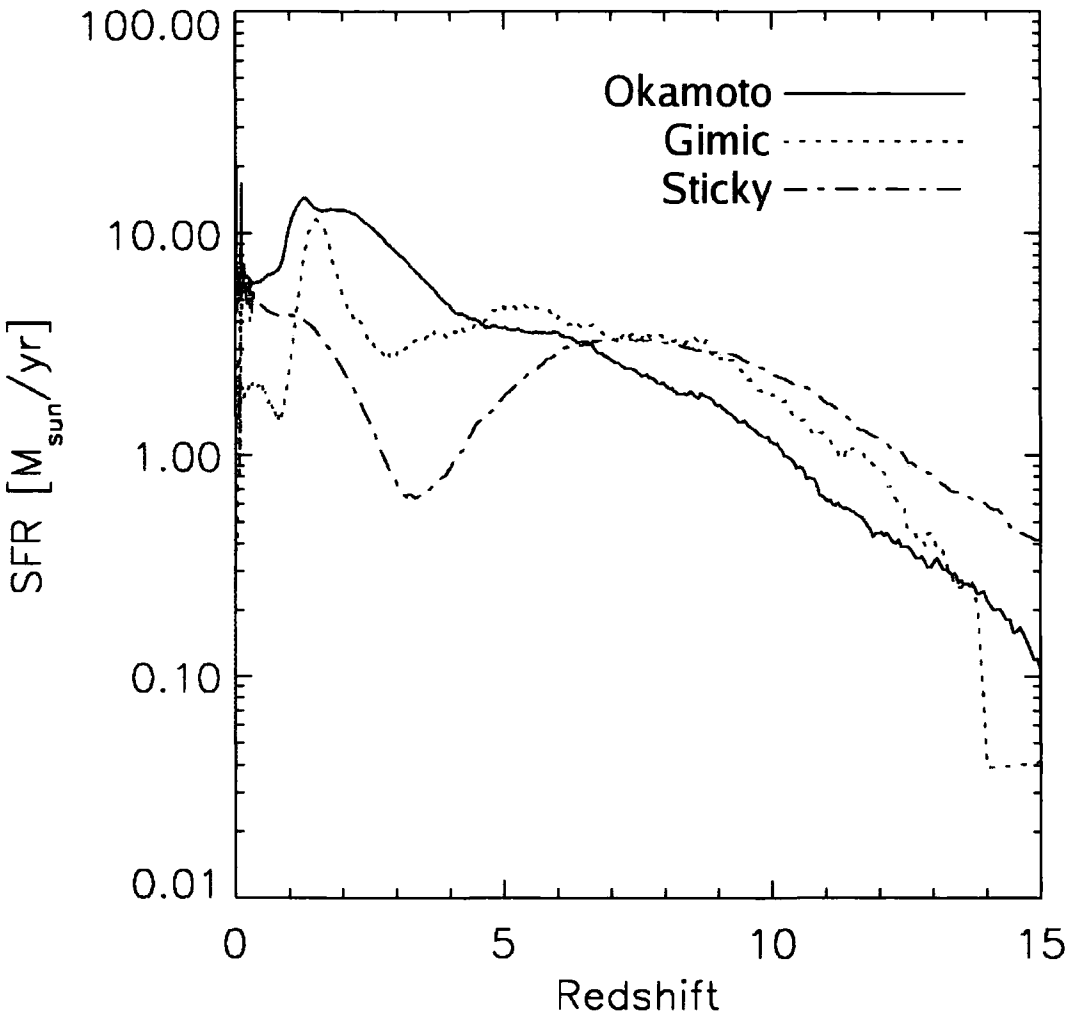

Figure 5.14: Comparison of star formation histories of the same galaxy run with three different codes. The three different codes are described in the text.

Chapter 6 | *Conclusions*

6.1 Discussion

6.1.1 Computational Cosmology

We have introduced an initial conditions code suitable for the resimulation of individual haloes at extremely high resolution and verified that the basic properties of the haloes – including density profiles and velocity dispersion profiles – remain the same regardless of the mass resolution of the halo. We also introduced a conceptually simple way of marking out the lagrangian regions of haloes and presented details of automated tools for carrying out this process. We also presented some work on code validation on two different codes were compared with one of the standard numerical tests. Both were found to perform adequately.

6.1.2 Statistical Models of the Interstellar Medium

Motivated by the fact that we cannot reasonably resolve the Jeans scale for molecular clouds in galaxy simulations we have introduced a new star formation and feedback prescription. We model the ambient phase of the ISM using a hydrodynamic simulation code and the unresolved molecular gas using a sticky particle prescription. Our model leads to a tightly self-regulating multiphase ISM. The multiphase nature of our star formation prescription avoids a lot of the problems of overcooling that were present in the first generation of star formation models. With the exception of the parameter that controls the molecular cloud coagulation timescale, $v_{\rm stick}$, all the parameters in our model can be tightly constrained by observation, leaving the cloud coagulation timescale as a free parameter that we can adjust to match the observed properties of galaxies. Where possible our model of the ISM has been formulated in such a way that the results of a simulation should be independent of mass resolution. We demonstrated that the large scale properties of our simulations were unchanged over a two orders of magnitude shift in mass resolution.

6.1.3 The Interstellar Medium in Isolated Galaxies

We have applied the sticky particle star formation model to two different types of simulation: the rotating collapse of a gas and dark matter sphere and a model of a quiescent galactic disk. We find that after using the one zone simulation to set the value of the parameters that cannot be determined observationally, the sticky particle model can be applied to the other simulations without any parameter changes.

The simulations of a quiescent disk galaxy reproduce the observed Schmidt law with a slope of 1.4 due to the opposing effects of cloud coagulation and feedback effects. The galaxy also developed a natural three component ISM. Finally we observe supernova heated gas in the galaxy being ejected from the disk either in the form of a galactic fountain, or, when the star formation rate (and associated supernova rate) is sufficient, in the form of strong bipolar outflows. Both of these results arise as a natural consequence of the physics included in our star formation prescription.

Simulations of the collapse of a rotating sphere of dark matter and gas reproduced many of the observed properties of galactic disks, beginning from an initial condition well out of equilibrium. In particular we observe a stellar disk with distinct bulge and disk components, well fitted by the standard exponential and de Vacouleurs density profiles. The fraction of molecular gas in the disk as a function of radius is reproduced, and agrees well with recent observations of nearby galaxies. The observed relation between the disk midplane pressure and the fraction of molecular clouds is also reproduced. We also observe star formation rates comparable to those in disk galaxies and note that our model reproduces the formation of stars in the spiral arms of the galaxy.

6.1.4 Simulating Galaxy-Galaxy Interactions

Using the isolated galaxies that were investigated in the previous chapter we investigate the properties of the ISM during galaxy merger events. We found that the resulting galaxy expressed many of the properties of observed elliptical galaxies, the mass of molecular gas was found to fit will with that in elliptical galaxies of a similar total mass. The stellar density profile matched that found in other simulations, the projected brightness profiles were also well described by the observational fits. The temperature profile of the hot component of the ISM was found to fit well with that observed in nearby galaxies. During the interaction we see that strong tidal arms are generated. It was found that these arms exhibit strong bursts of star formation, as observed in interacting galaxies in

the local universe.

The fully self-consistent cosmological simulation produced a disk galaxy that matches many of the observed properties of local galaxies in spite of our crude treatment of metal enrichment by supernovae.

Overall our statistical model for star formation and feedback does a good job of reproducing many of the properties of both quiescent and interacting disk galaxies, and the properties of elliptical galaxies are also closely matched to those in the local universe.

6.2 Future Work

A natural continuation of this work is to extend our investigations to higher redshift through the use of fully cosmological simulations in which we can use our models of the ISM to probe the properties of galaxies of all morphologies over a range of redshifts.

In order to carry this out it is necessary that we incorporate additional levels of complexity into our code. Firstly the addition of stellar population synthesis codes into our outputs will facilitate comparisons between our simulations ond observations. Secondly although in the case of a quiescent disk galaxy it is a fair assumption that the metallicity of the galaxy remains approximately constant over the period we are investigating this is not the case in a fully cosmological simulation. Here the metallicity ranges all the way from 0 at high redshift to $\sim Z_{\odot}$ at redshift zero. The collapse of gas into galaxies will also be very strongly affected by its metallicity (since metallicity can change cooling rates by over an order of magnitude). Incorporation of these two pieces of physics into our simulations will allow us to perform simulations of galaxy formation with an unprecedented level of sophistication.

We can then analyse these galaxies and investigate in detail the buildup and evolution of present day disk galaxies. It will be particularly interesting to observe the effects of the strong galactic winds seen in chapter 4 on the intergalactic medium, both in terms of their effect on QSO spectra and the metal enrichment of the IGM. By combining sophisticated simulation techniques with high resolution resimulation techniques we also hope to be able to resolve the structure and properties of galaxies at all redshifts.

Our second area of active research is in attempting to gain a better understanding of the numerical effects that may affect our results. The two 'traditional' problems with the simulation of cosmological haloes are the 'angular momentum problem' and the 'substructure problem'. Recent results (see e.g. Governato et al. (2006)) suggest that

increasing the mass resolution of a simulated halo alleviates the angular momentum problem, and galaxies with enough particles ($\sim$ millions within the virial radius) begin to form extended stellar disks. It is additionally unclear in many circumstances how a particular author's star formation and feedback prescriptions are affected by the mass resolution of the simulation and how this may affect the properties both of the central galaxy in a halo and its subhaloes.

We plan to carry out a comprehensive study into the effects of mass resolution on the properties of simulated galaxies using the initial conditions code and simulations introduced in chapter 2 in order to gain an understanding of how particle number affects the star formation and feedback in the subhaloes of typical MW sized haloes and how resolution effects control the early history and buildup of a simulated galaxy.

Appendix A | *List of Symbols*

The following is a list of symbols used throughout the description of the sticky particle star formation model (see chapter 3)

α_c : Slope of the molecular cloud mass-radius relation. Eq 3.5

c_h : Sound speed of the ambient gas phase

$\epsilon_\star$: Fraction of a GMC converted to stars in a collapse. E_{51} : Energy ejected per SnII in units of 10^{51}ergs

E_b : Total energy in a supernova blast wave

E_m : Total kinetic energy in molecular clouds of mass m in a given volume

f_{cl} : Filling factor of cold clouds

$f_m(\sigma_1, \sigma_2)$: Fraction of collisions between clouds with velocity dispersions σ_1 and σ_2 that lead to mergers

$K(m, m')$: The kernel for aggregation of clouds of masses m and m'. Eq. 3.6

λ : Constant of proportionality relating cloud mass and destruction rate by thermal conduction. Eq. 3.50

Λ_N : Normalised radiative cooling rate

Λ_{net} : Net radiative cooling rate (ergs $cm^{-3}s^{-1}$)

M_c : Mass of a molecular cloud

M_{ref} : Reference cold cloud mass. Eq 3.5

$M_{\star,min}$: Minimum allowed star mass

$M_{\star,max}$: Maximum allowed star mass

n_b : Density internal to a supernova remnant in atoms / cm^3 n_c : Density of a molecular cloud in atoms / cm^3

n_h : Density of the ambient medium in atoms / cm^3

N_{SF} : The slope of the schmidt law. Eq 3.36

$n(m, t)$: The number of clouds with masses between m and $m + dm$

$N(m, t)$: The number density of clouds with masses between m and $m + dm$

ϕ : Efficiency of destruction of cold clouds by thermal conduction

Q : Porosity of the interstellar medium. Sec. 3.2.6

r_c : Radius of a molecular cloud

r_{ref} : Reference cold cloud radius. Eq 3.5

r_b : The radius of a spherical blast wave

ρ_c : Mean density of molecular clouds contained in a volume

ρ_h : Mean density of ambient gas contained in a volume

ρ_{th} : Density at which ambient gas becomes thermally unstable

ρ_{SFR} : Volume density of star formation

η : Fraction of cloud velocity lost to 'cooling' collision

T_b : Mean temperature inside of a supernova remnant

T_c : Internal temperature of cold clouds

T_h : Temperature of the ambient gas phase

u_b : Thermal energy per unit mass of supernova remnants

u_c : Thermal energy per unit mass of the cold clouds

u_h : Thermal energy per unit mass of the ambient phase

Σ : Cross section for collision between clouds. Eq. 3.7

Σ_{cond} : Efficiency of thermal conduction. Eq 3.46

v_{app} : Relative approach velocity of two molecular clouds

v_{stick} : Maximum relative velocity for cloud merger

x : Slope of the stellar IMF

Appendix B

The Green's Function of the Finite Differenced Laplacian

For some function ϕ, defined on a regular grid at points i, with grid spacing Δ the finite-difference approximation to the Laplacian at point i is given by

$$\nabla^2\phi_i \approx \frac{\phi_{i+1} + \phi_{i-1} - 2\phi_i}{\Delta^2}\,. \tag{B.1}$$

We now note that for some function $g(x)$, $\mathfrak{F}\big(g(t)\big) = G(k)$, where the notation $\mathfrak{F}$ represents a Fourier transform, defined as

$$g(x) = \int_{\infty}^{\infty} G(k)e^{2\pi ikx}dk\,. \tag{B.2}$$

k represents a frequency, we can write

$$\nabla^2\phi = \sum_k \frac{\hat{\phi}(k)e^{i2\pi k\Delta} + \hat{\phi}(k)e^{-i2\pi k\Delta} - 2\hat{\phi}(k)}{\Delta^2}e^{2\pi ikx}\,, \tag{B.3}$$

by using $\mathfrak{F}\big(g(t-a)\big) = e^{-i2\pi ak}G(k)$. Now noting that $e^{iax} = \cos(ax) + i\sin(ax)$ we can write

$$\nabla^2\phi = \sum_k \hat{\phi}(k)\frac{\cos(2\pi k\Delta) + i\sin(2\pi k\Delta) + \cos(-2\pi k\Delta) + i\sin(-2\pi k\Delta) - 2}{\Delta^2}e^{ikx}\,, \tag{B.4}$$

which, through symmetry, becomes

$$\nabla^2\phi = \sum_k \hat{\phi}(k)\frac{2\cos(2\pi k\Delta) - 2}{\Delta^2}e^{2\pi ikx}\,. \tag{B.5}$$

and substituting in $\cos(2x) = 1 - 2\sin^2(x)$ we obtain

$$\nabla^2\phi = \frac{2}{\Delta^2}\sum \hat{\phi}(k)\sin^2(\pi k\Delta)e^{2\pi ikx}\,, \tag{B.6}$$

which is equal to the right hand side of the Poisson equation. Then we can say that (after taking a fourier transform)

$$\frac{\hat{\phi}(k)}{\hat{\mathfrak{G}}(k)} = \hat{\rho}(k) \tag{B.7}$$

where we have defined the Greens function as

$$\hat{\mathfrak{G}}_{j,k,l} = \left(\frac{2}{\Delta^2} \sin^2(\pi k \Delta) \right)^{-1} \tag{B.8}$$

Bibliography

S. J. Aarseth. Dynamical evolution of clusters of galaxies, I. *MNRAS*, 126:223–+, 1963.

S. J. Aarseth, E. L. Turner, and J. R. Gott, III. N-body simulations of galaxy clustering. I - Initial conditions and galaxy collapse times. *ApJ*, 228:664–683, March 1979.

A. Albrecht and A. Stebbins. Perturbations from cosmic strings in cold dark matter. *Physical Review Letters*, 68:2121–2124, April 1992.

R. A. Alpher, H. Bethe, and G. Gamow. The Origin of Chemical Elements. *Physical Review*, 73:803, April 1948.

J. Ballesteros-Paredes, E. Vázquez-Semadeni, and J. Scalo. Clouds as Turbulent Density Fluctuations: Implications for Pressure Confinement and Spectral Line Data Interpretation. *ApJ*, 515:286–303, April 1999.

D. S. Balsara. von Neumann stability analysis of smoothed particle hydrodynamics–suggestions for optimal algorithms. *Journal of Computational Physics*, 121:357–372, October 1995.

J. M. Bardeen, J. R. Bond, N. Kaiser, and A. S. Szalay. The statistics of peaks of Gaussian random fields. *ApJ*, 304:15–61, May 1986.

J. M. Bardeen, P. J. Steinhardt, and M. S. Turner. Spontaneous creation of almost scale-free density perturbations in an inflationary universe. *Physical Review D*, 28:679–693, October 1983.

Z. Barkat, Y. Reiss, and G. Rakavy. Stars in the mass ratio range from 7 to 10 as candidates for pulsar progenitors. *ApJL*, 193:L21–L23, October 1974.

J. Barnes and P. Hut. A Hierarchical O(NlogN) Force-Calculation Algorithm. *Nature*, 324:446–449, December 1986.

J. E. Barnes. Transformations of galaxies. I - Mergers of equal-mass stellar disks. *ApJ*, 393:484–507, July 1992.

J. E. Barnes and L. Hernquist. Formation of dwarf galaxies in tidal tails. *Nature*, 360: 715–717, December 1992.

J. E. Barnes and P. Hut. Error analysis of a tree code. *ApJS*, 70:389–417, June 1989.

R. H. Becker, X. Fan, R. L. White, M. A. Strauss, V. K. Narayanan, R. H. Lupton, J. E. Gunn, J. Annis, N. A. Bahcall, J. Brinkmann, A. J. Connolly, I. Csabai, P. C. Czarapata, M. Doi, T. M. Heckman, G. S. Hennessy, Ž. Ivezić, G. R. Knapp, D. Q. Lamb, T. A. McKay, J. A. Munn, T. Nash, R. Nichol, J. R. Pier, G. T. Richards, D. P. Schneider, C. Stoughton, A. S. Szalay, A. R. Thakar, and D. G. York. Evidence for Reionization at z˜6: Detection of a Gunn-Peterson Trough in a z=6.28 Quasar. *AJ*, 122:2850–2857, December 2001.

M. C. Begelman and C. F. McKee. Global effects of thermal conduction on two-phase media. *ApJ*, 358:375–391, August 1990.

A. J. Benson, M. Kamionkowski, and S. H. Hassani. Self-consistent theory of halo mergers. *MNRAS*, 357:847–858, March 2005.

E. Bertschinger. Multiscale Gaussian Random Fields and Their Application to Cosmological Simulations. *ApJS*, 137:1–20, November 2001.

J. Binney and M. R. Merrifield. *Galactic Astronomy*. Princeton University Press, Princeton NJ., 1998.

M. Birkinshaw, S. F. Gull, and H. Hardebeck. The Sunyaev-Zeldovich effect towards three clusters of galaxies. *Nature*, 309:34–+, May 1984.

J. H. Black. The physical state of primordial intergalactic clouds. *MNRAS*, 197:553–563, November 1981.

L. Blitz, Y. Fukui, Kawamura A., Leroy A., and Mizuno N. Giant Molecular Clouds in Local Group Galaxies. *ArXiv Astrophysics e-prints*, May 2006.

L. Blitz and E. Rosolowsky. The Role of Pressure in Giant Molecular Cloud Formation. *ApJL*, 612:L29–L32, September 2004.

L. Blitz and F. H. Shu. The origin and lifetime of giant molecular cloud complexes. *ApJ*, 238:148–157, May 1980.

L. Blitz and P. Thaddeus. Giant molecular complexes and OB associations. I - The Rosette molecular complex. *ApJ*, 241:676–696, October 1980.

M. Boas. *Mathematical Methods in the Physical Sciences*. John Wiley & Sons, 1983.

A. M. Boesgaard and G. Steigman. Big bang nucleosynthesis - Theories and observations. *ARA&A*, 23:319–378, 1985.

I. A. Bonnell, M. R. Bate, C. J. Clarke, and J. E. Pringle. Accretion and the stellar mass spectrum in small clusters. *MNRAS*, 285:201–208, February 1997.

I. A. Bonnell, C. L. Dobbs, T. P. Robitaille, and J. E. Pringle. Spiral shocks, triggering of star formation and the velocity dispersion in giant molecular clouds. *MNRAS*, 365: 37–45, January 2006.

R. G. Bower, A. J. Benson, R. Malbon, J. C. Helly, C. S. Frenk, C. M. Baugh, S. Cole, and C. G. Lacey. Breaking the hierarchy of galaxy formation. *MNRAS*, 370:645–655, August 2006.

D. Branch. Type IA Supernovae and the Hubble Constant. *ARA&A*, 36:17–56, 1998.

D. Branch, S. W. Falk, A. K. Uomoto, B. J. Wills, M. L. McCall, and P. Rybski. The type II supernova 1979c in M100 and the distance to the Virgo cluster. *ApJ*, 244:780–804, March 1981.

A. Brandt. Multi-Level Adaptive Solutions to Boundary-Value Problems. *Mathematics of Computation*, 31:333–390, January 1977.

A. G. Bruzual and S. Charlot. Spectral evolution of stellar populations using isochrone synthesis. *ApJ*, 405:538–553, March 1993.

G. L. Bryan, Norman M. L., Stone J. M., Cen R., and Ostriker J. P. A piecewise parabolic method for cosmological hydrodynamics. *Comput. Phys. Comm.*, 89:149–168, July 1995.

G. L. Bryan and M. L. Norman. Simulating X-ray Clusters with Adaptive Mesh Refinement. In *Bulletin of the American Astronomical Society*, pages 1421–+, December 1995.

V. Buat. Global recent star formation in normal galaxies from a multiwavelength study - Comparison with their gas content. *A&A*, 264:444–454, October 1992.

E. M. Burbidge, G. R. Burbidge, W. A. Fowler, and F. Hoyle. Synthesis of the Elements in Stars. *Reviews of Modern Physics*, 29:547–650, 1957.

A. Burkert. The Turbulent Interstellar Medium. *ArXiv Astrophysics e-prints*, May 2006.

R. Cen. A hydrodynamic approach to cosmology - Methodology. *ApJS*, 78:341–364, February 1992.

R. Cen and J. P. Ostriker. Galaxy formation and physical bias. *ApJL*, 399:L113–L116, November 1992.

R. Cesaroni, E. Churchwell, P. Hofner, C. M. Walmsley, and S. Kurtz. Hot ammonia towards compact HII regions. *A&A*, 288:903–920, August 1994.

G. Chabrier. The Galactic Disk Mass Budget. I. Stellar Mass Function and Density. *ApJ*, 554:1274–1281, June 2001.

R. A. Chevalier. The Evolution of Supernova Remnants.IV. The Supernova Ejecta. *ApJ*, 200:698–708, September 1975.

R. A. Chevalier. The interaction of supernovae with the interstellar medium. *ARA&A*, 15:175–196, 1977.

A. F. Chorin. Random Choice Solution of Hyperbolic Systems. *Journal of Computational Physics*, 22:517–533, December 1976.

A. Coc and E. Vangioni. Lithium and Big-Bang Nucleosynthesis. In V. Hill, P. François, and F. Primas, editors, *IAU Symposium*, pages 13–22, 2005.

J. G. Cohen. H-alpha emission from the disks of spiral galaxies. *ApJ*, 203:587–592, February 1976a.

S. A. Cohen. Molecular hydrogen formation on interstellar dust grains. *Nature*, 261: 215–+, May 1976b.

S. Cole, C. G. Lacey, C. M. Baugh, and C. S. Frenk. Hierarchical galaxy formation. *MNRAS*, 319:168–204, November 2000.

P. Colella and H. M. Glaz. Efficient solution algorithms for the Riemann problem for real gases. *Journal of Computational Physics*, 59:264–289, July 1985.

P. Colella and P. Woodward. The Piecewise Parabolic Method (PPM) for gas-dynamical simulations. *Journal of Computational Physics*, 54:174–201, April 1984.

M. Colless, G. Dalton, S. Maddox, W. Sutherland, P. Norberg, S. Cole, J. Bland-Hawthorn, T. Bridges, R. Cannon, C. Collins, W. Couch, N. Cross, K. Deeley, R. De Propris, S. P. Driver, G. Efstathiou, R. S. Ellis, C. S. Frenk, K. Glazebrook, C. Jackson, O. Lahav, I. Lewis, S. Lumsden, D. Madgwick, J. A. Peacock, B. A. Peterson, I. Price, M. Seaborne, and K. Taylor. The 2dF Galaxy Redshift Survey: spectra and redshifts. *MNRAS*, 328: 1039–1063, December 2001.

J. W. Cooley and J. W. Tukey. An Algorithm for the Machine Calculation of Complex Fourier Series. *Mathematics of Computation*, 19:297–2301, April 1965.

H. M. P. Couchman, P. A. Thomas, and F. R. Pearce. Hydra: an Adaptive-Mesh Implementation of P 3M-SPH. *ApJ*, 452:797–+, October 1995.

R. Courant, K. Friedrichs, and H. Lewy. Uber die partiellen Differenzengleichungen der mathematischen Physi. *Mathematische Annalen*, 100:32–74, 1928.

L. L. Cowie. The early evolution of supernova remnants in a homogeneous medium - The effects of electron thermal conduction. *ApJ*, 215:226–231, July 1977.

D. P. Cox. The Three-Phase Interstellar Medium Revisited. *ARA&A*, 43:337–385, September 2005.

D. P. Cox and W. H. Tucker. Ionization Equilibrium and Radiative Cooling of a Low-Density Plasma. *ApJ*, 157:1157–+, September 1969.

P. Cox, E. Kruegel, and P. G. Mezger. Principal heating sources of dust in the galactic disk. *A&A*, 155:380–396, February 1986.

R. A. C. Croft, R. Davé, L. Hernquist, and N. Katz. Simulating the Effects of Intergalactic Gray Dust. *ApJL*, 534:L123–L126, May 2000.

T. M. Dame, E. Koper, F. P. Israel, and P. Thaddeus. A Complete CO Survey of M31. I. Distribution and Kinematics. *ApJ*, 418:730–+, December 1993.

W. de Sitter. On the relativity of inertia. Remarks concerning Einstein's latest hypothesis. *Proc. Akad. Weteusch. Amsterdam.*, 19:1217, October 1917.

J.-M. Deharveng, T. P. Sasseen, V. Buat, S. Bowyer, M. Lampton, and X. Wu. Ultraviolet observations of galaxies with the FAUST experiment. *A&A*, 289:715–728, September 1994.

A. Dekel and J. Silk. The origin of dwarf galaxies, cold dark matter, and biased galaxy formation. *ApJ*, 303:39–55, April 1986.

R. L. Dickman, M. A. Horvath, and M. Margulis. A search for scale-dependent morphology in five molecular cloud complexes. *ApJ*, 365:586–601, December 1990.

D. A. Dicus and V. L. Teplitz. Primordial synthesis of anomalous nuclei. *Physical Review Letters*, 44:218–221, January 1980.

C. L. Dobbs, I. A. Bonnell, and J. E. Pringle. The formation of molecular clouds in spiral galaxies. *MNRAS*, 371:1663–1674, October 2006.

P.-A. Duc and I. F. Mirabel. Young tidal dwarf galaxies around the gas-rich disturbed lenticular NGC 5291. *A&A*, 333:813–826, May 1998.

A. M. Dunn and R. Laflamme. The Least Action Principle and the Spin of Galaxies in the Local Group. *MNRAS*, 264:865–+, October 1993.

G. Efstathiou. A model of supernova feedback in galaxy formation. *MNRAS*, 317:697–719, September 2000.

G. Efstathiou, M. Davis, S. D. M. White, and C. S. Frenk. Numerical techniques for large cosmological N-body simulations. *ApJS*, 57:241–260, February 1985.

G. Efstathiou and J. W. Eastwood. On the clustering of particles in an expanding universe. *MNRAS*, 194:503–525, February 1981.

J. Einasto and D. Lynden-Bell. On the mass of the Local Group and the motion of its barycentre. MNRAS, 199:67–80, April 1982.

A. Einstein. Die Grundlage der allgemeinen Relativit"atstheorie. *Annalen der Physik*, 49: 769–822, May 1916.

J. H. Elias, K. Matthews, G. Neugebauer, and S. E. Persson. Type I supernovae in the infrared and their use as distance indicators. *ApJ*, 296:379–389, September 1985.

B. G. Elmegreen. Quiescent formation of bound galactic clusters. *MNRAS*, 203:1011–1020, June 1983.

B. G. Elmegreen. Star Formation in a Crossing Time. *ApJ*, 530:277–281, February 2000.

B. G. Elmegreen and D. M. Elmegreen. Fractal Structure in Galactic Star Fields. *AJ*, 121: 1507–1511, March 2001.

B. G. Elmegreen and E. Falgarone. A Fractal Origin for the Mass Spectrum of Interstellar Clouds. *ApJ*, 471:816–+, November 1996.

G. Engargiola, R. L. Plambeck, E. Rosolowsky, and L. Blitz. Giant Molecular Clouds in M33. I. BIMA All-Disk Survey. *ApJS*, 149:343–363, December 2003.

G. Fabbiano, D.-W. Kim, and G. Trinchieri. ROSAT PSPC observations of two X-ray-faint early-type galaxies: NGC 4365 and NGC 4382. *ApJ*, 429:94–104, July 1994.

S. M. Faber, S. Tremaine, E. A. Ajhar, Y.-I. Byun, A. Dressler, K. Gebhardt, C. Grillmair, J. Kormendy, T. R. Lauer, and D. Richstone. The Centers of Early-Type Galaxies with HST. IV. Central Parameter Relations. *AJ*, 114:1771–+, November 1997.

X. Fan, R. L. White, M. Davis, R. H. Becker, M. A. Strauss, Z. Haiman, D. P. Schneider, M. D. Gregg, J. E. Gunn, G. R. Knapp, R. H. Lupton, J. E. Anderson, Jr., S. F. Anderson, J. Annis, N. A. Bahcall, W. N. Boroski, R. J. Brunner, B. Chen, A. J. Connolly, I. Csabai, M. Doi, M. Fukugita, G. S. Hennessy, R. B. Hindsley, T. Ichikawa, Ž. Ivezić, J. Loveday, A. Meiksin, T. A. McKay, J. A. Munn, H. J. Newberg, R. Nichol, S. Okamura, J. R. Pier, M. Sekiguchi, K. Shimasaku, C. Stoughton, A. S. Szalay, G. P. Szokoly, A. R. Thakar, M. S. Vogeley, and D. G. York. The Discovery of a Luminous Z=5.80 Quasar from the Sloan Digital Sky Survey. *AJ*, 120:1167–1174, September 2000.

G. J. Ferland, K. T. Korista, D. A. Verner, J. W. Ferguson, J. B. Kingdon, and E. M. Verner. CLOUDY 90: Numerical Simulation of Plasmas and Their Spectra. *PASP*, 110:761–778, July 1998.

G. B. Field, D. W. Goldsmith, and H. J. Habing. Cosmic-Ray Heating of the Interstellar Gas. *ApJL*, 155:L149+, March 1969.

W. Forman, C. Jones, and W. Tucker. Hot coronae around early-type galaxies. *ApJ*, 293: 102–119, June 1985.

W. A. Fowler and F. Hoyle. Neutrino Processes and Pair Formation in Massive Stars and Supernovae. *ApJS*, 9:201–+, December 1964.

W. L. Freedman, B. F. Madore, B. K. Gibson, L. Ferrarese, D. D. Kelson, S. Sakai, J. R. Mould, R. C. Kennicutt, Jr., H. C. Ford, J. A. Graham, J. P. Huchra, S. M. G. Hughes, G. D. Illingworth, L. M. Macri, and P. B. Stetson. Final Results from the Hubble Space Telescope Key Project to Measure the Hubble Constant. *ApJ*, 553:47–72, May 2001.

C. S. Frenk, S. D. M. White, P. Bode, J. R. Bond, G. L. Bryan, R. Cen, H. M. P. Couchman, A. E. Evrard, N. Gnedin, A. Jenkins, A. M. Khokhlov, A. Klypin, J. F. Navarro, M. L. Norman, J. P. Ostriker, J. M. Owen, F. R. Pearce, U.-L. Pen, M. Steinmetz, P. A. Thomas, J. V. Villumsen, J. W. Wadsley, M. S. Warren, G. Xu, and G. Yepes. The Santa Barbara Cluster Comparison Project: A Comparison of Cosmological Hydrodynamics Solutions. *ApJ*, 525:554–582, November 1999.

C. S. Frenk, S. D. M. White, and M. Davis. Nonlinear evolution of large-scale structure in the universe. *ApJ*, 271:417–430, August 1983.

C. L. Fryer, S. E. Woosley, and A. Heger. Pair-Instability Supernovae, Gravity Waves, and Gamma-Ray Transients. *ApJ*, 550:372–382, March 2001.

B. Fryxell, K. Olson, P. Ricker, F. X. Timmes, M. Zingale, D. Q. Lamb, P. MacNeice, R. Rosner, J. W. Truran, and H. Tufo. FLASH: An Adaptive Mesh Hydrodynamics Code for Modeling Astrophysical Thermonuclear Flashes. *ApJS*, 131:273–334, November 2000.

Y. Fukui, N. Mizuno, R. Yamaguchi, A. Mizuno, and T. Onishi. On the Mass Spectrum of Giant Molecular Clouds in the Large Magellanic Cloud. *PASJ*, 53:L41–L44, December 2001.

J. S. Gallagher, D. A. Hunter, and H. Bushouse. Star-formation rates and forbidden O II emission in blue galaxies. *AJ*, 97:700–707, March 1989.

L. Gao, S. D. M. White, A. Jenkins, C. S. Frenk, and V. Springel. Early structure in ΛCDM. *MNRAS*, 363:379–392, October 2005.

J. M. Gelb and E. Bertschinger. Cold dark matter. 2: Spatial and velocity statistics. *ApJ*, 436:491–508, December 1994.

R. A. Gingold and J. J. Monaghan. Smoothed particle hydrodynamics - Theory and application to non-spherical stars. *MNRAS*, 181:375–389, November 1977.

J. Glimm. Solutions in the large for nonlinear hyperbolic systems of equations. *Communications on Pure and Applied Mathematics*, 18:697–715, November 1965.

N. Y. Gnedin. Softened Lagrangian hydrodynamics for cosmology. *ApJS*, 97:231–257, April 1995.

N. Y. Gnedin. Cosmological Reionization by Stellar Sources. *ApJ*, 535:530–554, June 2000.

N. Y. Gnedin and J. P. Ostriker. Reionization of the Universe and the Early Production of Metals. *ApJ*, 486:581–+, September 1997.

S. K Godunov. A Finite Difference Method for the Numerical Coputation and Discontinuous Solutions of the Equationd of Fluid Dynamics. *Mat. Sb.*, 47:271, 1959.

M. Gomez, B. F. Jones, L. Hartmann, S. J. Kenyon, J. R. Stauffer, R. Hewett, and I. N. Reid. On the ages of pre-main-sequence stars in Taurus. *AJ*, 104:762–773, August 1992.

A. Goobar, S. Hannestad, E. Mörtsell, and H. Tu. The neutrino mass bound from WMAP 3 year data, the baryon acoustic peak, the SNLS supernovae and the Lyman-α forest. *Journal of Cosmology and Astro-Particle Physics*, 6:19–+, June 2006.

R. J. Gould. Radiative recombination of complex ions. *ApJ*, 219:250–261, January 1978.

F. Governato, L. Mayer, J. Wadsley, J. P. Gardner, B. Willman, E. Hayashi, T. Quinn, J. Stadel, and G. Lake. The Formation of a Realistic Disk Galaxy in Λ-dominated Cosmologies. *ApJ*, 607:688–696, June 2004.

F. Governato, B. Willman, L. Mayer, A. Brooks, G. Stinson, O. Valenzuela, J. Wadsley, and T. Quinn. Forming disc galaxies in ΛCDM simulations. *MNRAS*, pages 1424–+, December 2006.

S. F. Gull. A numerical model of the structure and evolution of young supernovaremnants. *MNRAS*, 161:47–+, 1973.

J. E. Gunn and B. A. Peterson. On the Density of Neutral Hydrogen in Intergalactic Space. *ApJ*, 142:1633–1641, November 1965.

A. H. Guth. Inflationary universe: A possible solution to the horizon and flatness problems. *Physical Review D*, 23:347–356, January 1981.

A. H. Guth. Fluctuations in the new inflationary univers. *Phys. Rev. Lett. D*, 49:1110–1113, January 1983a.

Weinberg E. J. Guth, A. H. Could the universe have recovered from a slow first-order phase transition? . *Nuclear Physics B*, 212:321–364, February 1983b.

F. Haardt and P. Madau. *Clusters of Galaxies and the High Redshift Universe Observed in X-rays*. Bristol: Hilger, 1988, 2001.

Z. Haiman and A. Loeb. Observational Signatures of the First Quasars. *ApJ*, 503:505–+, August 1998.

S. Hanany, P. Ade, A. Balbi, J. Bock, J. Borrill, A. Boscaleri, P. de Bernardis, P. G. Ferreira, V. V. Hristov, A. H. Jaffe, A. E. Lange, A. T. Lee, P. D. Mauskopf, C. B. Netterfield, S. Oh, E. Pascale, B. Rabii, P. L. Richards, G. F. Smoot, R. Stompor, C. D. Winant, and J. H. P. Wu. MAXIMA-1: A Measurement of the Cosmic Microwave Background Anisotropy on Angular Scales of $10^{-}5$deg. *ApJL*, 545:L5–L9, December 2000.

S. Harfst, C. Theis, and G. Hensler. Modelling galaxies with a 3d multi-phase ISM. *A&A*, 449:509–518, April 2006.

S. W. Hawking. The development of irregularities in a single bubble inflationary universe. *Phys.Lett. B*, 115:295, October 1982.

A. Heger, C. L. Fryer, S. E. Woosley, N. Langer, and D. H. Hartmann. How Massive Single Stars End Their Life. *ApJ*, 591:288–300, July 2003.

A. Heger and S. E. Woosley. The Nucleosynthetic Signature of Population III. *ApJ*, 567: 532–543, March 2002.

M. Hénon. L'évolution initiale d'un amas sphérique. *Annales d'Astrophysique*, 27:83–+, February 1964.

L. Hernquist. Performance characteristics of tree codes. *ApJS*, 64:715–734, August 1987.

L. Hernquist and N. Katz. TREESPH - A unification of SPH with the hierarchical tree method. *ApJS*, 70:419–446, June 1989.

M. H. Heyer, J. M. Carpenter, and R. L. Snell. The Equilibrium State of Molecular Regions in the Outer Galaxy. *ApJ*, 551:852–866, April 2001.

J. C. Higdon, R. E. Lingenfelter, and R. Ramaty. Cosmic-Ray Acceleration from Supernova Ejecta in Superbubbles. *ApJL*, 509:L33–L36, December 1998.

R. W. Hockney and J. W. Eastwood. *Computer simulation using particles*. Bristol: Hilger, 1988, 1988.

Y. Hoffman and E. Ribak. Constrained realizations of Gaussian fields - A simple algorithm. *ApJL*, 380:L5–L8, October 1991.

S. Holland. The Distance to the M31 Globular Cluster System. *AJ*, 115:1916–1920, May 1998.

J. A. Holtzman. Microwave background anisotropies and large-scale structure in universes with cold dark matter, baryons, radiation, and massive and massless neutrinos. *ApJS*, 71:1–24, September 1989.

W. Hu and S. Dodelson. Cosmic Microwave Background Anisotropies. *ARA&A*, 40: 171–216, 2002.

E. Hubble. A Relation between Distance and Radial Velocity among Extra-Galactic Nebulae. *Proceedings of the National Academy of Science*, 15:168–173, March 1929a.

E. P. Hubble. A spiral nebula as a stellar system, Messier 31. *ApJ*, 69:103–158, March 1929b.

J. Hultman and A. Pharasyn. Hierarchical, dissipative formation of elliptical galaxies: is thermal instability the key mechanism?. Hydrodynamical simulations including supernova feedback, multi-phase gas and metal enrichment in CDM: structure and dynamics of elliptical galaxies. *A&A*, 347:769–798, July 1999.

P. J. Humphrey, D. A. Buote, F. Gastaldello, L. Zappacosta, J. S. Bullock, F. Brighenti, and W. G. Mathews. A Chandra View of Dark Matter in Early-Type Galaxies. *ApJ*, 646: 899–918, August 2006.

D. A. Hunter, F. C. Gillett, J. S. Gallagher, III, W. L. Rice, and F. J. Low. IRAS observations of a small sample of blue irregular galaxies. *ApJ*, 303:171–185, April 1986.

I. Iben, Jr. The life and times of an intermediate mass star - In isolation/in a close binary. *Royal Astronomical Society, Quarterly Journal*, 26:1–39, March 1985.

I. Iben, Jr. and A. Renzini. Asymptotic giant branch evolution and beyond. *ARA&A*, 21: 271–342, 1983.

Y. I. Izotov, T. X. Thuan, and V. A. Lipovetsky. The primordial helium abundance from a new sample of metal-deficient blue compact galaxies. *ApJ*, 435:647–667, November 1994.

J. G. Jernigan. Direct n-body simulations with a recursive center of mass reduction and regularization. In J. Goodman and P. Hut, editors, *IAU Symp. 113: Dynamics of Star Clusters*, pages 275–283, 1985.

J. G. Jernigan and D. H. Porter. A tree code with logarithmic reduction of force terms, hierarchical regularization of all variables, and explicit accuracy controls. *ApJS*, 71: 871–893, December 1989.

C. J. Jog and J. P. Ostriker. The velocity dispersion of the giant molecular clouds - A viscous origin. *ApJ*, 328:404–426, May 1988.

F. D. Kahn and L. Woltjer. Intergalactic Matter and the Galaxy. *ApJ*, 130:705–+, November 1959.

I. Kant. *Allgemeine Naturgeschichte und Theorie des Himmels.* Zeitz, Bei W. Webel, 1798. Neue aufl., 1798.

N. Katz. Dissipational galaxy formation. II - Effects of star formation. *ApJ*, 391:502–517, June 1992.

N. Katz and J. E. Gunn. Dissipational galaxy formation. I - Effects of gasdynamics. *ApJ*, 377:365–381, August 1991.

N. Katz, T. Quinn, E. Bertschinger, and J. M. Gelb. Formation of Quasars at High Redshift. *MNRAS*, 270:L71+, October 1994.

N. Katz, D. H. Weinberg, and L. Hernquist. Cosmological Simulations with TreeSPH. *ApJS*, 105:19–+, July 1996.

T. Kaufmann, L. Mayer, J. Wadsley, J. Stadel, and B. Moore. Cooling flows within galactic haloes: the kinematics and properties of infalling multiphase gas. *MNRAS*, 370:1612–1622, August 2006.

D. Kawata and B. K. Gibson. GCD+: a new chemodynamical approach to modelling supernovae and chemical enrichment in elliptical galaxies. *MNRAS*, 340:908–922, April 2003.

S. T. Kay, F. R. Pearce, C. S. Frenk, and A. Jenkins. Including star formation and supernova feedback within cosmological simulations of galaxy formation. *MNRAS*, 330: 113–128, February 2002.

W. T. Kelvin. . *Philosophical Magazine*, 6:161–177, October 1901.

R. C. Kennicutt. Star Formation in Galaxies Along the Hubble Sequence. *ARA&A*, 36: 189–232, 1998.

R. C. Kennicutt, Jr. The rate of star formation in normal disk galaxies. *ApJ*, 272:54–67, September 1983.

R. C. Kennicutt, Jr. Properties of H II region populations in galaxies. I - The first-ranked H II regions. *ApJ*, 334:144–158, November 1988.

R. C. Kennicutt, Jr. The star formation law in galactic disks. *ApJ*, 344:685–703, September 1989.

H. G. Khosroshahi, L. R. Jones, and T. J. Ponman. An old galaxy group: Chandra X-ray observations of the nearby fossil group NGC 6482. *MNRAS*, 349:1240–1250, April 2004.

I. J. Klamer, R. D. Ekers, E. M. Sadler, and R. W. Hunstead. Molecular Gas at High Redshift: Jet-induced Star Formation? *ApJL*, 612:L97–L100, September 2004.

A. Klypin, H. Zhao, and R. S. Somerville. ΛCDM-based Models for the Milky Way and M31. I. Dynamical Models. *ApJ*, 573:597–613, July 2002.

A. A. Klypin and S. F. Shandarin. Three-dimensional numerical model of the formation of large-scale structure in the Universe. *MNRAS*, 204:891–907, September 1983.

K. A. Knierman, S. C. Gallagher, J. C. Charlton, S. D. Hunsberger, B. Whitmore, A. Kundu, J. E. Hibbard, and D. Zaritsky. From Globular Clusters to Tidal Dwarfs: Structure Formation in the Tidal Tails of Merging Galaxies. *AJ*, 126:1227–1244, September 2003.

R. A. Knop, G. Aldering, R. Amanullah, P. Astier, G. Blanc, M. S. Burns, A. Conley, S. E. Deustua, M. Doi, R. Ellis, S. Fabbro, G. Folatelli, A. S. Fruchter, G. Garavini, S. Garmond, K. Garton, R. Gibbons, G. Goldhaber, A. Goobar, D. E. Groom, D. Hardin, I. Hook, D. A. Howell, A. G. Kim, B. C. Lee, C. Lidman, J. Mendez, S. Nobili, P. E. Nugent, R. Pain, N. Panagia, C. R. Pennypacker, S. Perlmutter, R. Quimby, J. Raux, N. Regnault, P. Ruiz-Lapuente, G. Sainton, B. Schaefer, K. Schahmaneche, E. Smith, A. L. Spadafora, V. Stanishev, M. Sullivan, N. A. Walton, L. Wang, W. M. Wood-Vasey, and N. Yasuda. New Constraints on Ω_M, Ω_Λ, and w from an Independent Set of 11

High-Redshift Supernovae Observed with the Hubble Space Telescope. *ApJ*, 598:102–137, November 2003.

H. Koyama and S.-I. Inutsuka. Molecular Cloud Formation in Shock-compressed Layers. *ApJ*, 532:980–993, April 2000.

P. Kroupa. The Stellar Mass Function (invited review). In R. Rebolo, E. L. Martin, and M. R. Zapatero Osorio, editors, *ASP Conf. Ser. 134: Brown Dwarfs and Extrasolar Planets*, pages 483–+, 1998.

M. R. Krumholz and C. F. McKee. A General Theory of Turbulence-regulated Star Formation, from Spirals to Ultraluminous Infrared Galaxies. *ApJ*, 630:250–268, September 2005.

K. Kuijken and J. Dubinski. Nearly Self-Consistent Disc / Bulge / Halo Models for Galaxies. *MNRAS*, 277:1341–+, December 1995.

J. Kwan and F. Valdes. Spiral gravitational potentials and the mass growth of molecular clouds. *ApJ*, 271:604–610, August 1983.

C. Lacey and S. Cole. Merger rates in hierarchical models of galaxy formation. *MNRAS*, 262:627–649, June 1993.

C. J. Lada and E. A. Lada. Embedded Clusters in Molecular Clouds. *ARA&A*, 41:57–115, 2003.

M. D. Lehnert and T. M. Heckman. The Nature of Starburst Galaxies. *ApJ*, 472:546–+, December 1996.

C. Leitherer and T. M. Heckman. Synthetic properties of starburst galaxies. *ApJS*, 96: 9–38, January 1995.

E. S. Levine, L. Blitz, and C. Heiles. The Spiral Structure of the Outer Milky Way in Hydrogen. *Science*, 312:1773–1777, June 2006.

M. Limongi, O. Straniero, and A. Chieffi. Massive Stars in the Range 13-25 M_{solar}: Evolution and Nucleosynthesis. II. The Solar Metallicity Models. *ApJS*, 129:625–664, August 2000.

A. D. Linde. A new inflationary universe scenario: A possible solution of the horizon, flatness, homogeneity, isotropy and primordial monopole problems. *Physics Letters B*, 108:389–393, February 1982a.

A. D. Linde. Scalar field fluctuations in the expanding universe and the new inflationary universe scenario. *Physics Letters B*, 116:335–339, October 1982b.

A. D. Linde. Chaotic Inflation. *Physics Letters B*, 129:171–181, February 1983.

R. Löhner. An adaptive finite element scheme for transient problems in CFD. *Appl. Mech. Eng.*, 61:323–338, October 1987.

E. L. Łokas and G. A. Mamon. Properties of spherical galaxies and clusters with an NFW density profile. *MNRAS*, 321:155–166, February 2001.

C.-P. Ma and E. Bertschinger. Cosmological Perturbation Theory in the Synchronous and Conformal Newtonian Gauges. *ApJ*, 455:7–+, December 1995.

J. Ma, Q.-H. Peng, and Q.-S. Gu. The Thickness of M31. *ApJL*, 490:L51+, November 1997.

M.-M. Mac Low and R. S. Klessen. Control of star formation by supersonic turbulence. *Reviews of Modern Physics*, 76:125–194, January 2004.

P. Madau, A. Meiksin, and M. J. Rees. 21 Centimeter Tomography of the Intergalactic Medium at High Redshift. *ApJ*, 475:429–+, February 1997.

S. Marri and S. D. M. White. Smoothed particle hydrodynamics for galaxy-formation simulations: improved treatments of multiphase gas, of star formation and of supernovae feedback. *MNRAS*, 345:561–574, October 2003.

C. D. Matzner. On the Role of Massive Stars in the Support and Destruction of Giant Molecular Clouds. *ApJ*, 566:302–314, February 2002.

P. D. Mauskopf, P. A. R. Ade, P. de Bernardis, J. J. Bock, J. Borrill, A. Boscaleri, B. P. Crill, G. DeGasperis, G. De Troia, P. Farese, P. G. Ferreira, K. Ganga, M. Giacometti, S. Hanany, V. V. Hristov, A. Iacoangeli, A. H. Jaffe, A. E. Lange, A. T. Lee, S. Masi, A. Melchiorri, F. Melchiorri, L. Miglio, T. Montroy, C. B. Netterfield, E. Pascale, F. Piacentini, P. L. Richards, G. Romeo, J. E. Ruhl, E. Scannapieco, F. Scaramuzzi, R. Stompor, and N. Vittorio. Measurement of a Peak in the Cosmic Microwave Background Power Spectrum from the North American Test Flight of Boomerang. *ApJL*, 536:L59–L62, June 2000.

C. F. McKee and L. L. Cowie. The evaporation of spherical clouds in a hot gas. II - Effects of radiation. *ApJ*, 215:213–225, July 1977.

C. F. McKee and J. P. Ostriker. A theory of the interstellar medium - Three components regulated by supernova explosions in an inhomogeneous substrate. *ApJ*, 218:148–169, November 1977.

G. R. Meurer, T. M. Heckman, M. D. Lehnert, C. Leitherer, and J. Lowenthal. The Panchromatic Starburst Intensity Limit at Low and High Redshift. *AJ*, 114:54–68, July 1997.

J. C. Mihos and L. Hernquist. Induced population gradients in galaxy merger remnants. *ApJ*, 427:112–124, May 1994a.

J. C. Mihos and L. Hernquist. Star-forming galaxy models: Blending star formation into TREESPH. *ApJ*, 437:611–624, December 1994b.

A. D. Miller, R. Caldwell, M. J. Devlin, W. B. Dorwart, T. Herbig, M. R. Nolta, L. A. Page, J. Puchalla, E. Torbet, and H. T. Tran. A Measurement of the Angular Power Spectrum of the CMB from l = 100 to 400. In *Bulletin of the American Astronomical Society*, pages 1458–+, December 1999.

C. W. Misner. The Isotropy of the Universe. *ApJ*, 151:431–+, February 1968.

S. Miyaji, K. Nomoto, K. Yokoi, and D. Sugimoto. Supernova Triggered by Electron Captures. *PASJ*, 32:303–+, 1980.

H. J. Mo, S. Mao, and S. D. M. White. The formation of galactic discs. *MNRAS*, 295: 319–336, April 1998.

P. Monaco. Physical regimes for feedback in galaxy formation. *MNRAS*, 352:181–204, July 2004.

J. J. Monaghan. Smoothed particle hydrodynamics. *ARA&A*, 30:543–574, 1992.

J. J. Monaghan and R. A. Gingold. Shock simulation by the particle method SPH. *Journal of Computational Physics*, 52:374–389, November 1984.

M. Moshir, G. Kopman, and T. A. O. Conrow. *IRAS Faint Source Survey, Explanatory supplement version 2*. Pasadena: Infrared Processing and Analysis Center, California Institute of Technology, 1992, edited by Moshir, M.; Kopman, G.; Conrow, T. a.o., 1992.

J. R. Mould, J. P. Huchra, W. L. Freedman, R. C. Kennicutt, Jr., L. Ferrarese, H. C. Ford, B. K. Gibson, J. A. Graham, S. M. G. Hughes, G. D. Illingworth, D. D. Kelson, L. M.

Macri, B. F. Madore, S. Sakai, K. M. Sebo, N. A. Silbermann, and P. B. Stetson. The Hubble Space Telescope Key Project on the Extragalactic Distance Scale. XXVIII. Combining the Constraints on the Hubble Constant. *ApJ*, 529:786–794, February 2000.

J. V. Narlikar and T. Padmanabhan. Inflation for astronomers. *ARA&A*, 29:325–362, 1991.

J. F. Navarro and W. Benz. Dynamics of cooling gas in galactic dark halos. *ApJ*, 380: 320–329, October 1991.

J. F. Navarro, C. S. Frenk, and S. D. M. White. A Universal Density Profile from Hierarchical Clustering. *ApJ*, 490:493–+, December 1997.

J. F. Navarro and S. D. M. White. Simulations of Dissipative Galaxy Formation in Hierarchically Clustering Universes - Part One - Tests of the Code. *MNRAS*, 265:271–+, November 1993.

J. F. Navarro and S. D. M. White. Simulations of dissipative galaxy formation in hierarchically clustering universes-2. Dynamics of the baryonic component in galactic haloes. *MNRAS*, 267:401–412, March 1994.

S. G. Neff, D. A. Thilker, M. Seibert, A. Gil de Paz, L. Bianchi, D. Schiminovich, D. C. Martin, B. F. Madore, R. M. Rich, T. A. Barlow, Y.-I. Byun, J. Donas, K. Forster, P. G. Friedman, T. M. Heckman, P. N. Jelinsky, Y.-W. Lee, R. F. Malina, B. Milliard, P. Morrissey, O. H. W. Siegmund, T. Small, A. S. Szalay, B. Y. Welsh, and T. K. Wyder. Ultraviolet Emission from Stellar Populations within Tidal Tails: Catching the Youngest Galaxies in Formation? *ApJL*, 619:L91–L94, January 2005.

K. Nomoto, F.-K. Thielemann, and J. C. Wheeler. Explosive nucleosynthesis and Type I supernovae. *ApJL*, 279:L23–L26, April 1984.

T. Okamoto, V. R. Eke, C. S. Frenk, and A. Jenkins. Effects of feedback on the morphology of galaxy discs. *MNRAS*, 363:1299–1314, November 2005.

J. H. Oort. Outline of a theory on the origin and acceleration of interstellar clouds and O associations. *Bulletin of the Astronomical Institute of the Netherlands*, 12:177–+, September 1954.

B. W. O'Shea, K. Nagamine, V. Springel, L. Hernquist, and M. L. Norman. Comparing AMR and SPH Cosmological Simulations. I. Dark Matter and Adiabatic Simulations. *ApJS*, 160:1–27, September 2005.

J. P. Ostriker, P. J. E. Peebles, and A. Yahil. The size and mass of galaxies, and the mass of the universe. *ApJL*, 193:L1–L4, October 1974.

P. Padoan and Å. Nordlund. The Stellar Initial Mass Function from Turbulent Fragmentation. *ApJ*, 576:870–879, September 2002.

P. Padovani and F. Matteucci. Chemical Evolution of Galaxies and Quasar Metallicities. *ApJ*, 419:485–+, December 1993.

C. Park, D. N. Spergel, and N. Turok. Large-scale structure in a texture-seeded cold dark matter cosmogony. *ApJL*, 372:L53–L57, May 1991.

R. B. Partridge and D. T. Wilkinson. Isotropy and Homogeneity of the Universe from Measurements of the Cosmic Microwave Background. *Phys. Rev. Lett.*, 18:557–559, October 1967.

J. A. Peacock. *Cosmological Physics*. Cambridge University Press, 1999.

F. R. Pearce, A. Jenkins, C. S. Frenk, J. M. Colberg, S. D. M. White, P. A. Thomas, H. M. P. Couchman, J. A. Peacock, G. Efstathiou, and The Virgo Consortium. A Simulation of Galaxy Formation and Clustering. *ApJL*, 521:L99–L102, August 1999.

F. R. Pearce, A. Jenkins, C. S. Frenk, S. D. M. White, P. A. Thomas, H. M. P. Couchman, J. A. Peacock, and G. Efstathiou. Simulations of galaxy formation in a cosmological volume. *MNRAS*, 326:649–666, September 2001.

P. J. E. Peebles. Recombination of the Primeval Plasma. *ApJ*, 153:1–+, July 1968.

P. J. E. Peebles. *The Large-Scale Structure of the Universe*. Princeton University Press, Princeton NJ., 1981.

P. J. E. Peebles. Tracing galaxy orbits back in time. *ApJL*, 344:L53–L56, September 1989.

P. J. E. Peebles. The gravitational instability picture and the formation of the Local Group. *ApJ*, 362:1–13, October 1990.

P. J. E. Peebles, S. D. Phelps, E. J. Shaya, and R. B. Tully. Radial and Transverse Velocities of Nearby Galaxies. *ApJ*, 554:104–113, June 2001.

U.-L. Pen. Generating Cosmological Gaussian Random Fields. *ApJL*, 490:L127+, December 1997.

A. A. Penzias and R. W. Wilson. A Measurement of Excess Antenna Temperature at 4080 Mc/s. *ApJ*, 142:419–421, July 1965.

J. E. Pringle, R. J. Allen, and S. H. Lubow. The formation of molecular clouds. *MNRAS*, 327:663–668, October 2001.

V. Quilis. A new multidimensional AMR Hydro+Gravity Cosmological code. *astro-ph/*, 0405389, May 2004.

T. Quinn, N. Katz, J. Stadel, and G. Lake. Time stepping N-body simulations. *ArXiv Astrophysics e-prints*, October 1997.

S. W. Randall, C. L. Sarazin, and J. A. Irwin. XMM-Newton Observation of Diffuse Gas and Low-Mass X-Ray Binaries in the Elliptical Galaxy NGC 4649 (M60). *ApJ*, 636: 200–213, January 2006.

M. Rauch, J. Miralda-Escude, W. L. W. Sargent, T. A. Barlow, D. H. Weinberg, L. Hernquist, N. Katz, R. Cen, and J. P. Ostriker. The Opacity of the Ly alpha Forest and Implications for Omega B and the Ionizing Background. *ApJ*, 489:7–+, November 1997.

D. Reed, F. Governato, T. Quinn, J. Gardner, J. Stadel, and G. Lake. Dark matter subhaloes in numerical simulations. *MNRAS*, 359:1537–1548, June 2005a.

D. S. Reed, R. Bower, C. S. Frenk, L. Gao, A. Jenkins, T. Theuns, and S. D. M. White. The first generation of star-forming haloes. *MNRAS*, 363:393–404, October 2005b.

M. J. Rees and J. P. Ostriker. Cooling, dynamics and fragmentation of massive gas clouds - Clues to the masses and radii of galaxies and clusters. *MNRAS*, 179:541–559, June 1977.

B. W. Ritchie and P. A. Thomas. Multiphase smoothed-particle hydrodynamics. *MNRAS*, 323:743–756, May 2001.

E. Rosolowsky and L. Blitz. Molecular Cloud Formation in Disk Galaxies: The Case of M33. *Astrophysics and Space Science*, 289:265–268, January 2004.

P. N. Safier, C. F. McKee, and S. W. Stahler. Star Formation in Cold, Spherical, Magnetized Molecular Clouds. *ApJ*, 485:660–+, August 1997.

J. Salmon. Generation of Correlated and Constrained Gaussian Stochastic Processes for N-Body Simulations. *ApJ*, 460:59–+, March 1996.

J. K. Salmon and M. S. Warren. Skeletons from the Treecode Closet. *Journal of Computational Physics*, 111:136–155, April 1994.

E. E. Salpeter. Nuclear Reactions in Stars Without Hydrogen. *ApJ*, 115:326–328, March 1952.

E. E. Salpeter. The Luminosity Function and Stellar Evolution. *ApJ*, 121:161–+, January 1955.

D. B. Sanders, B. T. Soifer, J. H. Elias, B. F. Madore, K. Matthews, G. Neugebauer, and N. Z. Scoville. Ultraluminous infrared galaxies and the origin of quasars. *ApJ*, 325: 74–91, February 1988.

W. C. Saslaw. *Gravitational physics of stellar and galactic systems*. Cambridge: CUP, 1985.

C. Scannapieco, P. B. Tissera, S. D. M. White, and V. Springel. Feedback and metal enrichment in cosmological SPH simulations - II. A multiphase model with supernova energy feedback. *MNRAS*, 371:1125–1139, September 2006.

J. Schaye. Star Formation Thresholds and Galaxy Edges: Why and Where. *ApJ*, 609: 667–682, July 2004.

M. Schmidt. The distribution of mass in M 31. *Bulletin of the Astronomical Institute of the Netherlands*, 14:17–+, November 1957.

M. Schmidt. The Rate of Star Formation. *ApJ*, 129:243–+, March 1959.

J. M. Schombert, J. F. Wallin, and C. Struck-Marcell. A multicolor photometric study of the tidal features in interacting galaxies. *AJ*, 99:497–529, February 1990.

M. J. Seaton. Thermal Inelastic Collision Processes. *Reviews of Modern Physics*, 30:979–991, July 1958.

L. Sedov. *Similarity and Dimensional Methods in Mechanics*. New York: Academic Press, 1959, 1959.

M. S. Seigar, A. J. Barth, and J. S. Bullock. A Revised Mass Model For The Andromeda Galaxy. *ArXiv Astrophysics e-prints*, December 2006.

U. Seljak and M. Zaldarriaga. A Line-of-Sight Integration Approach to Cosmic Microwave Background Anisotropies. *ApJ*, 469:437–+, October 1996.

B. Semelin and F. Combes. Formation and evolution of galactic disks with a multiphase numerical model. *A&A*, 388:826–841, June 2002.

S. F. Shandarin and Y. B. Zeldovich. The large-scale structure of the universe: Turbulence, intermittency, structures in a self-gravitating medium. *Reviews of Modern Physics*, 61: 185–220, April 1989.

M. Smoluchowski. Temporary Title. *Physik Zeit.*, 17:557, 1916.

G. F. Smoot, C. L. Bennett, A. Kogut, E. L. Wright, J. Aymon, N. W. Boggess, E. S. Cheng, G. de Amici, S. Gulkis, M. G. Hauser, G. Hinshaw, P. D. Jackson, M. Janssen, E. Kaita, T. Kelsall, P. Keegstra, C. Lineweaver, K. Loewenstein, P. Lubin, J. Mather, S. S. Meyer, S. H. Moseley, T. Murdock, L. Rokke, R. F. Silverberg, L. Tenorio, R. Weiss, and D. T. Wilkinson. Structure in the COBE differential microwave radiometer first-year maps. *ApJL*, 396:L1–L5, September 1992.

P. M. Solomon, A. R. Rivolo, J. Barrett, and A. Yahil. Mass, luminosity, and line width relations of Galactic molecular clouds. *ApJ*, 319:730–741, August 1987.

R. S. Somerville and J. R. Primack. Semi-analytic modelling of galaxy formation: the local Universe. *MNRAS*, 310:1087–1110, December 1999.

D. N. Spergel, R. Bean, O. Dore', M. R. Nolta, C. L. Bennett, G. Hinshaw, N. Jarosik, E. Komatsu, L. Page, H. V. Peiris, L. Verde, C. Barnes, M. Halpern, R. S. Hill, A. Kogut, M. Limon, S. S. Meyer, N. Odegard, G. S. Tucker, J. L. Weiland, E. Wollack, and E. L. Wright. Wilkinson Microwave Anisotropy Probe (WMAP) Three Year Results: Implications for Cosmology. *ArXiv Astrophysics e-prints*, March 2006.

D. N. Spergel, L. Verde, H. V. Peiris, E. Komatsu, M. R. Nolta, C. L. Bennett, M. Halpern, G. Hinshaw, N. Jarosik, A. Kogut, M. Limon, S. S. Meyer, L. Page, G. S. Tucker, J. L. Weiland, E. Wollack, and E. L. Wright. First-Year Wilkinson Microwave Anisotropy Probe (WMAP) Observations: Determination of Cosmological Parameters. *ApJS*, 148: 175–194, September 2003.

V. Springel. The cosmological simulation code GADGET-2. *MNRAS*, 364:1105–1134, December 2005.

V. Springel and L. Hernquist. Cosmological smoothed particle hydrodynamics simulations: the entropy equation. *MNRAS*, 333:649–664, July 2002.

V. Springel and L. Hernquist. Cosmological smoothed particle hydrodynamics simulations: a hybrid multiphase model for star formation. *MNRAS*, 339:289–311, February 2003.

V. Springel and S. D. M. White. Tidal tails in cold dark matter cosmologies. *MNRAS*, 307:162–178, July 1999.

V. Springel, N. Yoshida, and S. D. M. White. GADGET: a code for collisionless and gasdynamical cosmological simulations. *New Astronomy*, 6:79–117, April 2001.

S. A. Stanford, A. I. Sargent, D. B. Sanders, and N. Z. Scoville. CO aperture synthesis of NGC 4038/39 (ARP 244). *ApJ*, 349:492–496, February 1990.

A. A. Starobinsky. Dynamics of phase transition in the new inflationary universe scenario and generation of perturbations. *Phys.Lett. B*, 117:175–178, October 1982.

P. J. Steinhardt. Cosmological perturbations: Myths and facts. *Mod. Phys. Lett. A*, 19: 967982, October 2004.

M. Steinmetz. GRAPESPH: cosmological smoothed particle hydrodynamics simulations with the special-purpose hardware GRAPE. *MNRAS*, 278:1005–1017, February 1996.

M. Steinmetz and E. Mueller. The formation of disk galaxies in a cosmological context: Populations, metallicities and metallicity gradients. *A&A*, 281:L97–L100, January 1994.

G. Stinson, A. Seth, N. Katz, J. Wadsley, F. Governato, and T. Quinn. Star formation and feedback in smoothed particle hydrodynamic simulations - I. Isolated galaxies. *MNRAS*, 373:1074–1090, December 2006.

D. Sugimoto, Y. Chikada, J. Makino, T. Ito, T. Ebisuzaki, and M. Umemura. A Special-Purpose Computer for Gravitational Many-Body Problems. *Nature*, 345:33–+, May 1990.

R. A. Sunyaev and I. B. Zeldovich. Microwave background radiation as a probe of the contemporary structure and history of the universe. *ARA&A*, 18:537–560, 1980.

R. S. Sutherland and M. A. Dopita. Cooling functions for low-density astrophysical plasmas. *ApJS*, 88:253–327, September 1993.

g. 't Hooft. Magnetic monopoles in Unified Gauge Theories. *Nucl. Phys.*, B79:276–284, October 1974.

G. A. Tammann. Remarks on Outlying Supernovae and the Structure of Their Parent Galaxies. In C. B. Cosmovici, editor, *ASSL Vol. 45: Supernovae and Supernova Remnants*, pages 215–+, 1974.

G. A. Tammann. Supernova statistics and related problems. In V. L. Trimble, editor, *NATO ASIC Proc. 90: Supernovae: A Survey of Current Research*, pages 371–403, November 1982.

S. Tang and Q. D. Wang. Supernova Blast Waves in Low-Density Hot Media: A Mechanism for Spatially Distributed Heating. *ApJ*, 628:205–209, July 2005.

R. Teyssier. Cosmological hydrodynamics with adaptive mesh refinement. A new high resolution code called RAMSES. *A&A*, 385:337–364, April 2002.

F.-K. Thielemann, K. Nomoto, and M.-A. Hashimoto. Core-Collapse Supernovae and Their Ejecta. *ApJ*, 460:408–+, March 1996.

K. Thornton, M. Gaudlitz, H.-T. Janka, and M. Steinmetz. Energy Input and Mass Redistribution by Supernovae in the Interstellar Medium. *ApJ*, 500:95–+, June 1998.

P. B. Tissera, D. G. Lambas, S. A. Cora, and M. B. Mosconi. Nitrogen abundances in damped Lyman α systems: the combined effects of SNII and SNIa in a hierarchical clustering scenario. *MNRAS*, 337:L27–L30, December 2002.

A. Toomre. Mergers and Some Consequences. In B. M. Tinsley and R. B. Larson, editors, *Evolution of Galaxies and Stellar Populations*, pages 401–+, 1977.

A. Toomre and J. Toomre. Galactic Bridges and Tails. *ApJ*, 178:623–666, December 1972.

G. Tormen. The rise and fall of satellites in galaxy clusters. MNRAS, 290:411–421, September 1997.

C. Travaglio, K. Kifonidis, and E. Müller. Nucleosynthesis in multi-dimensional simulations of SNII. *New Astronomy Review*, 48:25–30, February 2004.

G. Trinchieri, G. Fabbiano, and C. R. Canizares. The X-ray surface brightness distribution and spectral properties of six early-type galaxies. *ApJ*, 310:637–659, November 1986.

W. H. Tucker and R. J. Gould. Radiation from a Low-Density Plasma at 10^6K - 10^8K. *ApJ*, 144:244–+, April 1966.

J. M. van der Hulst. The kinematics and distribution of neutral hydrogen in the interacting galaxy pair NGC 4038/39. *A&A*, 71:131–140, January 1979.

B. van Leer. Towards the ultimate conservative difference scheme. V. A second-order sequel to Godunov's method. *Journal of Computational Physics*, 32:101–136, October 1979.

K. Wada, G. Meurer, and C. A. Norman. Gravity-driven Turbulence in Galactic Disks. *ApJ*, 577:197–205, September 2002.

J. W. Wadsley and J. R. Bond. SPH P-cubed MG Simulations of the Lyman Alpha Forest. In D. A. Clarke and M. J. West, editors, *ASP Conf. Ser. 123: Computational Astrophysics; 12th Kingston Meeting on Theoretical Astrophysics*, pages 332–+, 1997.

J. W. Wadsley, J. Stadel, and T. Quinn. Gasoline: a flexible, parallel implementation of TreeSPH. *New Astronomy*, 9:137–158, February 2004.

D. Walsh, R. F. Carswell, and R. J. Weymann. 0957 + 561 A, B - Twin quasistellar objects or gravitational lens. *Nature*, 279:381–384, May 1979.

M. L. Weil, V. R. Eke, and G. Efstathiou. The formation of disc galaxies. *MNRAS*, 300: 773–789, November 1998.

J. C. Wheeler and R. Levreault. The peculiar Type I supernova in NGC 991. *ApJL*, 294: L17–L20, July 1985.

J. Whelan and I. J. Iben. Binaries and Supernovae of Type I. *ApJ*, 186:1007–1014, December 1973.

S. D. M. White. Formation and Evolution of Galaxies: Lectures Given at Les Houches, August 1993. *ArXiv Astrophysics e-prints*, October 1994.

S. D. M. White, C. S. Frenk, and M. Davis. Clustering in a neutrino-dominated universe. *ApJL*, 274:L1–L5, November 1983.

S. D. M. White and M. J. Rees. Core condensation in heavy halos - A two-stage theory for galaxy formation and clustering. *MNRAS*, 183:341–358, May 1978.

L. M. Widrow and N. Kaiser. Using the Schroedinger Equation to Simulate Collisionless Matter. *ApJL*, 416:L71+, October 1993.

J. P. Williams and C. F. McKee. The Galactic Distribution of OB Associations in Molecular Clouds. *ApJ*, 476:166–+, February 1997.

C. D. Wilson and N. Scoville. The properties of individual giant molecular clouds in M33. *ApJ*, 363:435–450, November 1990.

C. D. Wilson, N. Scoville, S. C. Madden, and V. Charmandaris. High-Resolution Imaging of Molecular Gas and Dust in the Antennae (NGC 4038/39): Super Giant Molecular Complexes. *ApJ*, 542:120–127, October 2000.

M. G. Wolfire, D. Hollenbach, C. F. McKee, A. G. G. M. Tielens, and E. L. O. Bakes. The neutral atomic phases of the interstellar medium. *ApJ*, 443:152–168, April 1995.

L. Woltjer. Supernovae and the Interstellar Medium. In *IAU Symp. 39: Interstellar Gas Dynamics*, pages 229–+, 1970.

L. Woltjer. Supernova Remnants. *ARA&A*, 10:129–+, 1972.

P. Woodward and P. Colella. The Numerical Simulation of Two-Dimensional Fluid Flow with Strong Shocks. *Journal of Computational Physics*, 54:115–175, April 1984.

S. E. Woosley and T. A. Weaver. The physics of supernova explosions. *ARA&A*, 24: 205–253, 1986.

S. E. Woosley and T. A. Weaver. The Evolution and Explosion of Massive Stars. II. Explosive Hydrodynamics and Nucleosynthesis. *ApJS*, 101:181–+, November 1995.

G. Xu. A New Parallel N-Body Gravity Solver: TPM. *ApJS*, 98:355–+, May 1995.

J. Yang, M. S. Turner, D. N. Schramm, G. Steigman, and K. A. Olive. Primordial nucleosynthesis - A critical comparison of theory and observation. *ApJ*, 281:493–511, June 1984.

G. Yepes, R. Kates, A. Khokhlov, and A. Klypin. Hydrodynamical simulations of galaxy formation: effects of supernova feedback. *MNRAS*, 284:235–256, January 1997.

D. G. York, J. Adelman, J. E. Anderson, Jr., S. F. Anderson, J. Annis, N. A. Bahcall, J. A. Bakken, R. Barkhouser, S. Bastian, E. Berman, W. N. Boroski, S. Bracker, C. Briegel, J. W. Briggs, J. Brinkmann, R. Brunner, S. Burles, L. Carey, M. A. Carr, F. J. Castander, B. Chen, P. L. Colestock, A. J. Connolly, J. H. Crocker, I. Csabai, P. C. Czarapata, J. E. Davis, M. Doi, T. Dombeck, D. Eisenstein, N. Ellman, B. R. Elms, M. L. Evans,

X. Fan, G. R. Federwitz, L. Fiscelli, S. Friedman, J. A. Frieman, M. Fukugita, B. Gillespie, J. E. Gunn, V. K. Gurbani, E. de Haas, M. Haldeman, F. H. Harris, J. Hayes, T. M. Heckman, G. S. Hennessy, R. B. Hindsley, S. Holm, D. J. Holmgren, C.-h. Huang, C. Hull, D. Husby, S.-I. Ichikawa, T. Ichikawa, Ž. Ivezić, S. Kent, R. S. J. Kim, E. Kinney, M. Klaene, A. N. Kleinman, S. Kleinman, G. R. Knapp, J. Korienek, R. G. Kron, P. Z. Kunszt, D. Q. Lamb, B. Lee, R. F. Leger, S. Limmongkol, C. Lindenmeyer, D. C. Long, C. Loomis, J. Loveday, R. Lucinio, R. H. Lupton, B. MacKinnon, E. J. Mannery, P. M. Mantsch, B. Margon, P. McGehee, T. A. McKay, A. Meiksin, A. Merelli, D. G. Monet, J. A. Munn, V. K. Narayanan, T. Nash, E. Neilsen, R. Neswold, H. J. Newberg, R. C. Nichol, T. Nicinski, M. Nonino, N. Okada, S. Okamura, J. P. Ostriker, R. Owen, A. G. Pauls, J. Peoples, R. L. Peterson, D. Petravick, J. R. Pier, A. Pope, R. Pordes, A. Prosapio, R. Rechenmacher, T. R. Quinn, G. T. Richards, M. W. Richmond, C. H. Rivetta, C. M. Rockosi, K. Ruthmansdorfer, D. Sandford, D. J. Schlegel, D. P. Schneider, M. Sekiguchi, G. Sergey, K. Shimasaku, W. A. Siegmund, S. Smee, J. A. Smith, S. Snedden, R. Stone, C. Stoughton, M. A. Strauss, C. Stubbs, M. SubbaRao, A. S. Szalay, I. Szapudi, G. P. Szokoly, A. R. Thakar, C. Tremonti, D. L. Tucker, A. Uomoto, D. Vanden Berk, M. S. Vogeley, P. Waddell, S.-i. Wang, M. Watanabe, D. H. Weinberg, B. Yanny, and N. Yasuda. The Sloan Digital Sky Survey: Technical Summary. *AJ*, 120: 1579–1587, September 2000.

J. S. Young, L. Allen, J. D. P. Kenney, A. Lesser, and B. Rownd. The Global Rate and Efficiency of Star Formation in Spiral Galaxies as a Function of Morphology and Environment. *AJ*, 112:1903–+, November 1996.

J. S. Young and N. Z. Scoville. Molecular gas in galaxies. *ARA&A*, 29:581–625, 1991.

S. Zaroubi and J. Silk. LOFAR as a probe of the sources of cosmological reionization. *MNRAS*, 360:L64–L67, June 2005.

Y. B. Zel'Dovich. Gravitational instability: an approximate theory for large density perturbations. *A&A*, 5:84–89, March 1970.

F. Zwicky. Die Rotverschiebung von extragalaktischen Nebeln. *Helvetica Physica Acta*, 6: 110–127, 1933.